THE UNIVERSITY *of* EDINBURGH

The optical and X-ray properties of galaxy clusters

Maria Manolopoulou

Doctor of Philosophy
The University of Edinburgh
July 2018

Abstract

Galaxy clusters are very useful astronomical tools; they are used as a means to study galaxy formation and evolution, large scale structure, but also as probes to constrain cosmological parameters. This work aims to explore some of the uses of galaxy clusters in cosmology by constructing an optically confirmed X-ray selected galaxy cluster catalogue and studying various aspects of galaxy clusters and their effect on cosmology.

I introduce the theoretical background of this work, describing the current cosmological model, the properties, dynamics and use of galaxy clusters. I describe the main tools that were used to create the XMM Cluster Survey (XCS) DR2 cluster catalogue in the SDSS region and proceed with a thorough outline of the construction and properties of the clusters in the catalogue.

The properties of these clusters, along with clusters from optical catalogues and clusters from simulations were studied further as a function of their environment. Possible differences in the properties, mass functions and luminosity–temperature relation of clusters in different environments show the influence of the latter on the formation and growth of galaxy clusters. Moreover, those differences can affect the results of cosmological studies that do not take into account this environmental selection effect.

Finally, I study the rotation of the constituents of the galaxy clusters. Rotating cluster galaxy members can change the result of the calculation of the virial mass of the galaxy clusters that is used in many types of studies, amongst which is cosmology.

A comparison of the rotation of the different constituents of the clusters give insight on their formation and the processes happening during their lifetime.

I close with the conclusions of the studies of galaxy clusters and the future prospects of this work.

Lay Summary

Large groups of galaxies, galaxy clusters, are useful astronomical tools that give insight to a range of questions, such as how galaxies form and evolve and what is the past and future of the Universe and its constituents. I introduce the theoretical background by describing our current knowledge of the Universe and the properties, dynamics and use of galaxy clusters as astronomical tools.

In order to use the galaxy clusters as described, the XMM Cluster Survey creates a catalogue of galaxy clusters selected by their emission on X-ray frequencies. Its construction and its optical and X-ray properties are thoroughly described in this thesis. Using the properties of this catalogue, such as the brightness and temperature, together with some other X-ray and optically selected cluster catalogues from both observational and simulation data, I attempt to find differences originating from the environment that the clusters reside, whether that is overdense or underdense. These differences should be taken into account when clusters are used to probe the Universe's constituents. Finally, I study the rotation of the clusters' constituents around an axis that passes through the cluster centre. A possible rotation should also be accounted for when calculating the masses of clusters to use them on studies of the Universe's lifetime and fate.

Declaration

I declare that this thesis was composed by myself, that the work contained herein is my own except where explicitly stated otherwise in the text, and that this work has not been submitted for any other degree or professional qualification except as specified.

The work presented in Chapter 5 was previously published in MNRAS as "Galaxy cluster's rotation" by M. Manolopoulou and M. Plionis (Manolopoulou and Plionis, 2017). This study was conceived by all of the authors. I carried out the vast majority of the work apart from Sections 5.5.3.4, 5.6.3.4 and 5.6.3.5. Exact details are described in the preface to that chapter .

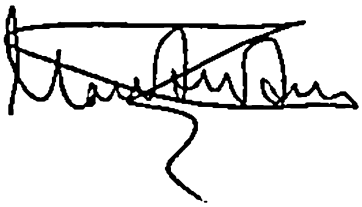

(*Maria Manolopoulou, July 2018*)

Acknowledgements

The journey of my PhD studies has been tough, exciting, stressful, rewarding and has taught me many lessons. Surely, I would not have reached this stage without the help of special people around me.

First of all, I want to thank the PCDS scheme which has provided the valuable means for me to do my studies at that top quality university, the University of Edinburgh. It has been a blessing for me to be given this opportunity; becoming an astronomer has been a dream coming true. I want to thank my supervisor, Bob Mann, for his valuable guidance, advice, support and patience through my studies, when I only had questions, uncertainty and impatience. When I started my PhD, I became member of the XCS collaboration, a group of people that have made me feel an equal and important member and has taught me how collaborating is the best way of achieving results. My special thanks go to Kathy Romer, who has supported, guided and believed in me throughout this. Moreover, even though we have not had much contact the last few years, I am grateful to have met and been a student of Manolis Plionis; he is the person who gave me the opportunity of doing astronomical research, believed in me and helped a great amount for me to become a PhD student. During my studies in Edinburgh, Toni Collis has been my mentor and has given me invaluable advice on keeping my PhD insecurities under control.

However, this journey being mostly mental, people outside my studies have contributed in making my time during this journey more enjoyable. I spent the majority of my free time in Edinburgh playing volleyball and beach volleyball, where I met a lot of nice people and made many good friends. It was definitely a great break from studies to play beach volleyball across all Scotland, with the non-beach volleyball-friendly Scottish weather and with amazing company, followed by pot luck dinners and dancing. My Italian friends have always made sure I have the best home-cooked dinners to keep me strong and motivated and have taught me about Italian culture. In addition to all the people in Edinburgh, people that even though we far away from me, supported me using technological advancements. Of course, my parents supporting me literally every day of this journey and being there whenever I needed, as always. Dafy as well. My Greek friends from all around Europe have been there in their own unique way. Last but not least, a huge thanks to the most patient person I have ever known, who has supported me greatly in going through these times, my partner, Kris.

Contents

List of Figures

List of Tables

Chapter 1

Introduction

1.1 Thesis aims

This thesis presents a galaxy cluster catalogue and studies the properties and dynamics of galaxy clusters and their effect on cosmological studies. Galaxy clusters are great tools in astronomy, used in a variety of studies. The details of their formation, their large scale properties such as mass and luminosity, and their number density, are invaluable tools to determine the cosmological parameters of the Universe and discover its beginning, growth and future. Galaxy clusters host a unique group of galaxies that nowhere else in the Universe are found, the red, old, elliptical galaxies, the clusters' red sequence. They are also the birthplaces of supermassive black holes that release huge amounts of energy and affect the thermodynamics of the galaxy clusters themselves and the life of the galaxy members substantially. Galaxy clusters are remarkable objects. They are the main subject of this thesis and, through it, the reader can, hopefully, become convinced of their importance.

The thesis thoroughly describes the construction of an optically confirmed X-ray selected cluster catalogue, using a variety of new and existing tools, which is aimed to be used for all the different research topics mentioned earlier. It explores the

optical and X-ray properties of the galaxy clusters residing in various environments and the influence their differences have on cosmological studies using galaxy clusters. Finally, it explores the dynamics of the galaxy clusters by focusing on the rotation of the constituents of the galaxy clusters. The conclusions extracted from this enrich our knowledge of the formation and growth of the galaxy clusters and introduce corrections in the calculation of their mass for cosmological studies.

In this Section, I will describe the various background areas that are covered in this introduction in order to give the reader the information needed to comprehend the rest of this thesis. I will begin with an introduction to Cosmology, describing the current cosmological model and its main dynamical and observational properties, a topic that is essential to understand why we need to constrain the cosmological parameters and what measurements we have available for that task. I will describe the observed large-scale structure of the Universe today and the current status of the quest to constrain the cosmological parameters.

Following that, I will present a thorough description of the largest overdensities of the large scale structure of the Universe, the galaxy clusters. I will outline their constituents and their observational signatures. I will describe methods for calculating their masses and follow with the various methods clusters can be used to constrain cosmological parameters. To end up, I will describe current galaxy cluster catalogues that are used mainly but not only for cosmological studies. This is an introduction that sets up the foundation of understanding how the cluster catalogue in Chapter 3 is created and how it can be used to constrain cosmological parameters. It also explains the dynamical status of galaxy clusters, which is used extensively in Chapter 5 to introduce corrections when calculating dynamical cluster masses.

Finally, in order for someone to study the environmental effects on the properties of clusters, (s)he needs to understand the various large scale environments. Therefore, in the last part of this chapter, I will introduce the largest underdensities of the Universe, the voids. I will discuss the methods of creating void catalogues that will be useful in Chapter 4 in order to define the large scale density of the environments in which a cluster resides.

1.2 Cosmology

Here, I give the reader an introduction to the current cosmological model: the history of the Universe, its dynamics, properties, constituents, structures of the Cosmic Web and the cosmological parameters describing the model. I describe how astronomers use observational measures and probes to constrain cosmological parameters. For a more thorough study of Cosmology one should consider reading Peacock (1999).

1.2.1 The current cosmological model

Our Universe is expanding, as Edwin Hubble discovered in 1929 while studying the distance and luminosity of variable stars called Cepheids in various galaxies (Hubble, 1929). This expansion is isotropic, meaning it is the same in all directions and from any observer (cosmological principle). Therefore, the Universe is also homogeneous, i.e. it has the same density everywhere at a given time (Lemaître, 1931).

1.2.1.1 The history until today

Knowing that the Universe is expanding and, therefore, its density is decreasing, that means that in the past it used to have very high density and temperature. These were the conditions soon after the Big Bang occurred.

Our knowledge originates when classical physics begin to describe the Universe, after the so-called Planck time (10^{-43} s). At that time, the Universe is in thermal equilibrium due to its high density. For almost any particle there is a corresponding antiparticle until the temperature drops under 10^{13} K. The particles and antiparticles annihilate, the density drops and the leftovers are particles without corresponding antiparticles (matter-antimatter asymmetry; Bonometto and Matarrese, 1982).

Under the assumption of adiabatic expansion, the Universe must have been dominated by radiation at some point in the past, before matter-radiation equality took place. At

Table 1.1 *Important events in the early history of the Universe. In the second column the temperature of the Universe in Kelvin is given and its age is in column three.*

	T(K)	Age
Classical physics starts	10^{32}	10^{-43}s
Grand unification	10^{28}	10^{-36}s
Electroweak unification	$10^{15.5}$	10^{-12}s
Nucleosynthesis	10^{10}	1 s
Radiation domination	9,500	$10^{4.7}$yrs
Recombination	3,000	$10^{5.6}$yrs

these times, photons were very energetic and interacted with matter, a fact that makes the Universe's temperature to be dictated by radiation. Hydrogen and Deuterium were the only nuclei that existed at that time, until temperature dropped enough for Deuterium to survive in order to then produce Helium. The density and temperature were high enough to prevent the stability of heavier elements such as Iron. When the Universe's temperature dropped enough, after the matter-radiation equality, ions could form neutral atoms; this was the recombination epoch. Photons used to be trapped in the ionised plasma which caused them to continuously scatter, but now they were free to travel and to be detected by humans today. This is the earliest in the history of Universe we can detect non-scattered photons from. The first "light" we observe from the Universe is called "Cosmic Microwave Background" (hereafter CMB) and was discovered accidentally in 1965 by Penzias and Wilson (Penzias and Wilson, 1965). The astonishing isotropy of the CMB radiation measured later is an important confirmation of the validity of the cosmological model. Its dipole anisotropy observed is entirely attributed to the motion of the Earth. In Table 1.1, some of the main events of the Universe history are displayed.

In order to explain several problems of the cosmological model that are beyond the aims of this thesis to describe, the epoch of inflation was inserted in the history of the Universe, following the Planck era (Guth, 2000; Linde, 2000; Steinhardt, 2000). During inflation, the Universe expanded at an ever-increasing rate, which initiated the later Hubble expansion. Initial perturbations grew by orders of magnitude, the particle horizon was extended in order all particles to be in causal connection with

each other and any curvature of the Universe at the time was smoothed out to end up with a very flat Universe today.

1.2.1.2 Mathematical foundation and dynamics of the Universe

Having established the history of the Universe until today, we can now discuss its dynamics and extract some of its properties using maths. Consider a distribution of galaxies expanding uniformly; this resembles a picture being magnified continuously. The expansion is the same as seen by any observer in the distribution, which means there is no centre of expansion - there is no centre of the Universe. Assuming the coordinates of the observer are $\mathbf{x}(t)$ and the expansion is described by the scale factor $R(t)$, then the observer's position is

$$\mathbf{x}(t) = R(t)\mathbf{x}(t_0), \tag{1.1}$$

where t_0 is an earlier time than t. By differentiating with respect to time t, this becomes

$$\dot{\mathbf{x}}(t) = \dot{R}(t)\mathbf{x}(t_0) = \frac{\dot{R}(t)}{R(t)}\mathbf{x}(t) = H(t)\mathbf{x}(t), \tag{1.2}$$

where $H(t)$ is the Hubble constant as a function of time.

Newton's gravity can only locally describe the expanding Universe and Einstein's general relativity needs to be used in order to describe it as a whole (Einstein, 1917). According to the latter, space and time are coupled and gravity can distort the geometry of spacetime. The metric used to describe the time interval between two events assuming isotropy is the Robertson-Walker (Robertson (1935); Walker (1935), RW hereafter) metric

$$c^2 d\tau^2 = c^2 dt^2 - R^2(t)[dr^2 + S_k^2(r)d\psi^2], \tag{1.3}$$

where r is the radial direction, c the speed of light, $R(t)$ the scale factor and $S_k(r)$ is

a function that depends on the geometry of the Universe (its curvature k) such that

$$S_k(r) = \begin{cases} \sin r, & \text{when} \quad k = 1, \\ \sinh r, & \text{when} \quad k = -1, \\ r, & \text{when} \quad k = 0 \end{cases} \tag{1.4}$$

Light travels in null geodesics, with the equation of motion being $dr = cdt/R(t)$. A photon travelling in the Universe has its wavelength stretched due to the expansion. If we consider two photons emitted at different times (and observed in equally different times) and travelling a constant comoving distance r, that would mean that

$$dt_{emit}/dt_{obs} = R(t_{emit})/R(t_{obs}). \tag{1.5}$$

Applying the same to the photons frequency, we get

$$v_{emit}/v_{obs} = R(t_{obs})/R(t_{emit}) \equiv 1 + z, \tag{1.6}$$

with z being called the redshift.

The dynamics of the Universe are described by a differential equation of motion that can be constructed by Newtonian physics but needs Einstein's general relativity equations in order to be proved. This is Friedmann's equation:

$$\dot{R}^2 - \frac{8\pi G}{3}\rho R^2 = -kc^2, \tag{1.7}$$

where G is the gravitational constant and ρ is the density of the Universe. Its importance is that it connects the geometry of the Universe with its density. The history of the scale factor R describes the dynamics and constituents of the Universe. There is a critical density $\rho_C = 3H^2/8\pi G$, for which $k = 0$ and the Universe has flat geometry. A universe with higher density than the critical is spatially closed, whereas a universe with lower density is an open universe. The dimensionless density parameter $\Omega = \rho/\rho_C$ is more often used to describe the dynamics of the Universe.

It is conventional to model the contents of the Universe as perfect fluids with their corresponding equation of state. Dividing the Universe in its three constituents, three perfect fluids, namely matter, radiation and vacuum energy, and using the equation of state $P = w\rho c^2$, which is different for each of them, allows us to learn about the history of the scale factor. For non-relativistic matter $w \approx 0$ and so $\rho \propto R^{-3}$, radiation with $w = 1/3$ and so $\rho \propto R^{-4}$ and vacuum evergy with $w = -1$ and so ρ constant, to be the Universe constituents and $k = 0$ (flat Universe) and using the normalised scale factor $a = R/R_0$, we get a form of Friedmann's equation (Friedmann, 1922) which is:

$$\frac{8\pi G\rho}{3} = H_0^2(\Omega_v + \Omega_m a^{-3} + \Omega_r a^{-4}), \tag{1.8}$$

with H_0 being the present value of the Hubble constant. The current values of H_0, Ω_v and Ω_m are given in Table 1.2. The vacuum energy is believed to be the cause of the expansion of the Universe; if the Universe contained only matter, the latter's pressure would keep the Universe's density constant in contrary to the density decrease with time that is observed. This idea was first proposed by Eddington (Eddington, 1932) and is the only explanation to the reason the Universe is expanding today. The solution of the Friedmann equation for a non-zero curvature is not straightforward and gives the dynamics of the constituents and the Universe itself.

However, it is simple enough to calculate the age of the Universe through the Friedmann equation. From equation 1.6, we can get

$$\frac{dz}{dt} = -\frac{R_0}{R^2}\frac{dR}{dt} = -H(z)\frac{R_0}{R} = -H(z)(1+z) \Rightarrow dt = \frac{dz}{(1+z)H(z)}, \tag{1.9}$$

which gives the age of the Universe by integrating from zero to infinity, given a known $H(z)$.

1.2.2 Observational cosmology

When trying to study the Universe through observations, there is only little information a cosmologist can extract from them. Therefore, this information needs to be

converted to physical properties of the objects observed to enable their further study.

A monochromatic flux density of an object can be converted to its luminosity L_v by assuming isotropic emission, using equation:

$$S_v(v_0) = \frac{L_v((1+z)v_0)}{4\pi(R_0 S_k(r))^2(1+z)}, \tag{1.10}$$

where v_0 is the observed frequency of the photons. The luminosity is divided by $4\pi(R_0 S_k(r))^2$ because the flux is radiated within a sphere and is divided by $1+z$ because the photon energies are redshifted. The emission frequency of the photons must be $v_0(1+z)$. One can integrate to find the bolometric luminosity of the object by assuming a luminosity law.

Using the redshift-time equation 1.9 one can convert the redshift of an object to its proper distance R_0 by replacing $dt = R_0 dr$. There are two additional distance measures used in cosmology, depending on the nature of the detection of the object:

- the angular diameter distance $d_A = (1+z)^{-1} R_0 S_k(r)$, which is calculated by comparing the expected size of an object to its angular extent on the sky,
- the luminosity distance $d_L = (1+z) R_0 S_k(r)$, the distance calculated for an object with known luminosity.

Another measurement for a cosmological object is its absolute magnitude M. This is the apparent magnitude m the object would have if it was at a luminosity distance of 10 pc from the observer and is given by

$$m = M + 5\log_{10}\frac{d_L}{10} + K(z), \tag{1.11}$$

where $K(z)$ is a correction that takes into account the flux dimming of the object radiating at a certain wavelength as a function of redshift with respect to its bolometric flux. For an assumed power-law luminosity, it is given by $K(z) = 2.5(\alpha - 1)\log_{10}(1+z)$ and is called K-correction (a description is given in Hogg et al., 2002).

An important tool in observational cosmology is the number density of sources with

luminosities between L and $L + dL$, the luminosity function $\phi(L)$. This is described by a Schechter function for a certain redshift (Schechter, 1976),

$$\phi(L)dL = \phi^*(L/L^*)^\alpha \exp^{-L/L^*} dL, \tag{1.12}$$

where ϕ^* is the normalisation factor, L^* is a characteristic luminosity and α is the faint-end slope. The luminosity function evolves with time either due to density evolution of the population or due to luminosity evolution. The evolution of the galaxy population is expected, since during their lifetime star formation begins to cease, gas runs out in the interstellar medium and the galaxies begin to become redder and to have fainter luminosities.

1.2.3 Large scale structure

We have discussed how the Universe was created, how it reached its current state and what information we can extract by observing it. But what can we see when observing the Universe today? What are the structures and how were they created?

The structure observed today was created from small perturbations $\delta(\mathbf{x})$ in the density field $\rho(\mathbf{x})$, where

$$\delta(\mathbf{x}) \equiv \frac{\rho(\mathbf{x}) - \langle\rho\rangle}{\langle\rho\rangle}, \tag{1.13}$$

which led to the mean variance of the perturbations $\langle\delta^2\rangle$ to be the sum of the power spectrum $|\delta_k|^2$ of the perturbations:

$$\langle\delta^2\rangle = \sum |\delta_k|^2. \tag{1.14}$$

This is a proxy of the abundance of structures of different sizes and allows us to study how the growth of structure varies in different scales. Small linear initial perturbations of $\delta << 1$ create gravitational instabilities which grow with time and expand. The instability reaches a maximum volume before it collapses under its own gravity. Random motions of the particles will occur due to the non-zero density of

the background and the new object will eventually reach its virial equilibrium, when its kinetic energy K is related to its potential energy V as $V = -2K$. This structure formation mechanism created the large scale structure of the Universe we observe today.

The observed galaxies are large conglomerations of stars and gas. They have morphologies that were categorised by Edwin Hubble in 1926 for the first time (Hubble, 1927): the large, early-type, elliptical galaxies and the smaller, late-type spiral galaxies. The former have redder colours, stellar members with random motions, low star formation rate and low amounts of gas. The latter have the shape of a disk with large amounts of gas where stars are born and usually display rotation around the centre of their disk.

Galaxies form groups and even larger clusters of galaxies that can have up to thousands of galaxy members. These are trapped in the large gravitational well together with large amounts of very hot gas that radiates at X-ray wavelengths. Galaxy clusters are the largest virialised objects of the Cosmic Web. More details about galaxy clusters will be discussed in Section 1.3.

Galaxy clusters, groups and galaxies form even larger, one or two-dimensional structures, the filaments and walls respectively (Bond et al., 1996). These intersect in areas where the largest overdensities of the Universe are seen, the superclusters. Superclusters accrete mass through axes aligned to the filaments, have elongated shapes and continue to accrete mass until today. This cosmic structure leaves the rest of the available space underdense over large volumes of the Universe that are called voids. A more detailed description of the voids follows in Section 1.4. A picture of the observed Cosmic Web is shown in Fig. 1.1.

1.2.4 Precision cosmology

Cosmology today has moved to seeking the details in order to constrain the cosmological model as accurately as possible.

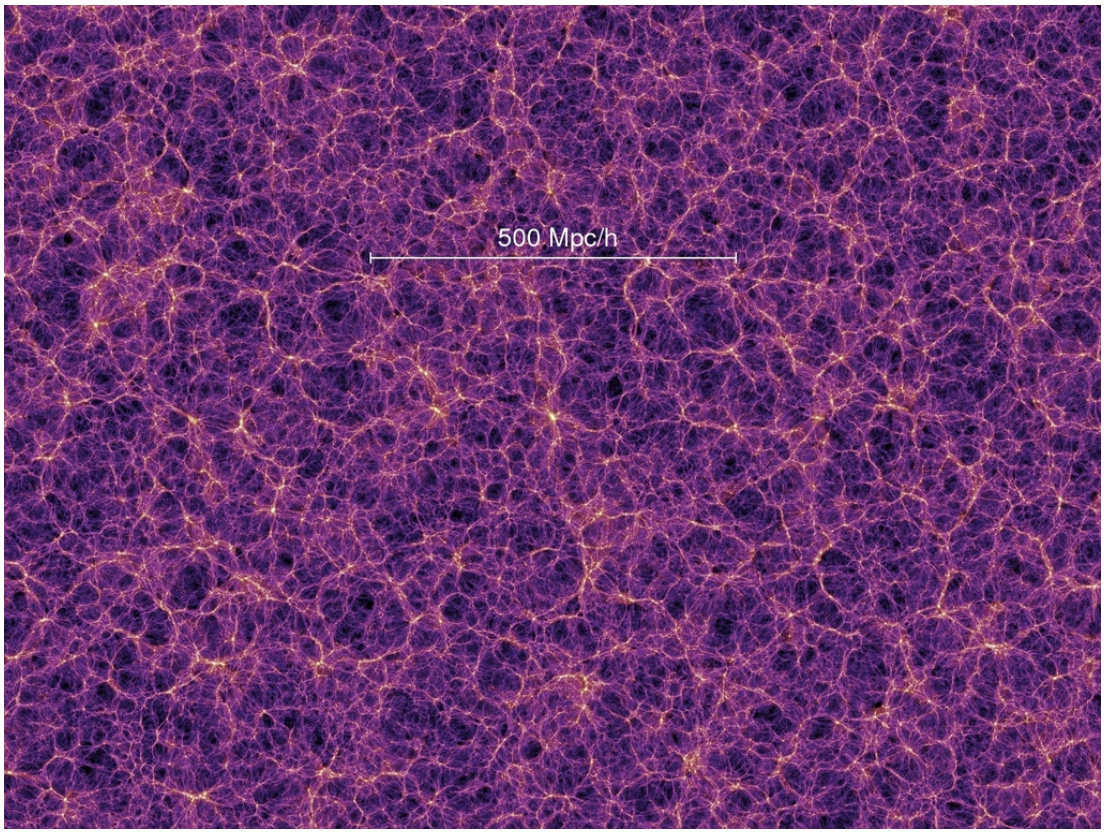

Figure 1.1 *The Cosmic Web structure as seen today, with voids, filaments, walls and superclusters, reproduced by the Millennium Simulation Project (Springel et al., 2005).*

Observations of the luminous mass of the Coma cluster and the motions of its galaxy members by Zwicky in 1933 forced him to propose a new form of non-luminous matter that interacts mainly by gravity, the dark matter (Zwicky, 1933). The existence of dark matter has been shown in many independent studies thereafter, mainly by measurements of the velocities of the stars in galaxies that were larger than expected assuming Kepler's law of rotational motion (Oort, 1932).

Modern cosmology tries to determine the cosmological model by constraining the cosmological parameters that affect the shape, size and abundance of the structure we observe today. A hierarchical structure formation model is accepted today, where smaller structures are created first; they create groups due to gravitational attraction and further collapse creating larger structures and so on. The cosmological parameters include: the density of the matter Ω_m, baryonic and non-baryonic; the density of the radiation Ω_r; the density of the vacuum energy, or as cosmologists named it, dark energy, Ω_v; the current value of the Hubble parameter H_0; the dark energy equation of state parameter w; and the normalisation of the power spectrum σ_8.

There are many ways in modern cosmology to constrain cosmological parameters, each of which suffers from different degeneracies, a fact that makes the ideal constraints to come from the combination of different probes. Many surveys and telescopes have dedicated their research to the quest for cosmological constraints and have obtained measurements with astonishing accuracy. In Table 1.2, some of the most recent constraints of cosmological parameters from the Planck collaboration combined with other probes are shown (Planck Collaboration et al., 2016b). However, for cosmology, the devil is in the detail; in order to gain all knowledge of our Universe, the quest has to continue.

Galaxy clusters are very important tools in constraining cosmology and are extensively used in many ways for that reason. In Section 1.3 I will describe the use of clusters as cosmological probes extensively.

Table 1.2 *Recent constraints on cosmological parameters from the Planck collaboration (Planck Collaboration et al., 2016b).*

Parameter	Measurement	68% uncertainty
H_0	67.74	0.46
Ω_v	0.6911	0.0062
Ω_m	0.3089	0.0062
σ_8	0.8159	0.0086

1.3 Galaxy clusters

Galaxy clusters are the main topic of this thesis and this Section aims to give a detailed description of them. I start with their constituents, followed by detection mechanisms and the measurement of the most important cosmological probe, the cluster mass. A description of their use in cosmology is a large part of this Section, which concludes with discussion of the construction of cluster catalogues that are used for cluster cosmology.

1.3.1 Constituents

Galaxy clusters are the largest gravitationally bound objects in the Universe. According to studies of their luminous matter, 90% of their matter is dark matter, which forms spherical halos, the cluster halos, and dictates the gravitational potential of the clusters. The density of the dark matter cluster halos has been found to follow the Navarro-Frenk-White (NFW hereafter) profile (Navarro et al., 1997):

$$\rho(r) \propto \frac{1}{\frac{r}{r_s}\left(1+\frac{r}{r_s}\right)^2}, \tag{1.15}$$

where r_s is the scale radius, the radius at which the profile agrees with the isothermal profile ($\sim r^{-2}$) and transitions from r^{-1} to r^{-3}. In the centre of this potential, large amounts of ionised intracluster gas are trapped, gain very large temperatures of the order of magnitude $10^7 - 10^8$ K and emit thermal Bremsstrahlung radiation at X-ray wavelengths. The gas comprises 9% of the galaxy cluster mass. The rest

(∼1%) is the optical luminous matter, the cluster galaxies. The galaxy members of the clusters tend to have unique properties compared to the field galaxies and form the red sequence of the cluster (Gladders et al., 1998).

The red sequence galaxies are large, early type, elliptical galaxies that have a tight colour-magnitude relation (CMR hereafter; Bower et al., 1992) and colours redder than the field population. The existence of the CMR makes cluster galaxies distinguishable from the field galaxies and enables the cluster selection from optical data. Red sequence galaxies exhibit little star formation and gas that has possibly been stripped out of them during their journey inside the intracluster medium (ICM hereafter). The more massive and brightest red sequence galaxies have been formed at an early epoch as suggested by their old stellar populations. The faintest ones appear to be less in number and to be transitioning from blue to red galaxies over long periods. The number of the faint red sequence galaxies seems to be larger in more massive clusters, which means that the red sequence population is more evolved in these cases (Zhang et al., 2017).

In the gravitational centre of galaxy clusters there usually lies the largest elliptical galaxy, the brightest cluster galaxy (BCG hereafter). These galaxies do not seem to be drawn from the global galaxy luminosity function (Tremaine and Richstone, 1977), a fact that has led to the conclusion that BCGs follow a different formation process. BCGs have probably acquired their mass through few major mergers in the early stages of their formation, which were then followed by smaller mergers (Dubinski, 1998). These mergers would have to be "dry", which means that the low star formation rate of the galaxies is kept the same. The details of the astrophysical processes taking place during the mass accretion are still to be discovered. BCGs are usually hosts of supermassive black holes which develop in their centres, accrete large amounts of matter, can release huge amounts of energy and form active galactic nuclei (AGN hereafter). AGN can warm up and enrich with metals the intracluster medium up to large distances and trigger the star formation of the BCG and the cluster galaxies. The effect of AGN on the properties of galaxy clusters and their members is a combination of many processes, the details of which remain to be solved.

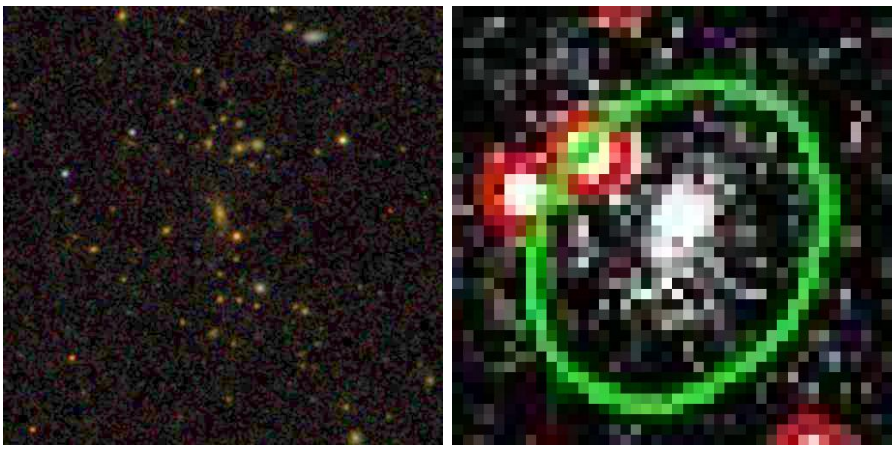

Figure 1.2 *The optical and X-ray emission of cluster XMMXCS J000235.8-020227.5. The left panel shows the optical emission using the SDSS DR13 survey (SDSS Collaboration et al., 2016) and the right panel shows the X-ray emission as observed with XMM Newton telescope (green ellipse represents the X-ray detected source). Both images have a 3×3 arcminute field of view. Note the poorer angular resolution of the X-ray data.*

The different constituents of galaxy clusters are detectable in different ways according to the radiation they emit. Dark matter does not radiate, so the only way of detecting it is indirectly through its effect on the optical emission of the background galaxies. According to general relativity, mass distorts light, which means that the large dark matter mass of a galaxy cluster can distort the light emitted from background galaxies that reaches the Earth and makes the galaxies appear more elongated or even creating arcs around the cluster core. These phenomena are named weak and strong gravitational lensing respectively. By measuring these distortions the total cluster mass can be calculated. On the other hand, the baryonic mass of the galaxy clusters emits radiation in various wavelengths. The ICM emits at X-ray wavelengths, making galaxy clusters the brightest diffuse sources in the X-ray sky. The cluster galaxies emit in optical wavelengths and appear as overdensities of red galaxies in galaxy surveys. Finally, there has been detected radio emission in cluster galaxies, possibly caused by shocks in the ICM from cluster mergers. The X-ray and optical emission of XMMXCS J000235.8-020227.5 cluster are shown in Figure 1.2 as an example.

1.3.2 Cluster mass measurements

A very important tool in order to constrain cosmology is to be able to measure or infer galaxy cluster masses. This is the first step in most cosmological studies using galaxy clusters. Below, I describe the various methods used to calculate cluster masses before I move on to describe how these are used in cosmology.

The X-ray emission of the ICM is a great probe of the cluster mass (Allen et al., 2011) mainly because clusters are easy to detect in X-rays since they are the brightest extended sources in the sky. Assuming hydrostatic equilibrium and spherical symmetry and knowing the temperature $T(r)$ and density profile of the gas $n(r)$, one can calculate the total cluster mass $M(r)$ within radius r by:

$$M(r) = -\frac{rkT(r)}{G\mu m_p}\left[\frac{d\ln n}{d\ln r} + \frac{d\ln T}{d\ln r}\right], \tag{1.16}$$

where G is Newton's constant, k the Boltzmann constant and μm_p the mean molecular weight. Even though this method is straightforward to apply, it makes some assumptions that one needs to be careful of. Hydrostatic equilibrium means that clusters need to be relaxed, with the main forces affecting them being gravity and gas pressure. Clusters undergoing any major mergers with unrelaxed ICM would have their temperature underestimated and hence their mass. Moreover, the application of the method is ideal at intermediate radii in the clusters. In the central regions, the existence and the feedback of the AGN adds more significant processes than just pressure and gravity and, at radii greater than r_{500}, the radius where the density is 500 times larger than the critical density of the Universe, the X-ray emission becomes faint and gas creates substructures which complicate the measurements. On the other hand, this method is insensitive to the triaxiality of the cluster. For relaxed clusters, the calculated masses have scatter of $\leq 10\%$ (Meneghetti et al., 2010; Nagai et al., 2007) and a bias of $5-10\%$ (Martizzi and Agrusa, 2016).

Using cluster galaxies and their velocites, one can calculate the mass $M(r)$ within radius r by assuming dynamical equilibrium (Allen et al., 2011), a density and velocity

dispersion profile, with:

$$M(r) = -\frac{r\sigma_r^2(r)}{G}\left[\frac{d\ln\sigma_r^2}{d\ln r} + \frac{d\ln v}{d\ln r} + 2\beta\right], \tag{1.17}$$

where $v(r)$ is the galaxy number density, $\sigma_r^2(r)$ is the 3-dimensional velocity dispersion and β is the velocity anisotropy parameter. This method is not affected by the non-thermal processes taking place in clusters and can give mass estimates out to larger radii than the X-ray method, due to the high contrast of the galaxy population with the background. However, one has to take into account the anisotropy of the velocities of the galaxies in order to have good quality measurements. The usually small number of galaxies available and the difficulty of defining the cluster centre can add large uncertainties to the estimated masses. The scatter can be $\sim 35\%$ (Andreon et al., 2017) and the bias $\sim 20\%$ (Maughan et al., 2016).

Measuring the shear profile of the galaxies caused by the clusters acting as gravitational lenses can lead to almost unbiased ($5-10\%$) mass estimates (Becker and Kravtsov, 2011; Marrone et al., 2012) without any assumptions about the dynamical state of the dark matter. Due to the triaxiality of the clusters, a large scatter of $20-30\%$ is introduced (Becker and Kravtsov, 2011; Marrone et al., 2012). Moreover, a good knowledge of the redshift distribution of the background galaxy distribution is needed. A comparison of the calculated lensing and X-ray hydrostatic mass from Zhang et al. (2010) for a list of clusters is shown in Fig. 1.3

An alternative way of estimating cluster masses is using mass proxies that correlate tightly with it. Having an observable-mass relation calibrated with other mass measurements, such as from lensing, can give cheap and promising estimates of the cluster masses. Galaxy clusters distort the CMB radiation due to the extremely high temperatures of the ICM, an effect called the Sunyaev-Zeldovich effect (SZ hereafter; Sunyaev and Zeldovich, 1970). The distortion leaves a signature on the CMB, the SZ signal. Observables such as the X-ray luminosity and optical richness have scatter at fixed mass of the order of 40% (Mantz et al., 2010a; Rozo et al., 2010; Vikhlinin et al., 2009a), while the SZ flux has a smaller scatter of $20-30\%$ (Hallman et al.,

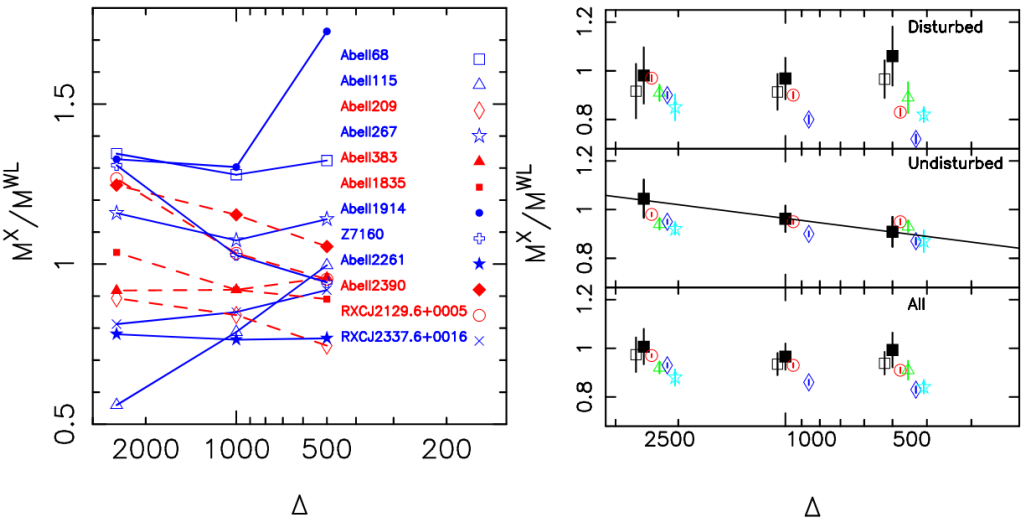

Figure 1.3 *Left panel: Ratio of X-ray hydrostatic to lensing mass as a function of the cluster density constrast for some individual clusters. Red lines represent relaxed and blue lines represent disturbed clusters. Right panel: Ratio of X-ray hydrostatic to lensing mass as a function of the cluster density constrast of the disturbed (top), relaxed (middle) and all (bottom) clusters in the list. Open black boxes exclude A1914, a known merging cluster, while filled black boxes include all clusters. The coloured points show results from various numerical simulations. The best fit for relaxed clusters is* $M_X/M_{WL} = (0.908 \pm 0.004) + (0.187 \pm 0.010) \times \log(\Delta_{500})$. *This figure is taken from Zhang et al. (2010).*

2007; Shaw et al., 2008). The cluster gas mass, temperature and their product have observed scatter of less than 10% for the former (Allen et al., 2008) and up to 15% for the remainder (Arnaud et al., 2007; Mantz et al., 2010a; Vikhlinin et al., 2009a). The calibration with low bias but high scatter lensing masses and its combination with the low scatter and high bias X-ray measurements make this method a very popular one nowadays. Today, most of the results of the scaling relations studies give power-law relations in a wide range of mass. The slope of the relations takes different values because of the different systematics of the observable, the instrument calibration, the selection function and the mass range studied.

1.3.3 Clusters as cosmological probes

Having calculated the most important cluster cosmological observable, the cluster masses, we can now move on to presenting the role of the clusters as probes of cosmology and the various ways they are used to constrain cosmological parameters. For a more detailed description one can further read Allen et al. (2011) and Borgani (2008).

Having calculated cluster masses, we can try to measure the shape of the cluster mass function (the number of clusters within certain mass bins) and its evolution with redshift. This measurement is highly dependent on the cosmological model and can constrain the density of the Universe constituents. Higher dark matter density and lower dark energy density, for example, would allow more overdensities to grow and at a' faster rate, which would result in larger abundances of clusters in any given redshift. de Haan et al. (2016); Mantz et al. (2010b); Planck Collaboration et al. (2014b); Rozo et al. (2010); Vikhlinin et al. (2009b) have used X-ray, optically and SZ selected cluster samples and gained competitive constraints on σ_8, Ω_m, Ω_v and w. Fig. 1.4 (left) shows an example of a measurement of the cluster mass function made by Vikhlinin et al. (2009b) and Fig. 1.5 shows cosmological constraints obtained with cluster abundances found by Mantz et al. (2010b). Similarly, the study of the spatial clustering of the clusters can give constraints on the cosmological parameters, such

as the galaxy clustering studies do.

The mass-to-light ratio of a cluster, or any object, compared to the mass-to-light ratio of the local neighbourhood, gives an estimate of the amount of dark matter and the object's contribution to Ω_m. For clusters, being the largest bound objects in the Universe, this ratio represents the Ω_m universal value, given a known universal baryon fraction Ω_b. Therefore, by measuring the mass-to-light ratio of galaxy clusters one can constrain the universal matter density parameter.

One can test the validity of the current cosmological model (ΛCDM) by analysing individual massive galaxy clusters that challenge the model, which assumes Gaussian initial perturbations. Hoyle et al. (2011),Jee et al. (2009) and Holz and Perlmutter (2012) have studied these extremely rare objects, massive and high-redshift clusters and reported possible tensions with the current cosmology. According to ΛCDM, these objects have very low possibility of existing, a fact that means that either the current cosmological model is wrong or the cluster mass estimates have larger errors than assumed.

A method that does not require the calculation of the cluster mass is the measurement of the gas mass fraction of the cluster within a certain radius from its centre at a certain redshift (Allen et al., 2011). This fraction gives the Universal baryon fraction, since clusters are the largest gravitationally bound objects and can be used to test the expansion of the Universe. The fraction $f_{gas}(z)$ is given from

$$f_{gas}(z) = \Upsilon(z) \left(\frac{\Omega_b}{\Omega_m} \right), \tag{1.18}$$

where Ω_b is the normalised density of the baryons and $\Upsilon(z)$ is a function which accounts for the star formation and other baryon effects within the radius r. For large radii, it becomes $|1 - \Upsilon| \leq 0.1$. The fraction can technically be measured in any radius from the centre, but, ideally, one would want to measure it for large enough radii where non-gravitational baryon effects do not introduce large scatter and small enough radii where instrument systematics are not important. When measuring f_{gas} from X-ray data within a specific aperture, this measurement will depend on

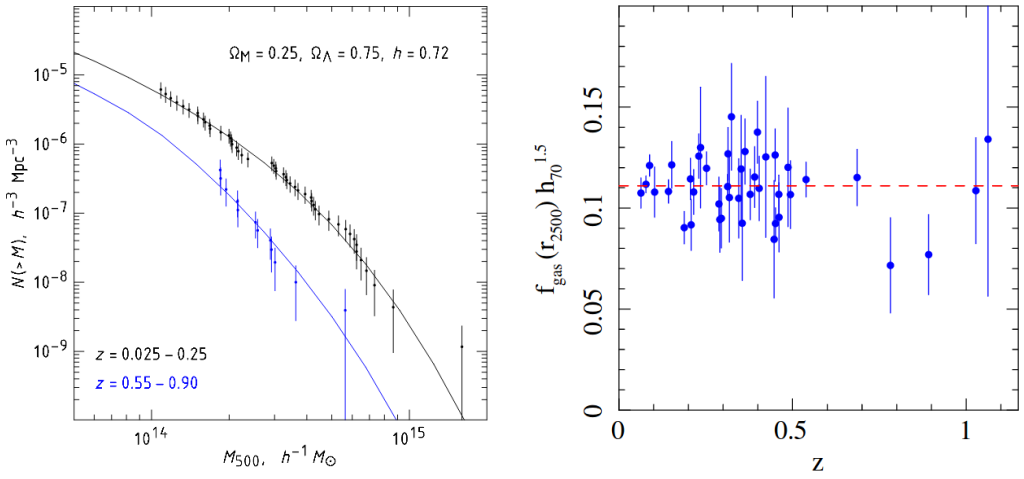

Figure 1.4 *Left panel: The cluster mass function for clusters split in two different redshift intervals compared to the prediction from the current cosmological model in black lines. Figure taken from Vikhlinin et al. (2009b). Right panel: f_{gas} measurements of relaxed clusters compared with the current cosmological model and consistent with the exp]ectation of no evolution. Figure taken from (Allen et al., 2008).*

cosmology through the angular diameter distance d_A (see Section 1.2.2) as:

$$f_{gas}(z) \propto d_A(z)^{3/2}. \tag{1.19}$$

Baryon fraction measurements yield competitive constraints on the constituents density and dark energy equation of state. An example of these measurements made by Allen et al. (2008) is shown in the right panel of Fig. 1.4 and its resulting constraints on cosmological parameters is shown on Fig. 1.5.

Another method of probing cosmology with clusters, using measurements from both X-rays and the SZ effect, is to compare the SZ signal y_{obs} of a cluster within a given aperture to the predicted signal y_{pred} given the X-ray observation of the same cluster (Allen et al., 2011). Due to the distance dependence of the X-ray signal, their fraction relates to the angular diameter distance of the cluster ($\propto d_A^{1/2}$) and can constrain the Hubble constant and the density of the Universe constituents. Calibration of the X-ray and SZ fluxes is very important to gain accurate constraints from this method. However, this method can only constrain one free parameter at a time.

The thermal and kinetic SZ effect affects the observations of the CMB radiation that

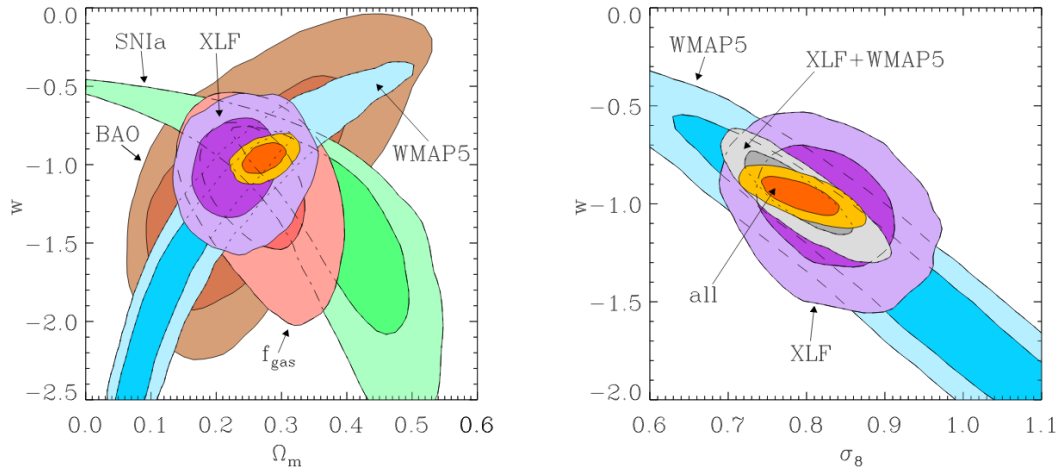

Figure 1.5 *Constraints on the dark energy equation of state parameter w and mean matter density on the left and σ_8 parameter on the right taken from the abundance of RASS clusters (labeled as XLF, Mantz et al., 2010b) and f_{gas} measurements (Allen et al., 2008), compared with contraints from other measurements from WMAP (Dunkley et al., 2009), SNIa (Kowalski et al., 2008) and BAO (Percival et al., 2010). The dark and light contours represent 68.3% and 95.4% confidence regions respectively and the gold contours show the constraints coming from the combination of all methods. The figure is taken from Allen et al. (2011).*

reaches the Earth. The fluctuations on small angular scales can probe cosmology, since they depend on the cluster mass function. This method has the disadvantage of showing degeneracies between the cosmological model and the astrophysical processes assumed. Uncertainties include the scatter of the observable-mass relation at low masses and high redshifts, the low magnitude of the kinetic SZ effect, the population of other radio sources and the electron pressure profile at large cluster radii.

Finally, one can measure the peculiar velocity field of the clusters by using the kinetic SZ effect. The peculiar velocities of the clusters depend on the amount and concentration of matter in the Universe and its expansion, which, therefore, makes the velocity field a probe of the amount of the dark energy in the Universe.

1.3.4 Galaxy cluster catalogues

In order to use clusters for all the research mentioned above, we need to have cluster catalogues in hand. Catalogues of different sizes, selected through different criteria

and by different observables, so as to be able to compare results coming from different selections and quantify the effect of the selection function on the results.

An ideal cluster catalogue should be complete and pure, i.e. containing all the clusters in a specific area and not any spurious ones respectively. It should have a well-defined selection function and cluster observables that correlate tightly with mass. During the past years, cluster catalogues have been constructed using the X-ray, optical or SZ cluster emission and provided the material for all the fruitful research mentioned so far. Fig. 1.6 shows the spatial distribution of some of the cluster catalogues described below.

1.3.4.1 Optical catalogues

The first large optical cluster catalogue was created by Abell (Abell, 1958) and contained ∼1,600 clusters in the northern hemisphere and was extended to the southern by Abell et al. (1989) having 4,000 clusters in total. Zwicky et al. (1961) followed with less strict selection criteria to create another optical cluster catalogue. Filtering algorithms and higher redshift surveys followed (Davis et al., 1985; Gunn et al., 1986) and more sophisticated methods began to arise, such as the modeling of projection effects (e.g. van Haarlem et al., 1997), which set up the basis for the modern optical cluster catalogues.

Later, the red sequence galaxies started to play their part in the optical selection. A selection of clusters by a single colour distinguished the red sequence galaxies and produced the Red-Sequence Cluster Survey (RCS; Gladders and Yee, 2005), which was followed by multi-colour surveys and algorithms that led to the catalogues used today in a large range of redshifts. Using the SDSS photometry, catalogues with thousands of clusters were constructed, the most popular of them being maxBCG (Koester et al., 2007) and GMBCG (Hao et al., 2010). The most widely used optical catalogue up until today is the redMaPPer cluster catalogue, containing hundreds of thousands clusters in SDSS (Rykoff et al., 2014) and DES (Rykoff et al., 2016) surveys. The major issue of the optical selection has always been and still is the projection effects,

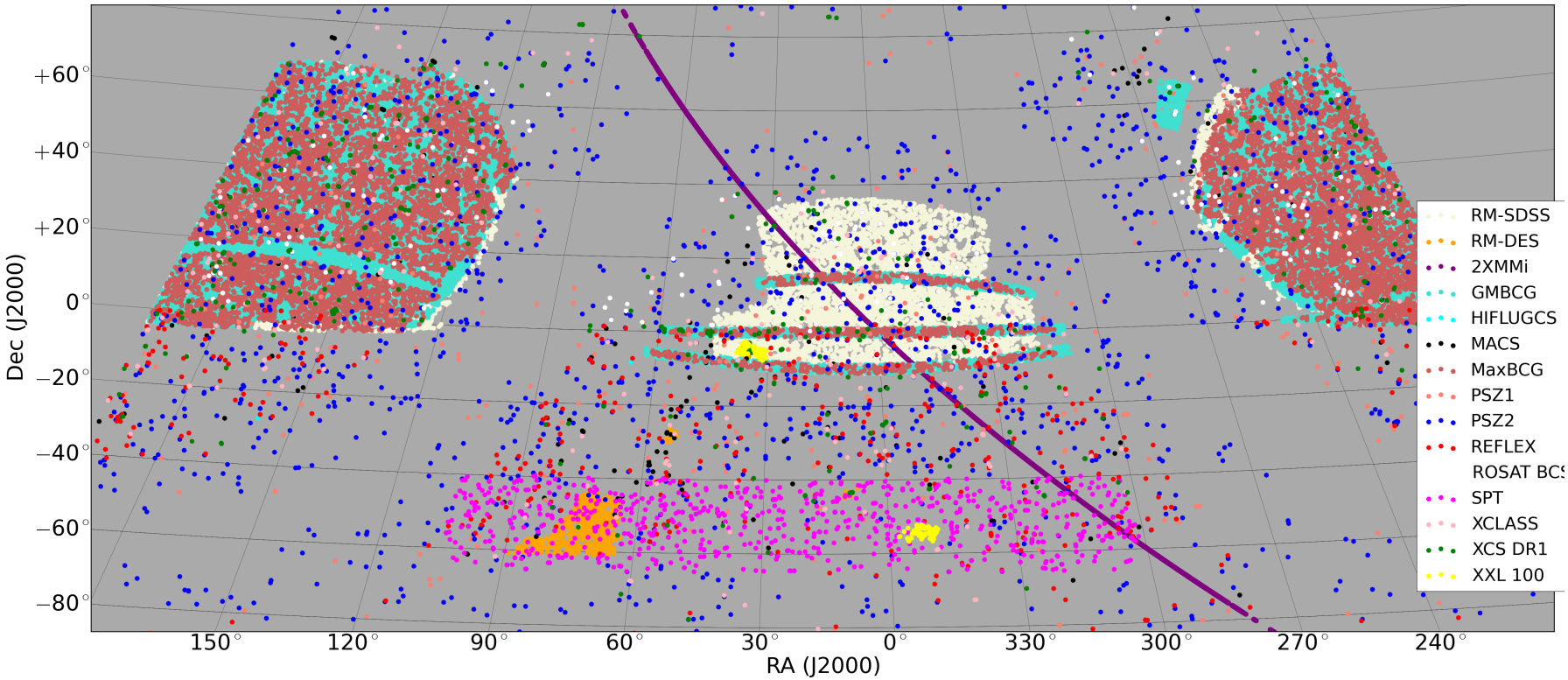

Figure 1.6 *The spatial distribution of various cluster catalogues on the sky, resulting from X-ray, optical or SZ selection. (RM-SDSS: Rykoff et al. (2014), RM-DES: Rykoff et al. (2016), 2XMMi: Takey et al. (2013), GMBCG: Hao et al. (2010), HIFLUGCS: Reiprich and Böhringer (2002), MACS: Ebeling et al. (2010), MaxBCG: Koester et al. (2007), PSZ1: Planck Collaboration et al. (2014a), PSZ2: Planck Collaboration et al. (2016a), REFLEX: Böhringer et al. (2004), ROSAT BCS: Ebeling et al. (1998), SPT: Bleem et al. (2015), XCLASS: Bleem et al. (2015), XCS DR1: Mehrtens et al. (2012), XXL100: Mehrtens et al. (2012))*

adding foreground and background galaxies to the cluster membership.

1.3.4.2 X-ray catalogues

X-ray cluster catalogues are the most widespread in the cluster cosmology community. The reasons are that they have high levels of completeness and purity, they provide tight correlations of observables with mass and clusters can simply be identified in X-rays as the only bright, extended sources in the sky which are not majorly affected by projection effects. The only disadvantage is that X-ray surveys can only take place in space, since X-rays are absorbed by the atmosphere, a fact that makes these surveys expensive.

The first X-ray cluster catalogues were created by pointed observations with the Einstein observatory and EXOSAT (Edge et al., 1990; Gioia et al., 1990). The ROSAT satellite that followed gave birth to numerous surveys, which were split in the all-sky survey part (ROSAT All-Sky Survey, RASS) and the pointed observations part of the telescope. The ROSAT Brightest Cluster Sample (BCS, Ebeling et al., 1998), the ROSAT-ESO Flux-Limited X-ray Galaxy Cluster Survey (REFLEX, Böhringer et al., 2004), the HIFLUGCS (Reiprich and Böhringer, 2002) and the Massive Cluster Survey (MACS, Ebeling et al., 2010) were created from the former, covering the northern and southern hemispheres in low redshfits, finding the brightest X-ray clusters and covering higher redshifts respectively. From the pointed observations, the ROSAT Deep Cluster Survey (RDCS, Rosati et al., 1998) and 400 Square Degree ROSAT PSPC Galaxy Cluster Survey (400d, Burenin et al., 2007) covered smaller areas but reached fainter limits.

ROSAT was followed by another X-ray satellite that provided the community with a wealth of data, mainly for galaxy clusters, the XMM Newton telescope. Surveys such as XMM LSS (Pacaud et al., 2007), XCLASS (Clerc et al., 2012), 2XMMi/SDSS (Takey et al., 2013), XCS (Mehrtens et al., 2012) and XXL (Pacaud et al., 2016) found clusters in either the whole sky (e.g. XCS) or in smaller areas (e.g. XXL, XMM LSS) and due to the high quality data, they made and are still making valuable

contributions to the quest for cosmological constraints.

1.3.4.3 SZ catalogues

Catalogues can be created from the SZ signature of the clusters on the CMB, the SZ effect (Sunyaev and Zeldovich, 1970). The distortion of the CMB radiation due to the high temperature and hence velocity of the trapped ions in the clusters' ICM creates extended imprints of the clusters' ICM on the map of the CMB radiation. This distortions can be detected and their source can be identified which results in SZ-detected cluster catalogues. The advantage of detecting clusters through this method is that the intensity of the signal does not dim with redshift, so massive clusters can be easily detected at high redshifts. Challenges include the calibration of the observable scaling with mass, the understanding of contamination from other sources and projection effects. Today, cluster catalogues constructed through the SZ effect have been created by the ACT (Hasselfield et al., 2013; Hilton et al., 2017), SPT (Bleem et al., 2015) and Planck collaborations (Planck Collaboration et al., 2014a, 2016a). These contain from few hundreds to more than a thousand galaxy clusters and have begun to yield competitive cosmological constraints (Hasselfield et al., 2013; Planck Collaboration et al., 2014b).

1.4 Voids

Another newly-developed probe for cosmology is the underdense regions of the Universe, the voids. They are useful to contrain the abundance, size and shape of large scale structures determined by the cosmological model similarly as clusters are used. Voids comprise a large volume of the Universe, taking the space between filaments, walls and superclusters. This large range of density environments offered for galaxies and clusters to be born in affects their evolution and creates a large variety of properties that they acquire during their lifetime. Here I descibe some key properties of the voids that are essential before reading Chapter 4 and the construction of void

catalogues that are used in the same Chapter in order to study the environmental effect on the galaxy cluster properties.

The formation, evolution or even presence of the voids can be a challenge to the current cosmological model, the most popular example being the CMB cold spot (e.g. Cruz et al., 2007; Martínez-González et al., 2006; Rudnick et al., 2007). While the CMB photons are traveling inside a void, the Universal expansion changes the void's gravitational potential and the energy the photons lose when they enter the void is not equal to the energy they gain when exiting it. This difference is imprinted as fluctuations on the CMB and is measured to verify the cosmological model; this effect is known as the integrated Sachs-Wolfe effect (ISW, Sachs and Wolfe, 1967).

Voids contain galaxies, which, despite their small number, can still form groups and clusters of galaxies through gravitational attraction. Galaxies and clusters in voids have been through a different formation process with more rare mergers due to the lower local density, and therefore developed different properties compared to the field galaxies (Hoyle et al., 2012; Poudel et al., 2016; Ricciardelli et al., 2017; Varela et al., 2012). This topic will be further discussed in Chapter 4, with an introduction on our current knowledge of the environmental effects in galaxy and cluster properties.

In order to use voids for cosmological and environmental studies on the properties of galaxies and clusters, one needs a catalogue of voids in a certain area of the sky. Typically, void catalogues are created by finding underdensities in galaxy surveys. One of the most popular methods, the ZOBOV algorithm (Neyrinck, 2008), splits the survey volume in Voronoi tesselations and calculates the local density on each galaxy based on the volume of the Voronoi cell relative to the mean volume of all cells. It then searches for local minima and "fills the space with water" which covers the lower density areas and gradually moves to higher densities, like water fills troughs when it rains. The resulting void catalogue depends only on the density field and there is no assumption about the void shape. The catalogue then needs to be pruned, as the algorithm detects very large numbers of voids, most of them being a result of shot noise (Nadathur and Hotchkiss, 2014). Mao et al. (2017); Nadathur (2016); Nadathur and Hotchkiss (2014); Sutter et al. (2014) have used this algorithm on SDSS and

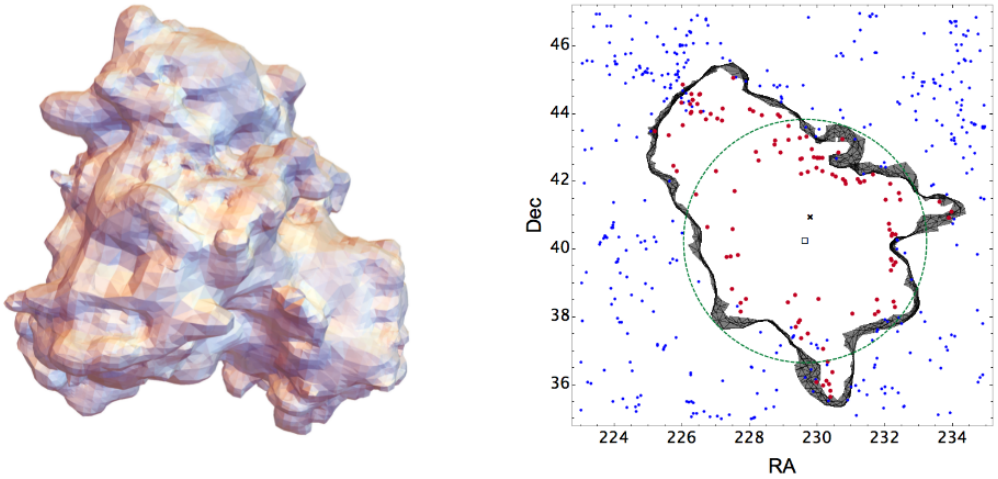

Figure 1.7 *Left panel: 3-dimensional representation of a BOSS void from the Nadathur (2016) catalogue. Right panel: A slice cut through a void (in black line) showing its lowest density centre (empty square), its barycentre (black cross), the galaxies lying in it (red points) and outside (blue points). The green circle has a radius equal to the effectine radius of the void. This figure is taken from Nadathur (2016).*

BOSS galaxy surveys, applying different selection criteria on the resulting void list and creating public void catalogues. The voids resulting do not have regular shapes, but complicated 3-dimensional shapes as shown in Fig. 1.7. They are characterised by an effective radius from their minium density centre and can be modeled by ellipsoidals for simplification.

1.5 Thesis structure

Having established the introductory foundation, we can now move to the main topic of the thesis.

In Chapter 2 I will describe in detail some of the tools I have used to create the second data release of XCS in the SDSS footprint, namely the GMPhoRCC cluster characteriser algorithm, the methods I used to create 3-colour optical images and the Zooniverse[1] project I used as a classification method for the XCS sources.

[1] www.zooniverse.org

In Chapter 3, I will present the second data release of the XCS cluster catalogue in the SDSS footprint. I will describe the X-ray and optical data analysis, the classification process and the X-ray and optical properties of the galaxy clusters in the catalogue. Finally, I will introduce some cluster sublists, ideal for specific research topics with galaxy clusters.

In Chapter 4, I study the dependence of the cluster properties on their environment. I use X-ray and optical cluster catalogues as well as cluster catalogue from MAGNETICUM[2] cosmological simulations. I use the large scale galaxy density as a probe of the cluster environmental density as well as the presence of the cluster inside a void or not.

In Chapter 5, I study the rotation of the galaxy clusters. I will analyse the rotation of the galaxy members of Abell clusters and its effect on the mass calculation of clusters through the virial equilibrium. I will compare the rotation signal from my algorithm to the rotation of the intracluster gas of simulation clusters and expand into looking the rotation of all the cluster constituents, the galaxies, gas and dark matter.

In Chapter 6, I will finish with conclusions from all the work presented and its future prospects.

[2] www.magneticum.org

Chapter 2

Prerequisites

In this chapter I give a detailed outline of the main tools that were used to create the XCS DR2–SDSS cluster catalogue, the XCS second data release of clusters in the SDSS footprint, fully described in Chapter 3. I begin with the Gaussian Mixture full Photometric Red sequence Cluster Characteriser algorithm (GMPhoRCC hereafter; Hood and Mann, 2017), which has been mainly used to calculate redshifts for X-ray detected clusters. I then describe the various processes used to create 3-colour images of clusters with overlaid X-ray contours, which helped the characterisation of the X-ray detections. These have been used for the confirmation of the XCS DR2–SDSS clusters.

2.1 GMPhoRCC

One of the main tools that was used to calculate cluster redshift, optical richness and other optical properties for the clusters in the XCS DR2–SDSS cluster catalogue is the GMPhoRCC algorithm (Hood and Mann, 2017). It has been the main photometric redshift calculator for this catalogue and has also been used to calculate the redshifts of the clusters in Wilcox et al. (2015) using SDSS DR10 photometry and spectroscopy (Ahn et al., 2014).

GMPhoRCC is a cluster-characterisation algorithm, mainly written in Python 2.7 with parts written in C and Fortran, which uses the redshifts and colours of galaxies from large surveys and the known cluster centres detected by other means such as X-ray and SZ observations. It takes advantage of two main cluster characteristics: the red sequence galaxies and the cluster BCG, and calculates the optical redshift, colour, colour-magnitude relation and richness of the cluster. GMPhoRCC was developed for and has mainly been applied to the XCS clusters (Romer et al., 2001), but can be used for any list of clusters. It has been adapted to extract data from SDSS DR10 (Ahn et al., 2014) and DR13 (SDSS Collaboration et al., 2016) catalogue, the first release of Atlas survey (Shanks et al., 2015) and CFHTLenS (Heymans et al., 2012).

GMPhoRCC's characterisation procedure takes place in five main steps as shown in Fig. 2.1. It firstly estimates the cluster's initial redshift, followed by the estimation of its initial red-sequence colour. Afterwards, the colour-magnitude relation of the red-sequence galaxies is determined, which then enables the calculation of the cluster's redshift. Finally, the algorithm computes the cluster richness using two different methods, the counting method and the luminosity function method. The results for each cluster are evaluated using flags appended during the characterisation procedure.

Before characterising, GMPhoRCC masks the cluster and its close background region in the following way: a list of small apertures is constructed, varying in right ascension and declination. Their number is such that the number of larger apertures that enclose 3×3 smaller apertures is an integer. If the number of galaxies inside a small aperture is zero, then this aperture is assigned to have zero area and is checked if it lies inside the cluster area; if it is, the corresponding flag is appended. An unmasked cluster region without galaxies detected could cause large errors in the richness estimation. If the empty region is lying in the cluster background area, then, by assigning zero area to it, the underestimation of the background density is prevented. This ensures that the cluster richness calculation is not affected by masked regions in the nearby cluster area. The radial profile of the cluster is also constructed as additional information.

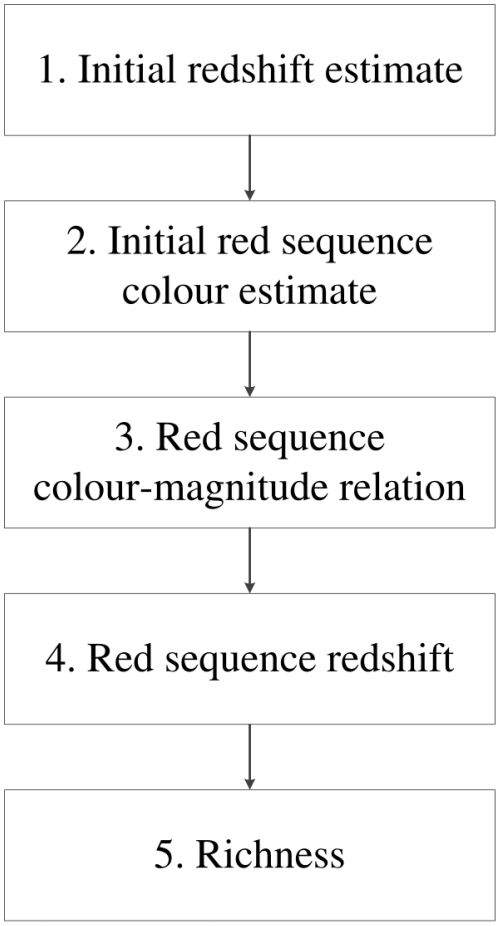

Figure 2.1 *GMPhoRCC overview flowchart taken from Hood and Mann (2017).*

2.1.1 Initial redshift

The first step of GMPhoRCC characterisation is to estimate the initial cluster redshift, a process shown in Fig. 2.2. Optical data are extracted around the cluster candidate region. An inner cone is applied to separate the cluster region dominated by cluster members from the background. The redshift histogram is constructed for both the cluster and the background region. The redshifts contain measurement errors and they cannot be fitted with the regular Gaussian mixture method, so the error-corrected Gaussian mixture (ECGMM; Hao et al., 2009) is applied, using a maximum number of three components. The first Gaussian component is always given a weight of 0.6, because a larger fraction of galaxies is described by it, whereas the other two peaks share equally the remaining 0.4. Next, the background is subtracted from the cluster field and the initial redshift distribution is calculated. The procedure described above is repeated for four different radii of cluster field cones: 1, 2, 3 and 4 arcminutes. For each cone, the redshift overdensity is computed as the sum of the peaks in the cluster redshift distribution. The cluster size selected is the one that maximises the redshift overdensity. Each peak in the redshift distribution is assumed to be a cluster candidate with an initial redshift estimation equal to the peak in the redshift distribution. If no peaks are found, the appropriate flags are appended to the cluster.

2.1.2 Red sequence colour

The second step of the algorithm is to measure the initial red sequence colour of each of the cluster candidates found in the previous step. The outline of this step is shown in Fig. 2.3. A redshift - colour band relation is assumed. Each cluster is studied in the colour band where the 4000 $\mathring{A}$ break in galaxies' spectra appears for the specific cluster redshift. The boundaries of the colour bands in each redshift bin overlap, so in the case where the cluster's redshift corresponds to two bands, the cluster is studied in both of them. The colour band that corresponds to the initial redshift found from the redshift–colour band relation is assumed as the cluster colour band. Both the background and cluster region galaxies are filtered in redshift and colour:

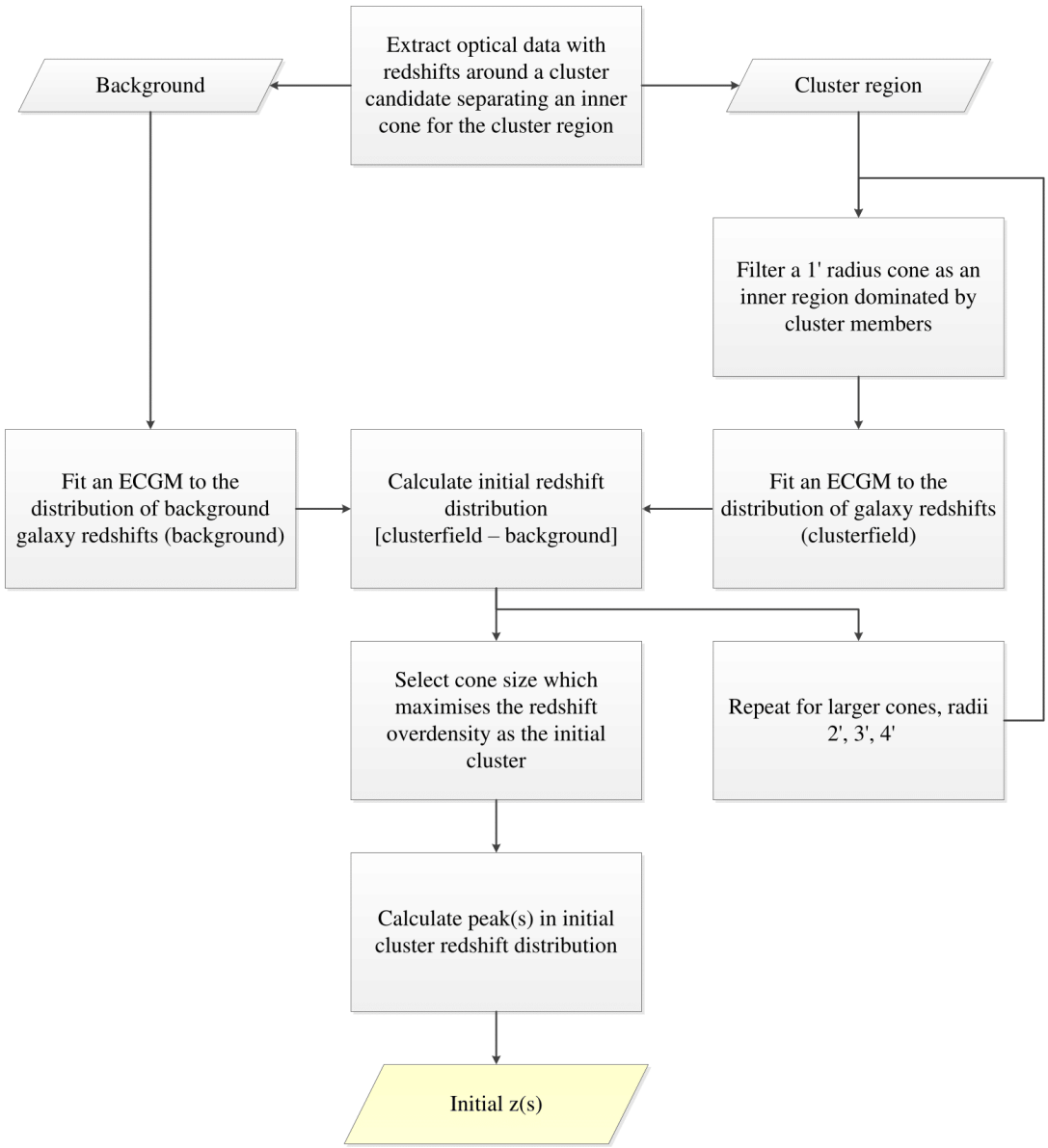

Figure 2.2 *Initial redshift estimate (Step 1) flowchart of GMPhoRCC taken from Hood and Mann (2017).*

the ones with redshifts larger than 0.25 compared to the cluster's initial redshift and fainter than $m^*(z) + 2$ are removed. The cluster region is additionally filtered with a cone of radius 1, 2, 3 or 4 arcminutes. The colour histogram is constructed for the background and cluster field galaxies and is fitted with ECGMM as in the previous step. By subtracting the two distributions, the initial colour distribution of the cluster is found. The process is repeated for all the possible cone-size filters and the colour overdensity is calculated for each one by summing the peak amplitudes in the colour histogram. The one that maximises the overdensity is selected as the cluster core radius. The peak in the colour distribution represents the initial colour estimation of the cluster candidate red sequence. If multiple peaks are found, then each one is a new cluster candidate. If no peaks are found, flags are appended to the cluster. After iterating over all candidates found in the initial redshift distribution, some of these candidates may have acquired additional cluster candidates in the colour distribution. Out of all these, one will be assessed as the primary cluster and, possibly, one of them will be the secondary cluster.

2.1.3 Colour-magnitude relation

The next step is to determine the colour-magnitude relation (CMR hereafter) of the red sequence galaxies for each of cluster candidates (sketched in Fig. 2.4). Galaxies in the cluster region are filtered once more in redshift and colour: the ones with redshifts larger than z =0.25 compared to the initial candidate redshift and fainter than $m^*(z) + 2$ are removed. The rest of the galaxies now constitute the cluster red sequence. The colour-magnitude diagram is constructed for the cluster's galaxies. The initial assumption for the CMR is a horizontal line. Afterwards, a sloped line is fitted to the galaxies using the BCES method (Akritas and Bershady, 1996) that takes into account the errors in the galaxies' colours. This line is approximately the CMR of the cluster's red sequence. The colour histogram is again constructed for these galaxies and an ECGMM is fitted, with standard deviation equal to the CMR intrinsic width. All steps up to this point are repeated once again in order to obtain more accurate results in redshift, colour and CMR of the cluster.

Figure 2.3 *Initial colour estimate (Step 2) flowchart of GMPhoRCC from Hood and Mann (2017).*

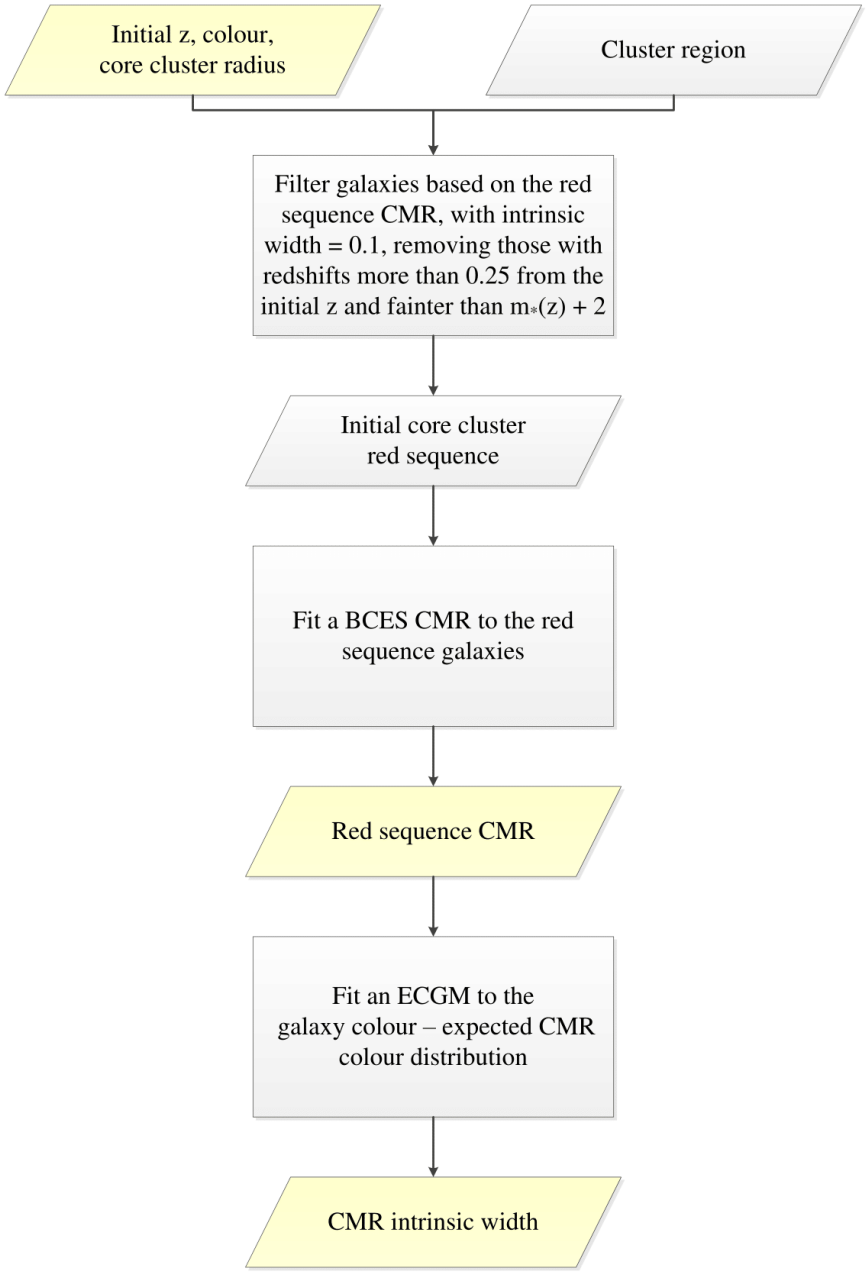

Figure 2.4 *Colour-magnitude relation calculation (Step 3) flowchart of GMPhoRCC taken from Hood and Mann (2017).*

2.1.4 Red sequence redshift

The fourth step is to determine the cluster redshift from the now established red sequence galaxies (Fig. 2.5). After having calculated the initial redshifts and CMRs of the cluster candidates, the background and cluster region galaxies are filtered again in redshift and colour: galaxies with redshift larger than 0.25 compared to the initial redshift and fainter than $m^*(z) + 2$ are removed. The result is a core cluster red sequence and a background red sequence. The cluster BCG is selected from the core cluster red sequence as the brightest galaxy in the i-band after having selected the three brightest ones in the cluster. If the BCGs have spectroscopic redshifts, their mean spectroscopic redshift determines the cluster's spectroscopic redshift. Redshift histograms are constructed for both background and cluster region red sequence and another ECGMM fitting takes place. The former distribution is subtracted from the latter to calculate the red sequence redshift distribution and the peaks represent the cluster's possible redshifts. This procedure is repeated for all cluster candidates (from all potential initial redshifts and CMRs). After that, the primary and secondary cluster are selected between the candidates through a procedure described below. The clusters' CMR, redshift and BCG are now determined.

The cluster selection process is complicated due to the numerous peaks in the colour and redshift distributions that can appear during the previous steps of the cluster characterisation. The process is outlined in Fig. 2.6. First of all, candidates with inappropriate redshifts given their colour bands are removed. All candidates are also given a cleanness band (one to four) depending on the redshift difference between the initial and the red sequence candidate's redshift and the BCG distance from the cluster centre. The primary cluster is set to be the cluster whose red sequence redshift best matches the initial redshift estimate and is also the cleanest one. The choice of the secondary cluster is a little more complicated. The importance of multiple peaks is lower as the characterising procedure carries on. This means that the multiple initial redshift peaks are the most important to determine the secondary cluster, followed by the multiple initial colour peaks and the multiple red sequence redshift peaks.

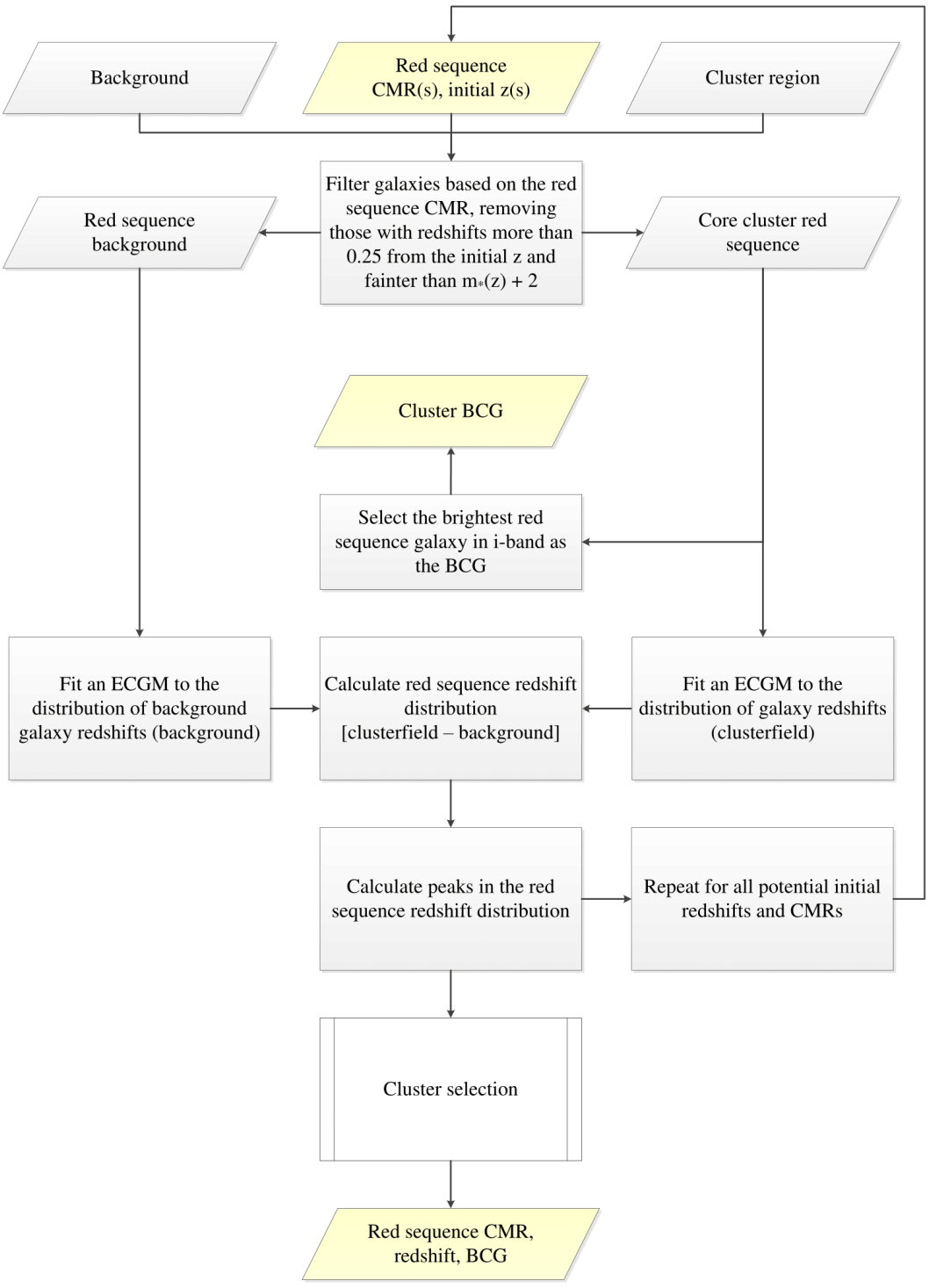

Figure 2.5 *Red sequence redshift calculation (Step 4) flowchart of GMPhoRCC taken from Hood and Mann (2017).*

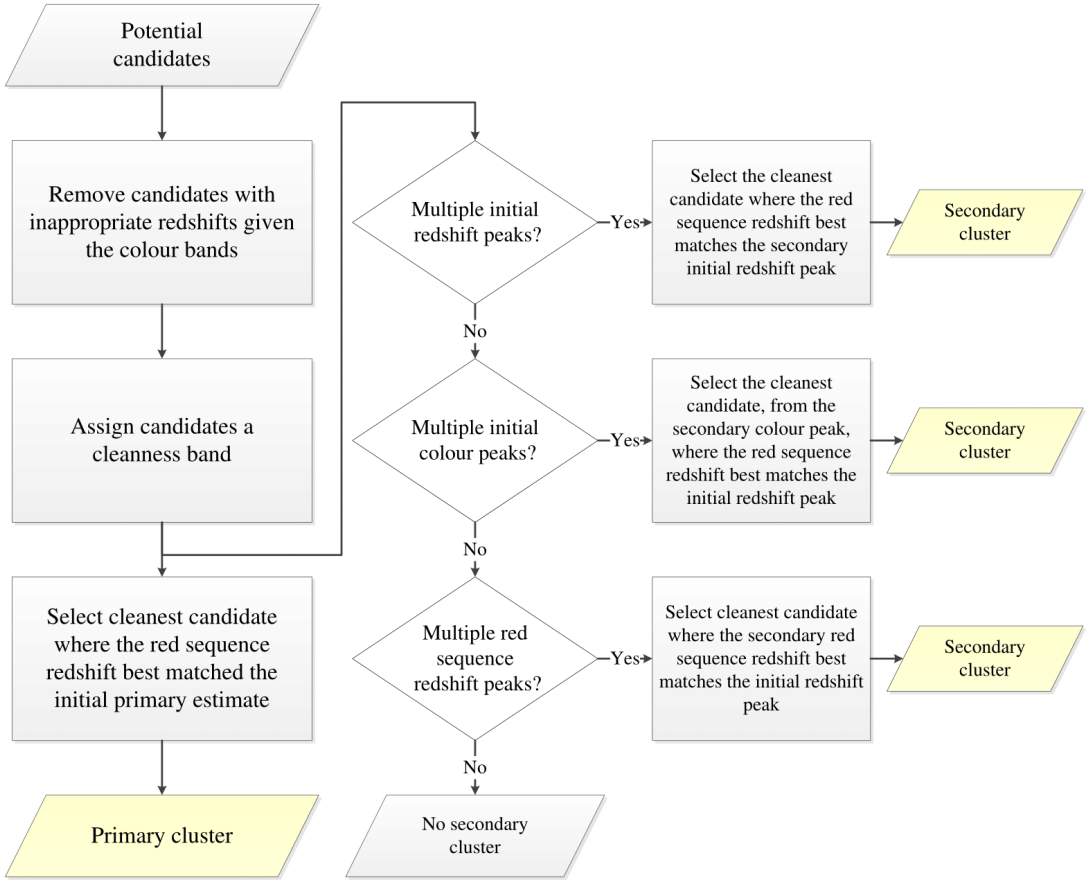

Figure 2.6 *Cluster selection flowchart of GMPhoRCC taken from Hood and Mann (2017).*

Therefore, the secondary cluster is the cleanest and most "important" candidate with red sequence redshift that best matches the initial redshift peak. If there are no multiple peaks, then there is no secondary cluster assigned.

2.1.5 Richness

The final step of the algorithm is the cluster richness calculation outlined in Fig. 2.7. Two methods are used for this calculation: the counting and the luminosity function fitting. After having determined the cluster CMR, redshift, BCG and radius, additional filtering is applied to the background and cluster region galaxies. Those fainter than $m^*(z) + 1$ and brighter than the BCG are removed. A top-hat redshift filter of 0.25 width centred at the cluster redshift is also applied to remove projection effects. The cluster region is additionally fitted by an input radius cone. Galaxies in the cone

and in the background are counted for each one of the small apertures discussed earlier and the mean value is found. From that, the mean background density is extracted and is converted again to a number of galaxies. The number of galaxies in the background is subtracted from the number of galaxies in the cone and the results is the counting richness estimate. For the luminosity function method, the distributions of background and cone galaxies are fitted with a Schechter luminosity function using the BCES method. The background distribution is subtracted from the cone distribution and the result is the luminosity fitting richness estimate. The point where the photometry becomes incomplete is found in order to fit within the correct magnitude integral. If $m^* + 1$ is brighter than the cluster's faint end, then this is set as the faint end. For the luminosity function fitting, characteristic magnitude m_* is either fitted or the redMaPPer value is used, slope a is always set to be equal to -1 and normalisation factor ϕ^* is always fitted (see equation (1.12)). In the background galaxies histogram, the bin of the fainter maximum shows where GMPhoRCC photometry becomes incomplete. With this procedure, the counting and luminosity fitting richness estimate is calculated for 0.5 Mpc and 1 Mpc fixed cluster radius and for r_{200} radius that is computed from the fixed 0.5 or 1 Mpc radii using the scaled richness - r_{200} from Hansen et al. (2009).

GMPhoRCC uses a quality control system that consists of flags appended to the clusters during the characterisation process. This helps identifying possible catastrophic failures. Flags are related to the redshift or colour distributions such as multi-modality, consistency of the BCG and red sequence redshifts (BCG redshifts are more reliable and usually spectroscopic) and richness (low richness might mean that the cluster has not been detected optically). The clusters are separated in three quality subsets: the "clean" one, which contains only clusters with no problems in richness and redshift estimation, the "mid" quality one, where clusters with very low richness or large discrepancies in redshifts are removed and the "detection" one, in which all the clusters detected are listed there. A mock cluster catalogue has been constructed to test the completeness and purity of the algorithm. It was also used to check various steps of the algorithm.

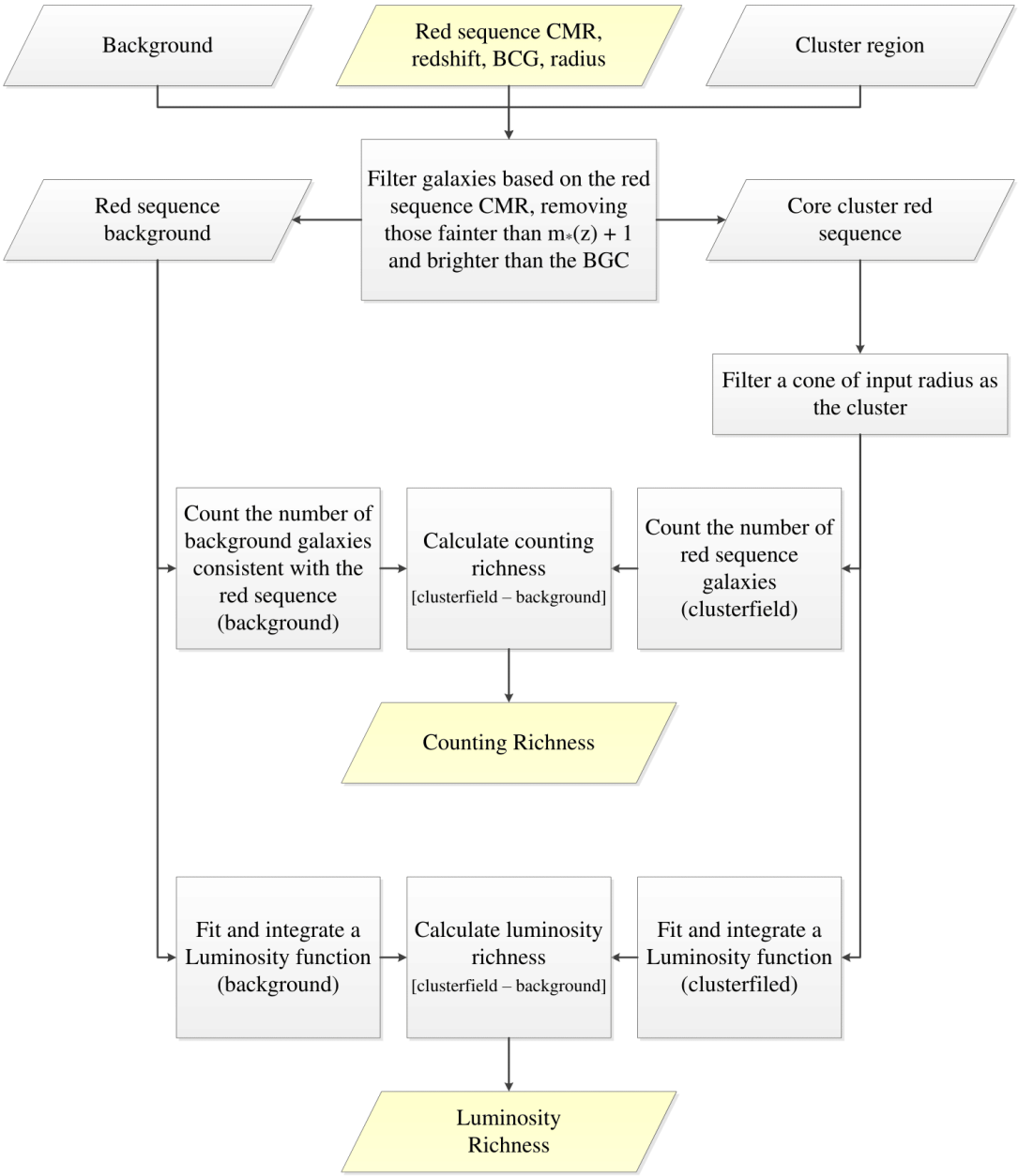

Figure 2.7 *Richness calculation (Step 5) flowchart of GMPhoRCC taken from Hood and Mann (2017).*

2.2 Cluster images

In order to study individual clusters, but also to confirm the detection of galaxy clusters, an invaluable method is to eyeball them using images as we will see in Chapter 3. Details about the reason optical confirmation of clusters is needed are discussed in Chapter 3. The more wavelengths one would have available for this task the easier it would be to distinguish the cluster red sequence galaxies from the background galaxies. Therefore, an important part of creating the XCS DR2–SDSS catalogue is to create 3-colour images using optical and/or near-IR surveys and overlay X-ray contours on them in order to compare the multi-wavelength emission of the given cluster candidate. For the construction of these images I used a variety of tools and a variety of surveys that I further describe below. These images were afterwards used to classify the cluster candidates by the members of XCS with the aim to include or not in the final XCS DR2–SDSS cluster catalogue through a project that is described in Chapter 3. The cluster images were also used in other studies using XCS clusters, including Zhang et al. (to be submitted) and Bermeo-Hernandez et al. (in preparation).

2.2.1 Imaging surveys

The main survey that has been used for this task is SDSS DR13 (SDSS Collaboration et al., 2016). The large sky coverage (14,555 degrees^2 of imaging) and the public access to the data were the main reasons for choosing SDSS to optically confirm the XCS DR2 clusters. The SDSS imaging is available in five filters, u, g, r, i and z. For every XCS cluster coordinates, I search and download all the available SDSS FITS files in all five filters containing the given coordinates using the Simple Image Access Protocol[1] (SIAP) service of SDSS. Having tens of FITS files for a specific filter and cluster, I use SWarp (Bertin et al., 2002) to create a "master" FITS file for each filter.

[1] http://skyserver.sdss.org/dr13/SkyserverWS/SIAP/getSIAPInfo?POS=RA,DEC&SIZE=$IMGSIZE$&FORMAT=image/fits&bandpass=gri

I cross-match the XCS DR2–SDSS cluster candidates with the Hyper Suprime-Cam survey (HSC, Aihara et al., 2017) with the aim to find possible biases in the cluster detection due to the different optical survey depths. HSC photometry is given in five filters, g, r, i, z and y, which reach fainter limits compared to SDSS, a fact that could make the cluster red sequence more distinguishable through optical imaging, therefore making the cluster detection easier. However, HSC survey lacks in sky area and therefore can detect significantly less amount of clusters. The HSC website[2] offers the service of directly downloading FITS files of a requested size, centred at specific coordinates.

As mentioned in Section 2.1, the colour or filter in which the cluster red sequence emission appears brightest changes with redshift. For high redshift clusters with roughly $z > 0.8$, the red sequence is almost unrecognisable in the optical SDSS filters. For that reason I experimented using near-IR imaging, where the high redshift cluster red sequence should be more prominent. I used the WFCAM Science Archive (WSA, Hambly et al., 2008) and VISTA Science Archive (VSA, Cross et al., 2012) (UKIDSS DR10, VHS DR3, VIKING DR4 and VIDEO DR4 surveys) which offer a combination of all of the Y, J, H and Ks filters. The FITS files centred in given coordinates and with a certain size were downloaded through the websites `wsa.roe.ac.uk` and `vsa.roe.ac.uk`.

2.2.2 Creating 3-colour images with contours

Having acquired the cluster FITS files in all possible filters, I create 3-colour images by choosing the 3 filters that make the cluster red sequence more distinguishable and the background noise the least possible. When all three filters used come from the same survey, then the filters chosen are g,r and i for SDSS and HSC and K or Ks, H and J for WSA and VSA surveys. In cases where both SDSS and near-IR filters are used, the "best" combination of filters found by visual inspection is either K, r

[2] `https://hsc-release.mtk.nao.ac.jp/das_quarry/cgi-bin/quarryImage?ra=$RA$&dec=$DEC$&sw=$SIZE$arcmin&sh=$SIZE$arcmin&type=coadd&image=on&filter=HSC-G&tract=&rerun=`

Table 2.1 *Best combination of filters to create 3-colour cluster images.*

SDSS:	gri
HSC:	gri
WSA/VSA:	KHJ
SDSS+WSA/VSA:	Krg or KHr

and g or K, H and r filters. These are summarised in Table 2.1.

To create the images, when all three FITS files have the same dimensions, which is true for exclusively HSC or WSA/VSA images, I used the STIFF package (Bertin, 2012) and manually changed the colour scaling parameters to better show the cluster red sequence. In the case where one or more SDSS FITS files were included in the image, the FITS files had to first be centred at the same coordinates using astropy (The Astropy Collaboration et al., 2018) in python, then cut in the same dimensions if possible (in a few cases the cluster was not in the centre of the SDSS observation, due to e.g. being on the edge of the coverage or mask, so the FITS file would not have the desired size) using IRAF[3] and finally creating the 3-colour images with APLpy (Robitaille and Bressert, 2012) in python. By uploading the XCS FITS file of the cluster observation, APLpy contains a function that overlays contours on a given image, the 3-colour image in this case. The contour levels, smoothness and colour can be changed through the function.

In Fig. 2.8 an XCS DR2 cluster image with overlaid X-ray contours is shown in both SDSS and HSC imaging. Although HSC offers deeper imaging, the different colour scaling in the images due to the different packages used to make them show only small differences in the number of objects and the detail of structure.

In Fig. 2.9 an XCS DR2 cluster 3-colour image is shown made from only SDSS, only VSA and a combination of filters from both surveys. The cluster is XMMXCS J134305.0-00056.9 with an estimated redshift of 0.715 calculated using galaxy spectroscopic redshifts from SDSS DR13 (the method is described in Chapter 3). The cluster red sequence is faint in optical imaging (top and middle left panels), but is enhanced when using a combination of optical and near-IR filters in the bottom

[3] http://iraf.noao.edu

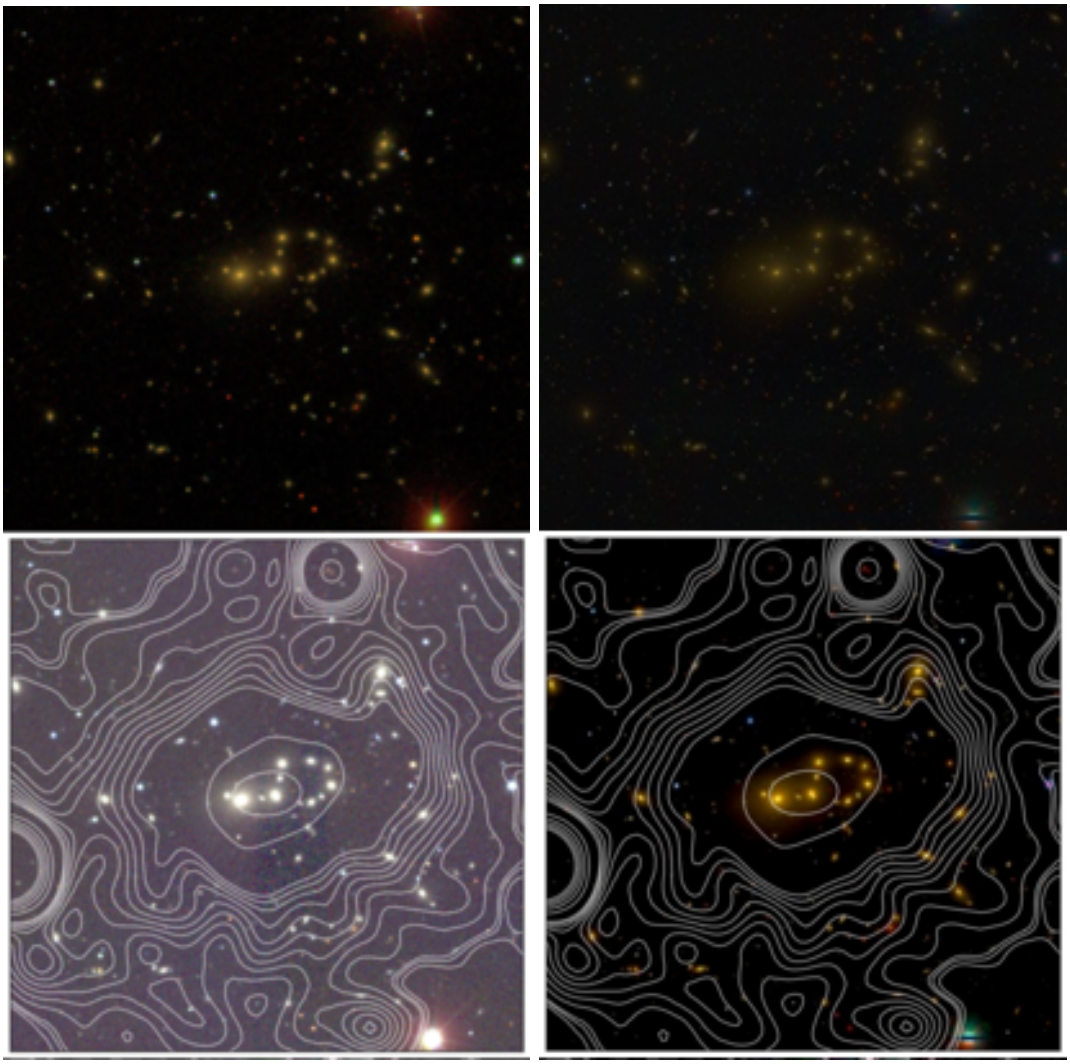

Figure 2.8 *Cluster XMMXCS J141507.1-002931.9 with SDSS DR13 (left) and HSC (right) imaging using gri filters and in a 6x6 arcmin field of view. The top panels show the colour images and the bottom ones show the images with overlaid contours. The top left one was downloaded directly from SDSS, while the rest were created with STIFF or APLpy.*

two panels. However, the shallower magnitude limit and the lower sky coverage of the VSA surveys do not sufficiently help the detection of the clusters and therefore VSA/WSA imaging was not officially used in XCS DR2 cluster confirmation.

2.2.3 Cluster zoo

The images I made for all XCS DR2 cluster candidates that are in the SDSS footprint can now be used in order to eyeball each one individually to confirm if they are clusters or not. Having thousands of candidates to be confirmed, this is a task to be given to a group of people, the XCS collaboration members. Therefore, I created an online project that selected people can access using the Zooniverse[4] platform. The structure, workflow, images and data extraction of this project are described in detail in Chapter 3.

[4] www.zooniverse.org

Figure 2.9 *Cluster XMMXCS J134305.0-000056.9 with estimated redshift 0.715 using SDSS galaxy spectroscopic redshifts (further details for the redshift estimation in Chapter 3) in a 3x3 arcmin field of view. Top images show the SDSS DR13 (left) and VSA (KHJ filters, right) downloaded images. Middle panels show the SDSS DR13 (left) image made using gri filters and VSA (right) image made using KHJ filters. Bottom images show combination of filters from SDSS and VSA: left image is made from Krg filters and right one from KHr filters. The middle and bottom panel images were created using APLpy.*

Chapter 3

The XCS DR2 - SDSS data release

3.1 Preface

The work presented in this chapter is going to be submitted after minor amendments to MNRAS as "The *XMM* Cluster Survey: The second XCS data release in the SDSS DR13 footprint" by M. Manolopoulou, M. Hilton, A. Bermeo-Hernandez, C. Vergara-Cervantes, P. A. Giles, A. K. Romer, R. G. Mann, L. Ebrahimpour, C. J. Miller, C. A. Collins, P. J. Rooney, J. P. Stott, H. Wilcox, K. E. Furnell, P. T. P. Viana, S. Bhargava, Y. Zhang and S. Rosborough. This study was conceived by all of the authors. I carried out the optical confirmation of the clusters, the GMPhoRCC redshift determination, the selection of the final sample, the subsample selection and the writing of the publication. The sections I have not written and figures I have not produced are Section 3.7 (only the first part), 3.8.2 and 3.11.2 and Fig. 3.1, 3.15, 3.16, 3.21, 3.23 (right panels), 3.25 and 3.26.

The chapter is a copy of the current draft of the publication Manolopoulou et al. (2018b).

3.2 Abstract

We present XCS DR2–SDSS, the subset of the second XCS Data Release that coincides with the SDSS DR13 footprint. This comprises 1,255 optically-confirmed clusters, 203 of which are entirely new to the literature. Almost all (1,225) of XCS DR2–SDSS clusters have associated spectroscopic or photometric redshifts. The vast majority (1,143) also have associated X-ray temperatures and luminosities that have been derived. The XCS DR2–SDSS catalogue is the largest X-ray cluster sample to date, with a large range of redshift, $0 < z < 1.18$ (median 0.28), and X-ray temperatures $T_{\rm X} <\sim 14$ keV (median 2.6 keV). It includes 23 high redshift clusters ($z \geq 0.8$), and 194 high temperature ($T_{\rm X} > 5$ keV) clusters.

3.3 Introduction

The XMM Cluster Survey (XCS) is a search for X-ray galaxy clusters using all suitable data from the XMM-Newton Science Archive. The main goals of XCS are to measure cosmological parameters, measure the evolution of the X-ray scaling relations, study galaxy properties in clusters up to high redshifts and provide a high quality, homogeneously selected cluster catalogue (Romer et al., 2001).

XCS research began prior to the first data release and includes the detection and follow-up observations of a $z = 1.46$ cluster (XMMXCS J2215.9−1738) (Hilton et al., 2007, 2010, 2009; Stanford et al., 2006), the evolution of the brightest cluster galaxies (BCG hereafter) in high-redshift clusters (Stott et al., 2010), the forecasts of the constraints on cosmology and cluster scaling relations using the XCS data (Sahlén et al., 2009). The optical and X-ray analysis of the first data release were published in Mehrtens et al. (2012) and Lloyd-Davies et al. (2011) respectively. A review of the status and science from the XCS data until 2013 has been described in Viana et al. (2013), which included applications of this data on studies of fossil groups in the XCS DR1 - Sloan Digital Sky Survey (SDSS) overlap area (Harrison et al.,

2012) and XCS DR1 clusters that could be observed by Planck (Viana et al., 2012). After that, applications included studies of the interaction between the BCG, the supermassive black hole and the intracluster medium (ICM hereafter) of the clusters (Stott et al., 2012), tests of chameleon modified gravity evidence on X-ray and lensing stacked cluster profiles (Wilcox et al., 2015) and direct measurement of the mean halo occupation distribution of cluster galaxies (Mehrtens et al., 2016). In addition, we have also focused on studies of the cluster scaling relations, particularly the X-ray luminosity–temperature (Hilton et al., 2012) and velocity dispersion–temperature (Wilson et al., 2016) relation and their evolution. In the meantime, the XCS DR1 cluster catalogue has been used for a variety of scientific research; some examples are the Sunyaev-Zeldovich effect observations of some of the hottest XCS clusters (AMI Consortium et al., 2013), the study of the brightest cluster galaxies stellar mass accretion (Zhang et al., 2016) and red sequence luminosity function (Zhang et al., 2017), the calculation of the black holes mass through X-ray observations (Mayers et al., 2018), the evaluation of the redMaPPer algorithm in the SDSS footprint (Rozo and Rykoff, 2014), the construction of the redMaPPer cluster catalogue in the DES footprint (Rykoff et al., 2016) and the study of the anisotropy of the luminosity–temperature relation anisotropy (Migkas and Reiprich, 2017).

Over recent years, cosmological studies with galaxy clusters have gained recognition, yielding cosmological parameter constraints competitive to other methods (e.g. Allen et al., 2011; Vikhlinin et al., 2009c). Cosmology with galaxy clusters has become possible mainly with well-defined galaxy cluster samples with accurate selection functions and cluster scaling relations between cluster observables and/or cluster mass measurements. Current X-ray cluster catalogues usually contain a few hundred clusters, tracing the brightest end of the cluster luminosity function and biasing the scaling relation studies. The growing need of more galaxy clusters shown from XCS research as well as various cosmological studies with clusters has motivated us to create a second XCS data release which contains many more objects than XCS DR1 and with improved measured properties.

In this Chapter, we present the XCS DR2 X-ray analysis, the process of optically

confirming the galaxy cluster candidates residing in the SDSS DR13 area (SDSS Collaboration et al., 2016) and the final cluster catalogue resulting from it. Catalogues of clusters overlapping with other surveys such as the Dark Energy Survey (DES) (Abbott et al., 2018) will follow. Our catalogue is the largest catalogue of X-ray detected clusters so far, with 1,255 galaxy clusters only in the SDSS area. These are optically confirmed galaxy clusters, the majority of them associated with spectroscopic redshifts, otherwise associated with photometric redshifts, X-ray luminosities and temperatures, the latter calculated with improved pipelines since the first data release (Lloyd-Davies et al., 2011). XCS DR1 contained 503 clusters, 464 of them associated with redshifts and 402 of them associated with X-ray temperatures, while XCS DR2 contains 1,255 clusters, 1,225 of them associated with redshifts and 1,097 of them associated with X-ray temperatures. The catalogue will enable more statistically accurate research due to the large number of clusters, homogeneously selected across the SDSS area and will lead to more reliable scaling relation measurements and cosmological parameter estimations.

This Chapter follows as: in Section 3.4, we briefly describe the analysis of the XMM-Newton observations that led to the XCS master source list, in Section 3.5 we discuss the procedure of optically confirming the XCS cluster candidates through a Zoo project and creating the galaxy cluster list in SDSS DR13. In Section 3.6, we discuss how we calculate and assign the cluster redshifts and compare them with data from other surveys and in Section 3.7 we discuss the improved way of measuring the X-ray luminosities and temperatures. In Section 3.8, we present the final cluster catalogue and compare it with other X-ray cluster catalogues and in Section 3.9 we discuss some interesting subsamples extracted from the catalogue (high temperature clusters, high redshift clusters, clusters with spectroscopic redshifts). Finally, in Section 3.10 we present a summary.

3.4 XCS DR2 observations

The first data release of XCS (Mehrtens et al., 2012) contains 503 X-ray serendipitously detected clusters distributed over the whole sky. With follow-up optical observations, photometric or spectroscopic redshifts were acquired for the clusters. Public archives like SDSS and other literature sources, were used to extract as many spectroscopic redshifts as possible for the XCS DR1 clusters. The cluster candidates underwent quality control mostly by an exercise named XCS-Zoo. The catalogue was split into seven subsamples, useful for different kinds of research: high-redshift clusters, high-temperature clusters, low-temperature clusters, high signal-to-noise clusters, clusters in the deep S82 (Annis et al., 2014) region of SDSS DR7 (Abazajian et al., 2009), clusters in the Dark Energy Survey footprint (Abbott et al., 2018) and clusters for statistical studies.

For XCS DR2, we downloaded the public observations from the XMM public archive, the remote storage facility at the European Space Astronomy Centre (ESAC) near Madrid, Spain. The number of observations analysed include all areas suitable for cluster searching as described in Lloyd-Davies et al. (2011), excluding areas such as the Milky Way ($|b| < 20^o$) and the Magellanic clouds. The area of the sky covered as a function of exposure time is displayed in a histogram in Fig. 3.1(left), and to the right of this image is a cumulative plot of the same data. The final bin in Fig. 3.1 (left) is due to all exposures being gathered together. These result in up to $10,742$ observations, each one associated with an objID, across the whole sky. The data have been calibrated and treated for background flares extensively in the same manner as Lloyd-Davies et al. (2011) with updated algorithms that are described in Section 3.7. Images and exposure maps are then produced with a 4.35 arcsec pixel size, a size smaller than the XMM point spread function (hereby PSF), in the soft ($0.5-2$ keV) and hard ($2-10$ keV) X-ray bands. The images are checked by eye to ensure if masking is needed. For the production of the XCS source catalogue, we used the XMM Automated Pipeline Algorithm (XAPA) as in XCS DR1. The code scans each observation in nine different wavelet scales and classifies all detected sources as

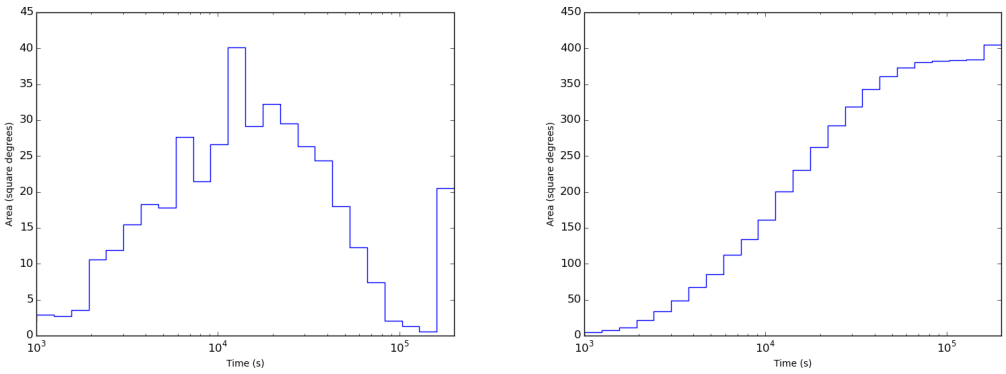

Figure 3.1 *Histogram (left) of the area of the sky covered as a function of cleaned exposure time and cumulative histogram (right) of sky covered in XCS DR2 as a function of the exposure time.*

point sources, *PSF sources* and *extended sources* by fitting them with an ellipse and comparing the source count distribution with the XMM PSF; extended sources slightly larger than the PSF are marked as PSF sources. In Fig. 3.2, we show some examples of XMM observations, where X-ray detections are overlaid with XAPA ellipses and the objects are classified as point (red ellipse), PSF-sized (purple ellipse) or extended (green ellipse) sources.

The above analysis led to a master source list of cluster candidates that are further analysed in the following sections to create the cluster list. In Fig. 3.3 we show the XCS-DR2 sources across the whole sky in black dots, overlapped with various optical galaxy surveys as well as the clusters found in the HSC area (Oguri et al., 2017). XCS DR2 has 128,756 sources overlapping with SDSS DR13, 13,053 of which are extended or PSF-size sources. The matching with SDSS was done using the Aladin software (Boch and Fernique, 2014; Bonnarel et al., 2000) and the pre-loaded SDSS survey.

3.5 Optical confirmation

It can be seen from Fig. 3.2 that XAPA extended sources are not always galaxy clusters. This is a result of the comparison of the source extent to the poorly

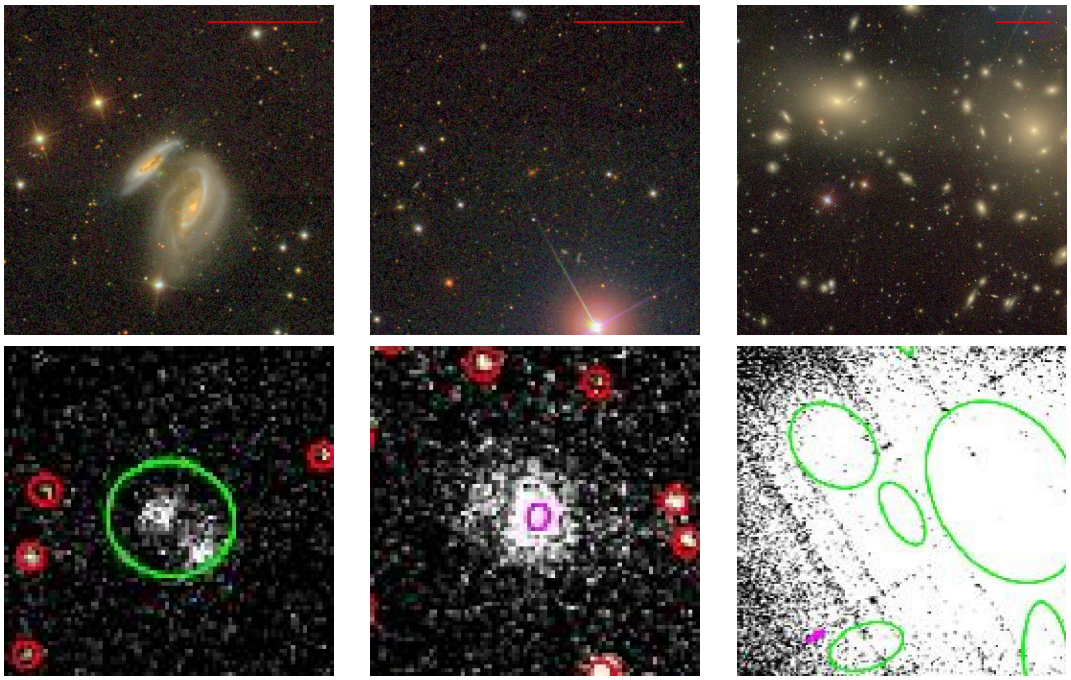

Figure 3.2 *Three examples of non-extended cluster and extended non-cluster classified XAPA sources. The upper panels show the SDSS images, while the bottom ones show the XMM observations. From left to right: XMMXCS J000140.2+232940.9, two foreground galaxies, blended as one extended source by XAPA (6×6 arcmin field of view), XMMXCS J001847.4+160217.1, an extended source, possible a high redshift galaxy cluster, classified as PSF-sized (6×6 arcmin field of view) and XMMXCS J125957.4+275607.0, an extended source in low redshift split in multiple sources (12×12 arcmin field of view, cyan ellipse represents a negative X-ray count source). The scale bar shows 2 arcminute distance in all 3 images.*

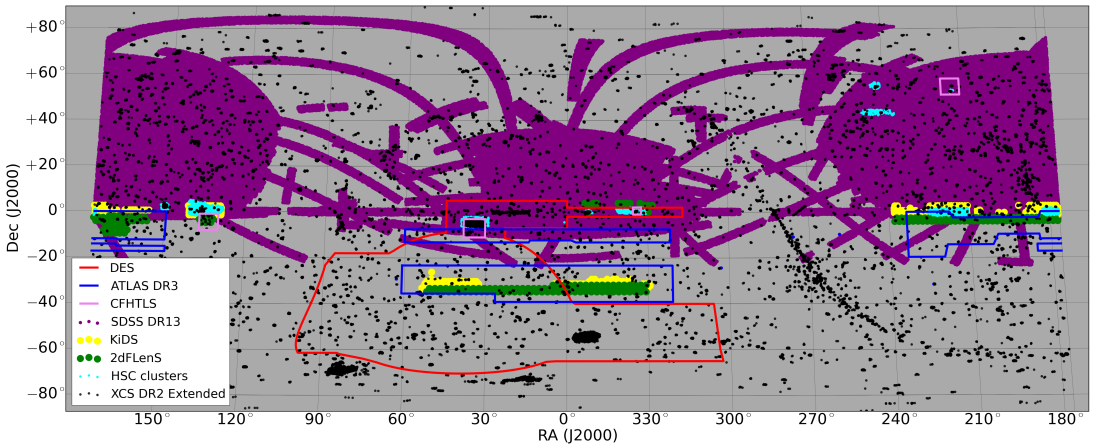

Figure 3.3 *The XCS DR2 extended sources across the whole sky. We also highlight optical and IR survey data which overlap with our sources. We use the SDSS DR13 and the HSC overlap regions in this data release.*

understood XMM Newton PSF, which depends on the angle of the object from the centre of the observation and number of photon counts, as has already been discussed in Lloyd-Davies et al. (2011). The XAPA code has sometimes been found to classify foreground stars or galaxies as X-ray extended sources; in the case of low-redshift objects, it has also been found to split one extended source into multiple ones. In Fig. 3.2, we show three examples of objects that were classified by XAPA as extended even though they are not clusters, or as PSF-sized while they are clusters; two point sources blended identified as extended, an extended source marked as PSF-sized and a foreground, low redshift extended source split into multiple extended sources. Deciding not to eyeball the XAPA classified sources would result in a contaminated cluster catalogue, with false and multiple cluster detections. In order to avoid this, we have to confirm that the PSF-sized and extended sources given by XAPA are indeed clusters, as discussed in the following.

3.5.1 XCS-SDSS Zoo

To this end, we decided that the XAPA cluster candidates should be optically classified as clusters or not clusters. We use the large SDSS imaging coverage to create optical

images of the cluster candidates. We initiated a cluster classification project in www.zooniverse.org, as opposed to the Zoo project created using our own code in XCS DR1, where members of the XCS collaboration classified our list of XCS cluster candidates in the SDSS DR13 region. This is a "scientist-crowd-sourced" effort which differs from the "crowd-sourced" Galaxy Zoo project (Land et al., 2008) and the recent Radio Galaxy Zoo project (Kapińska et al., 2017), in which public could voluntarily take part. The former has extracted morphological properties of hundreds thousands of galaxies (Lintott et al., 2008) which led to, e.g., studies of galaxy mergers (Weigel et al., 2017) and environmental dependence on the galaxies star formation (Smethurst et al., 2017). Zooniverse infrastructure offers a suitable environment for "scientist-crowd-sourced" analyses, offering options for various applications on images, discussion forums and different sets of subjects to be analysed, available as public or private projects.

In our project, the "project manager" creates a workflow, which, in this case, is a question whether the object is a galaxy cluster or not, along with some SDSS and XCS images of each object that will help with the classification. More specifically, the classifier has to choose one of the four options for each subject:

1. a cluster, an object with an X-ray extended source coincident with an overdensity of galaxies,
2. a possible cluster, an object with an X-ray extended source coincident with a moderate overdensity of galaxies or an object with an overdensity of galaxies coincident with an acceptable extended X-ray source,
3. an object that cannot be confirmed to be a cluster with the given data, or
4. a false-detection, as a foreground galaxy, a star, a source next to the edge of an observation or next to a very bright X-ray source.

These are similar to the "gold", "silver", "bronze" and "other" categories in XCS DR1 Zoo project. Each candidate has to be classified a minimum of three times by three different consortium members (as opposed to five times in XCS DR1). A

list of subjects is then uploaded by the project manager to be classified under this workflow. For each subject we showed three sets of three images: the SDSS DR13 colour image of the cluster candidate, the optical image with overlaid X-ray contours and the XMM observation, each of these in a 3×3, 6×6 and 12×12 arcmin field of view. A discussion board was made available for any comments on a specific subject by the classifiers. The "project collaborators", who are the XCS members, enter the project and classify the sources available, by switching between the three sets of images that are available. An example of such a classification as appeared in zooniverse is shown in Fig. 3.4.

Concerning the PSF-sized objects, we individually eyeballed each one in a smaller classification project to look for falsely-marked extended sources by the XAPA algorithm in this list. This is a new feature that has not appeared in XCS DR1 classifications. In the PSF sources project, the classifiers had to answer the question of whether this object should be added to the main project or not. The question was accompanied by the same set of images as the main project for each subject. In the end, the objects tagged with "yes" on this project were included in the main project.

The main classification project took part in two stages, by splitting the XCS cluster candidate list in two smaller ones. At the end, every candidate had a set of minimum three classification numbers associated with it; option *(i)* of the classification gave 1 point to the candidate, option *(ii)* gave 2 points, option *(iii)* gave 3 points and option *(iv)* gave 4 points. We defined a subject "score" of the mean of the classifications. After the end of the first stage, we re-classified within the same Zoo project one more time the subjects that were given 3 different values; as a result, some objects now have 4 Zoo classifications.

This led to a list of clusters associated with their score. The XCS list of clusters in SDSS was extracted from this list following the procedure:

- Every subject with mean classification above 2.5 was excluded.
- Subjects with scores between 2 and 2.5 were individually checked. The ones that had a larger amount of classification values 3 or 4 rather than 1 or 2 were

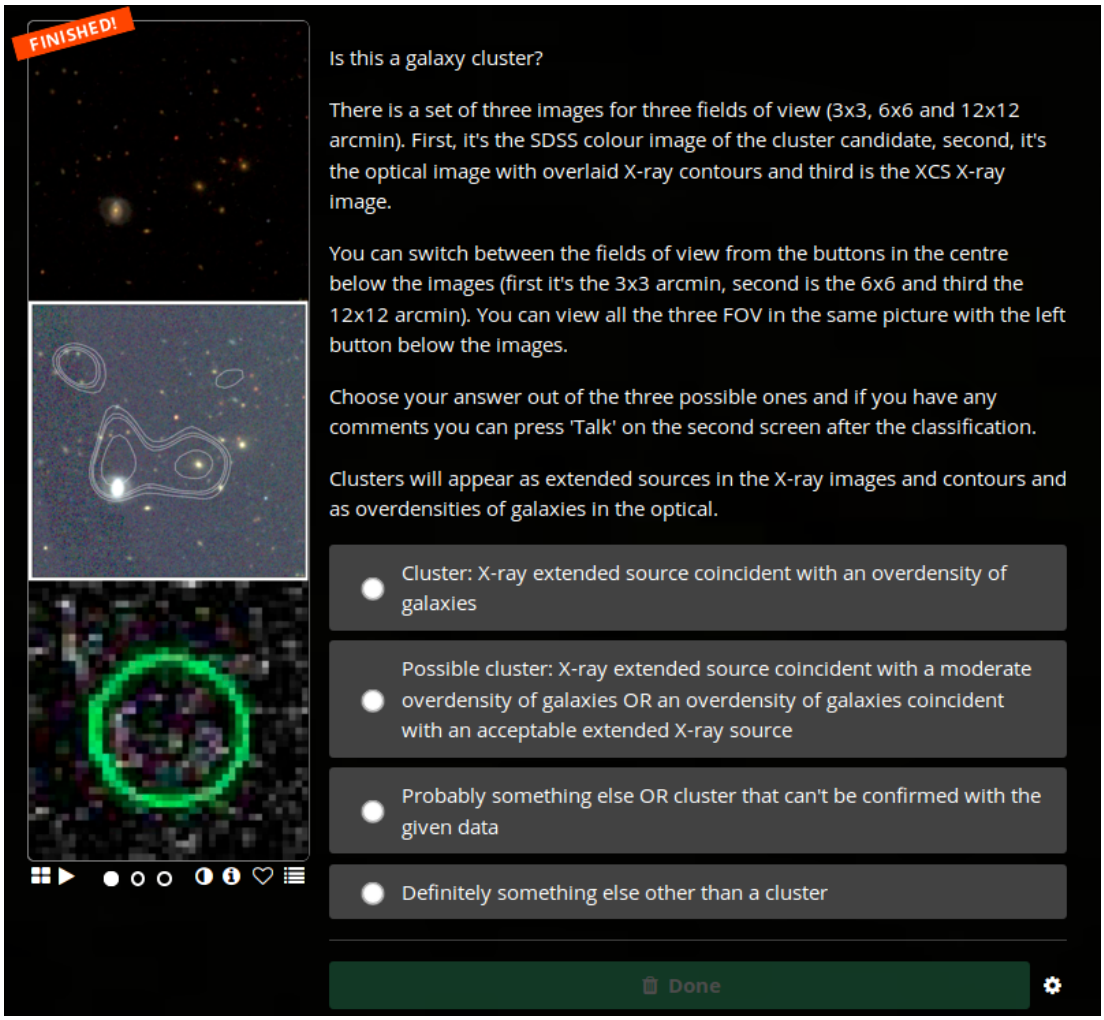

Figure 3.4 *Screenshot of the XCS-SDSS Zoo project which we used to classify XAPA extended sources as clusters. The classifiers used a set of 3×3 arcminute images, including colour composites with overlaid smoothed X-ray contours, and the raw X-ray data with the XAPA source location and shape. The 6×6 and 12×12 arcminute images are available if needed through the buttons under the images. The four classification options are on the right.*

Table 3.1 *Summary of numbers of objects that entered the XCS-SDSS Zoo project and that were successful in entering the main Zoo, in the case of the PSF sources, or entering the final XCS-SDSS cluster list, in the case of the sources entered the main Zoo.*

	entered	successful
PSF Zoo	1,384	268
Main Zoo	3,074	1,255

excluded. The ones that had same number of 3 or 4 with 1 or 2 we eyeballed and the ones that were certainly not clusters were excluded.

- The remaining list was checked for cases that are either multiple XMM observations of the same cluster or a cluster that was divided in multiple ones by XAPA and more than one of them were included in the sample.

The candidates entered the XCS-SDSS Zoo were chosen to have a low threshold value of 200 counts in the X-ray soft band ($0.5-2$ keV), as this is a value above which we can usually extract X-ray temperatures and luminosities from our algorithms (our algorithms converge to a temperature/luminosity value, see Lloyd-Davies et al. (2011)). The total XCS DR2 sources in SDSS DR13 with more than 200 counts in the X-ray soft band are 12,920, with 4,622 of them being either extended or PSF-size and 3,238 being only extended sources. The 1,384 flagged as PSF-sized objects were checked through the PSF Zoo project and 268 ($\sim 14\%$) of them made it to the main project as possible extended sources. After excluding some obvious duplicate sources, 3,074 candidates in total entered the main Zoo project. Analysis of the Zoo results led to the list of 1,255 optically confirmed XCS clusters in SDSS area. These numbers are summarised in Table 3.1. A map with the cluster positions on the sky is shown in Fig. 3.5. Some examples of sources that were classified unanimously as clusters, clusters with higher score (2-2.5) and sources that were classified as non-clusters are shown in Fig. 3.6.

In order to identify possible biases in the classification procedure, we present the clusters' score in the XCS-SDSS project within different redshift bins (for the 1,225 clusters with redshifts) in Table 3.2; the cluster redshifts were assigned through a procedure described in Section 3.6. We note that over a third of the clusters in the

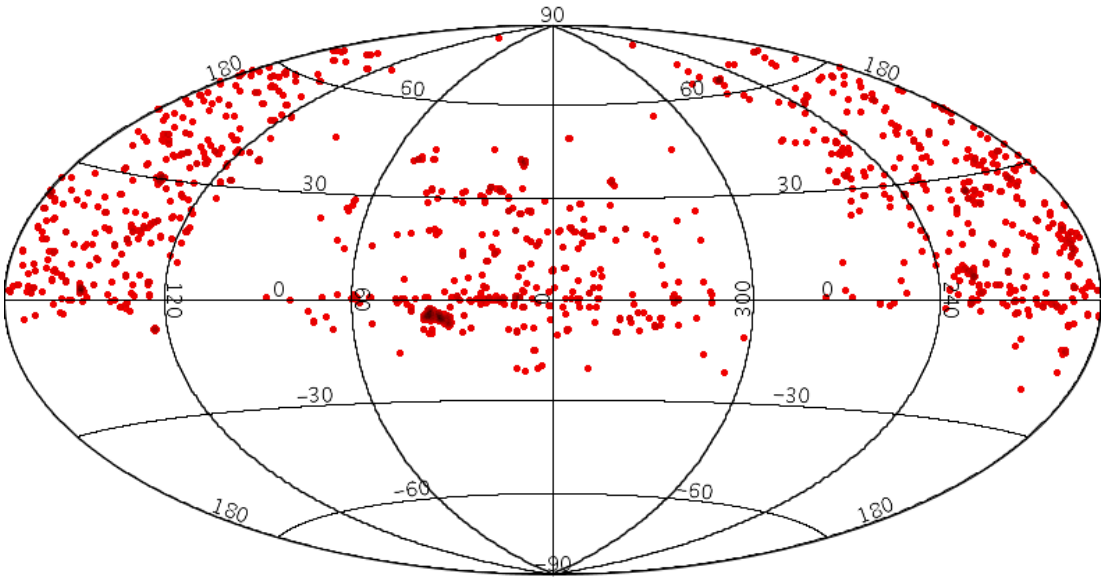

Figure 3.5 *The distribution of the XCS DR2 clusters in SDSS DR13 on the sky.*

Table 3.2 *Number and percentage of XCS clusters in SDSS with classification score equal to 1 or less or equal than 2 or 2.5 in different redshift ranges.*

	classification score $= 1$	classification score ≤ 2	classification score ≤ 2.5
$z \leq 0.1$	104 (8%)	223 (18%)	255 (20%)
$z \leq 0.2$	190 (15%)	422 (34%)	460 (37%)
$z \leq 0.4$	396 (32%)	823 (66%)	877 (70%)
$z \leq 1.2$	485 (39%)	1,132 (90%)	1,225 (98%)

whole redshift range were classified as definite clusters unanimously by the classifiers. Additionally, the cluster redshift does not seem to affect the classification score: it is the same fraction of unanimously definite clusters (score $= 1$) and non-definite clusters in all four redshift bins (score ≤ 2 or ≤ 2.5).

Moreover, we explore the individual classifiers Zoo points as a function of redshift to seek for possible selection biases introduced in the procedure. In Fig. 3.7, we calculate the number of "cluster" or "possible cluster" classifications per classifier as a function of redshift, normalised by the number of classifications for each classifier; we only include classifiers with more than 500 classifications both for clarity and because these are the ones who would bias more the selection function. Different line colours in the plot correspond to different classifiers and the black, thick line

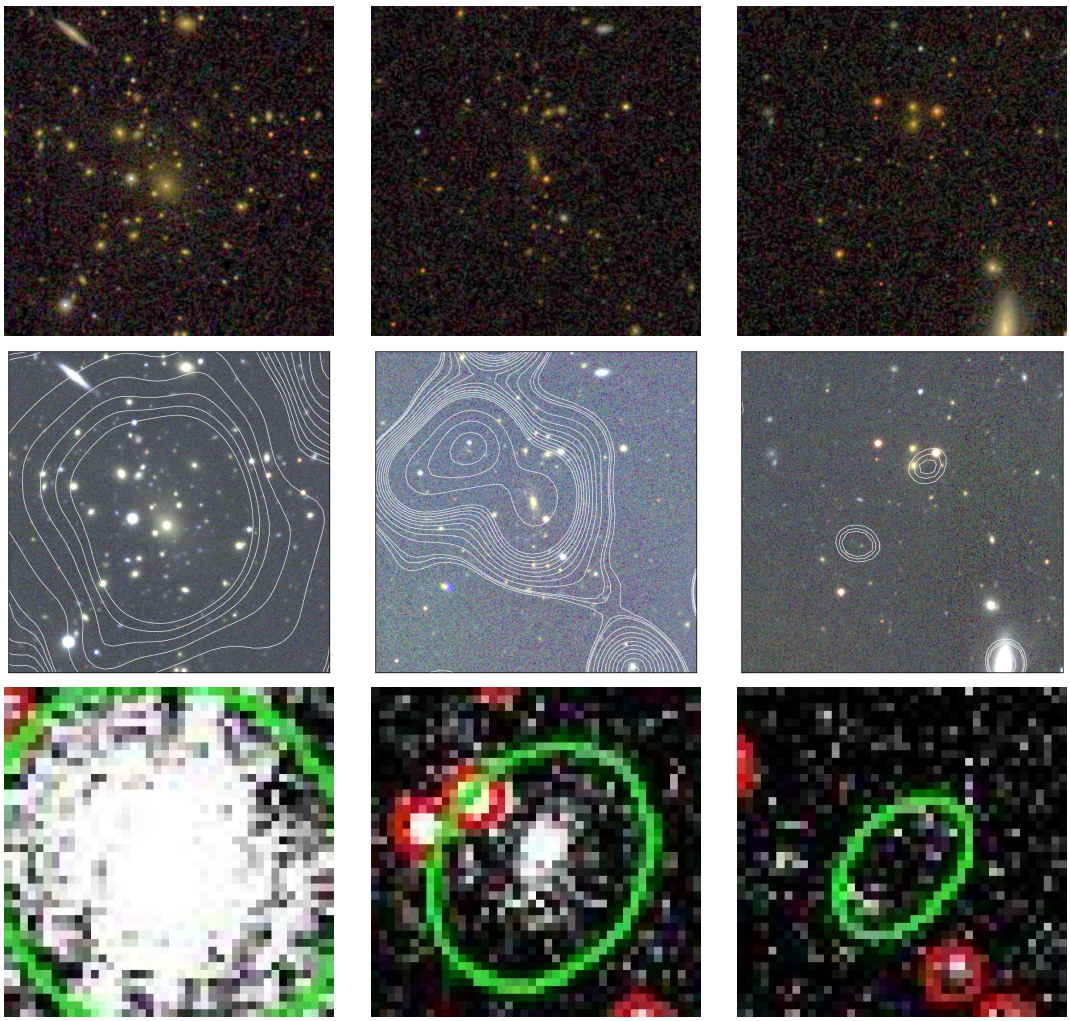

Figure 3.6 *Examples of three sources classified in SDSS cluster Zoo, from left to right, as definite cluster, possible cluster, something else. The sources from left to right are XMMXCS J0001737.5-008234.2 with Zoo score* $= 1$*, XMMXCS J000235.8-020227.5 with Zoo score* $= 2$ *and XMMXCS J001051.7+145227.2 with Zoo score* $= 2.67$*. Top panels: SDSS optical images, Middle panels: SDSS optical images overlaid with XCS contours, Bottom panels: XCS X-ray images. All are shown in 3*$\times$*3 arcminutes field of view.*

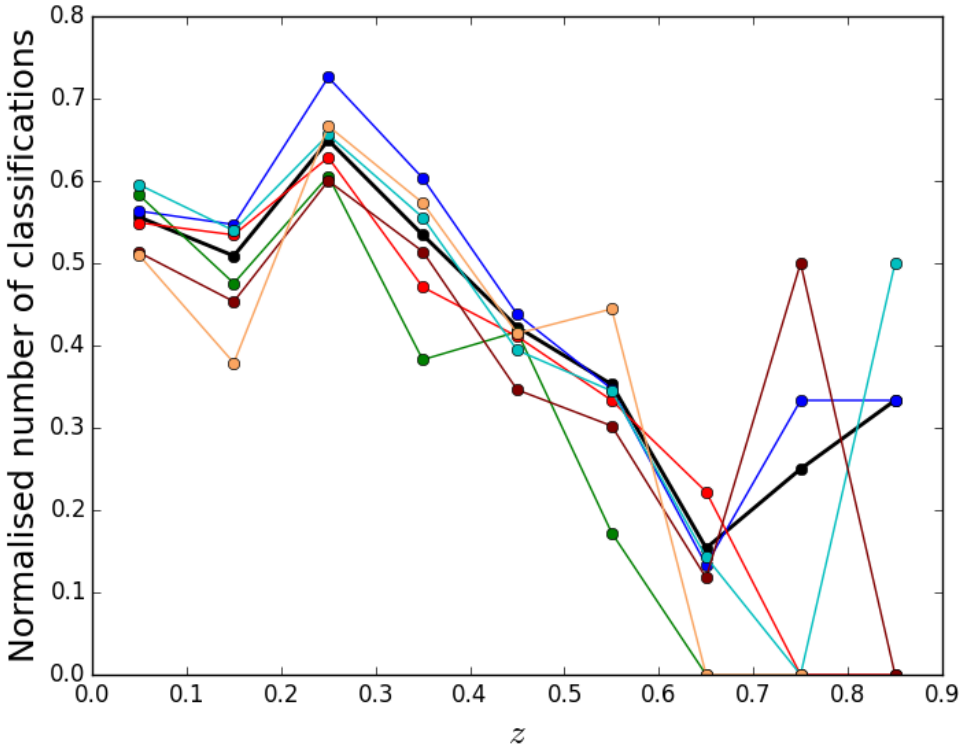

Figure 3.7 *Histograms of the "cluster" or "possible cluster" classifications per classifier as a function of redshift, normalised by the number of classifications for each classifier. Only the classifiers with more than 500 classifications are included both for clarity and because these are the ones who would bias more the selection function. Different line colours correspond to different classifiers and the black, thick line shows the classifications from all classifiers combined.*

shows the classifications from all classifiers combined. The trend seems to be similar between classifiers for $z < 0.6$, which means that classifications are consistent between classifiers. For $z > 0.6$, with the completeness and brightness of objects in SDSS dropping, it becomes more and more difficult to identify galaxy clusters. This explains the larger scatter in the classifications between individual classifiers in the higher redshifts. Finally, it is worth noting that the "ideal" redshift for a cluster to be identified in SDSS is between 0.2 and 0.3, possibly due to the angular size of the cluster which is similar to the field of view of the images used in our cluster Zoo.

3.5.2 XCS-HSC Zoo

In order to assess the quality of the classifications in SDSS and quantify the completeness and contamination of the SDSS catalogue, we use the Hyper Suprime-Cam of the Subaru Telescope (HSC hereafter) deeper imaging (Aihara et al., 2017) in the overlapping area with SDSS; the deeper imaging should lead to better quality classifications that can be compared with the SDSS ones to assess their quality.

The HSC classification project contained 154 XCS cluster candidates with more than 200 soft X-ray counts that reside in both HSC (Aihara et al., 2017) and SDSS area. The classification workflow and image configuration for each subject were the same as for the SDSS project. After following the exact same procedure, we create an HCS cluster list associated with the classification scores and compare it to the corresponding SDSS list for the same cluster candidates. We note here that the colour images in the SDSS and HSC cases were made using different tools (APLpy in python (Robitaille and Bressert, 2012) for the SDSS images and STIFF (Bertin, 2012) for the HSC images) which results in a different colour scaling.

In general, the HSC and SDSS objects turn out to have similar classifications; 145 of the clusters have similar classifications in both "Zoos", i.e. 83 candidates were classified as "clusters" or "possible clusters" in both HSC and SDSS Cluster Zoo and 62 of them were classified as "non-clusters" in both projects. The HSC candidate list contains 5 "clusters" or "possible clusters" that are "non-clusters" in the SDSS list and, on the contrary, 4 candidates are "clusters" or "possible clusters" in SDSS but "non-clusters" in HSC candidate list. The different colour scaling of the HSC images might have affected the classifiers' decision of observing a galaxy overdensity or not in the optical image; as a result, the final cluster catalogue was not considerably affected by the deeper HSC data. The images of the 9 (5+4) candidates that acquired opposite classifications in the two projects are shown in Fig. 3.8 and Fig. 3.9. For consistency reasons, we did not remove these objects from the final cluster list, since we would insert further biases in the subset of common SDSS and HSC clusters.

Figure 3.8 *HSC (top) and SDSS (bottom) images of the 5 XCS candidates that were classified as "clusters" or "possible clusters" in HSC and "non-clusters" in SDSS Cluster Zoo. From left to right the candidates are: XMMXCS J021641.0-041842.0, XMMXCS J021803.4-055526.5, XMMXCS J022105.5-044101.7, XMMXCS J022403.8-041332.8, XMMXCS J141652.4+522053.6.*

Figure 3.9 *HSC (top) and SDSS (bottom) images of the 4 XCS candidates that were classified as "clusters" or "possible clusters" in SDSS and "non-clusters" in HSC Cluster Zoo. From left to right the clusters are: XMMXCS J020517.4-043901.1, XMMXCS J020846.4-042608.2, XMMXCS J021341.4-052145.3, XMMXCS J021831.9-041349.5.*

From the above statistics we can quantify the completeness and contamination of the SDSS catalogue, given the HSC cluster catalogue in the common area. The completeness of a catalogue quantifies the percentage of objects included in the catalogue out of the total number of objects that exist and should have been included given the selection criteria; this is calculated to be 94.3% for the XCS DR2–SDSS catalogue. On the other hand, the contamination quantifies the percentage of objects in the catalogue that are falsely included given the selection criteria; this is 4.6% for the XCS DR2–SDSS catalogue. Those are both estimates of the real completeness and contamination of the catalogue, given that they have been calculated for a smaller area on the sky than the total area XCS DR2–SDSS includes and HSC classifications have been assumed to produce the "correct" cluster catalogue in the common HSC-SDSS area.

Overall, the HSC imaging helped the classifiers decide more easily if the object is a cluster or not, as we find that the resulting score of the objects in HSC Zoo is less evenly spread in the range of 1 to 4 and more concentrated to the values of 1 and 3 as shown in Fig. 3.10. This is shown by the fact that 25% of the objects have score $= 1$ as opposed to 19% in SDSS and 12% of the objects have score between 2 and 2.5 in HSC Zoo, compared to the 16% in the SDSS one. That means that it was easier for classifiers to decide if an object is definitely a cluster (score 1) or definitely something else (score 3-4) in HSC than in the SDSS Zoo project. However, the HSC classifications did not offer a significant difference in the resulting cluster catalogue list.

The HSC Zoo project resembles the S82 (Annis et al., 2014) and NXS (Miller et al., 2006) Zoo projects in XCS DR1; the deeper S82 and NXS imaging compared to SDSS DR7 helped optically identify some fainter clusters as HSC Zoo did. However, in XCS DR1 these classifications were taken into account when constructing the final cluster list, while in XCS DR2, the HSC classifications were only used to compare with the final cluster list from SDSS DR13 and assess its performance.

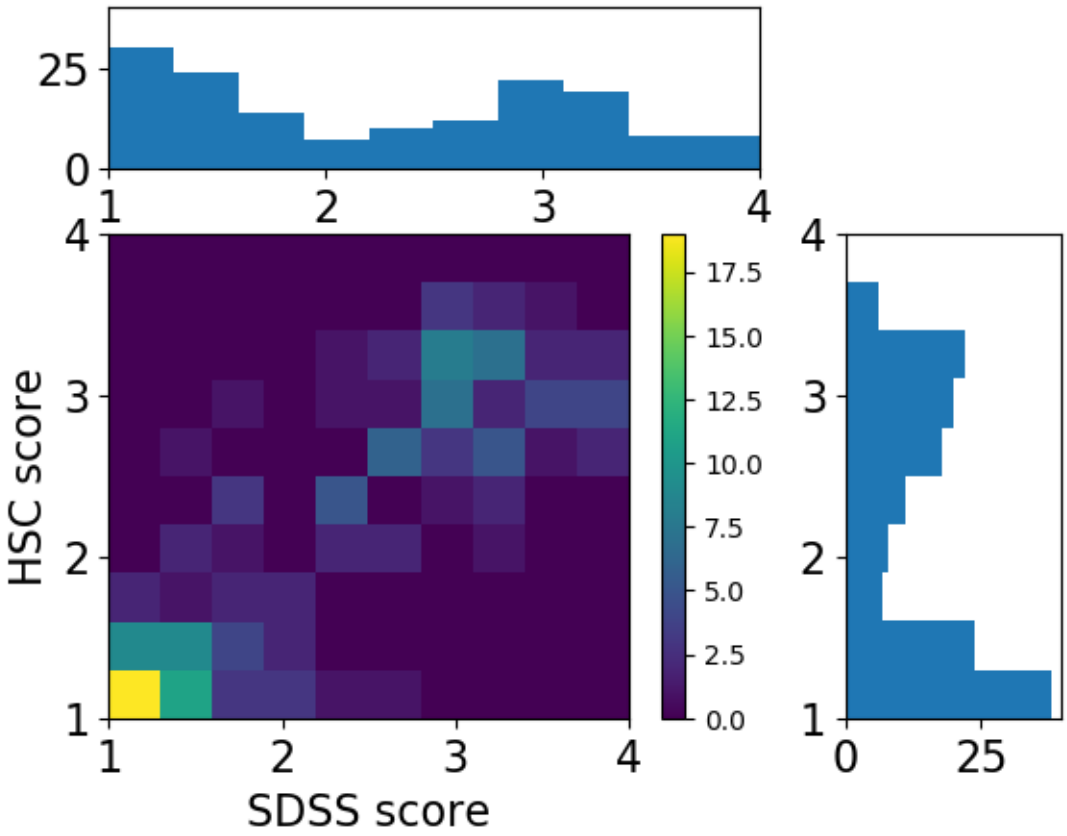

Figure 3.10 *Comparison between the HSC (x axis) and SDSS (y axis) classification scores of the 154 overlapping XCS sources. The SDSS score is more evenly spread in the whole range than the HSC, which is concentrated around the values of 1 and 3.*

3.6 Optical properties

The main source of acquiring redshifts for our clusters is by determining our own spectroscopic redshifts using spectroscopic galaxy surveys such as SDSS DR13 (SDSS Collaboration et al., 2016), the VIMOS Public Extragalactic Redshift Survey (Scodeggio et al., 2016, VIPERS Public Data Release 2) and DEEP2 (Matthews et al., 2013). Alternatively, in order of preference, we seek for spectroscopic redshifts for our clusters in the literature, calculate our own photometric redshifts using two different algorithms (GMPhoRCC, Hood and Mann (2017) or zCluster, Hilton et al. (2017)) or seek photometric redshifts in the literature.

In this section, we present a brief overview of our algorithms used to calculate spectroscopic and photometric redshifts for our clusters. We explain the redshift assignment and present our results by comparing them with those from other catalogues.

3.6.1 Spectroscopic redshifts

We cross-match our clusters with the SDSS DR13, VIPERS PDR2 and DEEP2 surveys and assign a cluster redshift using an iterative procedure. We start by combining all redshifts of galaxies within 1.5 arcminutes of the XCS cluster centre with the biweight location estimator Beers et al. (1990). A cut of ± 3000 km/s around the initial redshift is made and the redshift is re-estimated with the biweight location estimate for the galaxies within 1 Mpc projected distance from the centre. The number of galaxies used to calculate these redshifts is between 1 and 48 with a median of 3. This is the same method that has been used in Hilton et al. (2017) to calculate SZ-detected cluster redshifts.

We acquire 928 spectroscopic cluster redshifts from SDSS DR13, 2 from VIPERS PDR2 and 1 from DEEP2 with this process.

For the rest of the clusters we seek spectroscopic cluster redshifts in the literature.

When searching in NED, we look for clusters with redshift measurements and check if these are spectroscopic in the publication(s) listed as their source(s). There are no cases where the multiple spectroscopic redshift estimates available for the same cluster were significantly different from each other.

3.6.2 GMPhoRCC redshifts

We calculate photometric redshifts for our clusters using the Gaussian Mixture full Photometric Red sequence Cluster Characteriser (GMPhoRCC hereafter), primarily, and zCluster secondarily.

GMPhoRCC is a cluster-characterisation algorithm, which identifies clusters in optical surveys that have been previously detected by other methods. It takes advantage of two main cluster characteristics: the red sequence galaxies and the brightest cluster galaxy (BCG). GMPhoRCC uses the cluster centres of a cluster list along with magnitude and photometric redshift data from optical galaxy surveys to estimate the red sequence redshift, colour, colour-magnitude relation, richness of the clusters as well as the BCG properties. In this data release, we use photometric redshifts from SDSS DR13 (Csabai et al., 2003).

GMPhoRCC's characterisation procedure takes place in five main steps. After masking the cluster and its close background region, optical data is extracted around the cluster candidate region (outer aperture). The size of the outer aperture is between 1 and 4 arcminutes and is chosen as the one whose sum of colour overdensity peaks has the largest value. An inner cone is applied to separate the cluster region from the background (inner aperture). The redshift and colour histograms of the galaxies in the inner and outer apertures are fitted using the error-corrected Gaussian mixture (ECGM hereafter; Hao et al., 2009); different peaks are treated as different cluster candidates. The initial redshift and colour estimate are the peaks in the respective background-subtracted distribution of the cluster region. The code assumes a colour band where the 4000 Å break appears in galaxies' spectra depending on their redshift; so the cluster is studied in the colour band that corresponds to its redshift. Every

potential cluster's galaxies are initially fitted with an horizontal colour-magnitude relation (CMR hereby) using the BCES method (Akritas and Bershady, 1996) that takes into account the errors in the galaxies' colours. The cluster's red sequence galaxies colours and redshifts extracted are again fitted with ECGM and filtered to have appropriate colours for their redshifts (Gladders et al., 1998). Their final CMR is then fitted and the cluster BCG is selected from the cluster red sequence as the brightest galaxy in the i-band within 4 arcminutes or $0.5h^{-1}$ Mpc radius out of the three brightest ones in the cluster. The peak in the ECGM redshift histogram of the CMR filtered galaxies is the cluster red sequence and the BCG candidates mean spectroscopic redshift determines the cluster's spectroscopic redshift. The cluster chosen amongst the candidates is the one which has the most consistent initial, red sequence and BCG redshift with its colour. Finally, cluster richness is calculated using two different methods: counting the number of galaxy members within an aperture and fitting a Schechter luminosity function to them. For both of these methods, the number of galaxies is calculated in the whole aperture and in the whole aperture minus the inner cluster cone. The second is subtracted from the first to get the final richness measurement.

GMPhoRCC uses a quality control system consisting of flags appended to the clusters during the characterisation procedure. This helps to identify possible catastrophic failures. Flags are related to the cluster distributions, like redshift and/or colour multi-modality, consistency of the BCG and red-sequence redshifts (BCG redshifts are more reliable and usually spectroscopic) and richness (low richness might mean that the cluster has not been detected optically). Quality flag varies from 0 to 3, with 3 being the best and 0 the worst quality measurement. For more details, see Hood and Mann (2017).

The galaxy catalogue used is the full SDSS DR13 catalogue with a magnitude limit of $m_i < 21$ and with photometric or spectroscopic redshifts, when available, with the query similar to what described in Hood and Mann (2017). We acquire redshifts as well as richnesses for 1,223 clusters from our list. In Fig. 3.11 we show the redshift cumulative histograms of the clusters assigned with GMPhoRCC redshifts of different

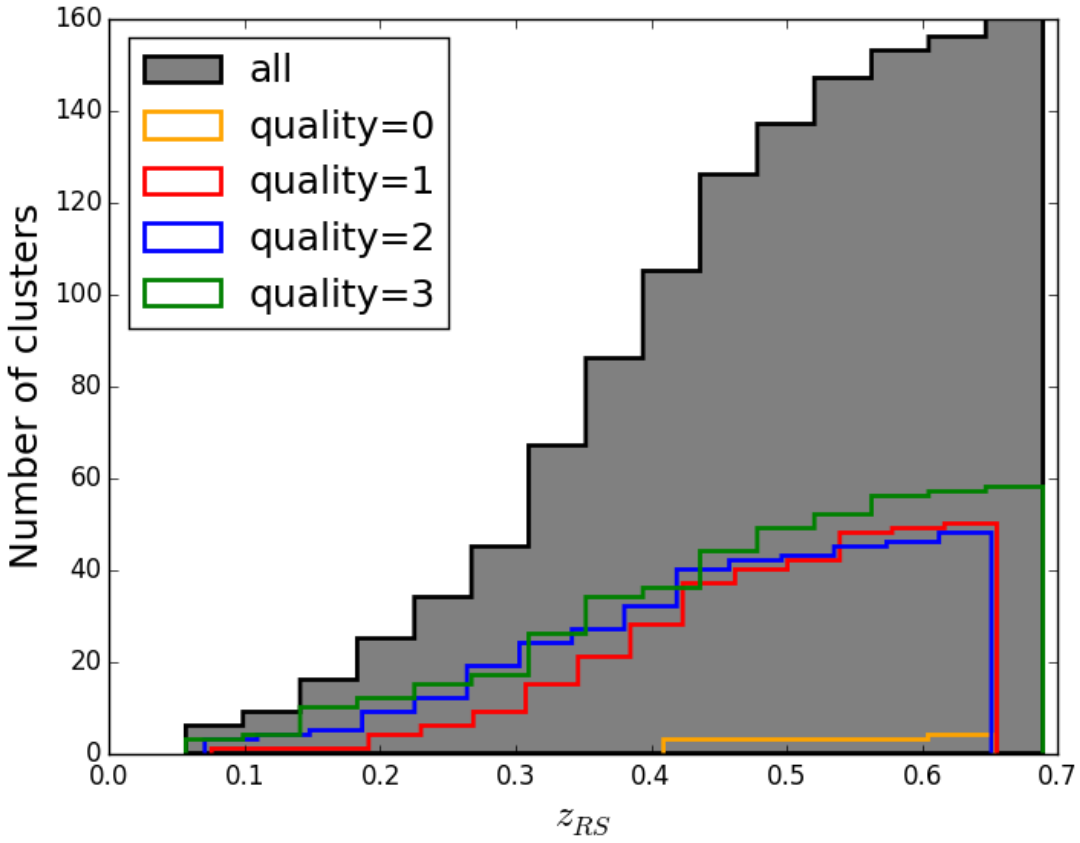

Figure 3.11 *Cumulative redshift histogram of XCS DR2-SDSS clusters assigned with GMPhoRCC redshifts, $z_{\rm RS}$, in grey. The different quality redshifts are shown in separate histograms, with green representing redshifts with quality 3 (best quality, 58 redshifts), blue for redshifts with quality 2 (48 redshifts), red for redshifts with quality 1 (50 redshifts) and orange representing redshifts with quality 0 (4 redshifts).*

GMPhoRCC quality.

3.6.3 zCluster redshifts

As an additional photometric redshift source we use a multi-band photometric redshift estimator, zCluster, which is also used in the redshift estimation of the ACTPol clusters (Hilton et al., 2017).

zCluster is a cluster redshift estimator that does not use the red sequence of the clusters, but a set of spectral templates instead. It takes into account all the galaxy photometric information available and has the difference of not making additional

assumptions about the optical properties of the cluster galaxies, since it calculates redshifts of clusters found by other methods.

zCluster compares the broadband SED (u, g, r, i, z for SDSS) of each galaxy around the cluster centre with the SED templates taken from BPZ (Benítez, 2000) and EAZY (Brammer et al., 2008). It then constructs a redshift distribution, $p(z)$, for every galaxy, using the χ^2 value between the galaxy and template SED distribution at every redshift z_i studied. The cluster photometric redshift is found from the weighted sum of the individual galaxy $p(z)$s, which are fitted with the projected two-dimensional Navarro-Frenk-White profile (Navarro et al., 1997) within a projected radius of 1 Mpc. Moreover, it uses a magnitude based prior and a prior for the photometric cluster redshift which depends on the optical survey depth ((0.05, 0.8) for SDSS). The final cluster redshift is the peak of the smoothed $n(z)$ distribution. Since the cluster redshift distribution depends on the survey depth, few clusters are expected to have $z > 0.5$ in SDSS. For more details on the zCluster algorithm, see Hilton et al. (2017).

We acquire zCluster redshifts for 1,248 of our clusters (false positive rate is $\sim 2\%$).

3.6.4 Redshift assignment

To sum up, the XCS DR2-SDSS cluster's redshift is assigned in the following way:

- if there is a spectroscopic redshift calculated by XCS using SDSS DR13, VIPERS or DEEP2, this is kept as the cluster's redshift. 931 clusters have redshifts assigned by this method. Else,

- if there is a spectroscopic redshift found in literature available, this is kept as the cluster's redshift. 117 clusters have redshifts assigned this way. Else,

- if there is a photometric redshift calculated by GMPhoRCC, this is kept as the cluster's redshift. 160 clusters have redshifts assigned by this method. Else,

- if there is a photometric redshift calculated by zCluster, this is kept as the cluster's redshift. 6 clusters have redshifts assigned this way. Else,

- if there is a photometric redshift found in literature available, this is kept as the cluster's redshift. 11 clusters have redshifts assigned this way.

Having so far redshifts for 1,225 clusters from our list leaves us with 30 clusters with no assigned redshift. Masked regions and incomplete SDSS photometry are the possible reasons that GMPhoRCC and zCluster have not found a galaxy overdensity and, therefore, a photometric redshift estimation for the rest of the clusters.

In total, 1,225 of our clusters have associated redshifts, either spectroscopic or photometric, either calculated by XCS or taken from literature. All these categories of redshifts are plotted in histograms in Fig. 3.12. All the clusters were eyeballed to provide reassurance that the redshifts assigned seem suitable and matching the optical and X-ray image of the cluster.

Next, we assess the GMPhoRCC and zCluster redshift cluster estimation by comparing the redshifts with spectroscopic redshifts calculated from SDSS as described earlier for the clusters with both available. We show the comparison in Fig. 3.13; the top panel uses all SDSS spectroscopic redshifts available, while the bottom panel uses SDSS spectroscopic redshifts calculated from at least 3 galaxy members in each cluster. The outliers rate ($(z_{\rm phot} - z_{\rm spec})/(1 + z_{\rm spec}) > 0.05$) in the top panel for GMPhoRCC is 17.4% and for zCluster is 20.6%, while for the bottom panel for GMPhoRCC is 11.1% and for zCluster is 16.9%, which are mainly coming from the peak at $z_{\rm phot} \sim 0.3$ for GMPhoRCC. This corresponds to the fact that the 4000 Å break shows between two SDSS filters. In this case, galaxies with this redshift have different fluxes in the same band, which causes the appearance of multimodality in the cluster colour histogram and makes the identification of the cluster's peak harder to identify by GMPhoRCC; the cluster redshifts in this case would have slightly altered redshifts and, if the peaks in the distribution are comparable, a bad GMPhoRCC flag. The outliers at the bottom part of the plots are underestimates of the cluster redshift by GMPhoRCC and zCluster; this is an artefact originating from the fact that the SDSS

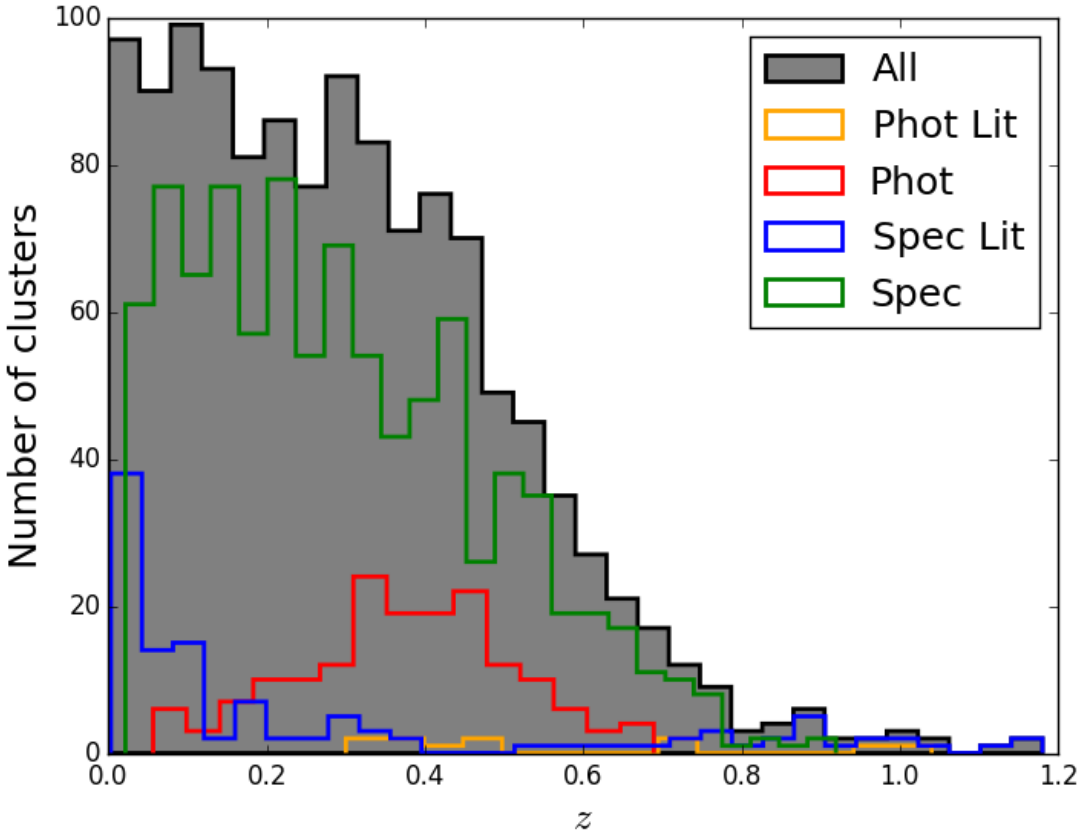

Figure 3.12 *Redshift histograms of all the XCS DR2-SDSS clusters (in grey). In green, the spectroscopic redshifts calculated by XCS are only plotted (931 redshifts), in blue the spectroscopic redshifts taken from literature are only plotted (117 redshifts), in red the photometric redshifts calculated with GMPhoRCC and zCluster are only plotted (166 redshifts) and in orange, the photometric redshifts taken from literature are plotted (11 redshifts).*

completeness drops at $z \gtrsim 0.5$ and hence so does the completeness of the redshift estimators. Those outliers are almost completely removed in the bottom panel of Fig. 3.13 where we only use clusters with at least 3 spectroscopic members. This is expected since the higher the cluster redshift, the less galaxies with spectroscopic redshifts are available to calculate the cluster's $z_{\rm spec}$.

Overall, the quality of the photometric redshifts calculated in SDSS worsens when exceeding the SDSS completeness limit of $z \gtrsim 0.5$. The GMPhoRCC redshifts at $z \sim 0.3$ have larger errors due to the 4000 Å break transisioning between two SDSS filters. Cluster spectroscopic redshifts are more reliable when more spectroscopic members are used for its estimation. Having all those uncertainties in mind, for each assigned cluster redshift, whether photometric or spectroscopic, we have eyeballed the SDSS optical image and checked against all redshifts available for each cluster in order to use the most reliable redshift as the XCS DR2–SDSS cluster redshift. As confirmed in Fig. 3.12, there are only few clusters with photometric redshifts above $z \gtrsim 0.5$.

Finally, we cross-match our clusters with clusters from the literature, shown in Table 3.3, within 1 arcminute distance from the positional information on the various catalogues (for ACT and ACTPol clusters we use 2.5 arcminutes separation and for PSZ1 and PSZ2 we use 10 arcminutes separation between the cluster centre coordinates); 1,052 clusters have already been detected by various surveys, and have calculated redshifts. That means that 203 of our clusters are new in the literature, X-ray, SZ or optically found, and 940 are new X-ray detections (not detected in XCS DR1, XXL100 or SPIDERS). In Table 3.3 we show the numbers of clusters with redshifts found in literature together with the literature source. Some of the clusters are detected in more than one of these surveys. Out of the 254 clusters in common with XCS DR1, 31 of them have assigned redshifts that differ more than 0.05 from the DR1 assigned redshift; for most of the cases (24 of the clusters) the DR1 redshift is photometric while the DR2 is spectroscopic and the rest of them were eyeballed and assigned the photometric redshift acquired from GMPhoRCC. For the 1 cluster left, none of the available redshifts were assigned (XCS DR1, GMPhoRCC or zCluster),

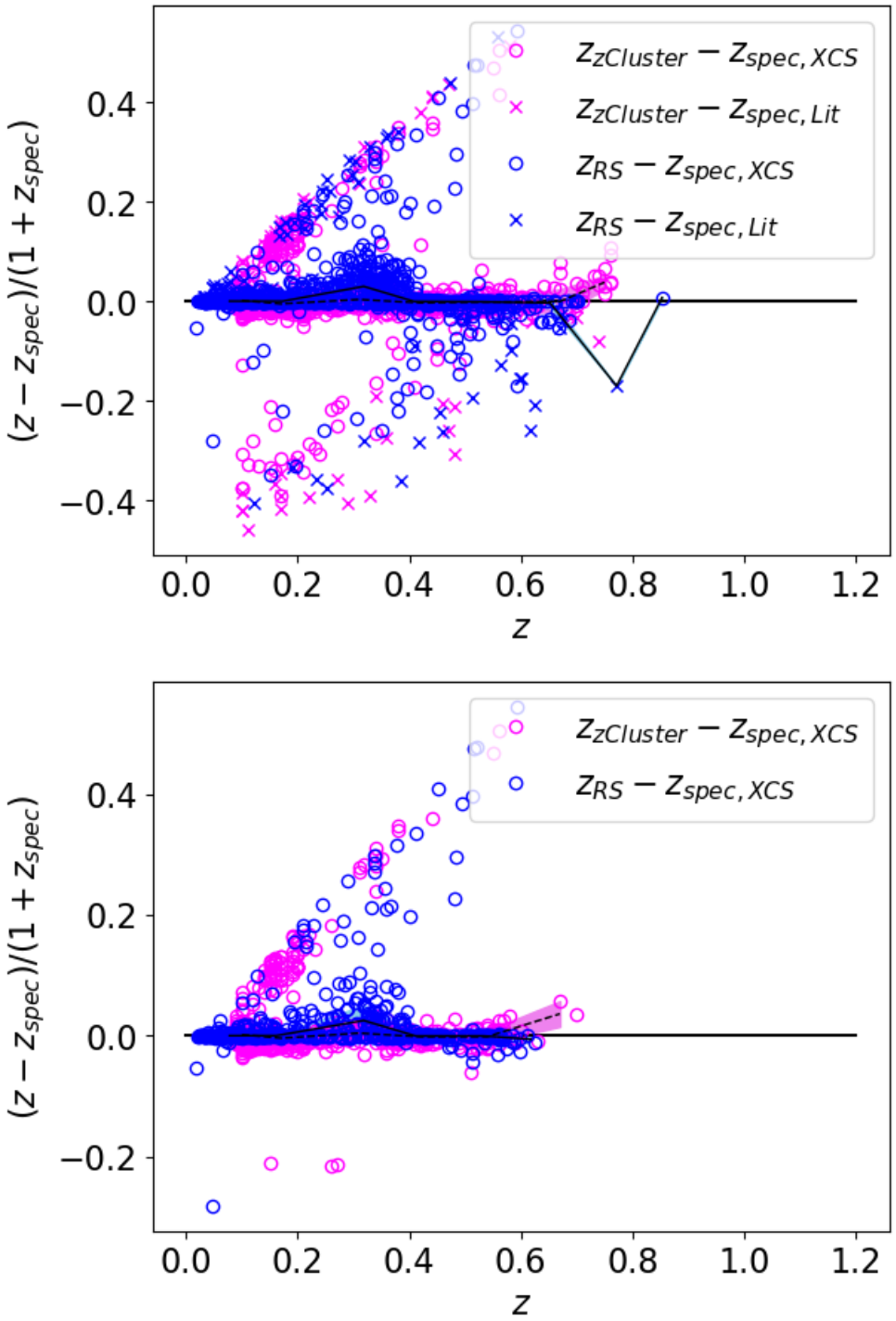

Figure 3.13 *Comparison of GMPhoRCC and zCluster cluster redshifts with spectroscopic redshifts calculated by XCS from SDSS spectroscopic galaxy redshifts or found in the literature. Blue circles represent GMPhoRCC redshifts compared to spectroscopic redshifts calculated by XCS, blue crosses represent GMPhoRCC redshifts compared to literature spectroscopic redshifts, magenta circles represent zCluster redshifts compared to spectroscopic redshifts calculated by XCS and magenta crosses represent zCluster redshifts compared to literature spectroscopic redshifts. The blue region shows the scatter of the GMPhoRCC redshifts while the pink region shows the scatter of the zCluster redshifts. The top panel uses all SDSS cluster spectroscopic redshifts calculated, while the bottom only includes those that were calculated using at least 3 galaxy spectroscopic redshifts.*

Table 3.3 *Number of clusters with redshifts in existing cluster catalogues. Note that these numbers include duplicates between the lists.*

No of clusters	No of clusters not in NED	No of ICM-selected clusters	Cluster catalogue	Reference
813	0	-	NED	https://ned.ipac.caltech.edu
254	70	254	XCS DR1	Mehrtens et al. (2012)
607	129	0	WHL	Wen et al. (2012)
15	1	15	ACT	Hasselfield et al. (2013)
196	42	196	Planck SZ (PSZ1)	Planck Collaboration et al. (2014a)
338	37	0	redMaPPer (RM)	Rykoff et al. (2014)
37	18	0	WHL high-z	Wen and Han (2015)
31	6	31	SPIDERS	Clerc et al. (2016)
45	12	45	XXL100	Pacaud et al. (2016)
216	44	216	Planck SZ (PSZ2)	Planck Collaboration et al. (2016a)
36	6	36	ACTPol	Hilton et al. (2017)
63	9	0	HSC	Oguri et al. (2017)

Data extracted on the 8^{th} of December, 2017.

since none of them seemed appropriate for this cluster.

3.6.5 Cluster richness

As mentioned earlier, GMPhoRCC calculates the cluster richness by counting the number of galaxy members within an aperture or by fitting a Schechter luminosity function to them. We have estimated richnesses for 1,223 of our clusters from GMPhoRCC. We compare the counting richness measurement, n_{200}, of GMPhoRCC with that of redMaPPer (Rykoff et al., 2014), λ, for the clusters in common in Fig. 3.14. For both catalogues, a magnitude limit of $m_i < 21$ for the SDSS galaxies is used to estimate clusters richness. We use good quality GMPhoRCC richness estimates and redMaPPer clusters centred in the XCS cluster centre with $\lambda > 20$ and $0.1 < z < 0.35$ where the catalogue is volume limited, hence robust according to Rykoff et al. (2014). The redMaPPer richness estimator is assigned by estimating a probability of each galaxy being a member of the cluster's red sequence by taking into account its projected distance from the cluster centre, its i-band magnitude and a colour variable through a filter function. The comparison shows differences, as expected; the two algorithms use different ways of defining cluster membership, so their estimates are not expected to be the same, but they are expected to correlate with a small scatter, as confirmed in Fig. 3.14.

The richness estimation is a very important part when studying the clusters mass-richness relation since it highly determines the relation (e.g. Rozo et al. (2011)). Rykoff et al. (2014) have conducted a variety of tests to ensure the quality of their richness estimator, λ, so the correlation to n_{200}, especially for higher values of n_{200}, is a confirmation of the latter's quality. Cluster centering issues between different wavelength observations of clusters also affects their richness estimation.

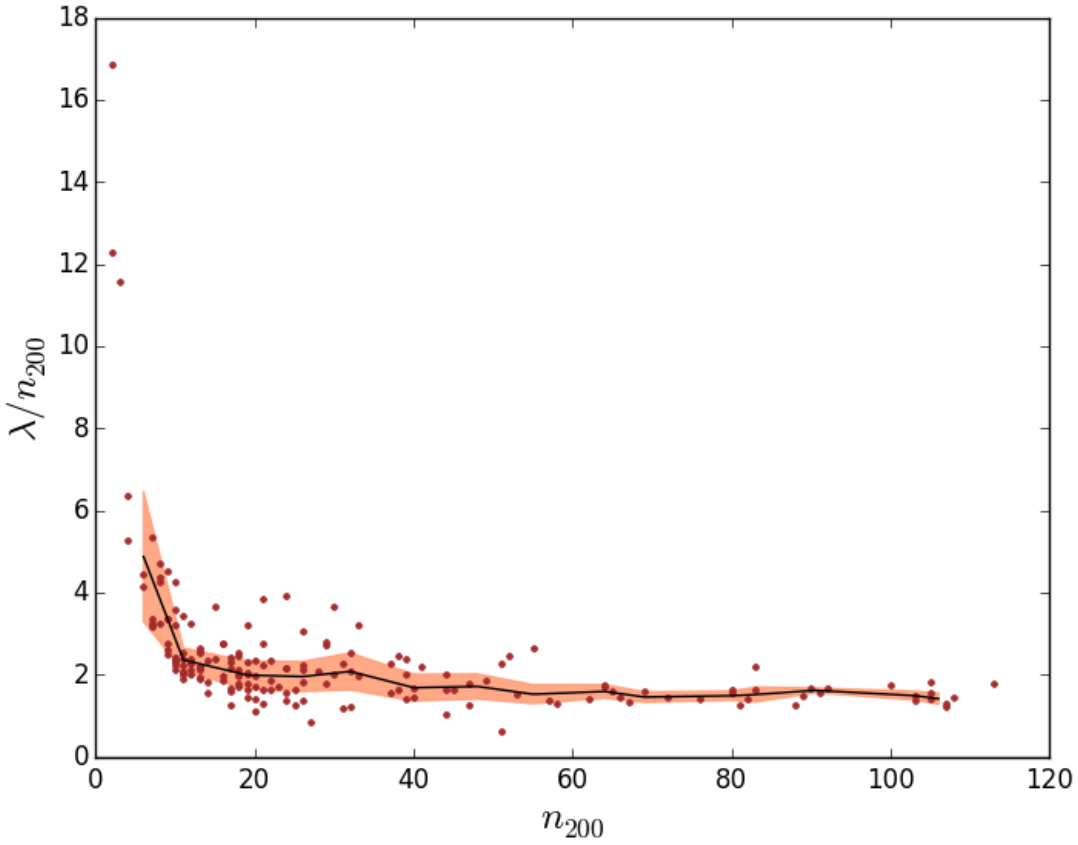

Figure 3.14 *Comparison of GMPhoRCC's n_{200} with redMaPPer's λ cluster richness estimate. The scatter of the richness estimation between the two algorithms is shown in the orange region. The different approach of the richness estimate between the two algorithms is obvious, as well as their correlation, which shows consistent measurements by GMPhoRCC.*

3.7 X-ray properties

We use the XCS Post Processing Pipeline (XCS3P) in order to derive the X-ray spectral properties of the clusters, namely their X-ray temperature ($T_{\rm X}$) and Luminosity ($L_{\rm X}$). The pipeline can be run in batch mode and applied to hundreds of clusters at a time, which is advantageous when studying the large number of clusters presented in this work. An overview of XCS3P, including methodology tests, can be found in Lloyd-Davies et al. (2011) (hereafter LD11). We briefly describe the analysis here and detail some of the improvements and corrections made since LD11.

Cluster spectra were extracted and fit using the XSPEC (Arnaud, 1996) package. The fits were performed in the 0.3-7.9 keV band with an absorbed MeKaL model (`wabs` $\times$ `mekal`) using the c-statistic. The `wabs` component accounts for photoelectric absorption by neutral hydrogen along the line of sight to the cluster, using cross sections defined in Morrison and McCammon (1983). The `mekal` (Mewe et al. 1986) component accounts for the emission from a hot diffuse gas enriched with various elements. Relative abundances of these elements are defined their ratios to Solar abundances ($Z_{\odot}$). During the fitting process, the abundance is fixed at $0.3Z_{\odot}$, the value typical for X-ray clusters (Kravtsov and Borgani, 2012). The redshift is also fixed, leaving the `mekal` temperature and normalisation free to vary.

As stated above, various improvements and corrections have been made to XCS3P, compared to the version described in LD11 and these are described below:

1. *Spectral extraction region*: In LD11, the spectral extraction region used was based on the XAPA (see Section 3.4) defined detection region: a circular aperture was defined using the length of the XAPA defined major axis as the radius. The spectral extraction region has now been updated to extract spectral properties within an estimate of r_{Δ}, i.e. within the radius at which the density of the cluster becomes Δ times the critical density of the Universe at the cluster redshift. We consider two radii commonly used in the literature i.e. r_{500} and r_{2500}. Cluster r_{500} values were estimated using the relation given in Arnaud

et al. (2005):

$$E(z)r_{500} = 1.104 \left(\frac{T_{\rm X}}{5{\rm keV}} \right)^{0.57} . \quad (3.1)$$

The process is iterative because we do not know a priori what $T_{\rm X}$ is: An initial temperature is calculated using the XAPA defined spectral region and this is used to estimate r_{500} using Equ. 3.1. Rather than using a circular region (as was the case for LD11), an ellipse is defined using the r_{500} estimate as the new major axis. The spectral ellipse retains the same aspect ratio and orientation as the original XAPA region. A new $T_{\rm X}$ value is defined within this ellipse, and this is in turn used to define a new r_{500} value. The process is repeated until r_{500} converges (the ratio of the new to old r_{500} defined to be >0.9 and < 1.1). To account for the background in the spectral analysis, we make use of a local background annulus centered in the cluster. For the background annulus, we used an inner and outer radius of $1.05r_{500}$ and $1.5r_{500}$ respectively (see blue outer annulus in Fig 3.16). During each iteration, a calculation of coefficient of variation (Koopmans et al., 1964) of the T_X is performed. This coefficient is defined as the ratio of the standard deviation (σ) to the mean (μ), given by $C_v = \sigma(T_{\rm X})/\mu(T_{\rm X})$. In this work, we adopted a value of $C_v < 0.25$ as an indicator of a reliable measurement.

Cluster r_{2500} were estimated via the same method as detailed above, with two main differences. First, r_{2500} values were estimated using the following relation:

$$E(z)r_{2500} = 0.491 \left(\frac{T_{\rm X}}{5{\rm keV}} \right)^{0.56} , \quad (3.2)$$

once again taken from Arnaud et al. (2005). Second, the background was taken into account using an annulus centered on the cluster with an inner and outer radius of $2r_{2500}$ and $3r_{2500}$ respectively.

2. *Selection of cluster spectra*: In LD11, all available spectra were used in a simultaneous XSPEC fit, typically comprising the usual PN, MOS1 and MOS2 cameras. However, for clusters that have multiple observations there can be

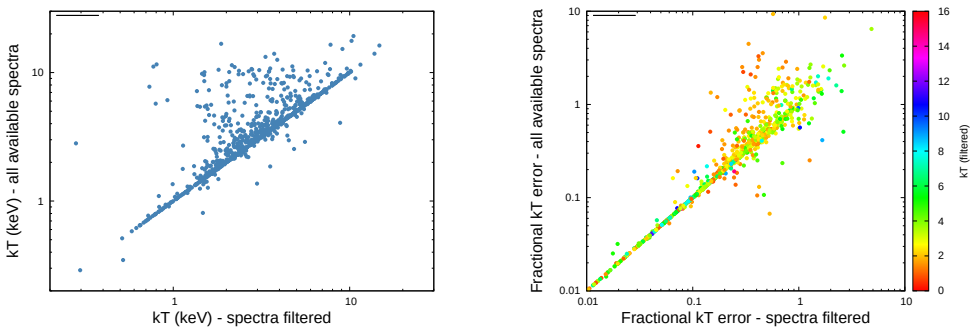

Figure 3.15 *Comparison of the fractional error on the temperature when using all available spectra, to the fractional error only using spectra satisfying the criteria as given in Section 3.7.*

more than three spectra. We found that using all available spectra, irrespective of quality, increases the relative error on $T_{\rm X}$. Therefore, each individual spectrum is fit in XSPEC, and only included in the simultaneous XSPEC analysis if the temperature is within the range $0.08 < T_X < 30$ keV, and contains both upper and lower 1σ errors. If either of these conditions are not met, then the respective spectrum is dropped from the simultaneous fit. The effect of our spectra selection method on the temperature error is shown in Figure 3.15.

3. *Measurement of luminosity*: While developing the latest version of XCS3P, it was found that the luminosity errors were calculated incorrectly. When estimating the luminosity in XSPEC, the absorption component (n_H) must be set to zero in order to represent conditions at the cluster. However, the luminosity errors will be in error if determined while n_H is set to zero (since the errors are determined from the spectral fit to the absorbed data), as was previously done in LD11. This was corrected in the current version of XCS3P using the following method. First, the errors are determined using an initial luminosity (L_{ini}) calculation before n_H has been set to zero. Then, n_H is set to zero and the luminosity is determined (L_0). The errors are then scaled by the ratio of L_0 to L_{ini} (i.e. $L_{err} \times L_0/L_{ini}$).

4. *Exclusion of extended sources*: The routine used to exclude nearby extended sources was found to overestimate the area to 'drill out' around the extended

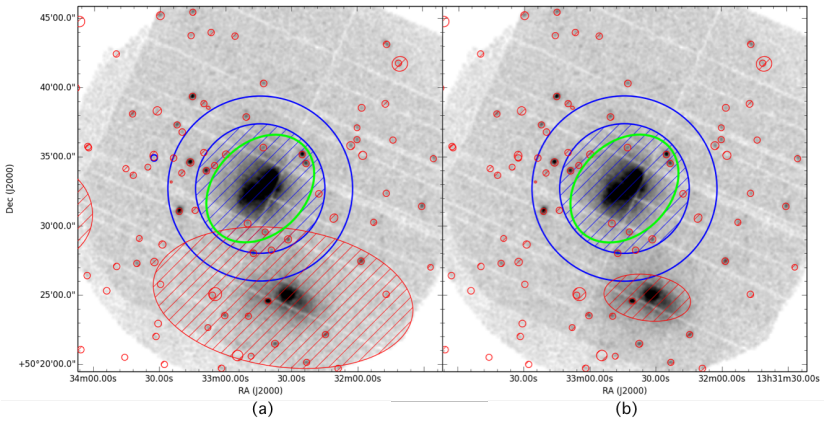

Figure 3.16 *In each image the green ellipse represents the cluster extraction region, the blue annulus represents the background region and the red small circles are excluded point sources. The nearby extended source is excluded using the red hashed ellipse based upon LD11 analysis (left) and the unscaled updated (right) analysis (see Section 3.7).*

source. The area to exclude was scaled based upon the number of counts of the contaminating source. Figure 3.16 (Left) highlights the region used to exclude a nearby bright extended source based upon the LD11 analysis (red hashed ellipse). The excluded region overlaps with the source extraction region (green circle), removing a fraction of the source flux. While this example will not have a significant effect, in some cases, the excluded region of the nearby source excluded a sufficient amount of the source region as to deemed the spectral fit unreliable. Therefore, the scaling factor was removed for the current analysis, improving the fit for clusters affected. Figure 3.16 (right) highlights the change to the area excluded with the scaling factor removed.

After applying the XCS3P the XCS-SDSS cluster catalogue, we obtain measurements of $T_{\rm X}$ and $L_{\rm X}$ for our clusters shown in Fig. 3.17 for 1,143 clusters. We also show the fractional $T_{\rm X}$ error in Fig. 3.18. The remaining 82 (1,225−1,143) XCS DR2-SDSS clusters with redshifts did not successfully run through XCS3P. The reasons for this include the cluster having a low signal-to-noise XMM detection, or a very high signal-to-noise detection but low redshift. In the latter case, XAPA often breaks a single cluster into multiple sources, all of which then have background regions that fall inside the cluster itself. A quantitative analysis of the SDSS-XCS DR2 $L_{\rm X} - T_{\rm X}$

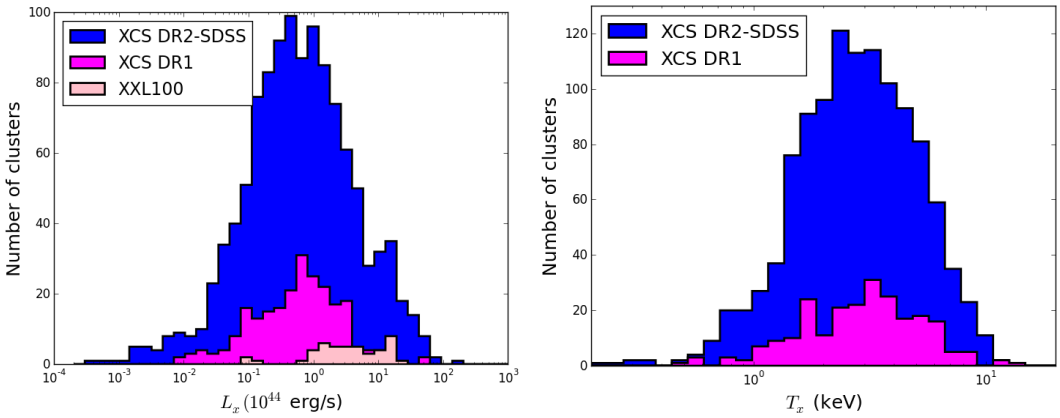

Figure 3.17 *X-ray bolometric luminosity (left panel) and X-ray temperature (right panel) histogram of the XCS DR2-SDSS clusters, in blue, XCS DR1 clusters in XCS DR2-SDSS list, in magenta, and XXL100 clusters in XCS DR2-SDSS list, in light pink.*

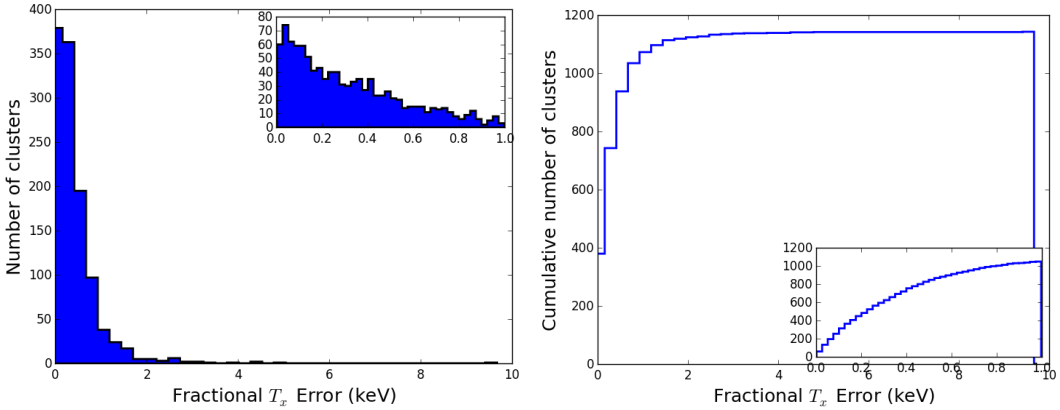

Figure 3.18 *Fractional X-ray temperature error histogram (left) and cumulative histogram (right) of the XCS DR2-SDSS clusters.*

relation is presented in Ebrahimpour et al. (2018).

3.8 The catalogue

The XCS-SDSS cluster catalogue contains 1,255 optically confirmed galaxy clusters:

- 1,225 of them are associated with redshifts: 931 have spectroscopic redshifts calculated by XCS, 117 have spectroscopic redshifts taken from literature, 160 have GMPhoRCC redshifts, 6 have zCluster redshifts and 11 have photometric redshifts taken from literature.

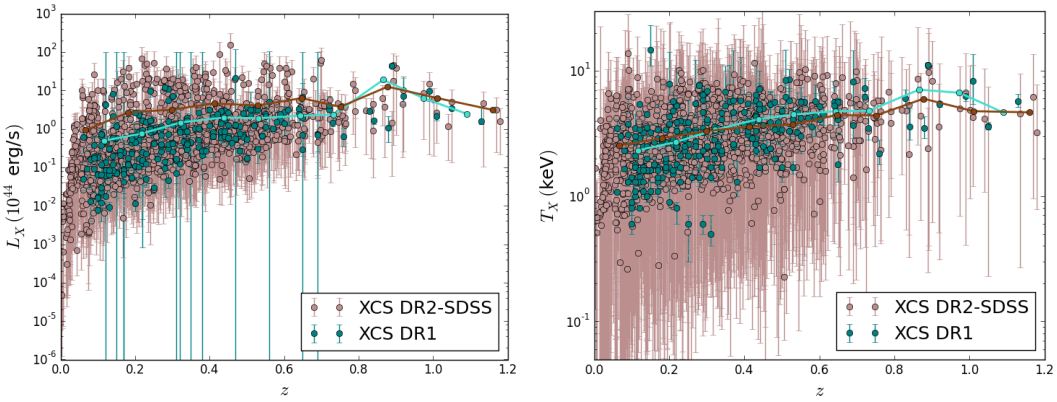

Figure 3.19 *$L_{\rm X}$ (left panel) and $T_{\rm X}$ (right panel) plotted as a function of redshift. Dark brown and turqoise dots are the mean of the property in the redshift bin and errorbars are their standard deviation.*

- 1,143 have calculated $L_{\rm X}$ and $T_{\rm X}$
- 1,223 have calculated richnesses from GPMhoRCC.

Their redshift range extends out to $z \sim 1.2$ with a median of 0.28, their luminosities and temperatures measured according to these redshifts are within the range of $0.2 - 13.8$ keV with a median of 2.6 keV and $(4.8 \times 10^{-5} - 1.6 \times 10^{2}) \times 10^{44}$ erg/s with a median of $4.8 \times 10^{-1} \times 10^{44}$ erg/s respectively. We present an excerpt of the public catalogue in Table 3.5; it includes cluster redshifts along with their source, GMPhoRCC richness, X-ray temperatures and luminosities with upper and lower limits and if the cluster is a targeted or a serendipitous detection. In Fig. 3.19, we show plots of $L_{\rm X}$ and $T_{\rm X}$ of the clusters as a function of redshift; as expected, we are detecting the brightest of the clusters towards higher redshifts.

3.8.1 Numbers of clusters

We compare our numbers of clusters and X-ray luminosity and redshift distributions with those from existing published X-ray cluster surveys. In Fig. 3.20 we present the cumulative redshift and X-ray luminosity and temperature distribution of the XCS-SDSS cluster catalogue, the 400 Square Degree ROSAT PSPC Galaxy Cluster Survey (400d hereafter; Burenin et al., 2007), the MACS cluster survey (Ebeling et al.,

2001), the MCXC cluster catalogue (Piffaretti et al., 2011), the Northern ROSAT All-Sky cluster survey (NORAS hereafter; Böhringer et al., 2000), the ROSAT-ESO flux limited X-ray (REFLEX hereafter; Böhringer et al., 2001), the ROSAT Brightest Cluster Sample (ROSAT BCS hereafter; Ebeling et al., 1998), the Wide-Angle ROSAT Pointed X-Ray Survey (WARPS hereafter; Scharf et al., 1997), the XCLASS cluster survey (Clerc et al., 2012), the XMM-LSS survey (Pacaud et al., 2007), the Swift X-Ray Telescope Cluster Survey (Swift hereafter; Liu et al., 2015), the 2XMMi/SDSS Galaxy Cluster Survey (Takey et al., 2013) and the XXL brightest cluster survey (XXL100; Pacaud et al., 2016). Our numbers of clusters in both cases are by at least an order of magnitude more, even though these are only clusters found in SDSS area and more XCS cluster catalogues overlapping with other optical surveys (e.g. DES) will follow. The range covered in redshift and luminosity is large and overrun by little from XCLASS concerning redshifts and Swift concerning temperatures. This confirms the quality of our catalogue for studies requiring specific cluster properties (high redshifts, high luminosity or temperature, etc); we do not provide a selection function of our cluster catalogue, which can be an issue in statistical studies with clusters, but a cross-match with an optical or other wavelength catalogue with a know selection function would enable high quality of statistical studies as well.

3.8.2 Serendipitous detections in XCS

The vast majority of XCS observations are serendipitous. Clusters are mainly present in the outskirts of these observations rather than the intended target of the objID. A threshold was applied to count the number of serendipitous objects in the XCS-SDSS cluster sample by classifying all objects with an off-axis angle lower than 3 degrees as targets (an average size of a well-defined target extended source). Subsequently, visual inspection of the objects was necessary to exclude low-redshift highly extended clusters. Additionally, visual inspection was needed to identify cases of extended sources that are physically associated with a target source, e.g if they both belong to the same system. These are common examples of non-serendipitous objects with off-axis angle > 3 shown in Fig. 3.21. Other target filters for the sample included

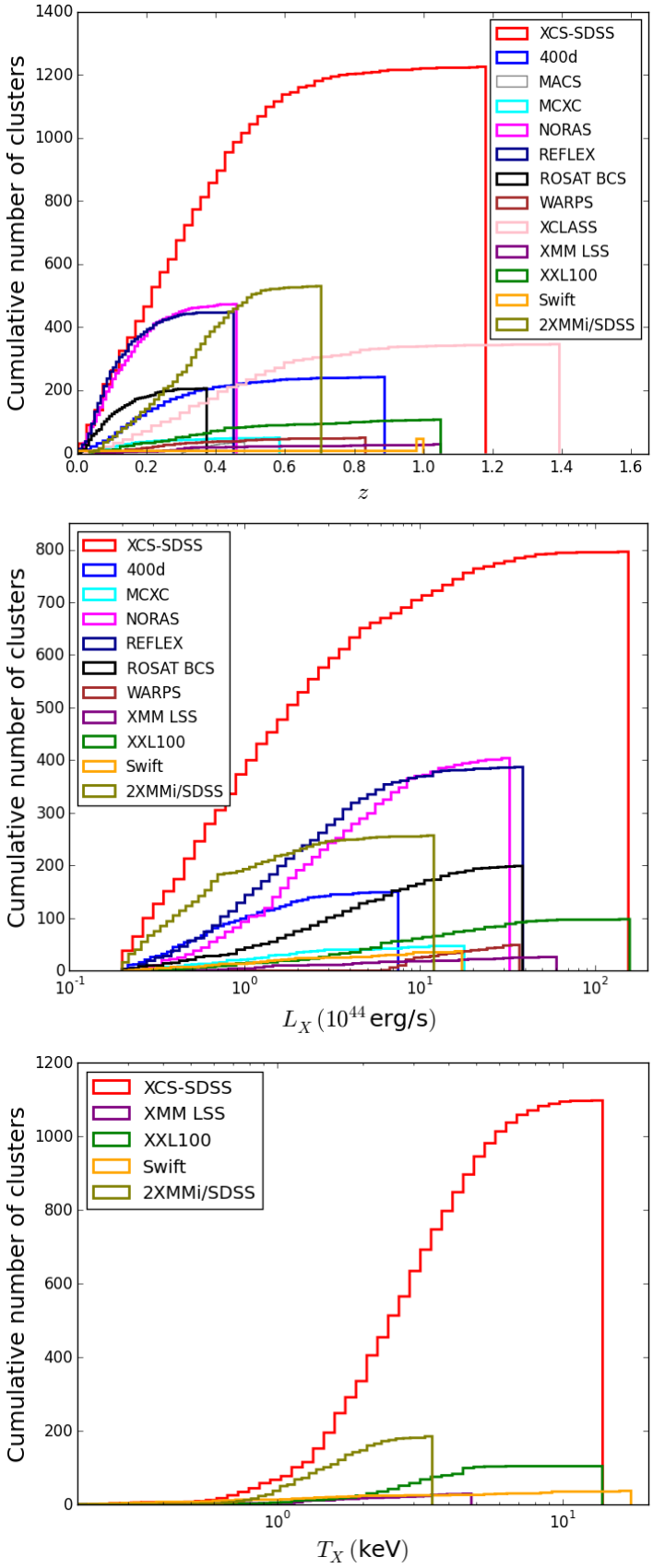

Figure 3.20 *Top panel: Comparison of redshift distribution of XCS-SDSS clusters to other X-ray cluster surveys. Middle panel: Comparison of X-ray luminosities of XCS-SDSS clusters to other X-ray cluster surveys. Bottom panel: Comparison of X-ray temperatures of XCS-SDSS clusters to other X-ray cluster surveys. There is higher number of XCS cluster numbers in all three plots, even though these are only clusters overlapping the SDSS area. The range of properties covered is also large, only being outruned by little by Swift in temperatures and XCLASS in redshifts.*

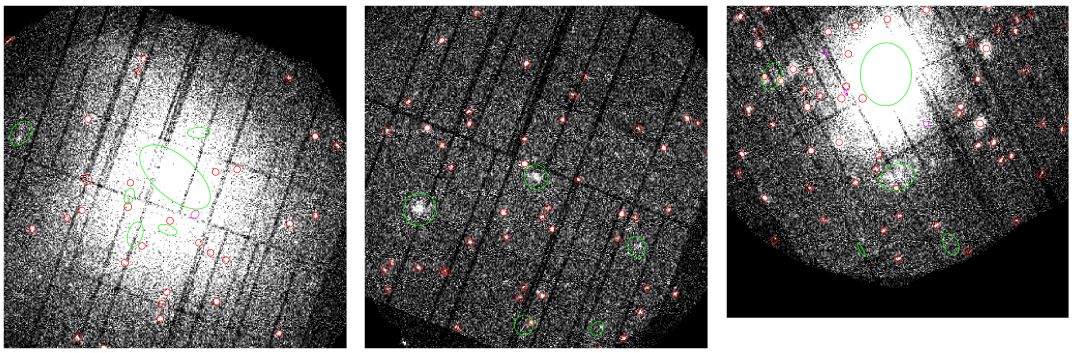

Figure 3.21 *Examples of three sources in the cluster catalog. From left to right: XMMXCS J005613.1-011520.9, a target source with off-axis* > 3*, XMMXCS J011901.6+112321.5, a serendipitous source with off-axis* < 3*, and XMMXCS J071753.0+374214.4 a serendipitous source which happens to be a substructure of the larger system XMMXCS J071819.3+374108.7.*

checks of the objects' positions against the objID file header and automated queries in NED. The cluster sample contains 363 clusters with off-axis < 3, where $\sim 81\%$ happened to be targets, and 892 with off-axis > 3. We found that in total 903 (98% w/off-axis> 3) of the 1255 clusters in XCS-SDSS sample were serendipitously detected by XCS.

3.9 Cluster subsamples

In this section, we divide the cluster catalogue in subsamples that are useful in various research fields:

- The clusters with spectroscopic redshifts: these clusters are a good sample for statistics with clusters, e.g. for scaling relation studies.
- The high temperature clusters: these clusters are useful for research combined with multi-wavelength cluster surveys, such as SZ cluster catalogues where the clusters can be detected easier.
- The high redshift clusters: these clusters are useful for galaxy evolution research, e.g. the brightest cluster galaxies (BCG).

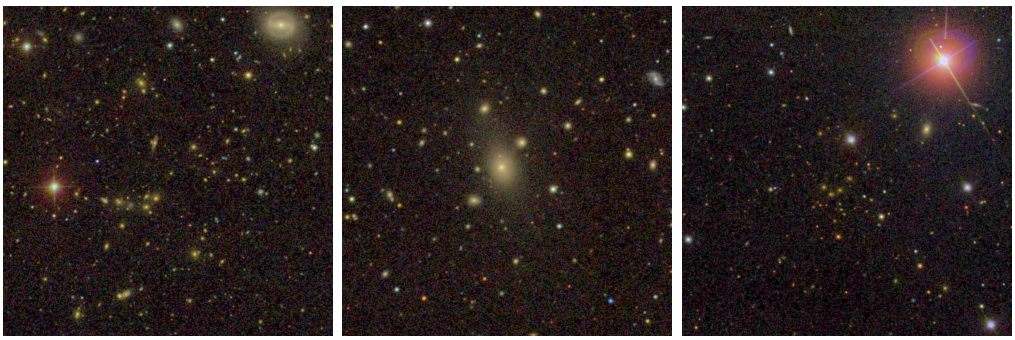

Figure 3.22 *SDSS images of clusters with spectroscopic redshifts calculated by XCS using SDSS in a 6×6 arcmin field of view. From left to right: XMMXCS J120352.5+014730.0 with* $z = 0.236$, $T_{\rm X} = 2.5$ *keV,* $L_{\rm X} = 0.1 \times 10^{44}$ *erg/s, XMMXCS J130918.7-013725.3 with* $z = 0.0832$, $T_{\rm X} = 3.4$ *keV,* $L_{\rm X} = 1.2 \times 10^{44}$ *erg/s and XMMXCS J234656.3+152928.1 with* $z = 0.405$, $T_{\rm X} = 1.5$ *keV,* $L_{\rm X} = 0.3 \times 10^{44}$ *erg/s.*

We explore each of the subsets in the sections below.

3.9.1 Clusters with spectroscopic redshifts

This sample of clusters contains 1,048 galaxy clusters with $z \leq 1.18$, $4.8 \times 10^{-5} < L_{\rm X}(10^{44}$ erg/s$) < 1.5 \times 10^{3}$ and $0.2 < T_{\rm X}$ (keV)< 13.8; the clusters cover a large redshift range and have reliable redshifts and, therefore, X-ray properties. This list of clusters provides an ideal sample for statistical studies, such as studies of cluster scaling relations and cosmology due to the reliable measurements and large number of them. The clusters of this sample have "spec" value in the "redshiftType" column of the catalogue (Table 3.5). We show the optical SDSS images of three of the clusters in this sample in Fig. 3.22.

3.9.2 High-$T_{\rm X}$ clusters

The clusters with high temperatures are the ones with $T_{\rm X} > 5$ keV as already defined in Mehrtens et al. (2012) and in the BAX database[1]. As already mentioned, the clusters with high X-ray temperatures disturb the Cosmic Microwave Background more prominently and make their detection easier through the SZ effect. This enables

[1] http://bax.ast.obs-mip.fr/

comparison studies between the X-ray and SZ cluster signatures, which is useful for studies to constrain cosmological parameters. The sample contains 194 clusters in a large redshift range, $0.037 \leq z \leq 1.169$, an increased number compared to the 66 in XCS DR1. Their X-ray properties range between: $4.1 \times 10^{-3} < L_{\rm X}(10^{44}$ erg/s$) < 8.8 \times 10^{1}$ and $5.0 < T_{\rm X}$ (keV)< 13.8. Fig. 3.23 shows the optical images and temperature spectra of three clusters of this sample; these are high membership clusters with a large extent on the sky. The clusters of this sample have "$T_{\rm X}$ (keV)"$>$ 5 in the catalogue (Table 3.5).

3.9.3 High-z clusters

Finally, we create a high redshift cluster sample for the objects with $z \geq 0.8$. These clusters are ideal for studies of the evolution of galaxy properties inside clusters. Given the fact that GMPhoRCC identifies the cluster BCG, the sample can be easily used for BCG studies in particular. There are 23 clusters in our catalogue with $0.8 \leq z \leq 1.18$ and $0.9 < L_{\rm X}(10^{44}$ erg/s$) < 4.6 \times 10$ and $2.2 < T_{\rm X,500}$ (keV)< 10.8. A high redshift cluster at $z_{\rm spec} = 0.839$ from SDSS is shown in Fig. 3.24; this cluster has also a GMPhoRCC redshift $z_{\rm RS} = 0.853$. We show the SDSS image as well as the CMR diagram within the 4 arcminute aperture produced by GMPhoRCC. The cluster is centred on the X-ray centroid, where faint red galaxies can be seen in good resolution images. The clusters of this sample have "redshift"≥ 0.8 in the catalogue (Table 3.5).

3.10 Summary

We presented the new X-ray cluster catalogue of the XMM Cluster Survey covering the SDSS DR13 area. The catalogue consists of 1,255 optically confirmed clusters, 203 of which are new to the literature, 903 serendipitous and 352 targeted detections. The vast majority of the clusters, 1,225 in number, have optically confirmed assigned redshifts, 1,048 of them spectroscopic and the rest 117 photometric. 1,143 of our clusters have calculated X-ray luminosity and temperature and 1,223 have richness

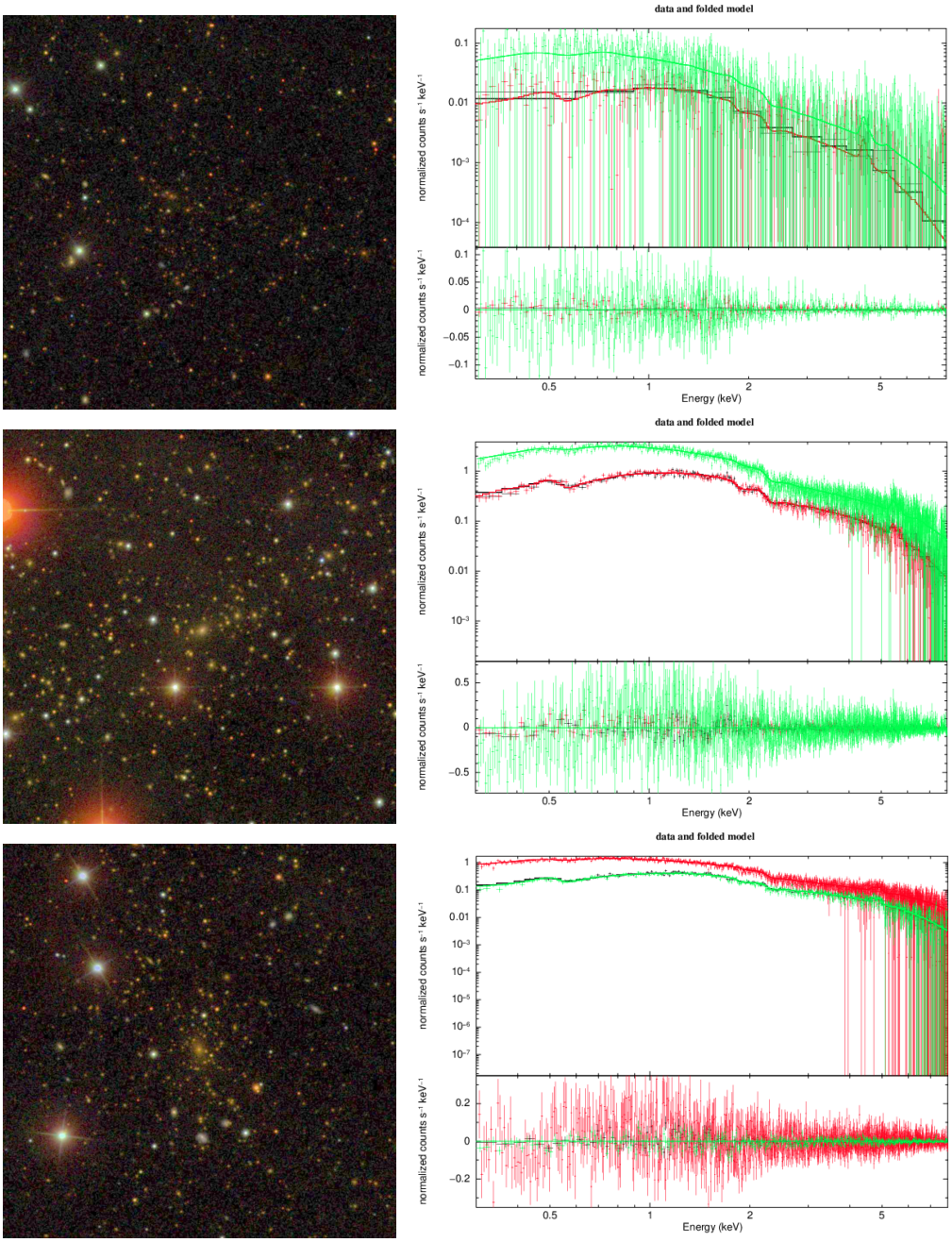

Figure 3.23 *Left panels: SDSS images of clusters with $T_{\rm X} > 5$ keV in a 6×6 arcmin field of view. From top to bottom: XMMXCS J091048.8+385007.5 with $z_{\rm spec} = 0.562$ from SDSS, $T_{\rm X} = 10.3$ keV, $L_{\rm X} = 37.9 \times 10^{44}$ erg/s, XMMXCS J215337.0+174146.9 with $z_{\rm spec} = 0.231$ from SDSS, $T_{\rm X} = 9.6$ keV, $L_{\rm X} = 50.6 \times 10^{44}$ erg/s and XMMXCS J221145.8-034936.8 with $z_{\rm RS} = 0.426$ from GMPhoRCC, $T_{\rm X} = 11.5$ keV, $L_{\rm X} = 88.7 \times 10^{44}$ erg/s. Right panels: the energy spectra and their fit of the same clusters from PN (green points/line), MOS1 (red points/line) and MOS2 (black points/line) camera. The normalised counts are shown in the top sub-panels and the residuals in the bottom ones.*

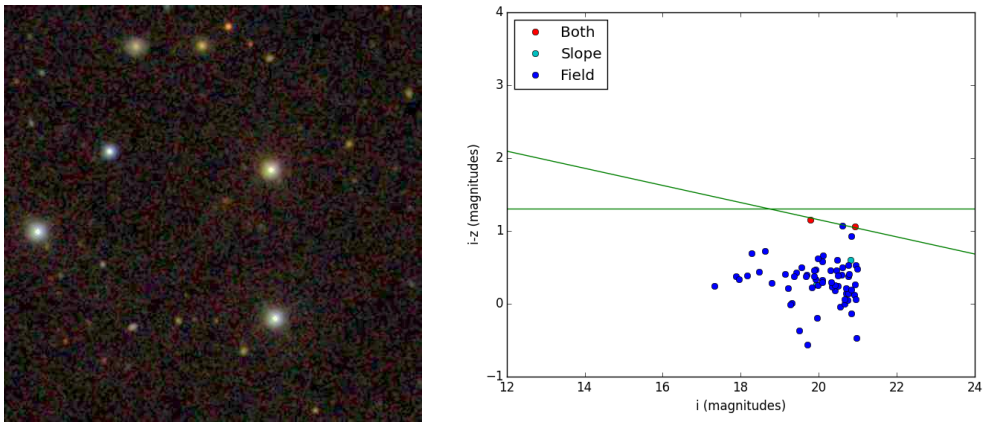

Figure 3.24 *Left panel: SDSS image of XMMXCS J093438.3+551339.4 in a 3×3 arcmin field of view. Right panel: The red sequence diagram in a 4 arcmin aperture. Green lines show the horizontal and sloped, fitted CMR, blue points show field galaxies, magenta points show red sequence galaxies according to the horizontal CMR, cyan points show red sequence galaxies according to the sloped CMR and red points show red sequence galaxies according to both CMRs. The clusters has* $z_{\rm spec} = 0.839$ *from SDSS and* $z_{\rm RS} = 0.853$ *from GMPhoRCC,* $T_{\rm X} = 2.2$ *keV and* $L_{\rm X} = 0.9 \times 10^{44}$ *erg/s.*

estimate. For the latter, also available are the colour-magnitude relation fitting parameters as well as their BCG properties. This is the largest catalogue of X-ray selected clusters to date.

The process starts by going through the XMM observations analysis pipeline which leads to our master source list of all 128,756 X-ray sources, 13,053 of which are extended or PSF-sized. We described our optical classification procedure of $\gtrsim$ 4,500 sources with X-ray soft band counts >200 through the XCS Zoo projects that led to the galaxy cluster catalogue. After assigning redshifts and calculating richnesses using GMPhoRCC, we estimated cluster X-ray temperatures and bolometric ($0.5 - 10$ keV) luminosities using our improved $L_{\rm X}$ and $T_{\rm X}$ pipelines. We presented these properties and compared them with clusters cross-matched with other cluster surveys to ensure their good quality. Finally, the catalogue was split into 3 useful cluster subsamples, each ideal for different kinds of studies with clusters: the scectroscopic redshift sample, with 1,048 clusters, ideal for statistical studies in need of accurate measurements of observables such as cosmology, the high-temperature clusters, with 194 clusters with $T_{\rm X}$ >5 keV, ideal for SZ studies with clusters, and the high-redshift clusters, with

23 members with $z \geq$0.8, ideal for studying galaxy evolution. We used HSC data to quantify the completeness and contamination of the catalogue, which were calculated to be 96.9% and 2.6% respectively.

We publish an X-ray selected cluster catalogue, the largest in numbers of clusters that has been published so far. The clusters cover a large range of redshift ($z \leq$1.2 with median of 0.28) and X-ray properties (luminosities range between (4.8 $\times 10^{-5}$ - 1.6 $\times 10^{2}$) $\times 10^{44}$ erg/s with a median of 4.8$\times 10^{-1} \times 10^{44}$ erg/s while temperatures range between 0.2 $-$ 13.8 keV with a median of 2.6 keV). The XCS collaboration is already using this cluster sample, studying their $L_{\rm X} - T_{\rm X}$ scaling relation and its evolution (Ebrahimpour et al., 2018) and comparing optical and X-ray properties of clusters in voids and outside voids (Manolopoulou et al., 2018a). A cluster catalogue in the DES area will also follow soon (Vergara-Cervantes et al., in preparation).

3.11 Appendices

3.11.1 Zoo score correlations with X-ray and optical properties

We study the dependence of the cluster Zoo score of extended sources analysed with X-ray and optical properties in order to find ways to minimise the sample needed to be classified in similar future cases, where we want to optically confirm the XCS clusters. A strong correlation of a source classification score with an X-ray or optical property would allow us to exclude a certain group of sources from cluster Zoo with a certain range of this property, and automatically name this group as clusters on not clusters, without inserting them to a Zoo project.

We first study the dependence of the cluster Zoo score of extended sources on the soft X-ray counts value of the source, its off-axis angle from the centre of the XMM observation and its azimuthal angle on the sky. We acquired these properties for the sources entered the main cluster Zoo project and performed the Pearson correlation

Table 3.4 *Excerpt of the XCS DR2-SDSS catalogue. First column presents the XCS DR2 name, second and third are the X-ray cluster centre coordinates, columns 4, 5 and 6 present the cluster redshift, redshift source and redshift type respectively, columns 7 and 8 give the cluster richness within R_{200} and its error from GMPhoRCC, where a GMPhoRCC redshift is chosen as the cluster redshift. Column 9 shows the GMPhoRCC quality for the clusters with GMPhoRCC redshifts. Columns 10, 11, 12 are the X-ray temperature, its lower and upper limit respectively and, similarly,columns 13, 14, 15 are the X-ray luminosity, its lower and upper limit respectively. The last column shows if clusters are targeted or serendipitous detections. Value -1 in any column means the calculation is not available.*

XCS name	RA (deg)	Dec (deg)	redshift	redshift source	redshift type	$n_{200,\mathrm{count}}$	$n_{200,\mathrm{count,err}}$	quality
XMMXCS J000007.0+081643.7	0.029	8.279	0.486	SDSSSpec	spec	-1	-1	-1
XMMXCS J000235.8−020227.5	0.649	-2.041	0.384	SDSSSpec	spec	-1	-1	-1
XMMXCS J000312.1−060530.5	0.801	-6.092	0.233	SDSSSpec	spec	-1	-1	-1
XMMXCS J000330.1−014851.7	0.875	-1.814	0.455	SDSSSpec	spec	-1	-1	-1
XMMXCS J000349.3+020404.8	0.956	2.068	0.0924	Lit	spec	-1	-1	-1
XMMXCS J000520.6+201517.5	1.336	20.255	0.407	SDSSSpec	spec	-1	-1	-1
XMMXCS J000623.9+195903.4	1.6	19.984	0.46	NXS	phot	-1	-1	-1
XMMXCS J001053.4+290939.6	2.723	29.161	0.329	SDSSSpec	spec	-1	-1	-1
XMMXCS J001335.8−192931.5	3.399	-19.492	0.0943	Lit	spec	-1	-1	-1
XMMXCS J001639.1−010210.0	4.163	-1.036	0.154	SDSSSpec	spec	-1	-1	-1

$T_{\mathrm{X},500}$ (keV)	$T_{\mathrm{X},500,\mathrm{l}}$ (")	$T_{\mathrm{X},500,\mathrm{u}}$ (")	$L_{\mathrm{bol},500}(10^{44}$ erg/s)	$L_{\mathrm{bol},500,\mathrm{l}}$ (")	$L_{\mathrm{bol},500,\mathrm{u}}$ (")	comment
2.0	1.9	2.1	21.7	21.1	22.4	target
2.1	1.9	2.4	0.6	0.6	0.6	serendipitous
6.8	6.7	6.9	17.8	17.7	18.0	target
3.0	2.3	4.2	0.3	0.3	0.4	serendipitous
4.5	4.4	4.6	2.6	2.5	2.6	target
2.6	2.2	3.2	0.3	0.3	0.4	serendipitous
-1	-1	-1	-1	-1	-1	serendipitous
4.8	4.6	5.1	8.6	8.4	8.9	target
4.6	4.6	4.7	2.5	2.5	2.5	target
0.9	0.7	1.2	-1	-1	-1	serendipitous

Table 3.5 *Pearson's correlation coefficient and 2-tailed p-value between the cluster Zoo classification and the soft X-ray counts value of the source, its off-axis angle from the centre of the XMM observation, its azimuthal angle on the sky and the GMPhoRCC quality flag.*

	Correlation coef.	p-value
Zoo score - X-ray counts	-0.039	0.030
Zoo score - off-axis angle	0.298	10^{-64}
Zoo score - azimuthal angle	10^{-4}	0.982
Zoo score - GMPhoRCC quality	-0.545	10^{-237}

test between the X-ray properties and the source classification score. The results of the Pearson correlation coefficient and the 2-tailed p-value for each of the properties are shown in Table 3.4. Weak correlation is found only between the cluster Zoo score and off-axis angle of the source. A source classified by XAPA as extended that has more than 1,000 counts in the soft X-ray band with an off-axis angle of less than 5 arcseconds and with a good quality GMPhoRCC redshift determination (GMPhoRCC flag=3) is 100% likely to be classified in the Zoo as a cluster (cluster Zoo score$\leq$2.5). If we relax these conditions, to 500 counts and GMPhoRCC quality value 2 or 3, the percentage of sources classified as clusters in Zoo drops to $\sim 95\%$. However, the lack of strong correlations does not allow us to skip any cluster Zoo classifications of sources with specific X-ray properties in future projects.

Next, we study if the GMPhoRCC quality value could serve the same purpose of eliminating the number of possible cluster SDSS-Zoo classifications, i.e. study the correlation of the cluster Zoo score and GMPhoRCC quality value for the 3,074 sources that entered the main SDSS Zoo project. The results of Pearson correlation test are shown in the last row of Table 3.4; a strong correlation is not again found. If we assumed all quality 3 objects are clusters, we would have found 51.0% of the clusters in the final cluster catalogue; 25.6% of them would not be clusters (they are not in our final cluster list). If we assumed all quality 2 and 3 objects are clusters, we would have found 71.0% of the clusters in the final cluster catalogue; 32.5% of them would not be clusters (they are not in our final cluster list). GMPhoRCC seems to calculate good quality properties for higher $L_{\rm X}, T_{\rm X}$ and richness clusters; this could mean that the optical Zoo classification is biased towards brighter and larger clusters.

Cluster Zoo seems to "find" more higher redshift clusters, while GMPhoRCC "finds" more lower redshift clusters. In addition, there are fewer Zoo-classified clusters or good GMPhoRCC quality flags in redshifts of $0.2 - 0.3$; that is due to the fact that the red sequence is not very prominent in the optical filters in these redshifts (the red sequence appears between two different SDSS colours). Finally, large angular-diameter clusters (according to GMPhoRCC) seem to have bad quality and non-cluster Zoo classification.

3.11.2 The X-ray luminosity–temperature relation using the XCS DR1 sample

Hilton et al. (2012, H12 hereafter) presented a study of the X-ray luminosity–temperature relation using the subset of clusters from the XCS-DR1 sample (Mehrtens et al., 2012) with spectroscopic redshift measurements. Since that work was published, the algorithms used to measure X-ray luminosity and temperature in the post-processing pipeline (`XCS3P`) have evolved, as described in Section 3.7. In this Appendix, we show the effect of these changes on the results of Hilton et al. (2012). Here we apply exactly the same orthogonal regression fitting methodology to a sample of 204 clusters from the H12 sample.

Figs. 3.25 and 3.26 show the results, and can be directly compared to Figs. 3 and 5 in H12. The key difference is that the evolution of the normalization of the relation, which was found to be negative in H12, is consistent with self-similar evolution, following the changes to `XCS3P`.

A revised measurement of the $L_{\rm X} - T$ relation using the full XCS-DR2-SDSS sample will be presented in a future paper.

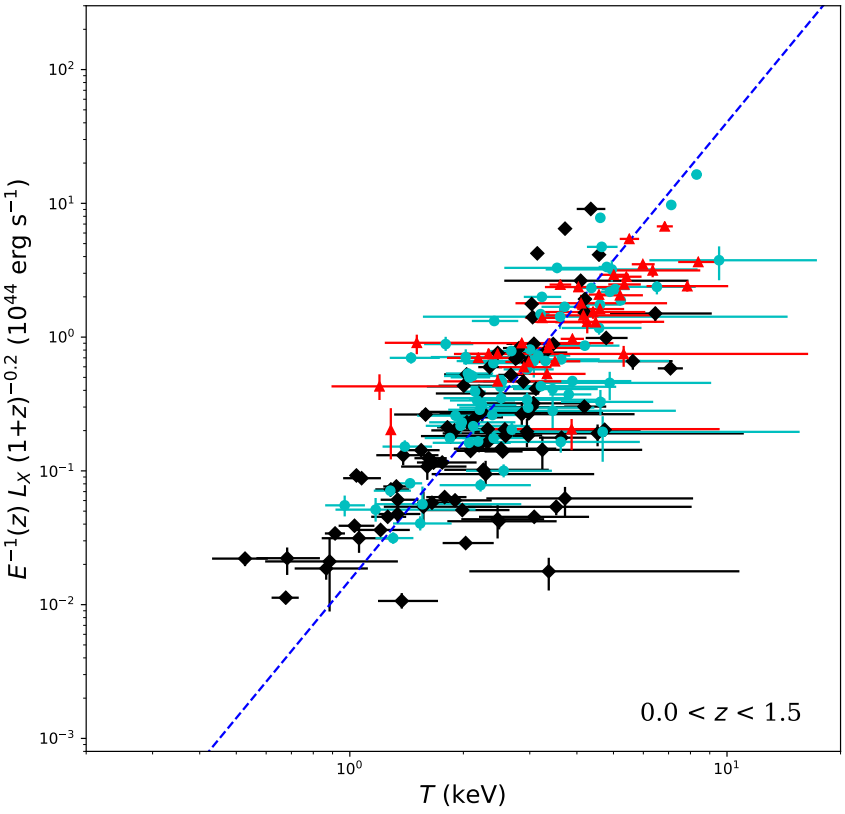

Figure 3.25 *The $L_X - T$ relation for 204 XCS-DR1 clusters with spectroscopic redshifts, with their X-ray properties measured using XCS3P as updated for DR2. This figure can be compared with Fig. 3 of H12. The dashed line is the best-fitting four-parameter model, determined using the orthogonal fitting method. The luminosities have been scaled to take into account the evolution in the normalization as a function of redshift inferred from the best-fitting model parameters, as well as the $E(z)^{-1}$ evolution expected in the self-similar case.*

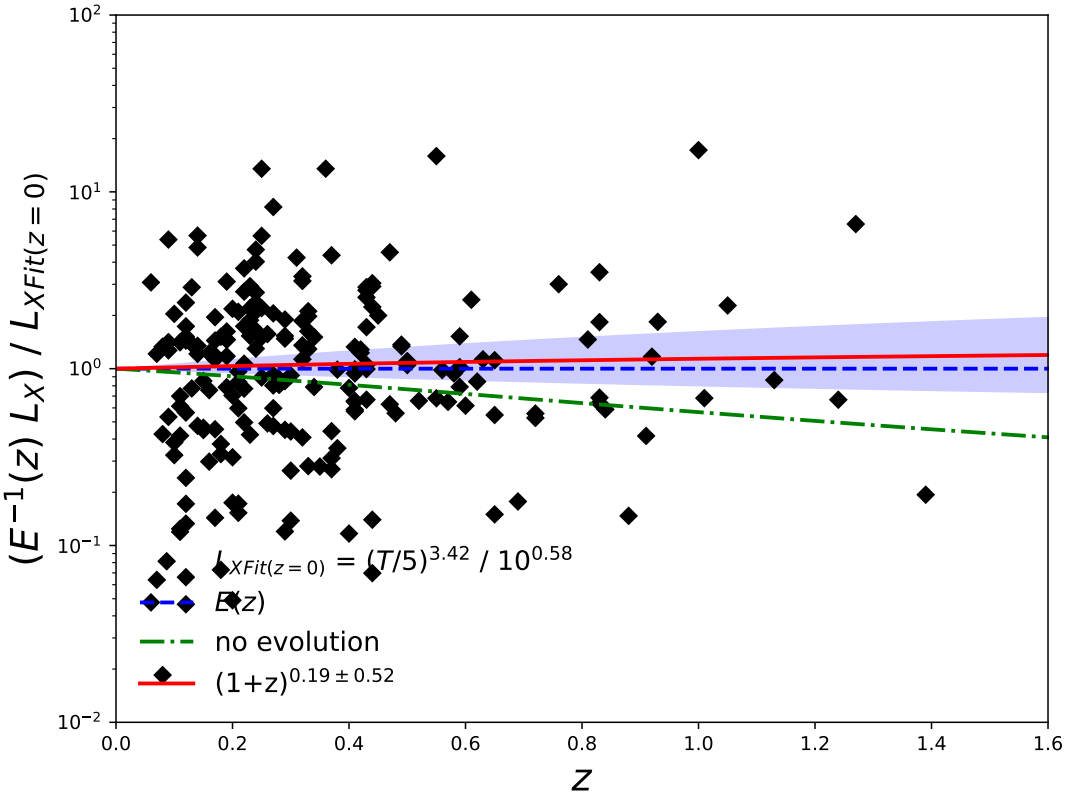

Figure 3.26 *Evolution of the normalization of the $L_X - T$ relation relative to the self-similar case $[E(z)]$, for 204 XCS-DR1 clusters with spectroscopic redshifts, with their X-ray properties measured using XCS3P as updated for DR2. These results were obtained using the orthogonal fitting method described in H12, and can be compared with Fig. 5 in that paper. The shaded area shows the marginalized 68 per cent confidence region on the evolution parameter derived using MCMC. The dotdashed line shows the track for no redshift evolution in the normalization of the relation. The black diamonds show individual XCS clusters (error bars are omitted for clarity).*

Chapter 4

Environmental dependence of X-ray and optical properties of galaxy clusters

4.1 Preface

The work presented in this chapter is going to be submitted after minor amendments to MNRAS as "The *XMM* Cluster Survey: Environmental dependence of X-ray and optical properties of galaxy clusters" by M. Manolopoulou, B. Hoyle, M. Sahlen, R. G. Mann and S. Nadathur. This study was conceived by all of the authors. I carried out all the analysis unless mentioned otherwise.

4.2 Introduction

Our current knowledge of the Large Scale Structure of the Universe incorporates a Cosmic Web formed of large numbers of galaxies forming galaxy groups and clusters in walls and filaments and accreting into galaxy superclusters where filaments meet (for

a review see Springel et al., 2006). The rest of the space is thought to be underdense compared to the rest of the structure, but not empty, containing small numbers of galaxies; these are the so-called voids.

Differences in the properties of the galaxy populations in different large scale structures have been found in the past. Ricciardelli et al. (2017) have found that galaxies in voids have later type morphologies in all stellar masses and that the later type galaxies appear in smaller void-centric distances than early-type galaxies. On the other hand, Darvish et al. (2018), concluded that the molecular gas content and the subsequent star-formation activity of star-forming and starburst galaxies are not affected by their local environment since z$\sim$3.5. Moreover, in Wang et al. (2018), the main sequence of central galaxies and the fraction of star-forming galaxies was found to have no significant dependence on halo mass, while for satellite galaxies, the position of the main sequence is almost always lower compared to the field one and the width is almost always larger. The fraction of star-forming galaxies decreases with increasing halo mass and this dependence is stronger towards lower redshift. Hoyle et al. (2012) have seen that void galaxies have bluer colours than galaxies in higher density environments with the same magnitude distribution. There has been found an alignment of the disk galaxies angular momenta with the void's radial direction in Varela et al. (2012).

Despite the small numbers of galaxies and large void volumes, galaxies can still gravitationally pull each other to form groups and clusters of galaxies. The latter are expected to have fewer members and, therefore, smaller sizes and masses and to have undergone fewer mergers in their formation history with respect to the "field" clusters; as a result of the latter, there would be more relaxed clusters in number inside voids than outside voids. The environmental dependence on the properties of galaxy groups has been studied in Poudel et al. (2016); groups in high density environments show more efficient galaxy formation and a higher abundance of satellite galaxies. In another recent study, Liao and Gao (2018) using hydrodynamical simulations showed that dark matter haloes in filaments have higher baryon and stellar fractions than the field counterparts. A possible difference in the properties of the clusters in different

environmental densities would stress the importance of the selection effects in studies of galaxy clusters, i.e. scaling relations between cluster observables and cluster mass function calculations for cosmology (e.g. Allen et al., 2011; Borgani, 2008). The lack of thoroughly accounting for selection effects in cosmological studies can affect the calculation of inferred cosmological constraints. Examples of reasons why we could observe differences in the observed cluster properties are possible different rate of mergers of the clusters in different environments, a possible modification of the general relativity or a variation of the cluster formation model in underdense regions.

In this study, we begin by searching for differences in the X-ray and optical properties of galaxy clusters by analysing them in the same way that has been done with galaxy catalogues in the past: by categorising clusters with geometrical criteria, whether they reside inside voids or not. We test the X-ray luminosities and temperatures of the clusters and their optical richness. Those properties are important observational measurements since they are widely used to infer the cluster mass; more massive clusters tend to have more galaxy members, i.e. are richer, and higher temperatures and luminosities in their cores. Therefore, if differences were to be found in those properties between clusters of different large scale environments that would imply that a correction of an environmental bias has to be introduced when inferring the cluster mass from those properties and failure to introduce so would affect the validity of the conclusions made using the uncorrected mass estimates. Since the cluster mass function is a very steep function in mass, also a relatively small systematic bias in mass estimate can potentially have a large impact on expected cluster number density. Discovering a difference between clusters in one of the properties, the luminosity for example, but not in another, for example the richness, would imply that environments that clusters live in can affect their formation and/or evolution in some yet unknown way. To model the large scale environment we use a common set of voids, those derived from BOSS spectroscopy, and both X-ray (XCS DR2–SDSS, Manolopoulou et al., 2018b, and an extension of it) and optically (redMaPPer SDSS, Rykoff et al., 2014) selected cluster samples. We compare and verify the X-ray results by using a larger set of catalogues from simulation data; we derive Magneticum[1] void and cluster

[1] http://magneticum.org/

catalogues to search for differences in X-ray cluster properties. Finally, we study the differences of the X-ray and optical properties of clusters as a function of local density directly, to avoid uncertainties introduced by the use of geometrical classification of irregular shaped voids.

This Chapter follows as: in Section 4.3 we present the observational and simulation cluster and void catalogues we use in this work. In Section 4.4, we identify clusters within and outside voids and calculate the density of their environment. We describe our method of matching samples of different environments and comparing their properties. In Section 4.5 we compare the distributions of redshift, richness, mass, luminosity and temperature of clusters different environments. We create the mass functions and the luminosity–temperature relations of clusters within and outside voids and in overdense and underdense regions. We seek possible differences that would need to be accounted for when doing cosmological analyses using those cluster properties. In Section 4.6, we discuss the differences in the properties found, the dependence of the sample size on our results, the correlation of splitting clusters in/out of voids and by local density, the effect of the richness estimators in the difference of richness between clusters identified to reside within voids and not, as well as future prospects of this project. Finally, we conclude in Section 4.7.

4.3 The catalogues

4.3.1 Cluster catalogues

We use a variety of cluster catalogues in order to explore both X-ray and optical properties of clusters in different environments. We use *(i)* the XCS DR2–SDSS catalogue (Manolopoulou et al., 2018b) to compare cluster X-ray luminosities and temperatures, *(ii)* the GMPhoRCC cluster catalogue, an X-ray selected cluster catalogue from XCS DR2 with optical properties extracted with GMPhoRCC (Hood and Mann, 2017) and *(iii)* the redMaPPer SDSS DR8 catalogue (Rykoff et al., 2014) because of the large numbers of galaxy clusters with associated optical properties.

The variation of the catalogue size enables us to study the effect of the sample size in our results.

4.3.1.1 XCS DR2-SDSS clusters

The XCS DR2–SDSS catalogue is the XCS second data release of galaxy clusters inside the SDSS area (Manolopoulou et al., 2018b) and contains 1,255 X-ray selected clusters. Here, we use all clusters with $z < 0.5$, where the redshifts are more reliable given the photometric redshift uncertainties as seen in Fig. 3.13. These have been extracted from archival observations from the XMM Newton telescope, they have an X-ray soft band (0.5-2 keV) counts threshold of 200 and have each been optically confirmed using SDSS imaging. The clusters are associated with a spectroscopic or photometric redshift in the range $0 < z < 1.18$ with median 0.28, as well as X-ray bolometric luminosities in the $0.5 - 10$ keV range and X-ray temperatures. For more information on the catalogue and the calculation of the properties refer to Chapter 3.

The cluster properties we use from the catalogue for our comparison are: cluster redshifts, X-ray soft band counts, X-ray temperatures within R_{500} with errors, where R_{500} is the cluster radius where the density is 500 times higher than the critical density of the Universe, and bolometric luminosities within R_{500} in the $0.5 - 10$ keV range with errors.

4.3.1.2 GMPhoRCC clusters

For a larger number of clusters and the availability of optical properties, we use an extension of the XCS DR2–SDSS catalogue, the GMPhoRCC catalogue. This contains 13,053 clusters, associated with optical properties such as red sequence redshift, richness, colour-magnitude relation (CMR hereafter) fitting properties that are calculated with GMPhoRCC (Hood and Mann, 2017) and X-ray luminosities and temperatures calculated as for XCS DR2–SDSS. These have not been optically confirmed through a cluster Zoo like the XCS DR2–SDSS sample or have the X-

ray soft band counts threshold, a fact that increases the sample size in the same SDSS area compared to the XCS DR2–SDSS catalogue, but the lower quality of redshifts can contaminate it by including spurious X-ray cluster detections. However, X-ray detected clusters with good quality GMPhoRCC flag coincide with a galaxy overdensity on SDSS catalogue, a fact that optically confirms that they are clusters. The subsample of clusters with good quality GMPhoRCC flag contains ∼4,000 clusters. Again, we only use clusters with reliable photometric redshifts ($z < 0.5$).

This catalogue offers a wealth of optical properties to study: red sequence redshifts, spectroscopic redshifts, where available, (coming from the galaxy members with available spectroscopic redshifts; these are usually 1-2 galaxies, but can be up to 5), red sequence colour, CMR width, CMR gradient, CMR intercept, richness within R_{200}, brightest cluster galaxy (BCG hereafter) distance from the cluster centre (in arcminutes) and finally X-ray temperatures within R_{500} and X-ray bolometric luminosities within R_{500} calculated using the same pipelines as the XCS DR2–SDSS catalogue.

4.3.1.3 redMaPPer clusters

The redMaPPer cluster catalogue is an optical catalogue which contains 396,047 galaxy clusters in the SDSS DR8 footprint created with the redMaPPer red sequence cluster finder (Rykoff et al., 2014). The catalogue contains the cluster redshift z_λ, richness λ, integrated luminosity in the i-band and BCG information (spectroscopic redshift, i-band magnitude and i-band luminosity). We use all six available properties in our analysis.

In Fig. 4.1 we present the redshift distribution of all three cluster catalogues described above.

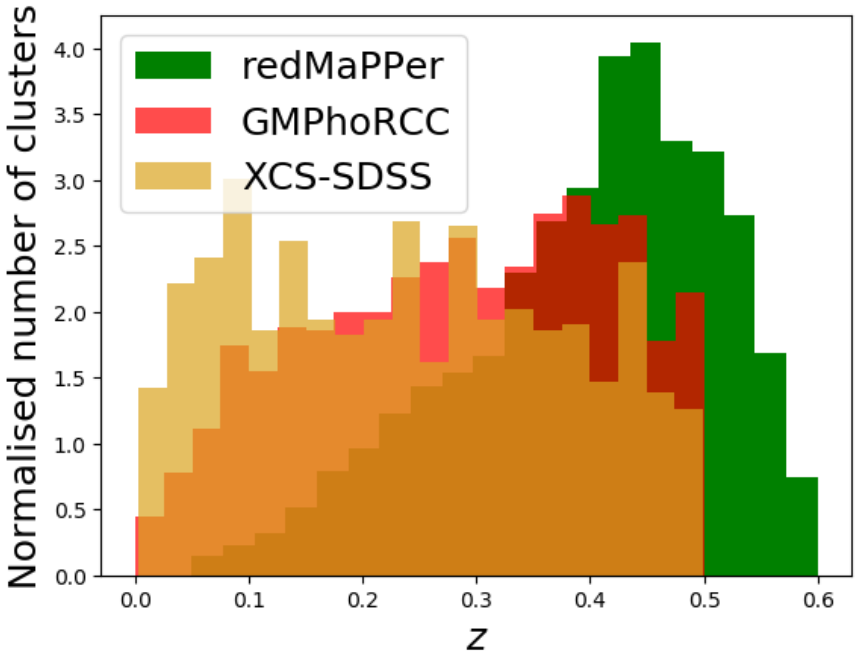

Figure 4.1 *The normalised redshift distribution of the three cluster catalogues. In green, the redMaPPer clusters, in yellow, the XCS DR2–SDSS clusters and in red, the GMPhoRCC clusters.*

4.3.2 Void catalogues

The void catalogues are created using a ZOBOV void-finding algorithm presented in Nadathur and Hotchkiss (2014). This splits the BOSS survey volume in Voronoi tesselations based on its galaxy coordinates and calculates the local density of each galaxy using the Voronoi cell volume. ZOBOV searches for local minima in the density field by filling up the space starting from low to higher density areas, similarly to watershed basins, which represent the voids. The resulting void catalogue depends only on the density field and there is no assumption about the void shape. The catalogue is pruned to exclude voids created due to shot noise. This version of the algorithm has a more robust method of dealing with survey boundaries and masks compared to previous ones.

The algorithm has been applied on BOSS DR12 and resulted in a BOSS LOWZ and a BOSS CMASS void catalogue (Nadathur, 2016); these voids cover $\sim 80\%$ of the survey volume. In order to achieve completeness of the void catalogues in given

redshift ranges and avoid biasing our numbers of clusters found inside and outside voids, we cut the redshift distribution of the two catalogues in two complimentary redshift bins: the LOWZ void catalogue, which contains 2,968 voids in a redshift range of $0.16 \leq z \leq 0.41$ and the CMASS void catalogue, which contains 7,057 voids in a redshift range of $0.45 \leq z \leq 0.67$. In the top panel of Fig. 4.2 we present the initial BOSS CMASS and LOWZ redshift distributions in grey and the ones after the redshift cuts are applied, in blue and magenta respectively. In the bottom panel of Fig. 4.2 we show the normalised distribution of the void effective radius in the two catalogues. The CMASS voids have larger sizes due to the sparser sampling of the CMASS catalogue compared to LOWZ, which causes the ZOBOV algorithm to "create" larger voids.

The void catalogues contain information about the void centre coordinates, void effective radius, void volume and minimum density of the voids. The voids constructed by the ZOBOV algorithm have peculiar 3-dimensional shapes (see Nadathur (2016) for further details), hence making a representation of their shape with a sphere unrealistic (see Fig. 1.7). A more realistic representation of their shape would be an ellipsoid. The information of the ellipsoidal shape of the voids is included in the BOSS void catalogues, i.e. the three main axes of the void ellipsoids and their axes orientation with respect to the line of sight. In our analysis we will be considering the BOSS voids as ellipsoids.

4.3.3 Magneticum clusters and voids

In addition to the observational data, we use the Magneticum simulations to study the galaxy clusters inside and outside voids in large numbers, without the effect of detection bias in our clusters and voids populations. The Magneticum simulations are large scale smoothed-particle hydrodynamic (SPH) simulations that use Langrangian method to follow the cosmological structures formed. They are based on the WMAP7 cosmology (Komatsu et al., 2011) and include a variety of physical processes, such as cooling, star formation and stellar winds, chemical enrichment, AGN feedback

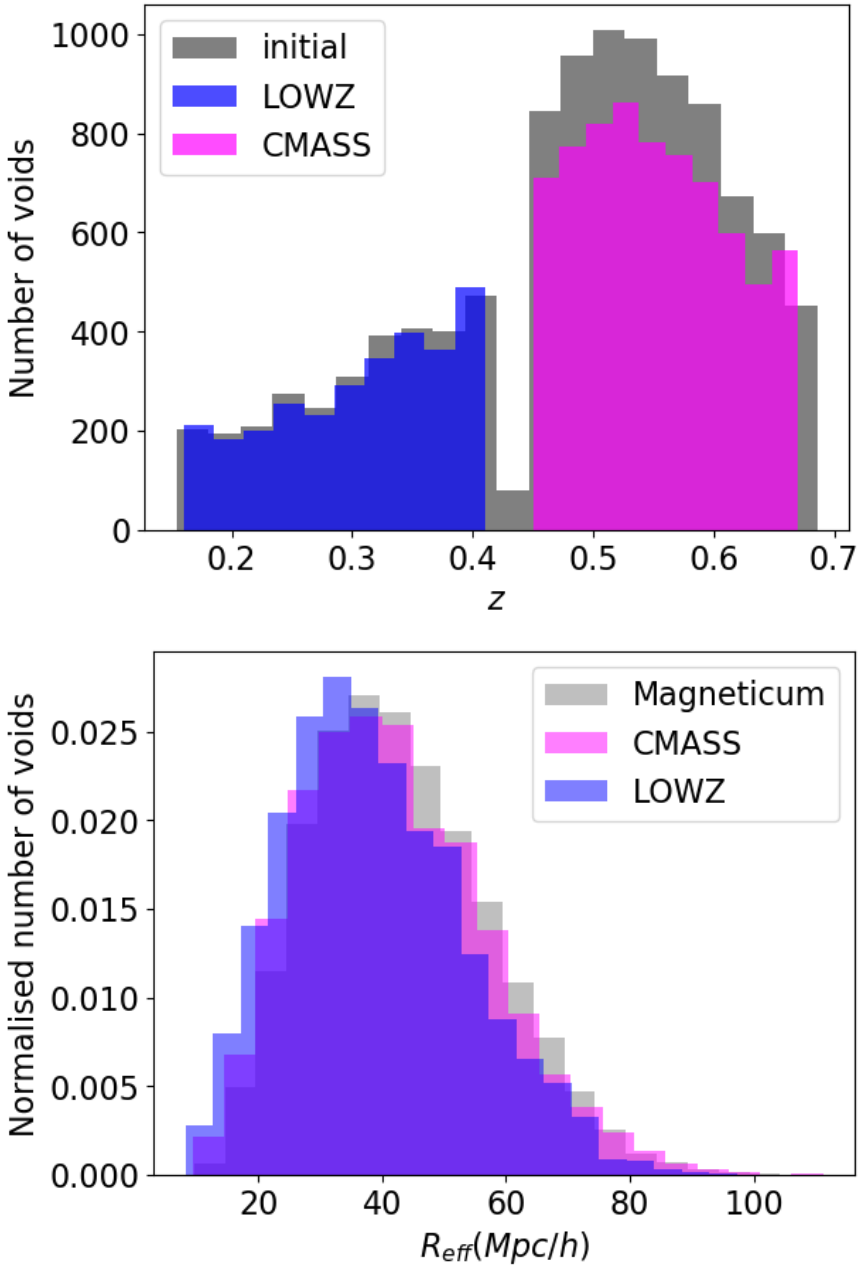

Figure 4.2 *Top panel: In grey, the initial redshift distribution of BOSS void catalogues as taken from Nadathur (2016). The blue and magenta histograms are the cut redshift distributions of LOWZ and CMASS void catalogues we study respectively. Bottom panel: The effective radius distribution of the voids in the two BOSS catalogues (LOWZ in blue and CMASS in magenta) and in Magneticum voids (grey). The sparser CMASS data produce larger in size voids than LOWZ ones through ZOBOV algorithm.*

and magnetic fields; for more information refer to http://magneticum.org/. For this study, we use the Box0 set of simulations, a lower resolution but large volume box, which has a side of 2688 Mpc length and contains 2×4536^3 particles. More specifically, we use a snapshot of the simulations at $z = 0.14$, a redshift that matches closely the redshift range of LOWZ catalogue, where the observational catalogues mostly correspond to, and therefore makes the simulation catalogues more similar to the observational ones.

The cluster catalogue is created using a friends-of-friends algorithm with a linking length of 0.16 (Davis et al., 1985) that links only the dark matter particles. For each halo, the SUBFIND algorithm (Dolag et al., 2009; Springel et al., 2001) is run in parallel to compute the mass M of the cluster particles within the region where the density is 500 times the critical density of the Universe (Gupta et al., 2017). The centre of each cluster is assigned as its deepest gravitational potential position. The cluster temperature is the mean, mass-weighted temperature within R_{500} and the X-ray luminosity is calculated from the emissivity of every particle in the simulation following Bartelmann and Steinmetz (1996). For each cluster in the catalogue we have the mass M within R_{500}, the temperature $T_{\rm X}$, and the bolometric X-Ray luminosity within R_{500}, $L_{\rm X}$. The catalogue covers a large range of cluster masses, from $10^{11}h^{-1}M_{\odot}$ to $10^{15}h^{-1}M_{\odot}$; however, we only use clusters with $M > 10^{14}h^{-1}M_{\odot}$, where the extracted X-ray luminosities and temperatures are reliable (K. Dolag, private communication); this mass cut has also been used for Magneticum clusters in Gupta et al. (2017). This is a catalogue of $\sim 105,000$ simulated clusters, a much larger X-ray cluster sample than XCS DR2–SDSS and GMPhoRCC, ideal to study differences of X-ray properties of clusters.

The void catalogue is created by S. Nadathur using the same ZOBOV algorithm as for the BOSS catalogues. A galaxy magnitude cut was applied in order to match the mean number density for LOWZ within the box. Although this selects the brightest galaxies to match the mean density, it is unlikely to match the clustering of LOWZ galaxies exactly. This along with the fact that the cluster finder algorithm is different from the one in the observational catalogues (red sequence algorithms in the latter

versus friends-of-friends in Magneticum) results in the voids having slightly different properties, they are larger voids compared to LOWZ, as shown in the bottom panel of Fig. 4.2. The galaxy bias is affected by the galaxy clustering and is important in the void properties reconstruction; the higher the bias the larger the voids in the catalogue are. The catalogue with galaxy magnitude cut makes better use of the data than applying a colour selection cut, since there are a lot more voids in the current catalogue (more than $40,000$). This large number of voids and clusters allows us to have statistically large samples to test the results from the observational data. The voids here are approximated as spheres; knowing that this approximation is not accurate, we introduce cuts described in Section 4.4 in order to tackle this issue.

4.4 Clusters in different environments

Having a variety of cluster and void catalogues we can now begin to study the cluster properties as a function of their environment. In order to determine the environment in which the clusters reside, we use as a probe the location of the cluster within the large scale structure, i.e. whether a cluster is inside a void or not.

To this end, we use the void catalogues described above to search for clusters inside their effective radius and, as a result, create a group of clusters outside voids and a group of clusters in voids. For that, we developed an algorithm that measures the distance between a cluster and a void and identifies if the cluster resides inside the ellipsoidal void. We measure the distance between the centres of the two objects, normalise it with respect to the three main axes of the ellipsoidal void or the radius of the spherical void (in the Magneticum case) and compare it with the distance of the void boundary to the void centre. If the distance is smaller, we assume the cluster resides inside the void.

However, the cluster centre residing inside the ellipsoidal void does not necessarily mean that the cluster as a whole is inside the void. As we mentioned earlier, the approximation of voids as spheroids or even as ellipsoidals is not satisfactory.

Moreover, if a cluster is close to the void boundaries, it is most possible that the cluster is not in an underdense region. Clusters next to the void boundaries are very likely to be part of overdense regions of the large scale structure, like filaments or walls, that shape the void boundaries. For that, we place some cuts on the void sizes by examining three different cases of galaxy cluster distributions:

1. the clusters residing in the inner 70% of the ellipsoidal/spheroid void radius (I7 category),
2. the clusters residing in the inner 50% of the ellipsoidal/spheroid void radius (I5 category) and
3. the clusters outside voids (O category).

We believe that the more conservative the threshold of the distance is the less contamination the sample has from clusters belonging to more overdense regions, hence the I5 category should contain clusters that are well within the realistic 3-dimensional voids.

In order to remove any concern about the effect of the irregular shapes of the voids on the clusters' assigned environment based on the simple geometrical selection that we discussed above, we will also estimate the local densities of the clusters' environments directly, rather than using void location as a proxy.

We will study the differences of the cluster properties by categorising clusters in different local density bins. For this, we calculate the galaxy number density within a shell with 10 Mpc inner and 20 Mpc outer radius from the cluster centre using either SDSS DR13 photometric galaxy catalogue (SDSS Collaboration et al., 2016) or the Magneticum galaxy catalogue. We study this shell in order to safely exclude the galaxies that belong to the cluster in the local density calculation. When studying the observational catalogues, we introduce a cut on redshift where the SDSS photometry becomes incomplete, in $z = 0.5$. With this, we avoid including biases in the density estimation of clusters with $z > 0.5$ from areas that the galaxy population is sparser. We then split the clusters in ten density bins, each bin having the same number

of clusters. For the comparisons of cluster properties, we consider three cluster categories:

1. the clusters in the lowest density bin, the clusters in the most underdense regions (U category),
2. the clusters in the highest density bin, the clusters in the most overdense regions (O1 category) and
3. the clusters in the second highest density bin, the clusters in overdense regions (O2 category).

The reason we include the O2 category complementary to the O is because the highest density bin is the broader in density values between all bins (as we will see in Section 4.6.4) and we want to investigate how this affects the results.

4.4.1 Comparing properties

Having assigned clusters to different environments, we are ready to compare the distributions of their various properties. To do so, we use two different non-parametric statistical tests that compare continuous distributions without the need of an input comparison distribution: the Kolmogorov-Smirnov k-sample test (KS hereafter Smirnov, 1948) and the Anderson-Darling test (AD hereafter Coronel-Brizio and Hernández-Montoya, 2010). The KS test compares all distributions with the KS distribution and returns a KS statistic, which corresponds to the "difference" of the two distributions, and the p-value, which shows the statistical significance of the result. The AD test has a similar approach, however, it is more sensitive to the tails of the distributions; when calculating the difference between two distributions, the weights applied on the tails of them are larger as opposed to the KS test which applies larger weights for the central parts of the distributions. AD test investigates the null hypothesis that the samples are drawn from the same population without having to specify the distribution function of that population and gives the AD statistic

and the statistical significance of that shown by the p-value. The AD p-values can sometimes be calculated by extrapolation from some known values, a fact that can give wrong results, so this value should be evaluated carefully. For this reason, we will be comparing the KS or AD statistic values and not the p-values.

For every cluster property in question, we compare the distribution of the clusters outside voids (O category) with one of the two clusters in voids distributions (I7 or I5 category) as well as the clusters in underdense regions (U category) with the clusters in overdense regions (O1 and O2 categories). As a result, we have four different KS test results, one for each of the four comparisons, and four AD test results for the same comparisons. Large KS or AD statistic value and p-value under 0.05 means that the null hypothesis of the two tests that the distributions come from the same parental distribution can be rejected with 95% probability. We initially use both tests for our results, but after ensuring they qualitatively provide the same results, we continue by using only KS test which is more efficient in computational time.

4.4.2 Significance of comparisons

However, having said that, a KS or AD test p-value lower than 0.05 might not necessarily mean that the given property is different between two different cluster distributions; differences could arise randomly from a selection of clusters in the field population. For that reason, we create a verification test, the random test, that help us identify if the differences found in the KS and AD tests are due to random choice of field clusters.

The random test is performed to confirm whether any measured difference could have arisen from random sampling of the field population - the clusters outside voids. For each of the two clusters-in-voids distributions, I7 and I5, we extract a random subsample with the same size from the clusters outside voids sample and replace all I7/I5 cluster properties by those of the random subsample. We perform the AD and KS tests between the "new" clusters in voids distributions and the clusters outside voids. We use the kernel density estimator (KDE hereafter) to fit the distribution of

the KS and AD p-values found after resampling ensuring that the bandwidth used in smaller than the 0.05 value that is the KS p-value threshold to show differences between two distributions. The bandwidth selection is important to avoid over or undersmoothing of the KDE, which will affect the calculations thereafter. Next, we evaluate the possibility of having extracted the given KS p-value in the real data randomly by calculating the fraction of the integral of the KDE function from zero to the KS p-value from the data to the integral of the KDE function from zero to one; we call this the KDE probability. We repeat the resampling process as many times needed to ensure convergence, i.e. that the KDE probability does not change more than 0.0001 after 100 randomisations.

We consider the distributions of a property for two samples to be different if the KS p-value is less than 0.05 and the KDE probability from the random test is less than 0.05. In that case, that would mean that possible difference between the initial distributions is not a random effect and could be due to real difference between the samples. On the other hand, if this test shows that distributions are the same (large KDE probability), then this would mean that the possible difference found between the initial distributions is only due to random choice and does not imply that the property of the clusters residing in voids is different from the property of the clusters outside voids.

4.4.3 Matched samples

In the following, we will always make sure the cluster samples we compare match in redshift and richness/mass (if available), before we compare the rest of the properties, i.e. the luminosities and temperatures. This process is followed in order to ensure that finding a difference between the luminosities of clusters in different environments is not caused by the difference of their redshift or richness distribution. To further explain, for each of the cluster catalogues, the following steps will take place when comparing properties.

For XCS DR2–SDSS, we have three properties in hand, the redshift z, the bolometric

X-ray luminosity $L_{\rm X}$ and the temperature $T_{\rm X}$. We first compare the redshift between the clusters within and out of voids and clusters in underdense and overdense regions. We normalise the redshifts to vary between 0 and 1. After that, we use the nearest neighbours algorithm on the normalised redshifts with a linking radius of 0.1 to match each cluster within voids (each cluster in overdense region) with a cluster outside voids (a cluster in underdense region). The linking radius or length represents the maximum distance between the normalised redshifts of two clusters that is used by the nearest neighbours algorithm to consider them matched. In this way the samples we compare have now the same size. Having the samples matched in z, we then compare their $L_{\rm X}$ and $T_{\rm X}$. To confirm the result of the comparison we use the random test that was described above. For this, we take a random sample out of the initial unmatched distribution of clusters outside voids (in underdense regions) and "name" it the clusters within voids (clusters in overdense regions). The random test is now applied between the initial unmatched distribution and the new clusters within voids (clusters in overdense regions) one.

The same procedure is followed for the Magneticum clusters, with the only difference being that instead of matching in redshift, we initially match in cluster mass M. The cluster catalogue comes from the same snapshot in redshift, so a redshift match is not needed.

For GMPhoRCC and redMaPPer the process is more complicated. After matching in redshift and having samples of the same size, we compare the richness of the z-matched samples. Then we use the nearest neighbours algorithm and find for each cluster within voids (cluster in overdense region) the closest cluster outside voids (cluster in underdense region) in both redshift and richness. We use their normalised values and a linking length of 0.1. The new samples have the same size as the z-matched ones, but they are both z and richness matched. We then compare the rest of the properties available for each of the cluster catalogues, such as the $L_{\rm X}$ and $T_{\rm X}$. To confirm the result of the comparison the random test is used as above; i.e., we take a random sample out of the initial unmatched distribution of clusters outside voids (in underdense regions) and name it the clusters within voids (clusters in overdense

Table 4.1 *Clusters residing within voids identified in the BOSS and Magneticum galaxy catalogues. First column is the name of the cluster catalogue. The second and third columns show the number of clusters inside the 70% of the void radius and inside the 50% of the void radius. The fourth column shows the number of clusters in each of the equally sampled category of clusters with similar background density.*

	I7	I5	equal density
XCS DR2–SDSS	16	5	90
GMPhoRCC	164	95	237
redMaPPer	34,523	20,061	31,774
Magneticum	28,125	17,672	35,312

regions) and apply the random test between the initial unmatched distribution and the new clusters within voids (clusters in overdense regions) one. In this way, if we measure a possible difference in the richness of clusters of different environments, it will not be because of a difference in their redshift distributions. Similarly, if we measure a difference in the luminosities of clusters in different environments, it will not be because of their different either redshift or richness distributions.

4.5 Results

4.5.1 Number of clusters

We apply our clusters in voids finder on the XCS DR2–SDSS, GMPhoRCC, redMaPPer and Magneticum catalogues and the BOSS and Magneticum void catalogues. In Table 4.1 we show the numbers of clusters within voids, which is same as the number of clusters outside voids once matched in redshift or another property, and in each of the equally sampled overdense/underdense regions.

It is obvious that the X-ray selected observational catalogues, XCS DR2–SDSS and GMPhoRCC catalogues have a smaller number of clusters, while redMaPPer and Magneticum contain thousands of clusters in each category, ideal for providing statistical significance to our results.

4.5.2 Redshift and mass distribution

As explained earlier, we begin with comparing the redshift distribution of clusters in the observational catalogues between the clusters within/outside voids and in overdense/underdense regions. For XCS DR2–SDSS, no differences were found whether looking at cluster environment by geometrical criteria or by their background density. On the other hand redMaPPer, clusters in different environments present significant differences in their redshift distributions, no matter how the environment has been defined. For GMPhoRCC, the results are the same as the ones for redMaPPer clusters, except for the case of comparing the clusters in I5 category and the clusters out of voids; only hints of differences are found, but no significant result. After doing these comparisons in redshift, we match the above catalogues to have as similar redshift distributions as possible before we compare other properties. The distributions compared along with the matched ones are shown in Fig. 4.3. The distributions on the left panels flatten at $z \sim 0.4$ because of the absence of voids at that redshift range - it is roughly the high-z end of the LOWZ voids and the lowz-z end of the CMASS voids.

The XCS DR2–SDSS redshift distributions look different from each other when looking at the histograms, however the KS p-value of their comparisons has not reached a lower than 0.05 value. This is a different behaviour from the other three catalogues that might be a reflection of the low number statistics the XCS DR2–SDSS catalogue presents.

For Magneticum clusters, where the redshift of all clusters is the same, we perform the comparisons and matching we did for the redshift distributions in the observational catalogues, only now for the mass of the Magneticum clusters. We find that the definition of the environment here plays a role in the comparisons. The mass distributions of clusters with different background densities are significantly different from each other, while there is no difference found between the clusters within and outside Magneticum voids. This might be a hint that the geometrical classification of the cluster environment might be naive, given the irregular shape of voids that is

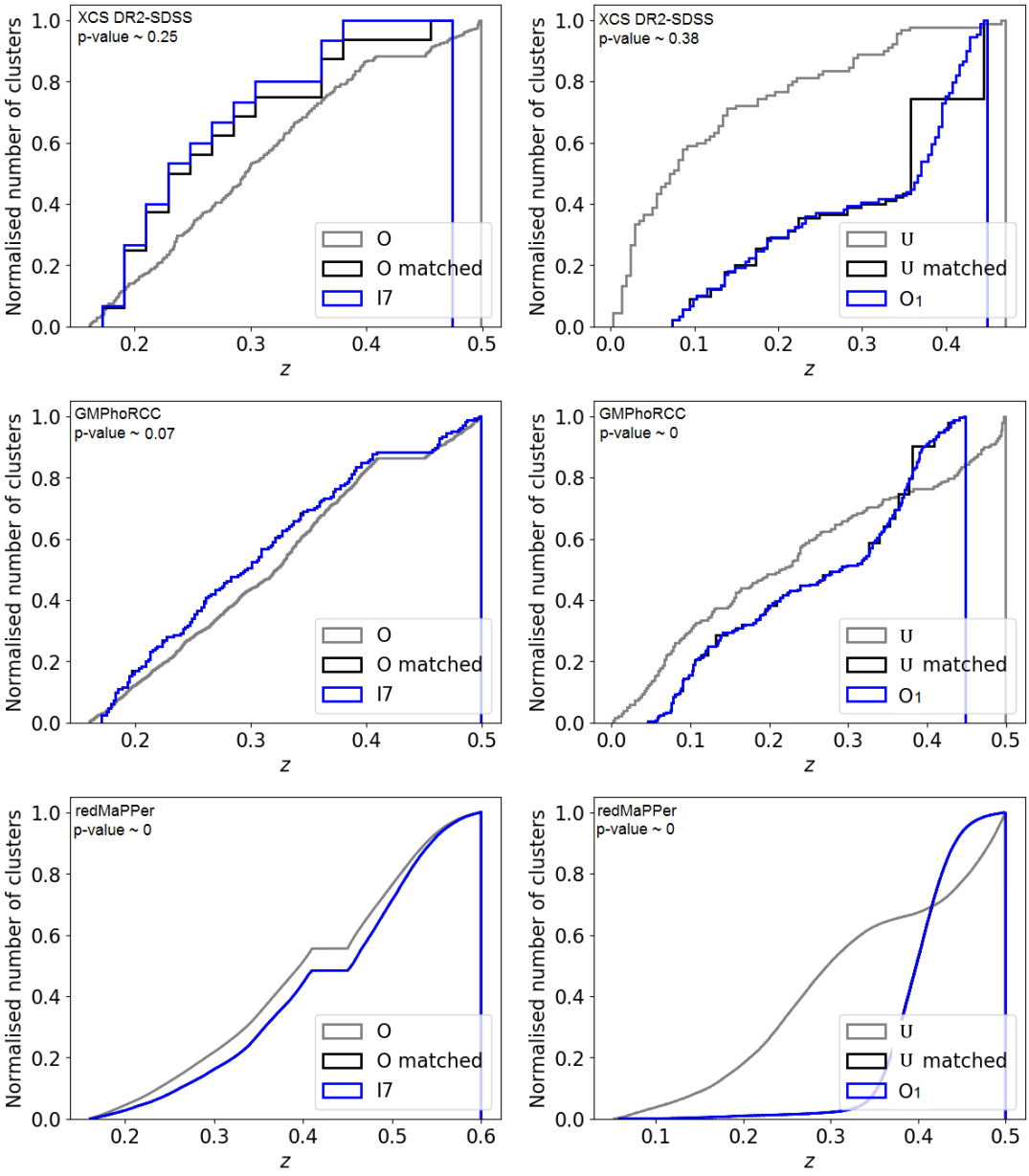

Figure 4.3 *The normalised cumulative redshift distributions of XCS DR2–SDSS (top), GMPhoRCC (middle) and redMaPPer (bottom) clusters in I7 and O categories (left panels) and most overdense and most underdense regions (right panels). The blue distributions are the clusters in I7 category (left panels) or the clusters in the most overdense regions O1 (right panels) and the grey distributions are the clusters outside voids (left panels) or the clusters in the most underdense regions U (right panels). Once redshift distributions are compared, the grey lines are matched to the blue ones and those matched ones are shown in black colour.*

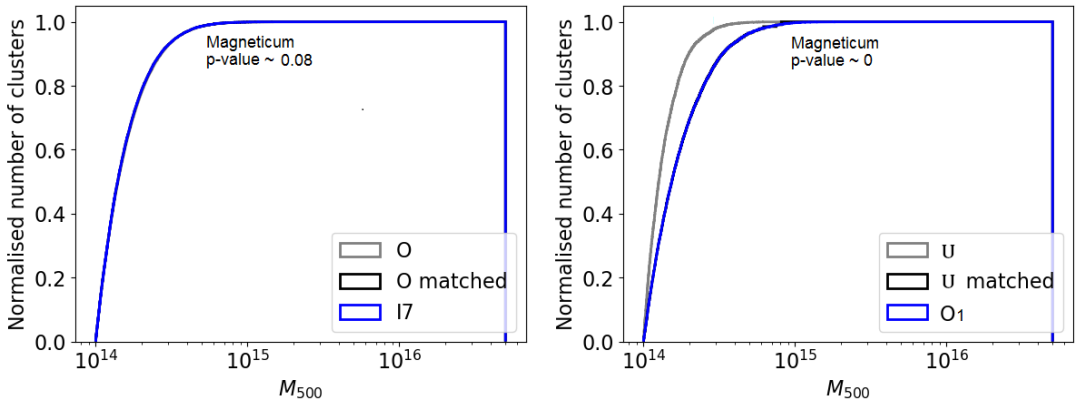

Figure 4.4 *The normalised cumulative mass distributions of Magneticum clusters in I7 and O categories (left) and most overdense and most underdense regions (right). The blue distributions are the clusters in I7 category (left panel) or the clusters in the most overdense regions O1 (right panel) and the grey distributions are the clusters outside voids (left panels) or the clusters in the most underdense regions U (right panels). Once mass distributions are compared, the grey lines are matched to the blue ones and those matched ones are shown in black colour.*

here modeled as spherical and the fact that Magneticum contains a larger amount of voids than the BOSS catalogues. Once again, after doing these comparisons in mass, we match the catalogues to have as similar mass distributions as possible before we compare other properties. The distributions compared along with the matched ones are shown in Fig. 4.4.

4.5.3 Richness

For GMPhoRCC and redMaPPer, where richness estimators of the clusters are available, n_{200} and λ respectively, we compare those between clusters in different environments with matched redshift distributions. For both catalogues and both definitions of environment, the richness distributions of clusters present significant differences, with KS p-values very close to zero (the maximum value of $p \sim 0.02$ in GMPhoRCC O-I5 case), with the only exception of clusters in I7 and clusters outside voids comparison for GMPhoRCC catalogue; however, the KS p-value of the latter comparison is $\sim$0.1, showing a hint of difference. After comparing the richness distributions, we match the samples in both redshift and richness for the GMPhoRCC

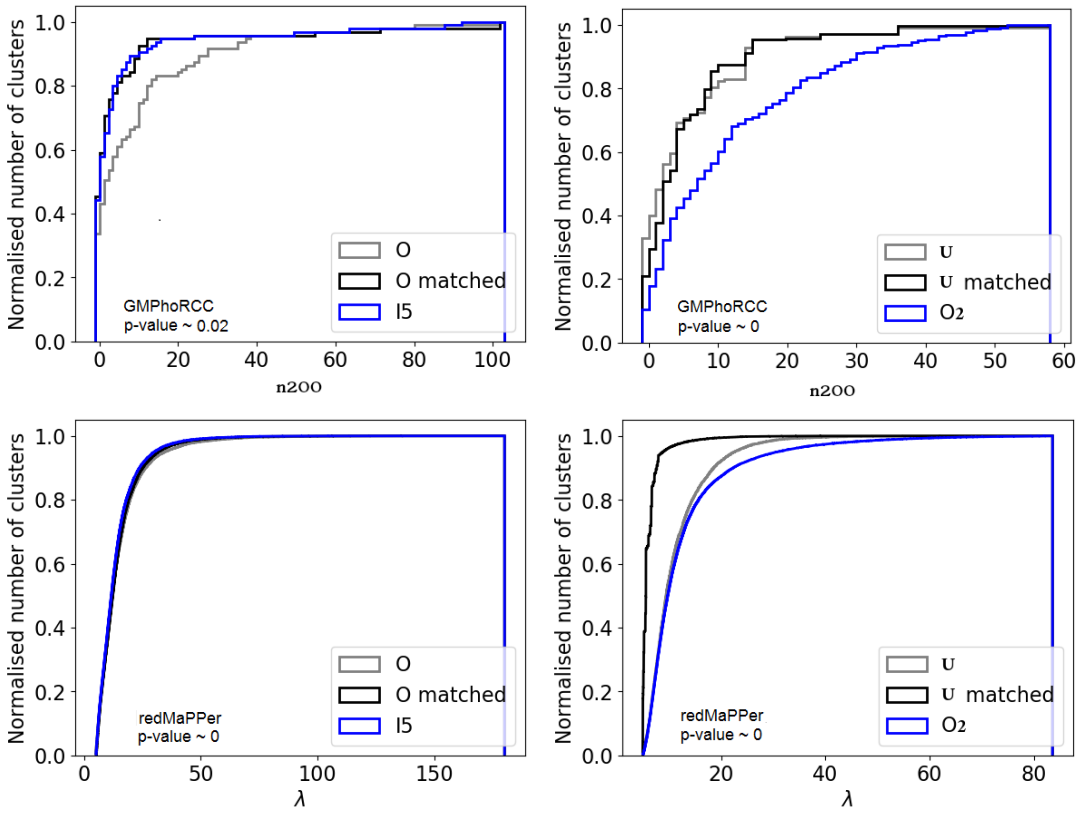

Figure 4.5 *The normalised cumulative richness distributions of GMPhoRCC (top) and redMaPPer (bottom) clusters in I5 and O categories (left panels) and most overdense and second most underdense regions (right panels). The blue distributions are the clusters in I5 category (left panels) or the clusters in the second most overdense regions O2 (right panels) and the grey distributions are the clusters outside voids (left panels) or the clusters in the most underdense regions U (right panels). Once richness distributions are compared, the grey lines are matched to the blue ones in both redshift and richness and those matched ones are shown in black colour.*

and redMaPPer catalogues, before moving on to compare the rest of the properties.

Those comparisons show clear evidence that clusters inside voids and in underdense regions have lower number of galaxy members but similar redshift distribution to clusters outside voids and in overdense regions respectively. The richness distributions are shown in Fig. 4.5. The reason why in the bottom right plot the matched distribution is not close to the O2 curve is because there are many clusters in overdense regions with very low richness values that do not exist in underdense regions and cannot be matched.

4.5.4 Luminosity and temperature

Having matched samples in all of our cluster catalogues, whether by redshift, mass or redshift and richness, we can now study differences in the luminosities and temperatures of the clusters in different large scale environments independently of the matched properties. We remind the reader that for XCS DR2–SDSS, GMPhoRCC and Magneticum cluster catalogues we compare the cluster X-ray luminosity and temperature, while for redMaPPer, we compare the clusters' i-band luminosity. For all catalogues and for both definitions of the cluster environment, we find significant differences between the X-ray and i-band luminosity of the clusters in overdense and underdense regions and within and outside voids (KS p-values are very close to zero except for XCS DR2-SDSS O-I7 case with p-value ~ 0.02 and XCS DR2-SDSS O-I5 case with p-value ~ 0.04) apart from the Magneticum clusters within and outside voids (KS p-value ~ 0.55 for O-I7). Voids and underdense regions host higher numbers of low luminosity clusters compared to overdense regions and regions outside voids. The luminosity distributions are shown in Fig. 4.6.

X-ray temperatures show more complex results. When splitting clusters within and outside voids, in all cluster catalogues (XCS DR2–SDSS, GMPhoRCC and Magneticum) no significant differences are found in the X-ray temperature distributions of clusters within/outside voids (O-I7 KS p-value ~ 0.11, 0.17 and 0.62 respectively). However, when splitting clusters according to the density of their environment, significant differences are found in all catalogues in the X-ray temperature distributions of clusters in overdense and underdense regions (KS p-values < 0.05), except for the GMPhoRCC U-O2 case with KS p-value ~ 0.1. It is not clear as to where to high and low temperature clusters reside in the larger scale environment, something that we will discuss in Section 4.6. The temperature distributions are shown in Fig. 4.7.

We note here that in the bottom, Magneticum panels of Fig. 4.6 and 4.7, just as in all similar figures in this chapter, the distributions are plotted so as to have the same maximum values in order to ease comparisons by eye. However, even though those Mgneticum distributions look very similar in the plots, the maximum values

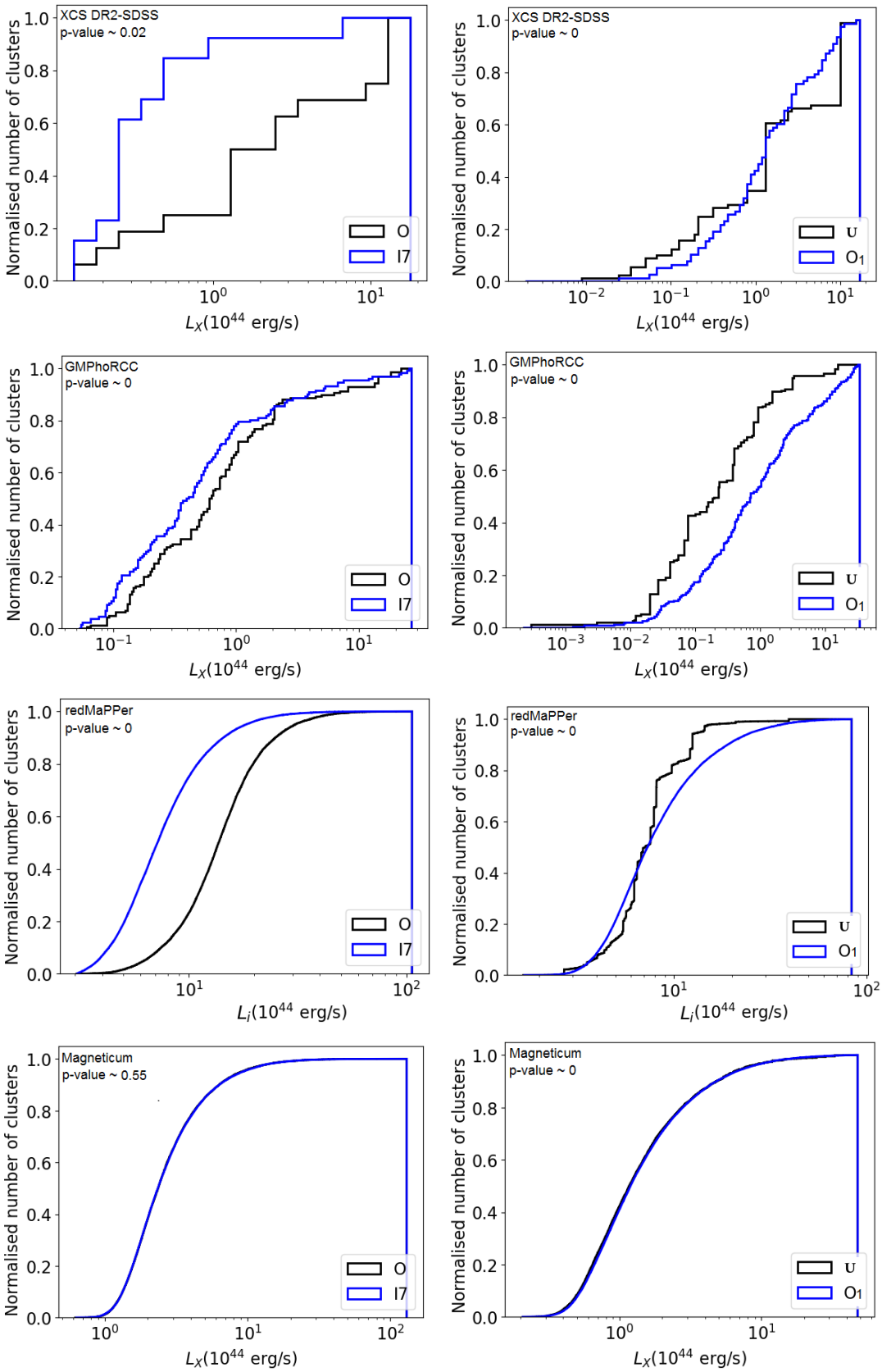

Figure 4.6 *The normalised cumulative luminosity distributions of matched samples of XCS DR2–SDSS (top), GMPhoRCC (second from top), redMaPPer (third) and Magneticum (bottom) clusters in I7 and O categories (left panels) and most overdense and most underdense regions (right panels). The blue distributions are the clusters in I7 category (left panels) or the clusters in the most overdense regions O1 (right panels) and the black distributions are the clusters outside voids (left panels) or the clusters in the most underdense regions U (right panels).*

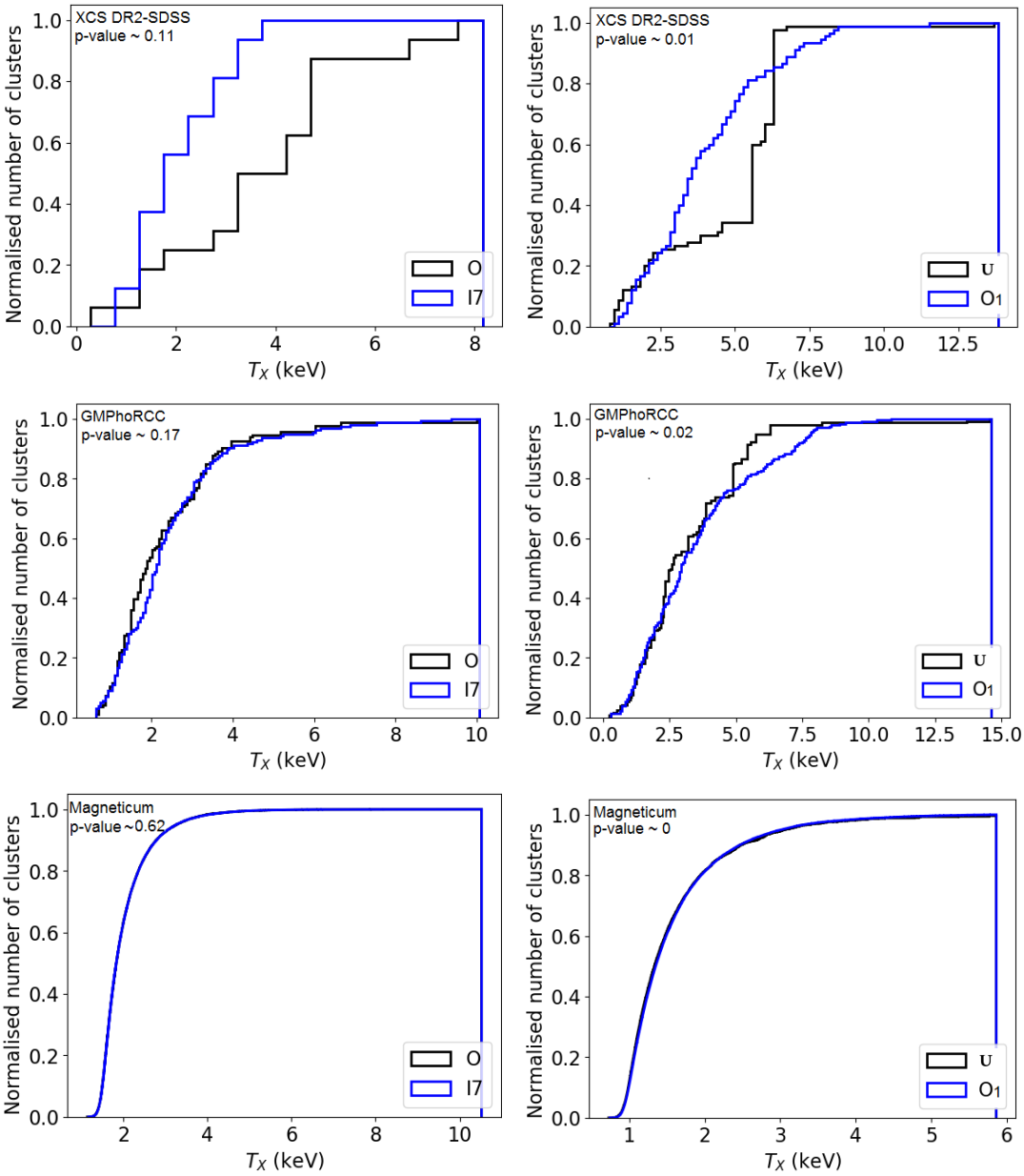

Figure 4.7 *The normalised cumulative X-ray temperature distributions of matched samples of XCS DR2–SDSS (top), GMPhoRCC (middle) and Magneticum (bottom) clusters in I7 and O categories (left panels) and most overdense and most underdense regions (right panels). The blue distributions are the clusters in I7 category (left panels) or the clusters in the most overdense regions O1 (right panels) and the black distributions are the clusters outside voids (left panels) or the clusters in the most underdense regions U (right panels).*

of luminosity and temperature of clusters within voids and in underdense regions are smaller than those of clusters outside voids and in overdense regions, explaining why KS p-values show that those distributions are significantly different from each other.

4.5.5 Other optical properties

GMPhoRCC and redMaPPer catalogues contain some additional optical properties of the clusters and allow us to study possible differences of those properties in clusters within different environments. GMPhoRCC optical properties contain the CMR fitting properties and the colour of the red sequence of the clusters (see Section 2.1 for more information on these properties), while redMaPPer contains the i-band magnitude and luminosity of the BCG of the clusters.

The CMR intercept, gradient and width and red sequence colour distributions of clusters in overdense and underdense regions present significant differences; the same is only true for clusters within and outside voids for the red sequence colour distributions (see Fig. 4.8). When looking at the BCG properties, those are significantly brighter in the i-band in clusters in overdense regions and outside voids compared to clusters in underdense regions and inside voids (see Fig. 4.9).

4.5.6 Mass and richness functions

We now want to see if the differences found between the different cluster populations can significantly affect cosmological studies that use galaxy clusters. We can do this by measuring the cluster richness functions for the redMaPPer clusters and the mass functions for the Magneticum clusters for the different cluster categories. XCS DR2–SDSS and GMPhoRCC catalogues do not have large enough numbers of clusters for this purpose. The richness functions are good approximation of the cluster mass functions since richness has proven to be a good mass proxy for galaxy clusters for redMaPPer SDSS DR8 clusters (Baxter et al., 2016).

We construct the richness functions of the redMaPPer clusters and the mass functions

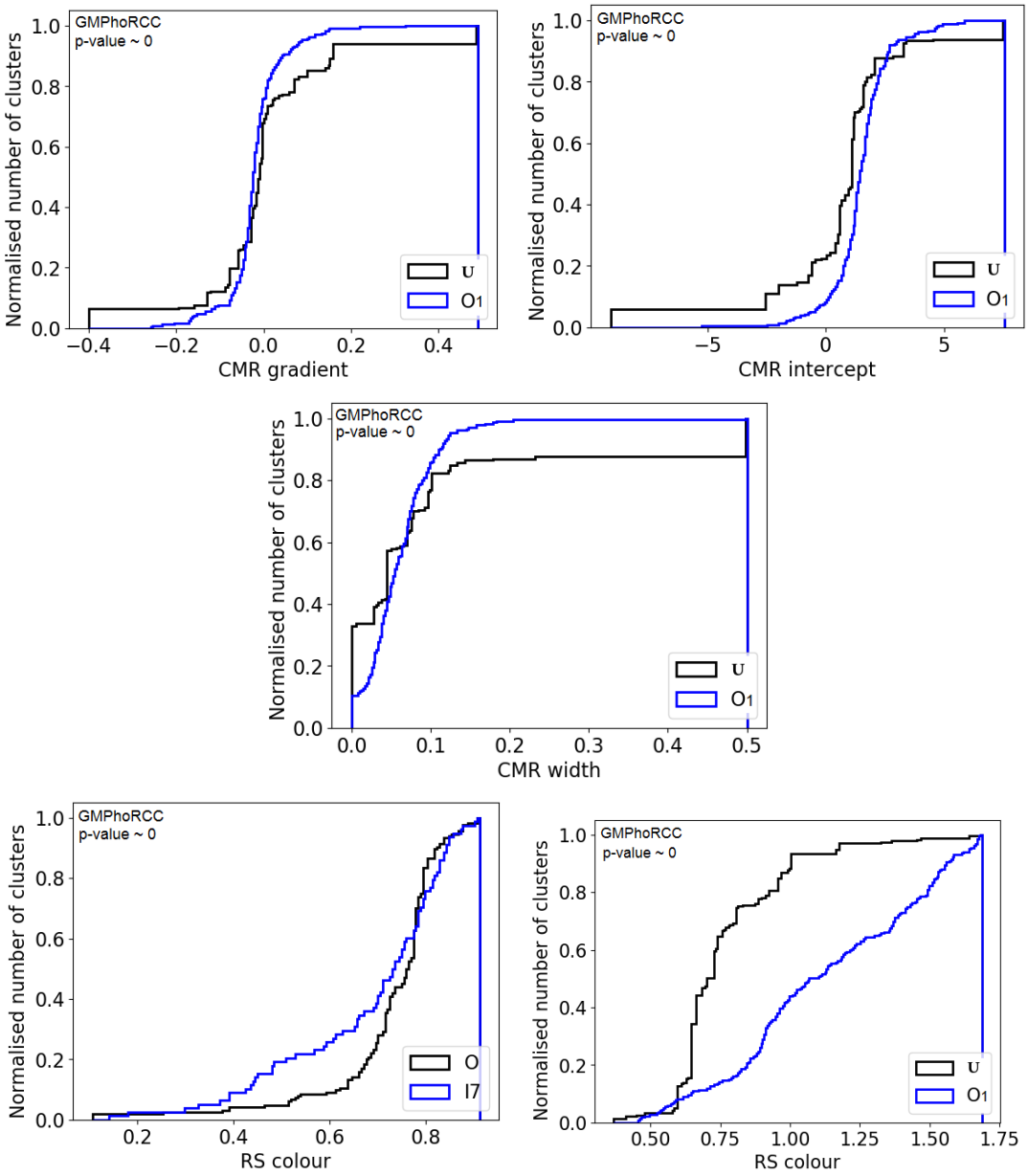

Figure 4.8 *The normalised cumulative CMR gradient (top left), intercept (top right), width (middle) and red seuqence colour (bottom) distributions of matched samples of GMPhoRCC clusters in underdense (black lines) and overdense (blue lines) regions and clusters within (blue line) and outside (black line) voids. Those distributions are found to be significantly different.*

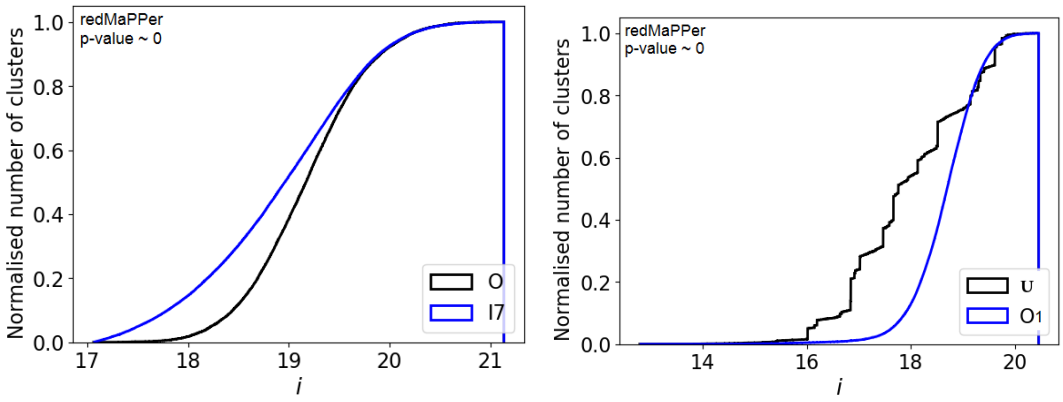

Figure 4.9 *The normalised cumulative BCG i-band magnitude distributions of matched samples of redMaPPer clusters within and outside voids (left panel) and in overdense and underdense regions (right panel). The blue distributions are the clusters in I7 category (left panels) or the clusters in the most overdense regions O1 (right panels) and the black distributions are the clusters outside voids (left panels) or the clusters in the most underdense regions U (right panels). Those distributions are found to be significantly different.*

Table 4.2 *The KS p-value of the comparison of the richness and mass function of redMaPPer and Magneticum clusters respectively in different environments.*

	O-I7	O-I5	U-O1	U-O2
redMaPPer	0.11	0.03	0.31	0.31
Magneticum	0.97	0.68	0.11	0.11

of the Magneticum clusters and present them in Fig. 4.10. The top panels show the richness and mass functions of redMaPPer and Magneticum clusters respectivaly within and outside voids and the bottom ones show the same functions but for clusters in overdense and underdense regions. The middle panels are constructed as the top ones, but the clusters within voids functions are normalised with respect to the clusters outside voids; this is to make comparison between the three functions easier in their high richness/mass end. In order to find whether the functions are significantly different from each other, we compare them by using the KS two sample test. Its p-value results are shown in Table 4.2.

Looking at Fig. 4.10, especially at the bottom panels, it seems that the most massive and rich clusters are found in the most overdense regions, while the same quantity of

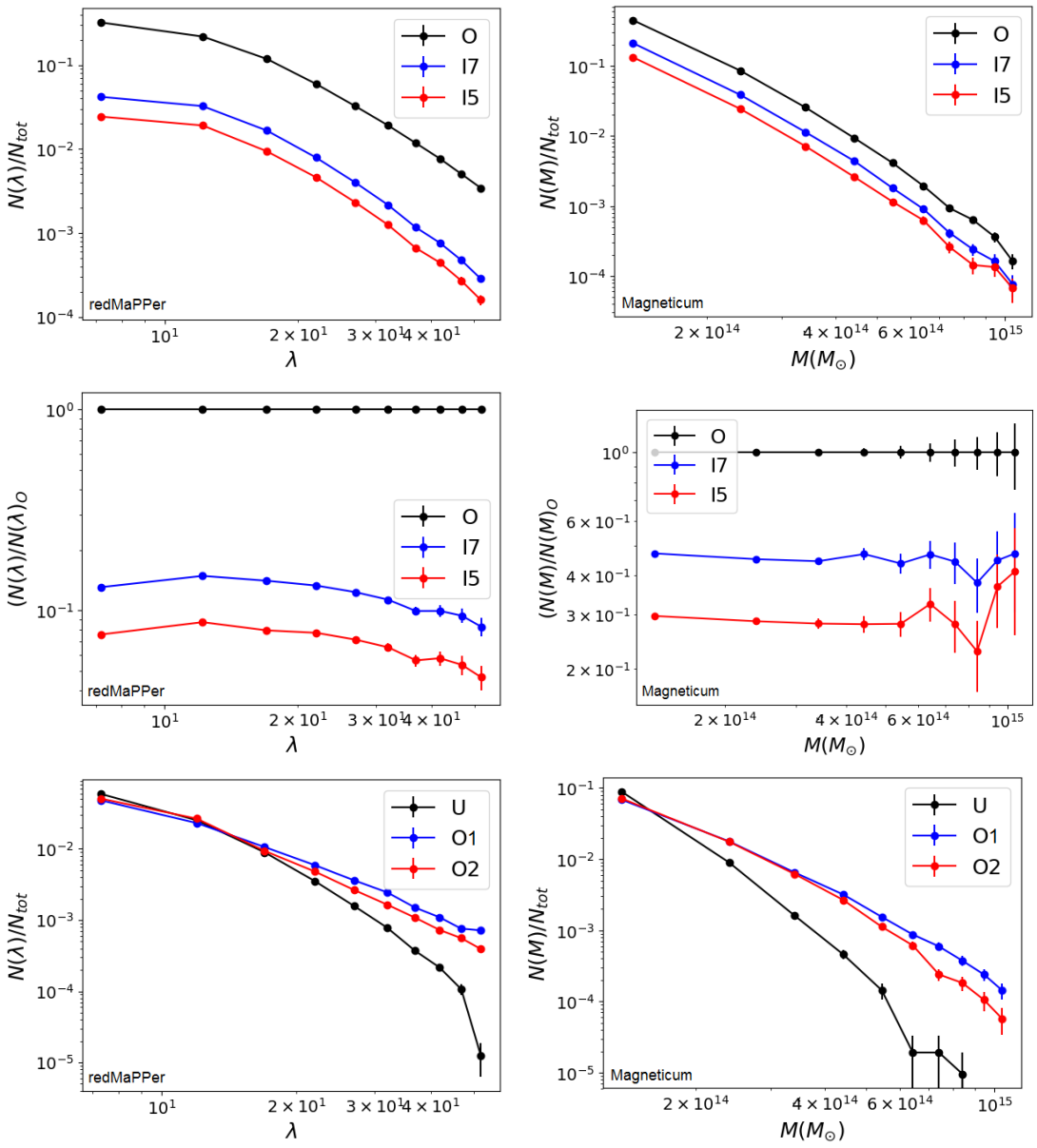

Figure 4.10 *The normalised richness and mass functions of redMaPPer (left) and Magneticum (right) clusters respectively with respect to the number of all clusters available in O, I7 and I5 categories (top panels), the normalised functions to the number of clusters in O category (clusters outside voids; middle panels) and the number of all clusters available in U, O1 and O2 categories (bottom panels). It is easier to see the discrepancies of the functions in the high richness/mass end of the top panels in the middle ones. Errors are included in all functions.*

low richness/mass clusters appears in overdense and underdense regions. However, this difference is not found to be consistent by the KS test. On the other hand, the exact opposite seems to be happening with the high-richness clusters inside the 50% of the void radius compared to the clusters out of voids, as seen in the top 2 left panels of the same figure: there are significantly less high-richness clusters inside voids compared to the ones outside voids. The shift in amplitude or the functions in the O-I5 case introduces a large difference between the two samples measured by the KS test, as opposed to the different shape in the U-O1 and U-O2 cases, which fails to show a significant KS test difference. The same trend is not observed as a significant difference in the Magneticum clusters, perhaps due to the higher error bars in the high-mass end of the functions. This difference found in redMaPPer clusters is a hint that, when selecting clusters by their mass for cosmological studies, a selection bias could be entered caused by the environment of the clusters. In this case, this effect needs to be taken into account when using cluster mass functions in order to avoid systematic errors in the calculation of cosmological parameters using cluster mass functions.

4.5.7 Luminosity–Temperature relation

Another important area of research where cluster selection plays an important role is the determination of the X-ray luminosity–temperature relation. Scaling relations are broadly used to determine cluster masses as discussed in the Introduction section. These are afterwards used for cosmological parameter estimation. Hence, the unknown selection effects can introduce unidentified errors in the estimation of the parameters of the relation.

We study the X-ray luminosity–temperature relation for clusters in different environments. To do so, we use a very simple algorithm (scipy.stats.linregress[2]) which calculates a regression line between two sets of measurements, in our case the common logarithm of the X-ray luminosity and the common logarithm of the X-

[2] https://docs.scipy.org/doc/scipy-0.14.0/reference/generated/scipy.stats.linregress.html

ray temperature. It returns the slope, intercept, correlation coefficient and standard error of the estimate. We calculate the errors of the measurements using bootstrap technique. No selection effects are accounted for in the estimates in this section. As shown in Ebrahimpour et al. (2018), and especially shown in Figure 3 of the publication, for model 0, which is the closest to our fitting process, the inclusion of selection effects does not affect the calculation of the intercept of the relation but affects the calculation of the slope in the first decimal. The intercept of the relation is 44.61 either including or not selection effects and the slope changes from 3.12 to 3.00 when excluding selection effects. The selection function of the Ebrahimpour et al. (2018) sample is very similar to the one of our XCS DR2–SDSS and GMPhoRCC samples. For the former, the Ebrahimpour et al. (2018) sample originates from the XCS DR2–SDSS catalogue. For the latter, GMPhoRCC is an extension of the XCS DR2–SDSS catalogue; it contains the same X-ray selection with the exclusion of the X-ray soft band counts threshold of 200; it also has not been through optical confirmation, however, an overdensity of galaxies has been found by GMPhoRCC in order to calculate the clusters' redshift. Therefore, any difference found in our analysis between the intercept or any difference larger than ~ 0.1 in slope of the L–T relation between clusters in different environments is very likely to originate from the environmental bias in the selection.

We present the results of the cluster L–T scaling relations in different environments from XCS DR2-SDSS, GMPhoRCC and Magneticum catalogues. In Fig. 4.11 we show the relation for the O, I7 and I5 cluster categories (left panels) and for the U, O1 and O2 categories (right panels) including the values of the slope, intercept and standard error of the relations. On Table 4.3 we present those values together with their estimated errors.

Looking at Fig. 4.11 and Table 4.3 for the properties of the L–T relations of clusters of all three catalogues within and outside voids, we see that there are indications that the clusters within voids of XCS DR2–SDSS and GMPhoRCC catalogues have different slope and intercept values compared to the clusters outside voids values (slope value differences are larger than 0.1 and intercept values are different). However, the

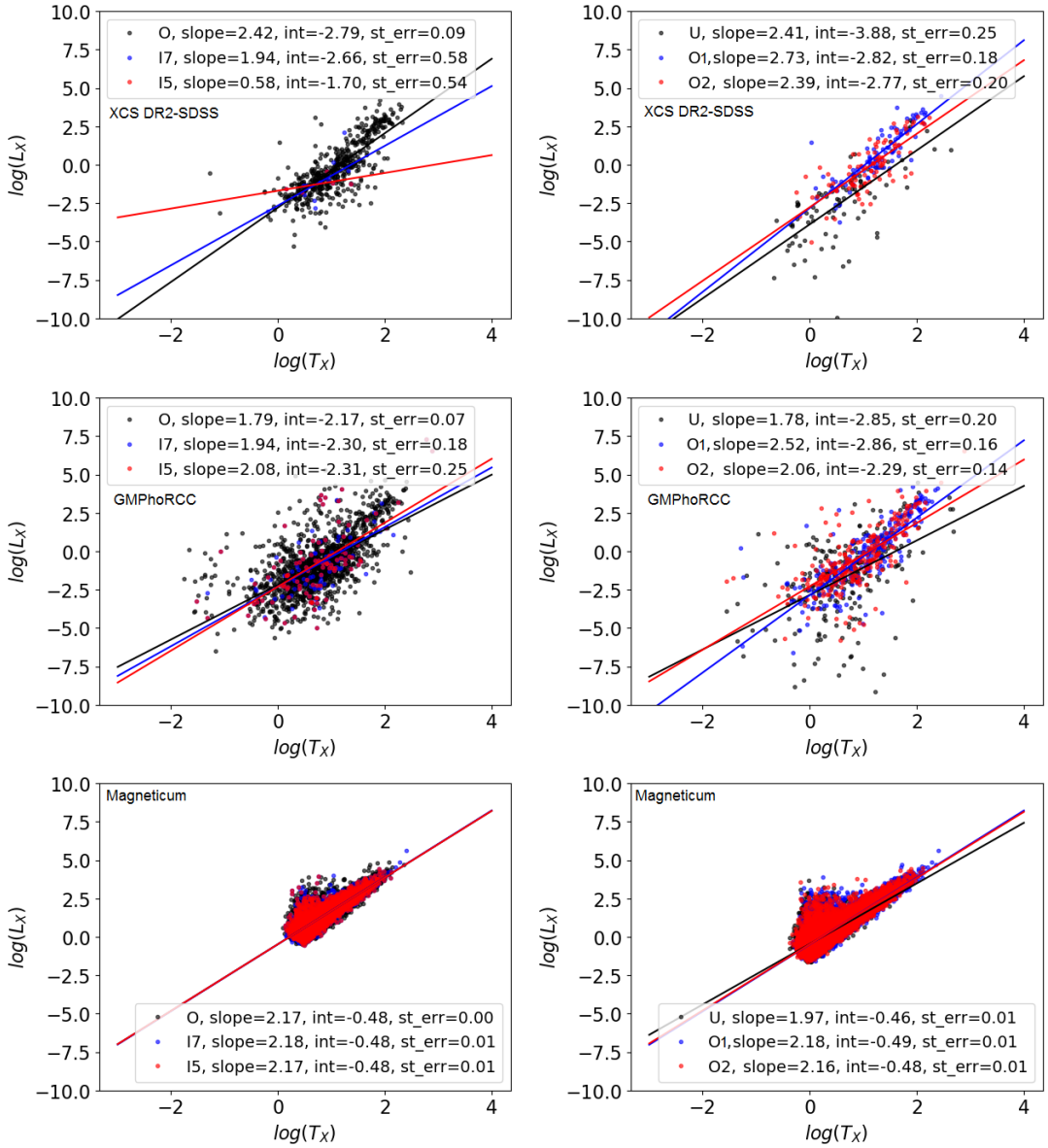

Figure 4.11 *The X-ray luminosity–temperature relations of XCS DR2–SDSS (top), GMPhoRCC (middle) and Magneticum (bottom) clusters, split in in/out of voids categories (O, I7, I5) - left panels - and in overdense (O1 and O2) and underdense regions (U) - right panels.*

Table 4.3 *The slope, intercept and standard error of the L–T relations of the XCS DR2–SDSS, GMPhoRCC and Magneticum clusters in different environments with their bootstrap errors as calculated from the linear regression algorithm.*

XCS DR2–SDSS

	within/outside voids			over/underdense regions		
	O	I7	I5	U	O2	O1
slope	2.42 ± 0.12	1.94 ± 0.68	0.58 ± 2.46	2.41 ± 0.65	2.39 ± 0.23	2.73 ± 0.19
intercept	-2.79 ± 0.14	-2.66 ± 0.51	-1.70 ± 2.27	-3.88 ± 0.24	-2.77 ± 0.37	-2.82 ± 0.23
standard error	0.09 ± 4.24e-3	0.58 ± 0.18	0.54 ± 1.30	0.25 ± 0.01	0.20 ± 0.02	0.18 ± 0.02

GMPhoRCC

	within/outside voids			over/underdense regions		
	O	I7	I5	U	O2	O1
slope	1.79 ± 0.09	1.94 ± 0.22	2.08 ± 0.30	1.78 ± 0.40	2.06 ± 0.66	2.52 ± 0.86
intercept	-2.17 ± 0.09	-2.30 ± 0.18	-2.31 ± 0.25	-2.85 ± 0.10	-2.29 ± 0.67	-2.86 ± 1.00
standard error	0.07 ± 8.50e-3	0.18 ± 0.02	0.25 ± 0.03	0.20 ± 0.01	0.14 ± 0.01	0.16 ± 0.01

Magneticum

	within/outside voids			over/underdense regions		
	O	I7	I5	U	O2	O1
slope	2.17 ± 4.77e-3	2.18 ± 6.61e-3	2.17 ± 8.39e-3	1.97 ± 0.27	2.16 ± 0.63	2.18 ± 0.08
intercept	-0.48 ± 3.60e-3	-0.48 ± 5.64e-3	-0.48 ± 7.98e-3	-0.46 ± 0.12	-0.48 ± 0.39	-0.49 ± 0.04
standard error	4.75e-3 ± 2.99e-5	7.03e-3 ± 6.11e-5	8.88e-3 ± 8.90e-5	8.96e-3 ± 2.23e-3	5.56e-3 ± 1.20e-3	5.24e-3 ± 1.06e-3

large value of error estimates, scatter (reported as standard error) and the low number of clusters inside voids in XCS DR2–SDSS catalogue do not allow us to make reliable conclusions. There are no differences in the Magneticum clusters L–T relation; clusters in different environments defined by geometrical criteria present almost identical L–T relations. Looking at the L–T relations of clusters in different density environments, it seems that clusters in underdense regions present less steep relations compared to clusters in overdense regions. This is hinted by the clusters in all three catalogues, but the results are not significant within the errors.

Comparing the results above to the forecasts of the cosmological parameter constraints from a known L–T scaling relation in Section 5.4.1 of Sahlén et al. (2009), we see that a no-evolution L–T relation with slope=2.5 and intercept= -1.90 can produce different constraints from a self-similar evolution L–T relation with slope=3.5 and intercept= -1.92. When measurement errors are unaccounted for, Ω_m constraints vary from 0.27 to 0.29 and σ_8 constraints vary from 0.81 to 0.83, looking at the realistic error columns of the Table 7 of the publication. However, when measurement errors are accounted for in the analysis, the constraints of Ω_m and σ_8 seem to remain the same, 0.30 and 0.80 respectively, but their uncertainty can change from 0.02 to 0.03 when going from a no-evolution L–T relation to a self-similar evolution one. Considering that here we found possible discrepancies in the calculation of the relation parameters, slope and intercept, from clusters in different environments, this would potentially affect the calculation of the cosmological parameters in a greater amount. It shows once again the importance of including environmental selection effects when selecting a cluster sample.

4.6 Discussion

4.6.1 Causes/implications of different property distributions

Gathering all the above results, we attempt to understand their causes and implications in various research topics such as cosmology and cluster and galaxy

evolution.

Starting with the redshift distributions, GMPhoRCC and redMaPPer clusters showed that there are more clusters in underdense regions and less clusters in overdense regions in low redshift ranges. These results were consistent in both definitions of cluster environment, the geometrical one and the cluster local density. XCS DR2–SDSS catalogue showed no differences between the redshift distributions of clusters in differene environments, a fact that could be a result of the low number statistics in the XCS DR2–SDSS catalogue, as can be seen in Table 4.1.

Attempting to reason this, an assumption would be that in underdense regions or within voids there could exist a variant of the known cluster formation model, by which clusters form easier within voids and underdense regions, which cover a larger fraction of the volume of the Universe in the most recent times. The difference between the distributions is most prominent in the bottom right panel of Fig. 4.3, where there is higher number of low-redshift clusters within underdense regions. This implies that clusters in lower redshifts are potentially more likely to be created in low density environments. If cluster evolution also depends on the parameters of the environment that means that those "new generation" clusters could follow different evolution and have different properties than the older generation. Given those differences in the redshift distributions, one should be careful when studying cluster samples from different redshift ranges and compares them directly without being aware of the environmental factor the clusters reside in.

Moving on from redshifts, we continued by comparing the masses of Magneticum clusters. For the case of splitting clusters by their local density, we found significant signs that there are higher numbers of low-mass clusters in underdense regions compared to the overdense ones (refer to Fig. 4.4). The fact that this was only found only when categorising clusters by local density hints that this proxy might be better in determining the cluster environment compared to the geometrical criterion. The void shape and the larger void size in Magneticum might have played a role in the accurate definition of clusters residing within or outside a void.

A reason why there are more low-mass clusters in underdense regions could be the fact that there are lower possibilities of cluster mergers taking place in those environments. As a result, clusters accumulate less mass during their lifetime or in the same timeframe compared to clusters in overdense regions. In addition, clusters in underdense regions are more likely to have formed from less massive initial overdensities that collapsed into lower-mass clusters eventually. The possibility of a "quieter" merger history of clusters in underdense regions implies a slower and smoother evolution of those clusters compared to ones in overdense structures. Research on the evolution of low-mass clusters could unintentionally be focused on clusters in underdense regions and vice versa - research of cluster evolution in underdense regions selects clusters with possibly quieter merger history. Another possible explanation of different cluster mass distributions in different environments could again be a different cluster formation model taking place in low density regions or within voids.

Having matched our samples in redshift, we compared the cluster richness using the GMPhoRCC and redMaPPer catalogues. For both catalogues and both environment definition it has been found that clusters with similar redshift distributions have less galaxy members in underdense regions or within voids compared to the ones in overdense regions or outside voids (refer to Fig. 4.5). This can be explained by possibly different merger histories that the clusters of different environments have: clusters in overdense regions usually undergo more mergers and, as a result, can acquire more member galaxies throughout their lives. As a result, a cluster selection based on richness can unintentionally include more clusters from higher density environments and introduce an environmental bias within the sample. Another possible explanation could be a variation of the known cluster formation model taking place in underdense regions and within voids. This should be accounted for if selection effects play important role, for example in cosmological research.

After matching all cluster samples in redshift, mass and richness (when available), we moved into comparing the rest of the properties available, and first the luminosities and temperatures. For XCS DR2–SDSS, GMPhoRCC and Magneticum, we have X-

ray luminosities and temperatures available, while for redMaPPer, we have i-band luminosity. In all catalogues and for both environment proxies, clusters in underdense regions and within voids are less X-ray and i-band luminous (see Fig. 4.6). In all catalogues, but only when using local density as an environment proxy, clusters in underdense regions have lower X-ray temperatures than those in overdense structures (see Fig. 4.7). The fact that temperature differences are not found when splitting clusters within and outside voids hints again that this might not be the best environment proxy; a further discussion about the types of voids is made in Section 4.6.4.

The differences in both L and T can be explained once again by assuming different merger histories of clusters of different environments. The bolometric luminosity L_{bol} of a cluster is related to the density ρ and, therefore, mass M of the gas as (Ritchie and Thomas, 2002):

$$L_{bol} = \frac{M\rho\Lambda(T, Z)}{(\mu \times m_H)^2}, \tag{4.1}$$

where $\mu \times m_H$ is the mean molecular mass of the gas particles, Λ is the emissivity, T is the temperature and Z is the metallicity of the gas. The temperature and luminosity of the cluster are connected with a scaling law of $L \sim T^2$ (Randall et al., 2002), which means that the temperature of the cluster also depends on the mass and density of the ICM. During cluster merging events the ICM is shocked and the gas can vary in density within the cluster core due to the complex dynamics taking place. The luminosity and temperature can increase 10 and 3 times more than the values before the merger respectively, before they drop again to values lower than the sum of the values of the individual pre-merger clusters when the new cluster is virialised (Poole et al., 2007; Randall et al., 2002; Ritchie and Thomas, 2002). Even though the qualitative increase is the same for luminosities and temperatures during mergers, the luminosity increases in greater amount (since $L \sim T^2$), hence the temperature distributions are not as different between relaxed and non-relaxed clusters compared to the luminosity ones. Moreover, merging events are more likely to happen in overdense environments. That is a possible reason of observing clearer differences in luminosities regardless of the cluster environment proxy compared to

temperatures. This effect can be more prominent in lower mass clusters, where small merging events can produce energies of a similar magnitude to the energy already in the gas. The possibility of a variation of the cluster formation model existing within underdense regions cannot be excluded once again. Scaling relations using luminosities, temperatures and richness can be affected by this environmental effect if it is not taken into account - as we discussed in Section 4.5.7, the cosmological contraints derived from scaling relations are very sensitive to sample selection bias.

We looked at the BCG i-band luminosity and magnitude of redMaPPer clusters and found that those have lower values for BCGs in clusters in underdense regions and within voids (Fig. 4.9). The possibility of a quieter merger history of clusters in those environments would mean that BCGs themselves have not gone through as many mergers as those that live in clusters of overdense environments and hence have not grown enough in mass and therefore luminosity. The BCGs of those clusters follow a different evolution compared to the rest of the BCGs, just as their host clusters follow a different evolution compared to the rest of the clusters. This effect could also be an outcome of a different cluster formation model taking place within voids and underdense regions.

The CMR intercept, gradient and width have higher values for the clusters in overdense regions compared to the clusters in underdense structures. In addition, the red sequence colour of the clusters outside voids or in overdense regions has a significantly higher value than the clusters in underdense regions or within voids (Fig. 4.8). These findings show that there are more galaxy members in clusters in overdense regions and outside voids with redder colours than the galaxy members in clusters in uderdense regions and within voids; a finding that has been reported by other studies of differences in properties of galaxies in various environments (e.g. Hoyle et al., 2012). Just like their host clusters, galaxies in clusters in underdense regions seem to be younger, hence their bluer colour, and as a result spirals, as opposed to more old, elliptical galaxies found in clusters outside voids and in overdense regions. The cluster environment seems to affect the evolution of their galaxy members, not only their BCG.

As mentioned before, clusters are great cosmological tools. Cluster mass, its determination and distribution is an important proxy for the cosmological model and is widely used to constrain cosmological parameters. For that reason we created the clusters' L–T relation and mass and richness functions and compared them within clusters in different environments. It is important that if an environmental effect exists on those cluster cosmological tools this is taken into account.

Magneticum mass functions have not presented any differences between clusters of different environments and redMaPPer richness functions only presented differences between clusters within and outside voids and not between those of different local density (refer to Fig. 4.10). The large errorbars on the high-end mass range of Magneticum clusters is not allowing to define significant differences on the mass functions. On the other hand, redMaPPer catalogue shows once again that there are less high-richness clusters within voids, something that can be explained by the assumption that those clusters have undergone less mergers in their lifetime or that have formed following a different cluster formation model. XCS DR2–SDSS and Magneticum L–T relations of clusters in different environments seem to be similar within errors. However, GMPhoRCC clusters within voids have significantly steeper relation than those outside voids (see Fig. 4.11). Given that those clusters we found earlier to have significantly different luminosities and similar temperatures, this result is not a surprise.

For both mass functions and L–T relations there are hints of cluster environmental effects which are however not consistent within environment proxies and cluster catalogues. Care should be taken to account for possible selection effects when working with those cosmological tools due to the sensitiveness of the cosmological constraints on them.

4.6.2 Sample size

The study of the different-sized catalogues has not given clear conclusions of the dependence of the comparison results on the sample size. The redMaPPer and

Magneticum cluster catalogues offer a large number of clusters, large enough to enable the study of the dependence of the detected differences between two distributions of cluster properties to the number of clusters available. To this end, we take 100 random subsamples of various sizes from each of the two cluster catalogues and repeat all the above analysis. We then plot the distribution of the 100 KS p-values and the KDE probability distributions from the random test. Moreover, we plot the KDE probability for the random test as a function of the KS p-value for each of the 100 realisations. A low KS p-value (< 0.05) combined with a low KDE probability (< 0.05) is a sign that the distributions compared are significantly different from each other. Hence, we present the number of realisations out of the 100 where we find that KS p-value$<$0.05 and KDE prob$<$0.05 for the random test.

We study the difference between the luminosity distributions (i-band for redMaPPer and X-ray for Magneticum) of clusters within 70% of the voids radius and outside voids and of clusters in the most overdense and most underdense regions. In Table 4.4 we see the nunber of times we find that the luminosity distributions are significantly different when we use random subsamples of the initial catalogues. The sample size seems to affect the two catalogues in different degree. For Magneticum, the difference in the X-ray luminosity distributions of clusters within and outside voids has already disappeared when we take 70% of the initial Magneticum cluster. In the case of comparing overdense and underdense regions, the difference signal is degrading slower and smoother; it is fully observed when taking 70% of the initial sample and degraded to half when taking 20% of the initial sample. In redMaPPer catalogue, the signal is a lot more persistent, slowly degrading when comparing the within and outside voids distributions and remaining full when comparing clusters in overdense and underdense regions. The fact that the geometrical environmental proxy is more sensitive than the local density one can be explained by the fact that the samples of clusters within voids are smaller than the similar density ones, as can be seen in Table 4.1. The fact that the signal is more sensitive in the Magneticum catalogues compared to the redMaPPer one could be due to the different way of defining the clusters and their properties in the two catalogues.

Table 4.4 *The number of realisations (out of 100) where the luminosity distributions of redMaPPer and Magneticum clusters in different environments were found significantly different - KS p-value<0.05 and random test KDE prob<0.05. For the Magneticum catalogue, we took subsamples of 70%, 50% and 20% of the initial catalogue, while for redMaPPer we took subsamples of 50%, 10% and 5% of the initial catalogue.*

Magneticum			
	70%	50%	20%
O-I7 comparison	8	3	2
U-O1 comparison	100	95	52
redMaPPer			
	50%	10%	5%
O-I7 comparison	100	71	38
U-O1 comparison	100	100	100

In Fig. 4.12, we show the distribution of KS p-values and random test KDE probabilities of comparisons of the luminosity distributions of Magneticum (left panels) and redMaPPer (right panels) clusters in overdense/underdense regions and within/outside voids respectively. The sample size decreases from top panels towards the bottom ones and the peak of KS p-value< 0.05 and KDE prob<0.05. The corresponding number of times we detect difference between the luminosity distributions drops the smaller the sample size is as confirmed by Table 4.1.

These results show that the number of clusters available for those comparisons affect the signals observed. The small number of clusters in the XCS DR2–SDSS catalogue are insufficient to give statistically significant results on the difference between the X-ray properties of clusters inside and out of voids. As seen in Section 4.5, there were cases where amongst all the catalogues, XCS DR2–SDSS was the only one that no differences have been observed. A larger X-ray cluster catalogue would be needed for this study, which will be available with eRosita mission (Predehl et al., 2010).

4.6.3 Richness estimators

Here, we want to investigate possible richness calculation biases of our algorithms between clusters in voids and outside voids. A bias in the richness calculation would

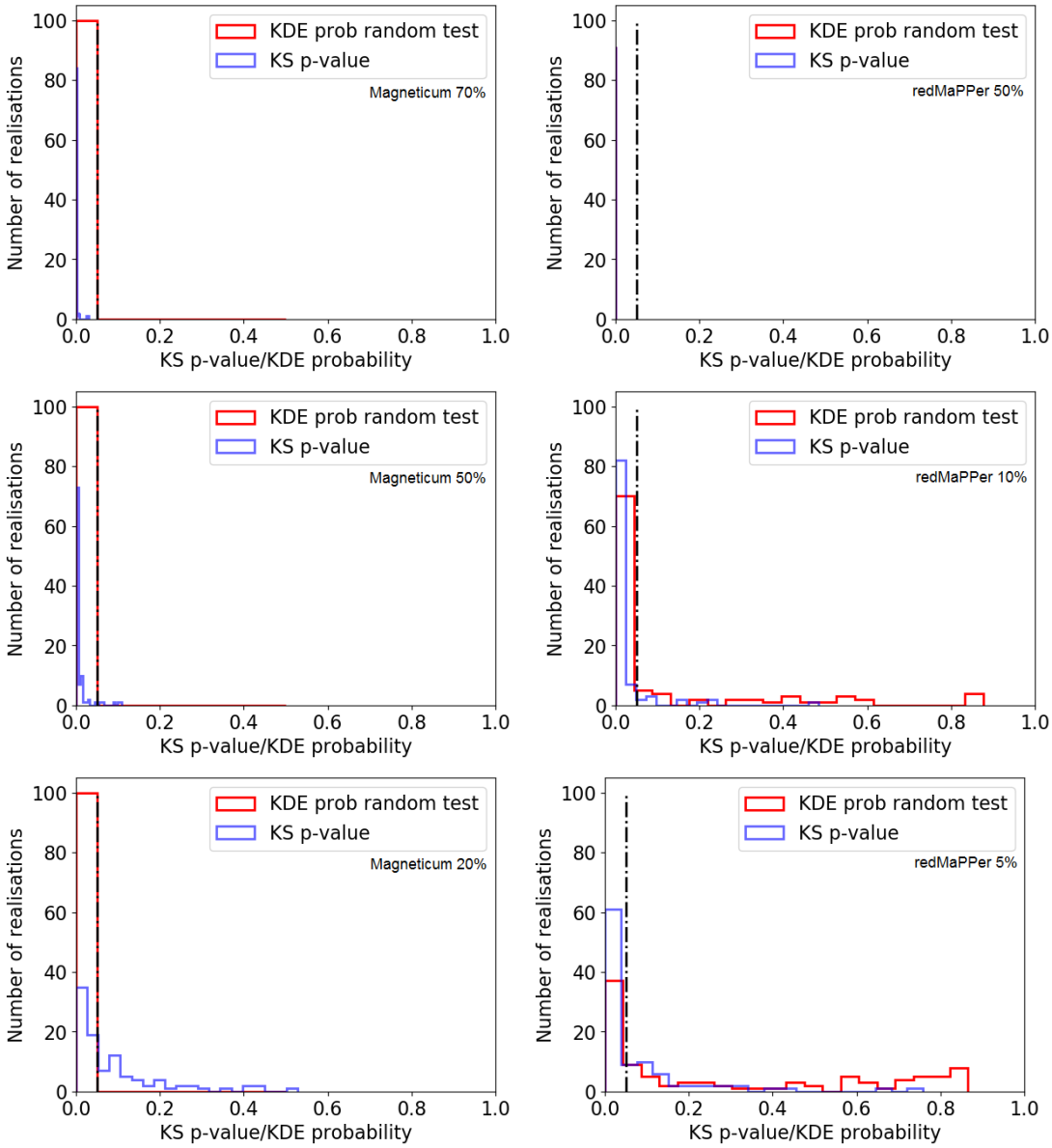

Figure 4.12 *The distribution of the 100 KS p-values and the random test KDE probability distributions for the i-band luminosuty of redMaPPer clusters (right panels) and X-ray luminosity of Magneticum clusters (left panels). The signal degrades from top to bottom panels Top panels: The samples are 70% (left) and 50% (right) of the initial sample size. Middle panels: The samples are 50% (left) and 10% (right) of the initial sample size. Bottom panels: The samples are 20% (left) and 5% (right) of the initial sample size.*

mean that the difference in the richness estimation between the two populations is an artefact of the richness estimator algorithm.

For the XCS DR2–SDSS and GMPhoRCC cluster catalogues, the same algorithm, GMPhoRCC, has been used to calculate the richness inside the R_{200} cluster radius. The richness estimation is made by simply counting the numbers of galaxies within a cone with an aperture of $1-4$ arcminutes (depending on the cluster's angular size) and subtracting the number of galaxies in the background in the same aperture. In order to see whether the fact that a cluster resides in a void significantly affects the richness estimation, we can assume a cluster inside a void, like the one in Fig. 4.13, where the cluster centre is the closest void boundary to us, in order to study the maximum effect. The cluster cone can extend behind the void, depending on the cluster aperture used by GMPhoRCC and the void size. If the error of the background number of galaxies of clusters outside voids, $N_{b,out}$, is larger than the fraction of background galaxies in the part of the cluster cone inside the void, $N_{b,void}$ to all the background galaxies in the cluster cone of clusters inside voids, $N_{b,all}$, then the richness estimation of the clusters inside voids is not significantly biased with respect to that of the clusters outside voids:

$$Err(N_{b,out}) > \frac{N_{b,void}}{N_{b,all}} = \frac{V_{void}}{V_{all}} \times \frac{n_{void}}{n_{all}} \tag{4.2}$$

where N is the number of background galaxies, V is the volume of the cone, n is the density of the background galaxies and the pointers "void", "out" and "all" show the property is computed inside the voids, outside the voids or both inside and outside of voids respectively. Equation (4.2) says that the fraction of galaxies in the part of the cone inside the void to the galaxies in all the cone is equal to the fraction of the volume of the cone inside the void to its total volume times the fraction of the number density in the part of the cone inside the void to the total number density in the cone.

The values of V_{void}/V_{all} are calculated by using the void ellipsoidal shapes in LOWZ and CMASS catalogues to find the volume of the cluster cone inside the void and by using the GMPhoRCC aperture to find the total volume of the cluster cone. We calculate the median value of V_{void}/V_{all}, which corresponds to the median of the void

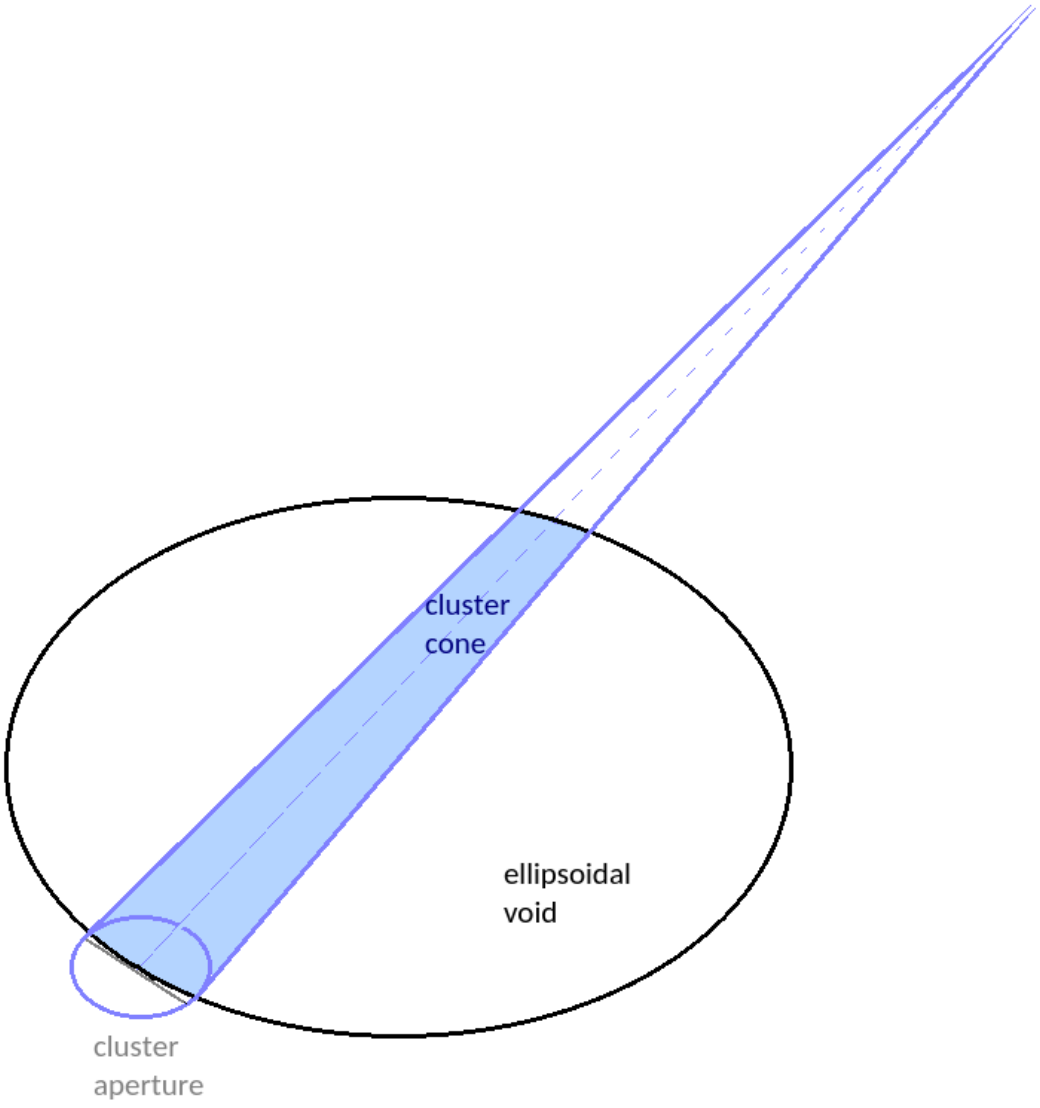

Figure 4.13 *A cluster inside an ellipsoidal void and the cluster cone (in blue) where the GMPhoRCC richness is calculated.*

Table 4.5 *The median (maximum value) of the V_{void}/V_{all}, n_{void}/n_{all} and their product (last column) which are the right hand side of the equation (4.2.*

	V_{void}/V_{all}	n_{void}/n_{all}	Product
LOWZ voids	0.1112 (0.1119)	0.2544	0.0283
CMASS voids	0.0766 (0.1322)	0.2722	0.0209

volumes in the catalogue, the median of the void redshifts and a GMPhoRCC cluster aperture of 2.5 arcminutes. We also calculate the maximum values of V_{void}/V_{all}, which correspond to the maximum void volume in the catalogue, the lowest void redshift (the lower redshift the larger fraction of the cone is inside a void so the larger the effect) and a GMPhoRCC cluster aperture of 4 arcminutes. The values for n_{void}/n_{all} are the medians of the density contrast values of the voids as defined in Nadathur (2016) for LOWZ and CMASS. The results for the right hand side of equation (4.2) are shown in Table 4.5. We compare the last column with the values of the median (and median absolute deviation) error of the background number of galaxies in the XCS DR2–SDSS catalogue, which is 0.3098 (with median absolute deviation 0.2159) and in the GMPhoRCC catalogue, which is 0.1443 (with median absolute deviation 0.1184). These values confirm that equation (4.2) holds, which means that the difference found between the richness distributions of clusters in voids and outside voids in the two cluster catalogues is not an artefact of the algorithm that used to calculate the cluster richness.

Concerning the redMaPPer catalogue, this has a different richness estimator than the XCS cluster catalogues. It has been shown that, during the richness estimation, projection effects depend on both the background galaxy density field and the large cluster-to-cluster fluctuations on the density field. The former only boosts the cluster richness by an unimportant amount and the latter can affect severely 5-15% of the clusters (Rozo et al., 2011). Therefore, the richness estimation of a small percentage of redMaPPer clusters might be affected by the large scale structure density field and hence the presence of a cluster in a void or an overdensity.

4.6.4 Types of voids

When comparing cluster properties inside and outside voids, we found that the results are most of the times different from the ones when comparing clusters in different background densities. In the latter case, the properties seem to present differences in the majority of catalogues/properties, mass functions, luminosity–temperature relations, while in the former case, differences are found only in some properties and catalogues and not in mass functions and luminosity–temperature relations. The reason behind that is that the void definition does not necessarily track the density distribution of the large scale structure. The void catalogues used in this study include all the underdensities found with ZOBOV algorithm, as explained in Nadathur (2016). However, there are two types of voids included in this selection: the voids embedded in overdense shells and the voids without overdensities surrounding them (Paz et al., 2013; Sheth and van de Weygaert, 2004). The first ones, tend to have negative gravitational potential (Nadathur and Hotchkiss, 2015), are smaller, reduce in size and end up collapsing due to the overdensities surrounding them (Ceccarelli et al., 2013). The second ones, have positive gravitational potential and expand with time. One can segregate between the two types of voids by introducing a new parameter that depends on the size and potential of the voids. For example, the second type of voids would be useful for cosmological studies that trace voids as underdensities with non-linearities (Nadathur and Hotchkiss, 2015). However, the small voids with negative gravitational potential are not likely to contain large number of clusters given their size ($<$10 Mpc), so the vast majority of the clusters in voids would be inside the large, expanding voids.

In Fig. 4.14, we plot the number of clusters in and out of voids in each density bin for all cluster catalogues. One would expect that the background density correlates with the geometrical criteria of a cluster being within a void or now; i.e. the lower the background density (left-side density bins) the more clusters would be found inside voids and fewer outside voids and vice versa for higher background density (right-side density bins); this is only true for the redMaPPer catalogue. However, a constant

amount of clusters in voids is found in all density bins, showing that splitting clusters within and outside voids does not trace their density environment. The brown dashed lines in the figure show the number of clusters we would expect in voids considering the percentage of the volume survey that are voids. The fact that this number is much higher than the number of clusters in voids found is possibly due to the fact that clusters are assumed to be ellipsoidals (for XCS DR2–SDSS, GPhoRCC and redMaPPer) and spheroids (for Magneticum) as opposed to their true 3-dimensional shaped. As a result, voids with that approximated spheroidal or ellipsoidal shape may overlap and contain less clusters overall compared to the number they would contain if they had their real 3-dimensional shape. Moreover, adding up the clusters inside and outside voids in each density bin in the observational catalogues does not sum to the number of clusters in each density bin as shown in Table 4.1. This is because the clusters within/outside voids have gone through a redshift cut in order to match the redshift range of the BOSS voids catalogue. These plots also confirm the importance of our conservative cuts when studying clusters in voids; we have only used clusters within 50% or 70% the void radius.

4.6.5 Future prospects

This work can be extended to other surveys with available void and cluster catalogues, for various cluster properties, such as the XCS or redMaPPer (Rykoff et al., 2016) cluster catalogue in the Dark Energy Survey (Abbott et al., 2018). As we discovered in Section 4.6.2, the number of clusters available can affect the difference between clusters in voids and out of voids and, therefore, the selection biases occurring as a result. As shown in Table 4.4 and Fig. 4.12, the difference starts to disappear in samples $\sim$ 5% of the redMaPPer sample; that means that we need approximately a thousand clusters to be able to detect this signal in observational data. eRosita (Predehl et al., 2010) will give the opportunity to have such large X-ray cluster catalogues and it would be very interesting to extend this study using those catalogues in the future.

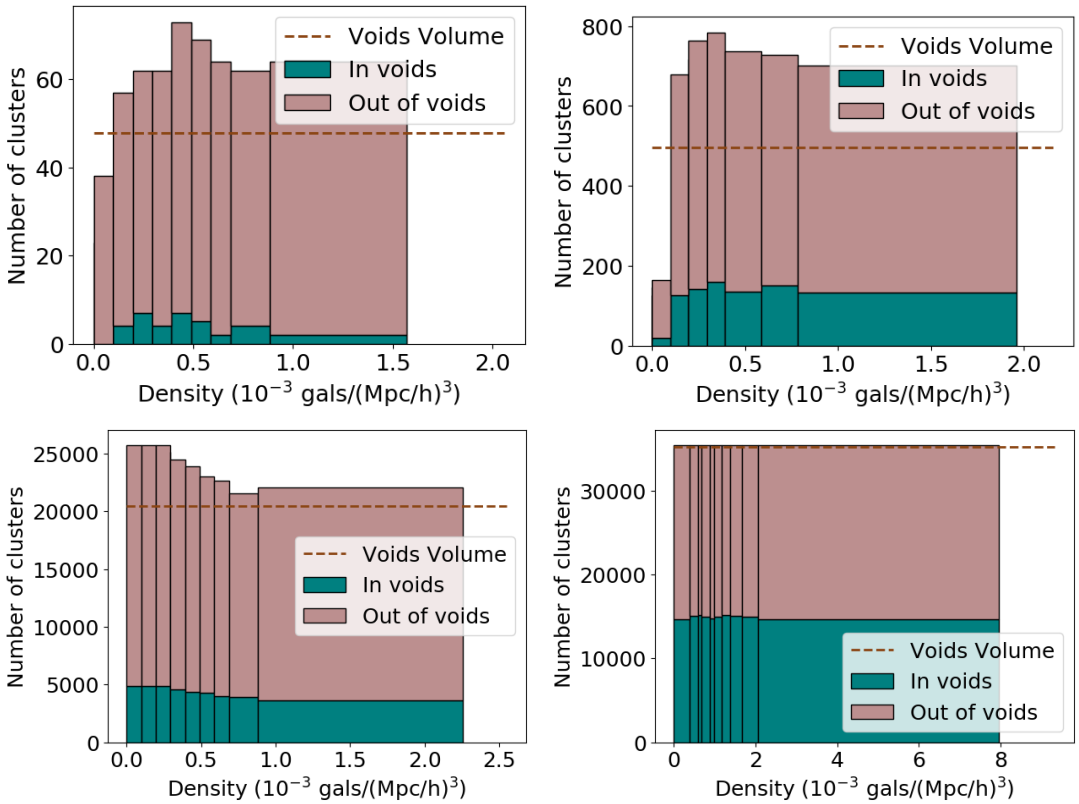

Figure 4.14 *The number of clusters in and out of voids in each density bin for XCS DR2–SDSS (top left), GMPhoRCC (top right), redMaPPer (bottom left) and Magneticum (bottom right) cluster catalogue. The brown dashed line shows the number of clusters we would expect in voids considering the percentage of the volume survey that are voids.*

4.7 Conclusions

In this Chapter, we studied the environment effects on cluster properties, following similar studies on galaxy properties, which have either found or not differences between the colours and star formation rates of galaxies in different properties (e.g., Darvish et al., 2018; Hoyle et al., 2012; Ricciardelli et al., 2017; Varela et al., 2012; Wang et al., 2018). We extensively studied the effect of the cluster environment on the X-ray and optical cluster properties, such as X-ray luminosity, X-ray temperature and richness. We used both observational and simulation cluster catalogues to compare the properties of clusters in different environments and used two different proxies of the clusters' environment, their location inside or outside voids and and their local density within the shell 10-20 Mpc distance from their centre. We evaluated the significance of our results using a random test, taking into account the possibility of random selection of a cluster sample.

We discovered differences in the redshift distributions of GMPhoRCC and redMaPPer clusters of different environments. There are more clusters in underdense regions in lower redshifts, a fact that can be associated with a possibly different cluster formation model existing in underdense regions and within voids that results in more new clusters being created in low density regions in more recent times. Additionally, significant suggestions of more low mass, richness, luminosity and temperature clusters with matched redshift distributions within voids and in underdense regions compared to clusters outside voids and in overdense regions. We believe that the possible lower merger rate in the underdense regions couls have caused the cluster evolution to be slower, resulting in more clusters with low masses, less galaxy members, less luminous cores and lower ICM temperatures in those areas for a given redshift range. The results can also be explained by a different cluster formation model in underdense regions with smaller initial overdensities collapsing into clusters. For specific combinations of environment proxy and cluster catalogue, we also found differences in the mass functions and L–T relations of clusters within different environments. These reinforce the fact that environment can play an important role when selecting a cluster sample,

especially when this is intended for cosmological studies, where selection effects can significantly alter the contraints imposed.

Moreover, the results showed that the cluster local density and the categorisation of clusters within/outside voids give in general consistent results. Discrepancies were found for the Magneticum catalogue, possibly due to the larger size of the voids in the catalogue compared to the observational catalogues. Similar results have been found for galaxies, where significant differences have been detected on the basis of geometrical membership (Hoyle et al., 2012; Ricciardelli et al., 2017). The detection of difference between two distributions was found to depend on the number of objects in the distributions, a fact that shows the importance of having large observational cluster catalogues.

Overall, this study showed that cluster properties depend on the environment they have formed and evolved in. This was hinted to be due to a different merger rate of clusters in underdense regions, but could also be either due to a different cluster formation model in underdense regions. When selecting a cluster sample based on observables, especially for high precision research such as extraction of cosmological parameters, one should be aware of the environmental biases that are included and take into account the bias inserted in the calculations due to the cluster environment. Failing to do so, additional errors can be introduced to the calculation of the constraints, as showed in Sahlén et al. (2009). Further research with larger observational X-ray cluster catalogues such as from the future eRosita mission (Predehl et al., 2010) will be invaluable to further study this effect with more accuracy.

Chapter 5

Galaxy cluster's rotation

5.1 Preface

The work presented in this chapter has its origins in my MSc project at the Aristotle University of Thessaloniki, supervised by Prof Manolis Plionis, and subsequently published in MNRAS as Manolopoulou and Plionis (2017). During my time in Edinburgh, I worked on the validation test analysis with different configurations in Section 5.4, as well as the identification of the significance of the rotational signal (Section 5.5.3) and the correction of the cluster velocity dispersion for rotation (Section 5.6.3.4). The preparation of the paper was all undertaken during my PhD period: I re-generated most of the plots (all those included here except for Figures 5.1, 5.2, 5.3 and 5.9) and converted the text from my MSc dissertation into the form appropriate for a journal paper (most of which is reproduced verbatim here). After submission of the paper, I performed the analysis reported in Section 5.7 and 5.9.2, applying to MUSIC simulation data the same methodology used by Manolopoulou and Plionis (2017) for observational data. All the material presented in this chapter is my own work, except for Sections 5.5.3.4, 5.6.3.4, 5.6.3.5 and Fig. 5.10 and 5.14, which were prepared by the co-author of the publication.

5.2 Introduction

When calculating the cluster mass using the velocities of the individual cluster members, we assume that the cluster is in virial equilibrium; the gravitational potential equals two times the sum of the kinetic energy of the members and that galaxy orbits are roughly isotropic. This does not take into account the possible contribution to the galaxy velocities of a rotational component. Clusters could be rotating due to an initial angular momentum that survives since their formation or due to recent mergers or interactions with close neighbours. Not taking into account the rotation could result in an erroneous dynamical cluster mass, which could ultimately affect the cosmological constraints provided by the cluster mass function. The difficulty to distinguish a rotating cluster from two closely interacting or merging ones is probably the cause for the few early attempts to investigate the rotation of galaxy clusters (eg., Materne and Hopp, 1983; Tovmassian, 2002). Hwang and Lee (2007) used the galaxy member velocities to search for indications of rotation and found $\sim$10% of their cluster sample to be rotating and in dynamical equilibrium (not undergoinng a recent merger). The relevant study of Hamden et al. (2010) used galaxy velocities, X-ray spectra of intracluster gas, and distortions of the cosmic microwave background (CMB). Chluba and Mannheim (2002) and Cooray and Chen (2002) studied the effect of the cluster rotation on the temperature and polarization of the CMB; while other groups have attempted to model the rotation of the intracluster medium (Bianconi et al., 2013; Fang et al., 2009). A particular case study is cluster A2107 which has been found to rotate in multiple studies (Kalinkov et al., 2005; Materne and Hopp, 1983; Oegerle and Hill, 1992). Recently, a new attempt to study cluster rotation using the SDSS spectroscopic sample concludes that some clusters are indeed rotating (Tovmassian, 2015).

This work aims in identifying the rotation of members of clusters by using their velocities taken from the SDSS DR10 spectroscopic data base (Eisenstein et al., 2011) and from simulations (Baldi et al., 2017). We construct a novel algorithm that can identify both the cluster rotation axis and amplitude. We apply the algorithm to

selected Abell clusters and seek for correlations between their rotation properties and their dynamical state. When required we use a flat Λ cold dark matter cosmology with $H_0 = 70h_{70}$ km s^{-1} Mpc^{-1}.

The paper is organized as follows: in Section 5.3 we present our rotation identification algorithm and compare it with that of Hwang and Lee (2007). In Section 5.4 we test the efficiency of our algorithm, while in Section 5.5 we present our cluster sample, systematic biases and the application of our algorithm. In Section 5.6 we present and discuss our results and in Section 5.7 we apply our method to clusters from simulation. We derive our conclusions in Section 5.8.

5.3 Rotation identification

First, it is important to clarify what we intend in our work as a rotating cluster. A rotational mode in clusters can be caused by a variety of mechanisms, among which the anisotropic infall of material, an initial angular moment of the proto-cluster that survives virialization, an off-axis merging, etc. Most probably all of them are related to the initial or secondary building of the cluster and therefore rotation should be expected in many phases during the cluster formation process.

The question however posed in our work is what is the fraction of virialized (or close to) clusters which retain a rotational mode. Therefore, as detailed in the following Sections, we have made all efforts to exclude from our sample clearly interacting clusters, clusters with multiple components, clusters with detectable substructures in velocity and projected space. However, clusters in post-merging phase that are at the process of virialization but not yet completely virialized and with no significant substructure indications, cannot be easily distinguished; in any case, we believe that they are rotating clusters. For those that disagree, we also make an effort, through targeted Monte Carlo simulations, to estimate the fraction of such false detections.

5.3.1 Our Method

We introduce a method to identify the possible coherent rotation of galaxies in galaxy clusters. The method provides both the rotational velocity amplitude and the orientation of the projected rotation axis, as well as a quantification of the rotation being a true feature or an artefact.

In order to explain our procedure let us first assume a counter-rotating cluster with constant rotational velocity of 600 km/s, ie., each galaxy member has the same velocity irrespective of its cluster-centric distance. In order to have a realistically "observed" cluster we then assign to each galaxy the line-of-sight component of its rotational velocity with respect to the cluster centre (which in our example we set to be stationary). Starting from the components v_x, v_y, v_z of the velocity of each galaxy and placing the y-axis on the plane of the sky, we calculate its line-of-sight velocity from the relation:

$$v_{los} = v_x \cos\phi + v_z \cos(90^\circ - \phi) \ ,$$

where ϕ is the vertical angle between the line of sight and axis x (see Fig. 5.1), ie., the z-axis is the axis of rotation. For $\phi = 0$, the line of sight coincides with the x-axis and the cluster rotation axis is perpendicular to the line-of-sight, the ideal case for observing rotation; as the angle ϕ increases, we also take into account the z-component of the velocity in the line-of-sight velocity. For $\phi = 90^\circ$, the line of sight coincides with the z-axis (see Section 5.4.3 for the effect of ϕ on the detection of rotation). A visual illustration of our example cluster, which has $\phi = 0$ and a horizontal projected rotation axis on the plane of the sky ($\theta_{rot} = 90^\circ$), and of our procedure is provided in Fig. 5.2, as detailed below.

The basic idea is to divide the projected distribution of galaxy cluster members in two semicircles (1 and 2; as shown in the left-hand panel of Fig. 5.2), measure the difference of the mean galaxy velocities between the two semicircles, $v_{dif} = \langle v_1 \rangle - \langle v_2 \rangle$, and rotate consecutively (on the plane of the sky) the galaxy positions by an angle θ in the clockwise direction (as shown in the left-hand panel of Fig. 5.2 by

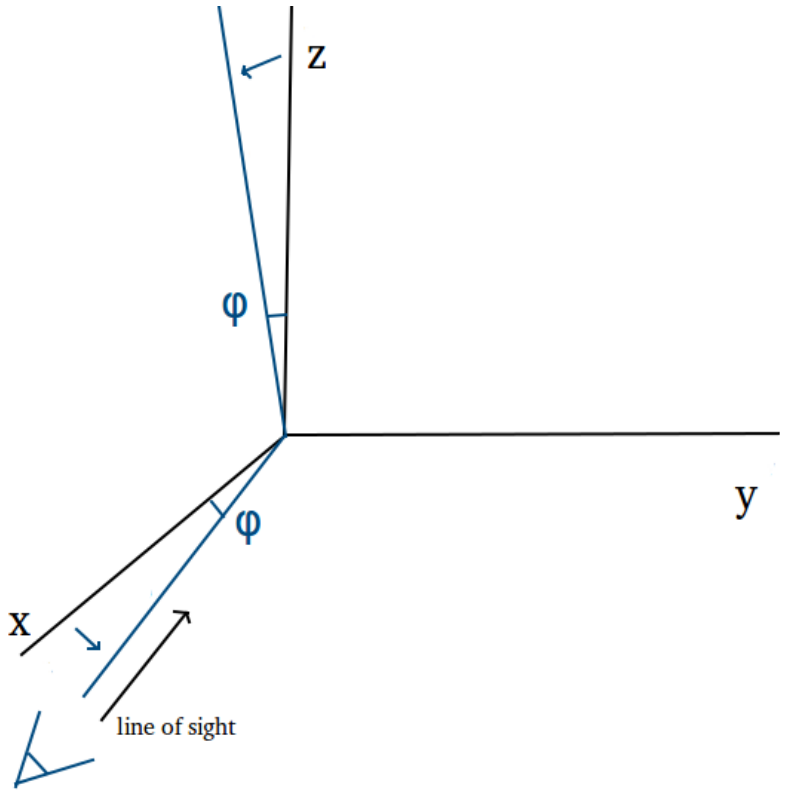

Figure 5.1 *The triaxial coordinate system and the line of sight direction (blue line). The y-axis remains intact.*

the red arrows), repeating the measurement of v_{dif} for each rotation. Consequently, we obtain the velocity difference $v_{dif}(\theta)$ as a function of the angle θ. We will use the graph of $v_{dif}(\theta)$ (right-hand panel of Fig. 5.2), which we call the rotation diagram, as our primary indication for the presence or not of a rotation mode.

We need now to relate the observed $v_{dif}(\theta)$ to the true rotation velocity of the cluster. Even in the ideal case of $\phi = 0^\circ$ we will not observe the whole v_{rot} of each galaxy but as already discussed only its projected component along the line of sight. We will observe (for those galaxies in the semicircle moving towards the observer) blueshifted velocities with magnitudes which depend on their 3D position in the cluster. For example, if they are located at an angle μ from the line of sight passing through the centre of the cluster (ie., the angle between the line of sight passing through the centre of the cluster and the cluster radius connecting the centre of the cluster to the galaxy), the observed rotational velocity magnitude of each galaxy will be $v_{obs} = v_{rot} \times \cos(90 - \mu)$, where μ takes values from 0^o to 180^o. The mean v_{obs} of all N galaxies in this projected semicircle will not add up to v_{rot}, but to:

$$\langle v_1 \rangle \simeq v_{rot} \times \sum_{i=1}^{N} \cos(90^\circ - \mu_i)/N$$

Similarly, in the other semicircle it will add up to $\langle v_2 \rangle = -\langle v_1 \rangle$. Thus,

$$v_{dif} = \langle v_1 \rangle - \langle v_2 \rangle = 2v_{rot} \times \sum_{i=1}^{N} \cos(90^\circ - \mu_i)/N \ ,$$

where for convenience we have assumed the same number of galaxies within each semicircle (projected hemisphere) and at symmetric positions to each other (ie., not respecting a realistic volume fill). In such a model configuration we find that:

$$\sum \cos(90 - \mu_i)/N \sim 0.636$$

The realistic observational situation, where most of the galaxies are at small angles μ from the cluster centre due to the larger volume projected, can be estimated directly from our Monte Carlo cluster of Fig. 5.2, where we find $v_{obs} \sim 0.503 v_{rot}$ and therefore

$v_{rot} \simeq v_{dif}$. As a result, the rotational velocity of the cluster will be read from the rotation diagram as:

$$v_{rot} = \mathrm{MAX}[v_{dif}(\theta)] \ .$$

To be more detailed, our rotation detection procedure entails rotating on the plane of the sky the galaxy-member positions by an angle θ starting from the vertical axis clockwise, in the range $0^\circ - 360^\circ$ and with a step, say, of 10°. In our example, for $\theta = 0$, we will not observe any significant velocity difference between the East-West hemispheres; ideally, in the absence of noise we should obtain $v_{dif} = 0$. As θ increases, the velocity difference should increase until it reaches its maximum value at $\theta = 90^\circ$. In this case, the galaxies in one semicircle would seem to move away and in the other semicircle would seem to approach us, with respect to the cluster centre. Then as θ increases to 180° the amplitude of the rotation signal will decrease and increase again towards $\theta = 270^\circ$ until it approaches again $v_{dif} = 0$ at $\theta = 360^\circ$. This behaviour is depicted in the right-hand panel of Fig. 5.2 which shows the periodic rotation diagram for an ideally rotating cluster with a constant velocity of 600 km/s.

A few interesting and important issues, that will be addressed in the following sections, are as follows.

- The orientation of the rotational axis with respect to the line of sight can hamper the detection of a rotational mode, if such exists (see Section 5.4.1).

- Based on whether the troughs or the peaks appear first in the rotation diagram, we infer the rotating or counter-rotating nature of the cluster (as an example, in Fig. 5.2 the cluster is counter-rotating). In an initial irrotational Universe the expectation of course is for a statistically equivalent number of both type of rotating clusters.

- If a non-rotating cluster has one or more small-sized subgroups with a significant velocity difference with respect to the rest of the cluster then, in the rotation diagram, we may observe narrow peaks or troughs at some angle θ but not a clearly sinusoidal signal. However, most such cases will be identified and

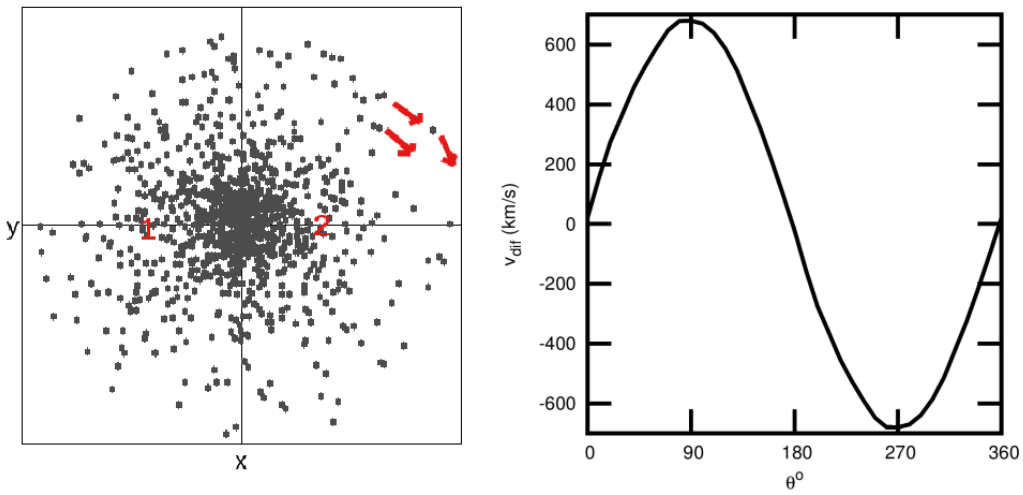

Figure 5.2 *An illustration of our method. We show a Monte Carlo cluster which has been set to counter-rotate with an amplitude $v_{rot} = 600$ km/s and with its projection rotation axis at an angle $\theta_{rot} = 90^{\circ}$ with respect to the North. Our rotation identification method entails rotating consecutively the galaxies of the cluster by an angle θ in the clock-wise direction (as indicated by the red arrows) and estimating the velocity difference between the East-West semicircles (details are presented in the main text). The right-hand panel shows the resulting rotation diagram, ie., the velocity difference between the two semicircles against the angle θ.*

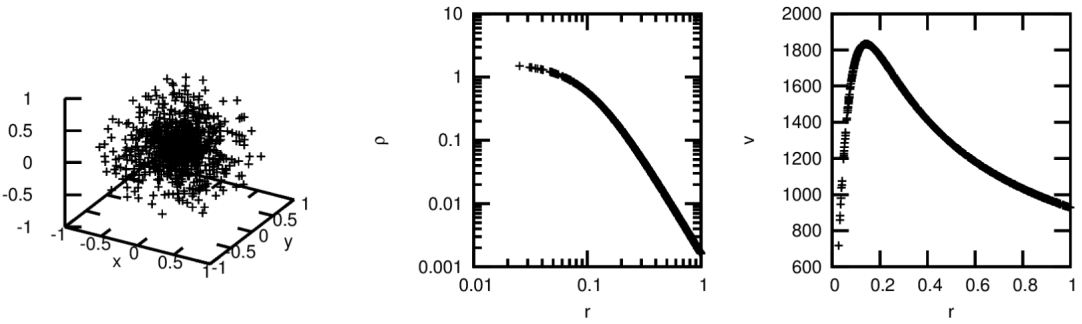

Figure 5.3 *(a) A Monte Carlo cluster in 3D, (b) the density ρ as a function of the cluster-centric distance r, and (c) the amplitude of the virial velocity as a function of the distance r from the cluster centre.*

excluded from our analysis at an early stage (see Section 5.5.1). However, there are cases where global rotation and infalling substructures cannot be easily distinguished: (a) a subgroup occupying a relatively large fraction of the cluster projected area; (b) two significant subgroups of galaxies moving at opposite directions within the cluster potential, although such a case requires fine tunning and thus should be rare.

In general, the expectation for a non-rotating cluster, with no significant infalling substructures, is to have a random rotation diagram (no systematic dependence of $v_{dif}(\theta)$ on θ) with relatively small values of $v_{dif}(\theta)$.

5.3.2 The Hwang and Lee method

Another method to identify cluster rotation, with which we will compare our own, has been proposed by Hwang and Lee (2007). They use a sinusoidal relation to compute the angle of the rotation axis, Θ_o, and the rotational velocity v_{rot}:

$$v_p(v_{rot}, \Theta) = v_{sys} + v_{rot} \cdot \sin(\Theta - \Theta_o) \ , \tag{5.1}$$

where v_p is the predicted radial velocity of each galaxy due to the cluster rotation, v_{sys} is the peculiar velocity of the cluster and Θ is projected on the plane of the sky position angle of each galaxy, setting off from North to East. Since in our case we use velocity differences with respect to the cluster mean recessional velocity, we set

$v_{sys} = 0$.

A χ^2 minimization procedure can be used to determine the best-fitting values of Θ_o and v_{rot}, assuming that the sinusoidal model of equation (5.1) represents well the velocity data. Namely, we use a grid of Θ_o and v_{rot} values and calculate χ^2 for each pair of parameters:

$$\chi^2(v_{rot}, \Theta_o) = \sum_i \frac{(v_{p_i} - v_{los,i})^2}{\sigma_i^2} \ ,$$

where $v_{los,i}$ is the observed line-of-sight velocity of every galaxy and σ_i its measurement error.

5.4 Validation of our method

Before applying our method to real galaxy cluster data, we should validate and confirm that it can provide unambiguous indications of rotation for the case of realistic clusters and that it can correctly provide the amplitude of rotation and its axis orientation. To this end, we construct, using the Monte Carlo simulation method, a virialized cluster with a mass of $4 \times 10^{14} M_{\odot}$, radius $R_{cl} = 1$ Mpc, core radius $r_c = 0.1$ Mpc and having a King profile density distribution (King, 1962):

$$\rho(r) = \frac{\rho_0}{(1 + (r/r_c)^2)^{3/2}} \ , \tag{5.2}$$

where $\rho(r)$ is the density included within radius r and ρ_0 is the density in the centre of the cluster. To estimate the value of ρ_0 we use the cluster mass M_{cl},

$$M_{cl} = \frac{4}{3} \frac{\pi R^3 \rho_0}{(1 + (r/r_c)^2)^{3/2}} \tag{5.3}$$

from which by using $M_{cl} = M(< R_{cl})$ and $r = R_{cl}$ we estimate $\rho_0 = 6.56 \times 10^{-12}$ kg/km^3. Although it is known that the NFW (Navarro et al., 1997) profile is a more accurate representation of the dark matter and galaxy density profiles in clusters of galaxies, while the King profile is applicable mostly to the intracluster gas, it is acceptable to use the latter for the purpose of just testing our methodology. A

realization of one such Monte Carlo cluster can be seen in Fig. 5.3.

Assuming that the cluster is dynamically relaxed (virialized) we can estimate, using the virial theorem, the amplitude of the expected 3D velocity, v_k, of each galaxy, which depends on its distance from the cluster centre according to: $v_k^2 = GM(r)/2r$, and from equation (5.3) we obtain:

$$v_k(r) = \sqrt{\frac{2}{3}\frac{G\pi\rho_0 r^2}{\left(1+(r/r_c)^2\right)^{3/2}}}\ , \tag{5.4}$$

where $M(r)$ is the mass within a sphere of radius r.

Note that each Cartesian component $v_{k_x}, v_{k_y}, v_{k_z}$ of the virial velocity $v_k(r)$ is assumed to be randomly orientated, while the rotational velocity will have a coherent orientation perpendicular to some rotation axis (in most cases we will assume it to be lying on the plane of the sky). We will further set a counterclockwise direction on the velocity components $v_{rot_x}, v_{rot_y}, v_{rot_z}$, by:

$$\vec{v}_{rot} \cdot \vec{r} = 0$$
$$v_{rot}^2 = v_{rot_y}^2 + v_{rot_x}^2\ ,$$

with the first relation ensuring that the coordinate vector $\vec{r}$ is perpendicular to the rotation velocity vector $\vec{v}_{rot}$. The second implies that the z-component of the velocity is set 0, in order the rotational velocities to be perpendicular to the rotation axis z.

We can now assign to each galaxy a 3D velocity which could be either of:

(a) a constant rotational velocity (independent of the cluster-centric distance of each "galaxy") having an amplitude, say a fraction of the maximum virial expectation and a coherent orientation around a chosen axis,

(b) a rotational velocity having as amplitude a constant fraction of the virial expectation, ie., different at the different cluster-centric distances and a coherent orientation around a chosen axis,

(c) the vectorial sum of the virial expectation and any of the above two rotational velocity models. This case corresponds to a more realistic cluster velocity profile and we model it by assigning to each "galaxy" the randomly oriented virial velocity that corresponds to its distance from the cluster centre, adding vectorially the rotation velocity.

To investigate the systematics related to the realistic observational situation we will attempt to identify the cluster rotation on the plane of the sky. To this end, we project the 3D cluster on one plane, estimating the line-of-sight component of the total (rotational or rotational+virial) velocity of each mock galaxy and imposing its rotation axis to be perpendicular to the line of sight ($\phi = 0$, which is the ideal case). We then apply both algorithms (ours and that of Hwang and Lee) to investigate their performance for both rotational velocity models and for a variety of axis orientations on the plane of the sky. Furthermore, to study sampling effects we simulate mostly two cases; a cluster with 1000 and a cluster with 50 "galaxies".

5.4.1 Model (a): constant rotational velocity

Using as input rotational velocity a constant one with $v_{rot} = 540$ km/s (30% of the maximum virial velocity), we obtain the results shown in Fig. 5.4, where in the upper panels we present results based on a cluster with $n_{mem} = 1000$ and in the lower panels a cluster with $n_{mem} = 50$, while in the left-hand panels we present the case of a purely rotational velocity and in the right-hand panels the case of a total velocity based on the vectorial addition of the virial expectation and the rotational velocity.

For this rotational velocity model we can actually clearly address the issue of how well does each method recover the input rotational velocity (and axis orientation). In Table 5.1 we present the output v_{rot} and θ_{rot} for all four cases shown in Fig. 5.4. For the case of dense sampling, which provides an estimate of the intrinsic performance of the two methods, we find a significant underestimation (by $\sim 35\%$) of the amplitude of v_{rot} by the Hwang and Lee method, and a small ($\lesssim 10\%$) overestimation of v_{rot} by our method. The rotation axis orientation is well recovered by both methods.

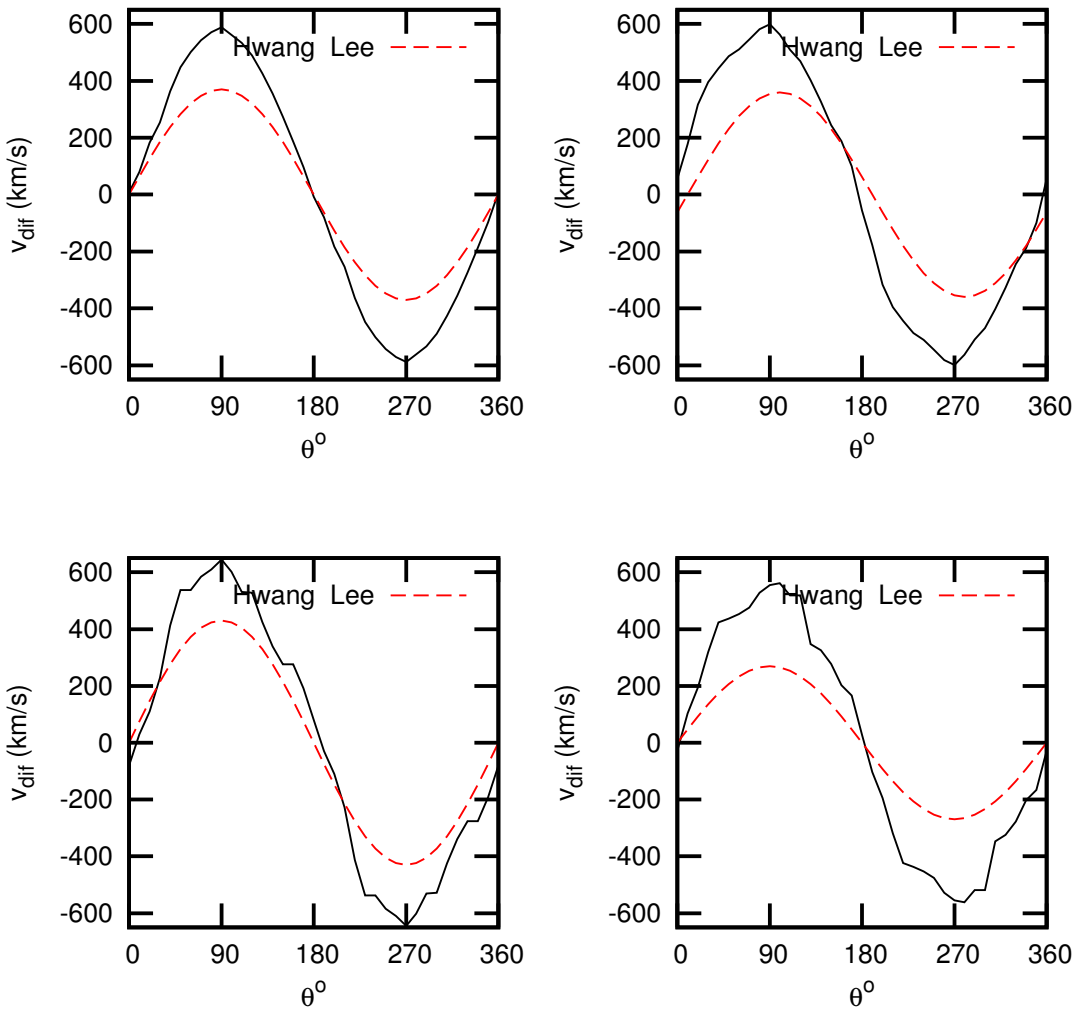

Figure 5.4 *Comparison of the rotation diagrams of our method (black continuous line) and of that of Hwang and Lee (red dashed line) for the cases of* $n_{mem} = 1000$ *(upper panels) and* $n_{mem} = 50$ *(lower panels). In the left-hand panels we present the case of a purely rotational velocity and in the right-hand panels the case of a total velocity based on the vectorial sum of the virial expectation and the rotational velocity. The input rotational velocity has a constant value of* $v_{rot} = 540$ *km/s.*

Table 5.1 *Output rotation parameters for our and Hwang and Lee methods for a Monte Carlo cluster with input parameters:* $v_{rot} = 540$ *km/s and* $\theta_{rot} = 90°$*, analysed in Fig. 5.4.*

		Our method		Hwang & Lee	
n_{mem}	Rot.model	v_{rot}	θ_{rot}	v_{rot}	θ_{rot}
1000	only rot.	589	90	370	90
1000	rot+virial	599	90	360	100
50	only rot.	645	90	430	90
50	rot+virial	562	100	270	90

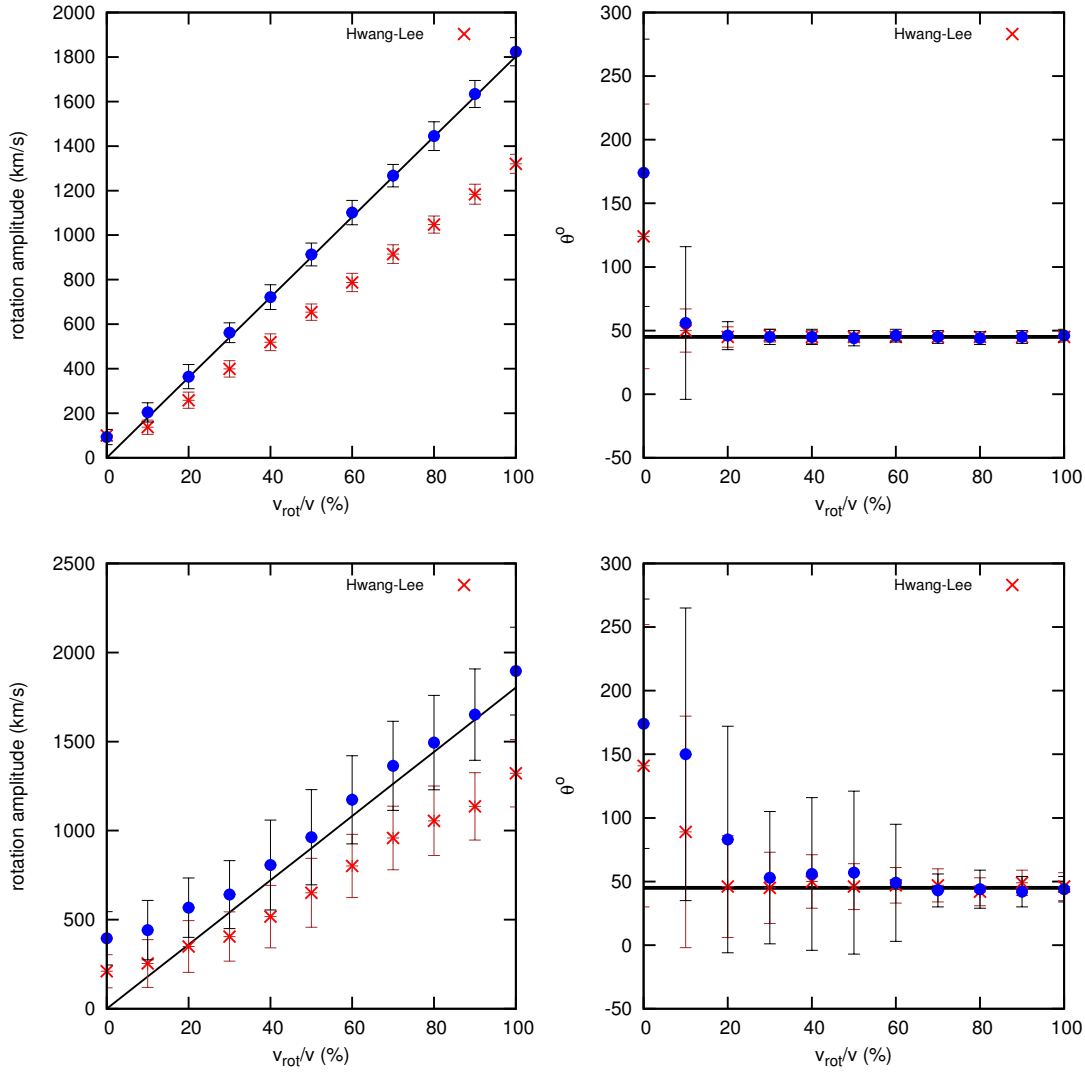

Figure 5.5 *Recovery of cluster rotational properties as a function of* v_{rot}/v_{virial}*: left-hand panels: rotation amplitude, right-hand panels: orientation of the rotation axis. The black line indicates the input rotation amplitude and orientation, while the blue and red symbols represent results of our method and Hwang and Lee (2007) method, respectively. Upper panels: for* $n_{mem} = 1000$ *and lower panels: for* $n_{mem} = 50$*.*

When we assume sparse sampling, ie., a cluster membership of 50 galaxies, which is towards the lower limit of the realistic observational cases, we verify that we can still successfully identify the cluster rotational properties but apparently with larger deviations from the input rotational parameters. To substantiate this claim we perform our next important test which is to investigate the rotation identification as a function of the cluster rotational velocity. To this end we simulate sets of 50 Monte Carlo clusters each, all with the same statistical properties, but of which the constant rotational velocity is an increasing fraction of the maximum virial one (from 0% to 100%), keeping the same rotation axis orientation ($\theta_{rot} = 45^{\circ}$). In order to investigate the convolution of systematics related to the rotation amplitude and to sampling effects, we repeat the procedure for $n_{mem} = 1000$ and 50. For each set we calculate the mean and standard deviation of the recovered rotation amplitude and of the orientation of the rotation axis. Their recovery success provides us with the range of cluster parameters for which our method can successfully identify rotation.

In Fig. 5.5 we present the mean and standard deviation of the recovered rotation amplitudes (left-hand panels) and of the orientation of the rotation axis (right-hand panels) as a function of the ratio $v_{rot}/\mathrm{MAX}[v_{virial}]$, where $\mathrm{MAX}[v_{virial}] = 1800$ km/s (see right-hand panel of Fig. 5.3). In the ideal case of very good sampling (upper panels), we see that our method correctly recovers the rotation amplitude with negligible uncertainty, except for the case of no rotational velocity where both methods will tend to detect an artificial rotational velocity of $\lesssim 80$ km/s. The already identified problem of the Hwang and Lee (2007) method, that of underestimating the rotation amplitude, is shown here as well to be true for all v_{rot}, being an increasing function v_{rot}. For the sparse sampling cases we have similar overall behaviour as in the dense-sampling cases for both methods but, as expected, a larger scatter of the resulting rotational parameter values. In addition we have a larger systematic ovserestimation of v_{rot} by our method, specially for $v_{rot}/v_{virial} \lesssim 0.2$. In general, the uncertainties in the orientation of the rotation axis are quite large for the sparse sampling case, while the Hwang and Lee method performs slightly better in recovering, on average, the correct angle of the orientation axis.

Table 5.2 *Output rotation parameters for our and Hwang and Lee methods for a Monte Carlo cluster with input parameters:* $v_{rot}(r) = 0.3 v_{virial}(r)$ *km/s and* $\theta_{rot} = 90^{\circ}$*, analysed in Fig. 5.6.*

		Our method		Hwang & Lee	
n_{mem}	Rot.model	v_{rot}	θ_{rot}	v_{rot}	θ_{rot}
1000	only rot.	450	80	280	90
1000	rot+virial	457	100	273	90
50	only rot.	421	100	256	90
50	rot+virial	499	110	430	110

5.4.2 Model (b): fractional rotational velocity of the virial one

For this case we assume a rotation velocity amplitude being a constant percentage (30%) of the virial; thus $v_{rot}(r)$ depends on the different cluster-centric distances; for example $v_{rot}(r = 1\mathrm{Mpc}) \simeq 278$ km/s. Note that for such a rotational velocity field, the output v_{rot} that will be provided by both methods presented in Section 5.3, is an integrated value that depends on the galaxy density and velocity profiles. In Fig. 5.6 we present the rotation diagrams for this case and the output rotational parameters for both methods and for both n_{mem} cases are shown in Table 5.1. Again, we see the same v_{rot} underestimation of the Hwang and Lee (2007) method, discussed in Section 5.4.1 for the case of a constant rotational velocity field, which implies that such an understimation is independent of the rotation velocity model.

The analysis of the performance of the two methods when $v_{rot}(r)$ is an increasing fraction of $v_{virial}(r)$ has provided qualitatively similar results as those of Fig. 5.5 and thus we do not present the corresponding figure.

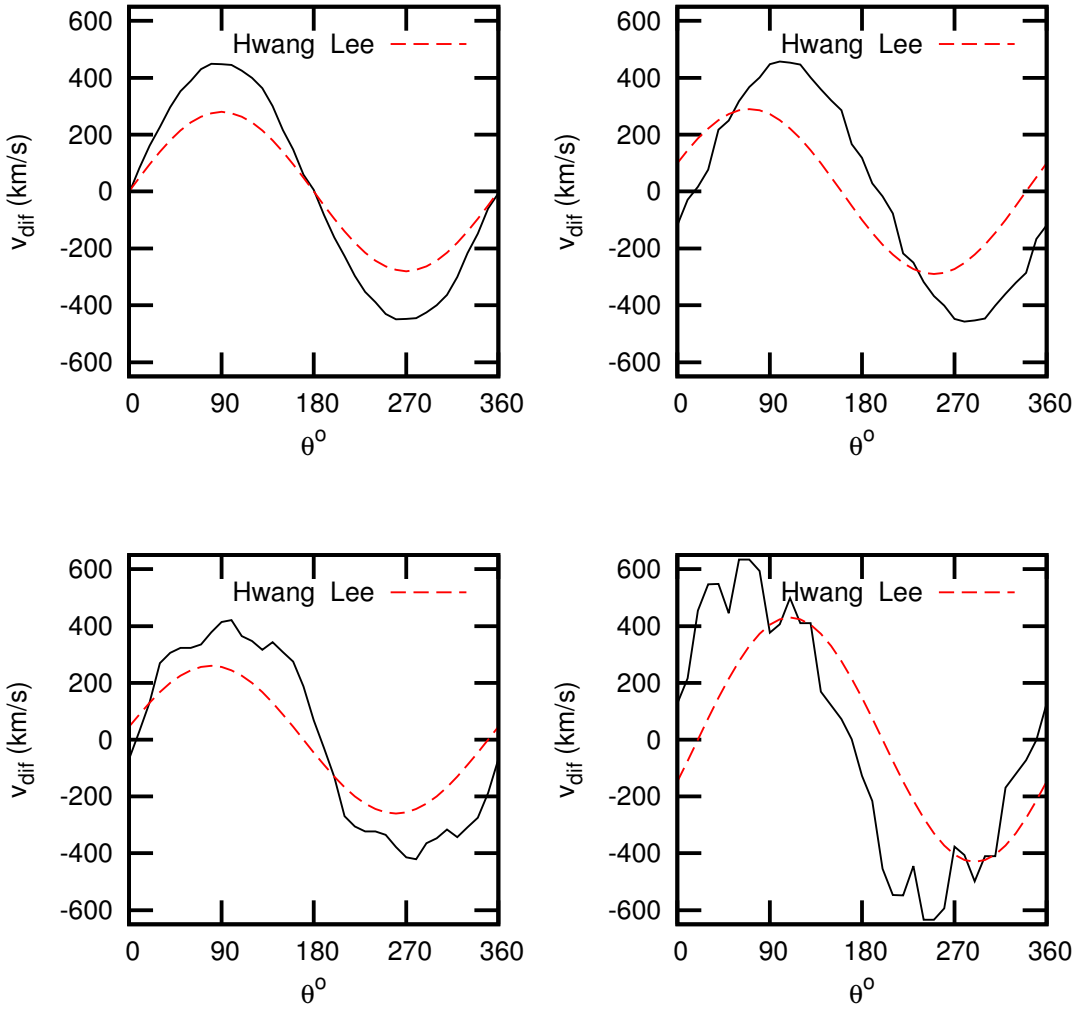

Figure 5.6 *Comparison of the rotation diagrams of our method (black continuous line) and of that of Hwang and Lee (red dashed line) for a rotation model in which $v_{rot}(r)$ is a constant fraction of the virial velocity at the different cluster-centric distance and for the cases of $n_{mem} = 1000$ (upper panels) and $n_{mem} = 50$ (lower panels). In the left-hand panels we present the case of a purely rotational velocity and in the right-hand panels the case of a total velocity based on the vectorial sum of the virial expectation and the rotational velocity.*

5.4.3 Effects of rotational axis orientations with respect to the line-of-sight

We wish to investigate the effect of different orientations of the 3D rotational axis with respect to the line-of-sight on the rotation identification by our method. In order not to mix the outcome of this test with issues related to sampling effects, we simulate a cluster with dense sampling (ie. having 1000 members). We set initially the rotation axis at a perpendicular position with respect to the line of sight and consequetively rotate the rotation axis with respect to the vertical position, so that it forms an angle ϕ with the line of sight in the interval $(0^{\circ}, 90^{\circ})$ until it is aligned with the line of sight.

We apply this procedure using the rotation model b (Section 5.4.2) and for two cases, an ideal one where we assign only the corresponding rotational velocity to each mock galaxy, and a more realistic one where we also vectorially add the corresponding randomly orientated virial velocity. The results for different values of the orientation of the rotation axis with respect to the line of sight are shown in Fig. 5.7 for both methods, ours and that of Hwang and Lee (2007). The upper panels corresponds to the ideal case while the lower panels to the more realistic one.

As expected, the rotation signal becomes weaker (the rotation amplitude decreases) as the angle ϕ increases. The counter-rotating direction of rotation is apparent due to the occurrence of the peak at $\theta_{rot} = 90^{\circ}$ (ie., because $< 180^{\circ}$). At $\phi \sim 90^{\circ}$ the rotation cannot be identified, as the rotation component of the velocity of the galaxies is perpendicular to the line of sight and thus it cannot be observed. Both methods give a flat rotation diagram in this case, as they should. We also see that the rotation amplitude in the ideal positional case ($\phi = 0^{\circ}$) is accurately recovered by our method while it is underestimated by $\sim 35\%$ when using the Hwang and Lee (2007) method. Their method, as in the ideal 2D case which is presented later, appears to have problems in recovering the correct input rotation amplitude for any value of ϕ. Furthermore, the accuracy of the recovered rotation axis angle is quite good for both methods (it decreases slightly with the increase of ϕ). Similar results we recover also

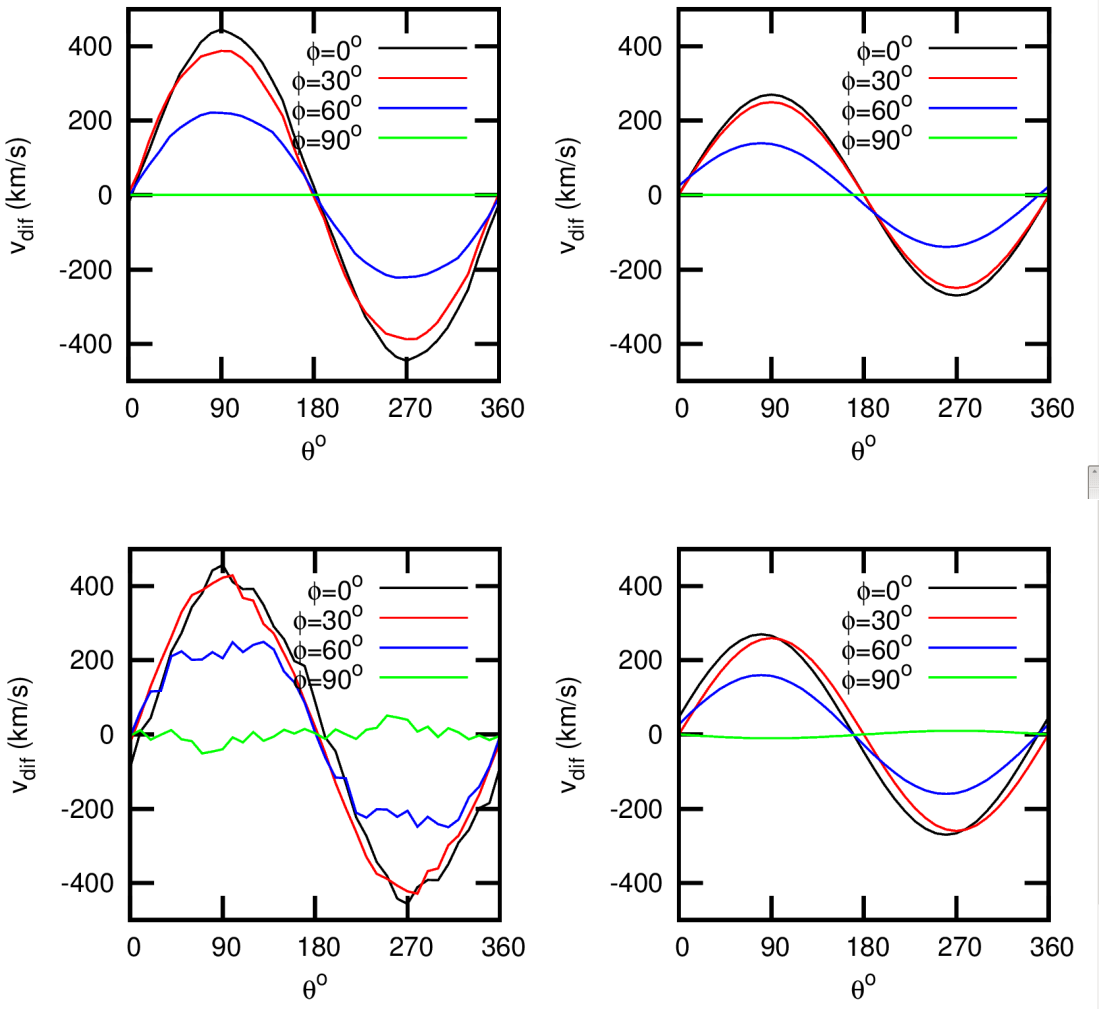

Figure 5.7 *The rotation diagram for the cluster of Fig. 5.3 with a rotational velocity 30% of the virial (which provides an integrated 3D rotational velocity of ~ 450km/s), as the rotation axis shifts from perpendicular to parallel to the line of sight, ie., $\phi \in [0°, 90°]$. Upper panels correspond to the ideal case where only rotational velocities are assigned, while lower panels correspond to the more realistic case of a 3D vectorial sum of virial and rotational velocities. Also, the left-hand panels correspond to the results of our method, while right panels to results of the Hwang and Lee (2007) method.*

in the more realistic case (lower panels), with the addition that the rotation signal becomes practically undetectable for ϕ¿60°.

Therefore, we conclude that we will miss a fraction of intrinsically rotating clusters due to axis orientation effects, even in the best case of dense sampling. If we make the reasonable assumption that the rotation axis of each cluster is randomly orientated with respect to the line of sight, the fraction of missed rotating clusters can be estimated as the ratio of the solid angle that corresponds to an angle $\delta\phi \sim 30^{\circ}$ to the solid angle of the whole sphere, ie.,

$$f_{missed} \simeq \sin^2(\delta\phi/2) \simeq 0.10$$

This should be considered a strict lower limit to the expected number of missed rotating clusters, since sparser sampling will detariorate the detectability of rotation.

5.4.4 Conclusions on the method performance

We can conclude the following from the extended Monte Carlo simulation analysis of the performance of the rotation indentification procedure that:

- On the limit of dense-sampling our method recovers very well both the input rotation amplitude and the orientation of the rotation axis, while the Hwang and Lee (2007) method although accurately identifies the rotation axis orientation, it systematically understimates the rotation amplitude by $\sim 35\%$,
- On the limit of sparse-sampling our method systematically overestimates by $\lesssim 10\%$ the input rotation amplitude. Identifying the correct orientation of the rotation axis is more demanding with typical uncertainties being as large as $\sim 50^{\circ}$. The Hwang and Lee (2007) method performs better than our method in identifying the correct axis orientation,
- One should not expect to recover correctly the rotation characteristics if the rotation velocity is $\lesssim 10 - 15\%$ of the virial velocity (ie., typically $\lesssim 200$

km/s) and the sampling of the cluster members is low (< 50 galaxies/cluster), ie., the richer the cluster the easier the rotation signal can be identified and the more accurately the rotation properties can be recovered,

- A fraction of rotating clusters will be missed due to the orientation of the rotation axis being close to the line of sight. A crude estimate indicates this fraction to be at least 10%.

5.5 Data Analysis

5.5.1 Cluster and Galaxy Data

Our original sample consists of all Abell/ACO clusters (Abell et al., 1989) of richness class $R \geq 1$ and distance class 4 or 5 that are located in the SDSS survey area and have more than 50 galaxies with SDSS DR10 spectroscopy within a rest-frame radius of 2.5 h_{70}^{-1} Mpc from the cluster centre and within a redshift separation of $\delta z = 0.01$ from the central cluster redshift (as provided by the NASA/IPAC Extragalactic Database). After excluding a few clusters that are affected by the survey borders we are left with a sample of 103 Abell clusters, presented in Table 5.3.

Note that the line of sight velocity of each galaxy is given by (Danese et al., 1980):

$$v_{los} = c \times \frac{z_{gal} - z_{cl}}{1 + z_{cl}} \ ,$$

where z_{cl} is the cluster redshift, while the cluster velocity dispersion is then provided by:

$$\sigma_v = \sqrt{\sum_{i=1}^{N} \frac{v_{los,i}^2}{N-1}} \ ,$$

where N is the total number of galaxies used in the estimation.

Table 5.3 *The Abell clusters of our sample. From left to right the columns correspond to: Abell names, redshifts, celestial coordinates, BM type and a measure of the cluster richness, provided by the number of bright* $(M > M^*)$ *members within the 1.5*h_{70}^{-1} *Mpc radius.*

Cluster	z	RA($^\circ$)	Dec($^\circ$)	BM	N_*
85	0.0551	10.408	-9.343	1	3
87	0.055	10.757	-9.793	3	7
168	0.045	18.791	0.248	2.5	10
257	0.0703	27.247	13.982	2.5	4
279	0.0797	29.093	1.061	1.5	4
426	0.0179	49.652	41.515	2.5	2
659	0.1005	126.02	19.404	-	6
690	0.0788	129.81	28.84	1	3
724	0.0933	134.575	38.573	2.5	5
727	0.0951	134.78	39.422	3	5
957	0.036	153.489	0.915	1.5	2
1024	0.0734	157.073	3.761	2	2
1035	0.0684	158.03	40.209	2.5	9
1066	0.0699	159.85	5.173	2	6
1137	0.0349	164.404	9.6156	3	4
1168	0.0906	166.859	15.913	2.5	7
1169	0.0586	167.028	43.946	3	8
1173	0.0759	167.297	41.579	2.5	2
1185	0.0325	167.699	28.678	2	7
1187	0.0749	167.915	39.578	3	5
1190	0.0751	167.943	40.845	2	4
1203	0.0751	168.489	40.294	2.5	5
1205	0.0754	168.343	2.511	2	5
1213	0.0469	169.121	29.26	3	7
1228	0.0352	170.374	34.326	2.5	8
1235	0.1042	170.733	19.626	2	5

1238	0.0733	170.742	1.092	3	6
1291	0.0527	173.019	56.024	3	2
1307	0.0832	173.2	14.524	2	6
1318	0.0578	173.993	55.033	2	8
1345	0.1095	175.295	10.689	3	2
1346	0.0975	175.293	5.689	2.5	10
1358	0.0809	175.694	8.223	2	5
1367	0.022	176.123	19.839	2.5	10
1371	0.0687	176.355	15.507	3	3
1377	0.0514	176.741	55.739	3	8
1383	0.0597	177.038	54.622	3	4
1385	0.0831	177.019	11.556	3	0
1408	0.1102	178.443	15.388	2.5	2
1424	0.0768	179.391	5.038	3	6
1436	0.0658	180.117	56.255	3	8
1474	0.0801	181.988	14.955	3	9
1516	0.0769	184.739	5.239	2.5	6
1526	0.0799	185.535	13.739	3	7
1541	0.0893	186.861	8.84	1.5	9
1552	0.0858	187.458	11.741	2	3
1650	0.0838	194.693	-1.753	1.5	5
1656	0.0231	194.953	27.981	2	15
1658	0.085	195.295	-3.436	2.5	2
1663	0.0843	195.694	-2.518	2	2
1668	0.0634	195.964	19.265	2	3
1691	0.0721	197.847	39.201	2	11
1749	0.0573	202.385	37.626	2	2
1767	0.0703	204.001	59.212	2	3
1773	0.0765	205.536	2.248	3	5
1775	0.0717	205.482	26.365	1	8
1780	0.0786	206.159	2.883	3	7

1795	0.0625	207.252	26.585	1	3
1809	0.0791	208.329	5.154	2	7
1827	0.0654	209.561	21.707	2	2
1831	0.0615	209.793	27.991	3	3
1864	0.087	212.076	5.447	2	1
1904	0.0708	215.533	48.556	2.5	7
1913	0.0528	216.716	16.676	3	12
1927	0.0948	217.759	25.663	1.5	5
1939	0.0881	219.309	24.834	2.5	4
1983	0.0436	223.183	16.746	3	5
1986	0.1185	223.289	21.913	3	3
1991	0.0587	223.626	18.631	1	6
2022	0.0578	226.082	28.423	3	6
2028	0.0777	227.388	7.527	2.5	5
2029	0.0773	227.745	5.762	1	3
2030	0.0919	227.85	-0.073	1.5	2
2034	0.113	227.555	33.528	2.5	12
2040	0.046	228.188	7.43	3	9
2048	0.0972	228.825	4.382	3	12
2061	0.0784	230.314	30.655	3	7
2062	0.1122	230.4	32.067	2	4
2063	0.0349	230.758	8.639	2	2
2065	0.0726	230.678	27.723	3	8
2067	0.0739	230.812	30.906	3	6
2069	0.116	230.991	29.891	2.5	8
2079	0.069	232.02	28.878	2.5	8
2089	0.0731	233.172	28.016	2	5
2092	0.0669	233.331	31.149	2.5	2
2107	0.0411	234.95	21.773	1	5
2122	0.0661	236.122	36.127	2.5	0
2124	0.0656	236.247	36.061	1	0

2142	0.0909	239.567	27.225	2	4
2147	0.035	240.572	15.895	3	13
2151	0.0366	241.313	17.749	3	18
2152	0.041	241.343	16.449	3	2
2175	0.0951	245.095	29.915	2	7
2197	0.0308	247.044	40.907	3	12
2199	0.0302	247.154	39.524	1	10
2244	0.0968	255.683	34.047	1.5	8
2245	0.085	255.687	33.53	2	12
2255	0.0806	258.129	64.093	2.5	9
2356	0.1161	323.938	0.123	2.5	3
2399	0.0579	329.386	-7.794	3	8
2428	0.0851	334.061	-9.35	2	3
2644	0.0693	355.291	0.094	2	3
2670	0.0762	358.543	-10.405	1.5	10

5.5.1.1 Clearing projection effects

Once we have selected our cluster sample and before we apply our rotation algorithm, we wish to clean each cluster of possible galaxy outliers and projection effects. Indeed, projected galaxies along the line of sight, but separated in velocity space would be a source of noise and could hide or erroneously enhance a rotation signal.

To this end, we plot the relative to the cluster centre galaxy velocity distribution for each cluster, which has a mean value of zero. We expect that a virialized cluster should have a roughly Gaussian frequency distribution of line-of-sight velocities (Chincarini and Rood, 1977; Halliday et al., 2004; Łokas et al., 2006). Therefore a Gaussian is fitted to the data using the usual χ^2 minimization procedure. Then, outliers are identified as those galaxies with velocities $> 3\sigma$ away from the mean, which then are not considered in the rotation analysis.

5.5.1.2 Separating substructures

Furthermore, projected groups along the line of sight, but separated in velocity space, or substructures which have coherent infall velocities towards the parent cluster centre, could provide an erroneous rotation signal. In many occasions, it is easy to identify such cases due to either the fact that in projection the substructures are clearly spatially separated from the main cluster, or in other occasions where the different subclusters are clearly separated in velocity space but may appear as a unique cluster in projection. We have carefully inspected all of our clusters and identified those with significant subclumps and each was separately analysed for rotation. As an example, we show in Fig. 5.8 the case of Abell 1228. The left-hand panel shows the projected galaxy distribution, within a radius of 2.5 h_{70}^{-1} Mpc, which appears as a typical centrally concentrated cluster, while the right-hand panel shows the relative velocity distribution which reveals three clearly separate subclumps (each separated by $\delta v \sim 1900$ km/s from the central one) projected along the line of sight. Had we analysed the whole "cluster", without separating the individual subclumps, we would have found a clear and strong signal of rotation. The two larger clumps have more than 50 members each and were separately analysed for rotation (and as we will see they do show strong rotation indications; see the Appendix).

This procedure was finally applied to the following clusters, A659, A1035, A1228, A1291, A1775, A2067, A2197, A2245, A2255 and A2152, which were found to be composed of two or more subclusters, increasing our total sample of clusters under study to 110. However, only in five we managed to perform the separation procedure effectively (A1035, A1291, A1228, A1775, and A2152), with details being presented in the Appendix[1]. The rest were tagged as being dominated by substructures and were not included in our final analysis.

Finally, one must also ask what happens if the number of substructure member

[1]We wish to note that had we not separated these clusters they would all have shown significant and strong indications of rotation, exactly due to the coherent velocity differences of the subclusters. Nevertheless, in some cases, as we will see further below, one or even both separated subclusters show true evidence of rotation.

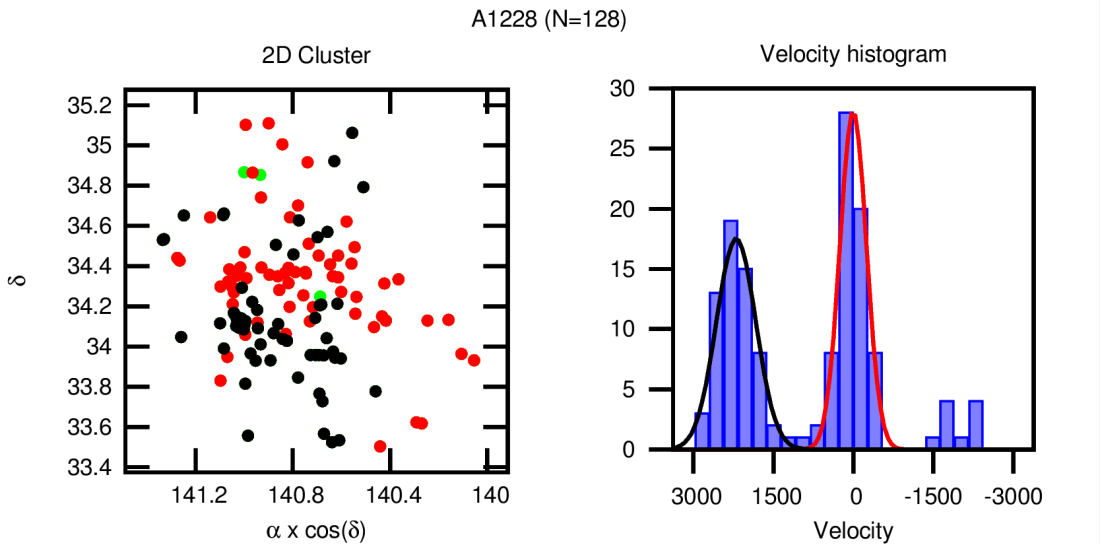

Figure 5.8 *Left-hand Panel: the projected distribution of galaxies in the A1228 cluster. Different colours indicate the galaxies belonging in the three different groups. Right-hand Panel: the relative velocity distribution of the A1228 galaxies. The colour of the fitted Gaussian is that of the corresponding members seen in the left-hand panel. The smallest group is depicted with green in the left-hand panel.*

galaxies is a relatively small fraction of the whole cluster and/or the infall velocity is not as large as to be clearly separated in velocity space. Could such non-rotating clusters be erroneously identified as rotating? In Section 5.5.3 we present extensive Monte Carlo simulations tailored to answer such a question and provide the expected fraction of false rotation detections. However, as a first step in excluding such cases, we have investigated in detail all clusters, even if their galaxy velocity distribution appears Gaussian, and we have tagged as being dominated by substructures those clusters which are spatially dispersed with no clear central core, or clusters for which we found in the literature strong and unambiguous substructure indications (eg., Einasto et al. (2012); Krause et al. (2013)). The following clusters fall in this category: A257, A1137, A1187, A1190, A1205, A1346, A1358, A1383, A1385, A1424, A1474, A1749, A1780, A1986, A2028 and A2069.

5.5.1.3 Cluster richness and mass

In order to have a more accurate determination of the cluster richness with respect to the original Abell's richness class and to investigate possible richness dependencies of our results, we calculate for each cluster the number of bright galaxies, N_*, ie. those with $M > M^*$ in the r-band (with $r \leq 17.7$), using the luminosity function of Montero-Dorta and Prada (2009) with the K and evolutionary corrections of Poggianti (1997). In order to check for obvious systematic effects we have tested whether the number of bright galaxies, N_*, correlates with the cluster redshift. No such correlation was found indicating that N_* is a redshift-free indication of the cluster richness and thus of the cluster mass.

Another indicator of the cluster mass is the cluster velocity dispersion, which is related to the mass via the virial theorem. A large velocity dispersion indicates a large cluster mass. Note however that cluster merging and significant cluster substructures can increase the measured velocity dispersion, but in this case it is not necessarily related to the cluster mass but to the highly unrelaxed cluster state.

One would expect the above two indicators of the cluster mass (velocity dispersion and richness N_*) to be correlated and indeed they have a Spearman correlation coefficient of $R_s \simeq 0.43$ with a probability of this correlation being random of $\mathcal{P} \simeq 3 \times 10^{-6}$ (velocity dispersion and richness are estimated out to 2.5 h_{70}^{-1} Mpc).

5.5.1.4 Cluster dynamical state

We also wish to investigate whether the possible cluster rotation is related to the cluster dynamical state. If, for example, the anisotropic accretion of matter along large-scale filaments entails infall with non-zero angular momentum, one may expect enhancement of rotational modes towards the cluster centre. To investigate this possibility we will use two well known indicators of the cluster dynamical state; their Bautz-Morgan (BM) type and the shape of their ICM X-ray profile.

The BM type (Bautz and Morgan, 1970) of Abell clusters is an indication of their

morphology and thus of their dynamical state. It can be numerically characterized by a value increasing from one to three (1-3) with two intermediate categories, which we index here as 1.5 and 2.5, respectively. The dynamical youth increases in the same order (or the dynamical evolution inversely), with BM type 1 indicating the most dynamically evolved cluster (spherically symmetric, centrally concentrated and cD dominated) while with BM type 3 the most loose, asymmetric and thus unrelaxed cluster.

Similarly, we will use all the available X-ray cluster images to characterize their dynamical state. We define the X-ray profile parameter, X_p, which can take three possible values, $X_p = 1$ for roughly spherically symmetric and smooth X-ray emission profiles (virialized and dynamically evolved), $X_p = 2$ for asymmetric and/or distorted profile (dynamically young) and $X_p = 0$ if the X-ray image is not available. The main source of the X-ray images used come from the *Einstein* observations (Jones and Forman, 1999). In total, we have available X-ray images for 49 out of the 110 Abell clusters of our sample.

Since both previously discussed parameters should reflect the cluster dynamical state, they should be correlated. Indeed, we find that the two parameters correlate nicely and provide a Spearman correlation coefficient of $R_s \simeq 0.53$ and a probability of this correlation being random of $\mathcal{P} \simeq 10^{-4}$.

5.5.2 Application of our algorithm

The rotation analysis is performed using galaxies within either a circular region around the cluster centre, having a radius of $1.5 h_{70}^{-1}$ or $2.5 h_{70}^{-1}$ Mpc, or within circular rings of different widths. The latter because we wish to investigate whether the cluster's possible rotation signal comes from the outskirts or the central cluster regions, but also because the central regions are affected more severely by projection effects that could contribute in weakening an existing rotation signal.

By identifying the cluster regions, if any, that show a rotational signal we may get hints

as to what is the mechanism producing it. In virialized clusters one may expect that virial relaxation would have erased any initial rotational mode. However, in oblate-like clusters [although clusters appear to be mostly prolate-like (eg., Basilakos et al., 2000; Plionis et al., 1991)] the collapse along their minor axis may retain and even enhance some initial rotation. On the other hand, if in dynamically young clusters the rotation is caused by interactions and merging, one should expect only the cluster outskirts to show more prominent rotational indications. Excluding from our analysis the cluster central regions, where projections along the line of sight are more severe, may be helpful in this respect.

Summarizing, we will investigate the cluster rotation in each cluster using four different angular configurations:

1. the circular area within 1.5h_{70}^{-1} Mpc radius;

2. the circular ring within 0.3-1.5h_{70}^{-1} Mpc;

3. the circular area within 2.5h_{70}^{-1} Mpc radius;

4. the circular ring within 0.5-2.5h_{70}^{-1} Mpc.

A further issue that could be important in identifying a rotational mode in clusters is the selection of the true rotational centre, if such exists. We therefore apply our rotation identification procedure using nine different possible centres, forming a rectangle around the nominal centre of the cluster (Fig. 5.9). The separation between the consecutive centres is usually 5% of the cluster radius (in some cases we used 10%, depending on the size of the cluster). We finally choose that centre as our optimum rotational centre for which the smooth sinusoidal "ideal rotation" curve (see Section 5.5.3) fits best the data rotation curve, ie. centre which corresponds to the minimum χ^2 value (see Fig. 5.9 for an example).

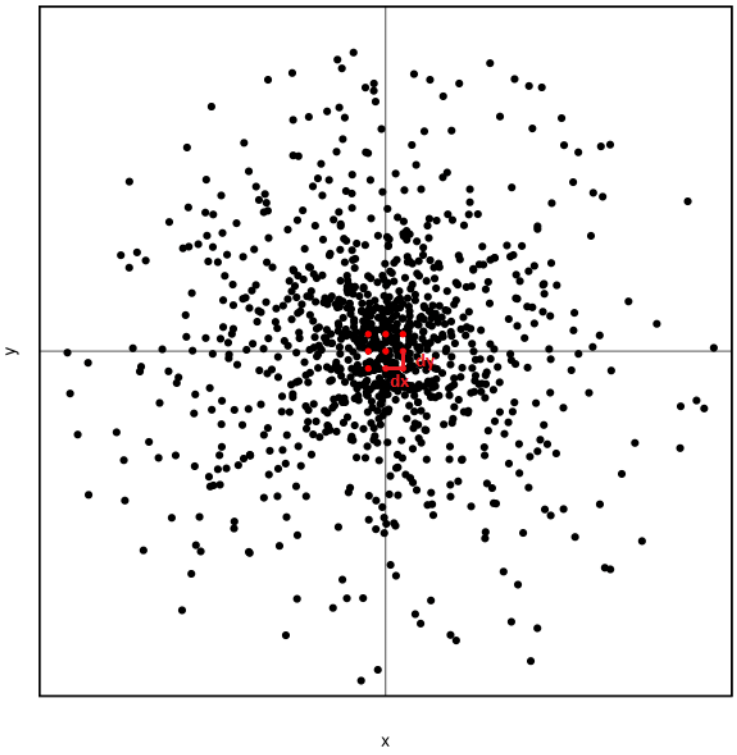

Figure 5.9 *A mock cluster with the nine different rotation centre candidates shown as red dots.*

5.5.3 Identification of significant rotation

In order to make a decision whether a cluster has a significant rotational mode or not we will use the combination of two tests, which consist of:

(a) comparing the distribution of relative velocities, in each of two hemispheres and for each rotation angle θ, using a Kolmogorov-Smirnov two-sample test, and

(b) comparing the data rotation curve separately with an "ideal rotation curve" and a "random rotation curve" suitably estimated for each cluster, by using the usual χ^2 statistic. If $v(\theta_i)$ and $v_m(\theta_i)$ are respectively the data and model mean velocity difference between the two semispheres at a rotation angle θ_i, we define:

$$\chi^2 = \sum_{\theta=0}^{360} \frac{(v_\theta - v_{m,\theta})^2}{\sigma_\theta^2 + \sigma_{m,\theta}^2} \tag{5.5}$$

with the data rotation curve uncertainty given, at each rotation angle θ, by:

$$\sigma_\theta^2 = \left(\frac{\sigma_{v,1}}{\sqrt{n_1}}\right)^2 + \left(\frac{\sigma_{v,2}}{\sqrt{n_2}}\right)^2 , \tag{5.6}$$

where $\sigma_{v,1}$ and $\sigma_{v,2}$ are the velocity dispersions and n_1 and n_2 are the number of galaxies in semicircles 1 and 2, respectively, at each rotation angle θ. The uncertainty of the model rotation curve, $\sigma_{m,\theta}$, is provided by the scatter among the different Monte Carlo realizations of the random or ideal rotation curves.

5.5.3.1 Test 1: ideal versus random rotation curves

In order to build the ideal rotation and random rotation curves we follow the following recipe: For each cluster we identify the angle at which the maximum velocity difference (MAX$[v_{dif}] \equiv v_{rot}$) is observed in its rotation diagram (θ_{rot}). This angle splits the cluster in two semispheres; and to the galaxies of each we attach a velocity $v_{los} = v_{rot}/2$ and $v_{los} = -v_{rot}/2$, respectively. We then apply our rotation identification algorithm on this new configuration to produce the "ideal rotation" diagram with which we compare the data rotation diagram, quantifying the goodness of fit by the χ^2 statistic (equation 5.5), which we name χ^2_{id}. A value of $\chi^2_{id}/df \lesssim 1$ (where df are the degrees of freedom, in our case the number of steps in θ) shows that the data rotation curve is well represented by the ideal one.

We also construct for each cluster a rotation curve which corresponds to that of a random distribution of velocity residuals. To this end, we shuffle the galaxy line-of-sight velocities randomly while keeping the same galaxy coordinates. Then, our rotation identification algorithm is applied and this process is repeated 10000 times. The final "random rotation curve", is the average over all the realizations, while the scatter $\sigma_{v_{r_i}}$ around the mean is also estimated. Finally, we determine the χ^2 statistic between the data and random rotation curves, which we tag χ^2_r.

We can now select the candidate rotational clusters as those for which

$$\chi^2_{id} \ll \chi^2_r ,$$

ie., those for which the ideal rotation curve fits the data rotation curves significantly better. If the opposite occurs then the cluster is likely not rotating. Therefore the ratio χ^2_{id}/χ^2_r is a useful parameter for assessing rotation or not.

5.5.3.2 Test 2: KS two sample test

We also apply the Kolmogorov-Smirnov two-sample test to the distributions of the relative velocities of the galaxies of the two cluster semicircles for each angle θ. This test practically calculates the probability, P_{KS}, that the two relative velocity distributions have the same parent distribution. The bigger the probability the more likely it is that the two distributions are mutually consistent. For a rotating cluster we expect a significant difference between the two velocity distribution, and the corresponding P_{KS} probability limit is taken, somehow arbitrarily, to be $P_{KS} = 0.01$ (ie., values lower than this limit are taken to signify significantly different distributions).

5.5.3.3 Final criteria for a rotating cluster

We therefore have four criteria that can be used to deduce a significant or not cluster rotation, which we call the strict criteria, and are as follows:

- χ^2_{id}/df between the real and ideal rotation curve, which should be less or equal to 1 for a rotating cluster,
- χ^2_r/df between the real rotation curve and random curve, which should be > 1 for a rotating cluster,
- χ^2_{id}/χ^2_r, which should be ideally $\ll 1$ for a rotating cluster, but practically we take it to be ≤ 0.2, and
- the Kolmogorov-Smirnov probability, P_{KS}, between the galaxy relative velocity distributions of the two semicircles of maximum difference, which should be: $P_{KS} < 0.01$.

These criteria can be relaxed to provide a less secure identification of rotation. For example, we also checked for clusters fullfilling only the following two criteria: $\chi^2_{id}/\chi^2_r < 0.4$ and $P_{KS} < 0.01$. We call these the *loose* criteria for cluster rotation.

5.5.3.4 The fraction of false detections

We wish to address the issue of what is the fraction of false detections of rotation according to the above selected criteria, when there is no intrinsic rotation present. Two such different possibilities of false detections exist:

- due to shot noise, related to small number statistics, and
- due to the presence of an unidentified substructure that has a coherent infall velocity with respect to the cluster mean, and which can be erroneously assessed as rotation. The substructures that could still remain unidentified after the procedure discussed in Section 5.5.1 are those which cannot be spatially or dynamically separated (ie., those which are near the cluster centre and which do not have a large infall velocity).

To investigate these possibilities we simulate 1000 Monte Carlo clusters, according to the basic recipe of Section 5.4 with either 50 or 100 members, which is the membership range most susceptible to rotation misidentification.

To address the first possibility we assign to the mock galaxies only virial velocities and find only a small fraction of our mock clusters showing a false rotational signal. Under the strict criteria we find a $\sim$1.9% false detection rate for clusters with either $N = 50$ or 100 members. Using the loose criteria, the corresponding fraction is $\sim$ 4.4%. These fractions are small enough to allow us to conclude that shot-noise effects are unimportant for the size of clusters considered in this work.

In order to address the second possibility, we introduce a subclump which contains between 10% and 28% of the main cluster members, positionally placed on one of the projected quadrants of the cluster at a distance of 420 h_{70}^{-1} kpc from the

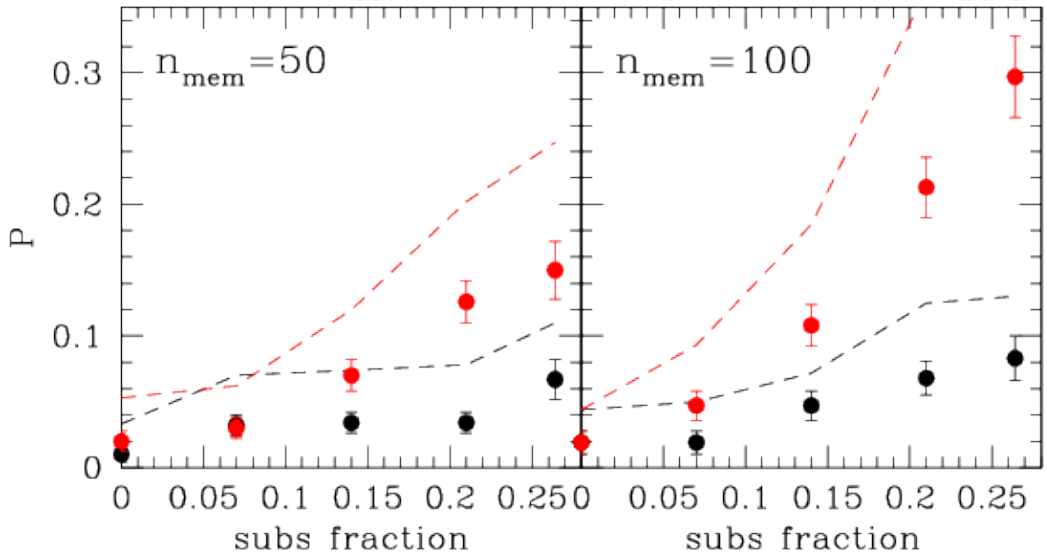

Figure 5.10 *The probability of misidentifying infalling substructures, if such exist, for cluster rotation as a function of substructure richness (in fraction of cluster members). In black we show results for the case where the infall velocity is 50% of the cluster velocity dispersion, while in red we show the corresponding results for the (more improbable) 100% case. Dots show results based on the strict criteria of rotation identification while dashed lines show results based on the corresponding loose criteria.*

cluster centre and having as a mean infall velocity a fraction (50% or 100%) of the cluster virial velocity dispersion (note that we randomly assign to each substructure member an infall velocity having the above mean and a standard deviation of 500 km/sec). The range of these parameters were selected after a number of trials in order to mimic cases where the 3σ clipping of the member velocity distribution or the clear positional identification of the substructure would have failed to identify the substructure as such. In Fig.5.10 we present the results as the probability of misidentifying an infalling substructure (with the previously discussed characteristics) for cluster rotation as a function of substructure richness (in percentage of main cluster membership). We see that for the case where such substructures exist the probability of them being misidentified as a cluster rotation is between $\sim 0.05 - 0.3$ depending on the substructure richness and infall velocity.

5.6 Results

5.6.1 Individual cluster results

Each cluster or subcluster in our sample is analysed in all four angular configurations according to the following sequence, the basic steps of which are already presented in Section 5.5.2. First, we search for the best centre of possible rotation among nine tested (a related diagram for A85 is shown in Fig. 5.11 as an example). Using the selected centre, we apply our algorithm and construct the rotational diagram of the data, the ideal rotation and that of the random velocity residuals, while we also construct the Kolmogorov-Smirnov (KS) probability curve as a function of rotation angle, θ. The results of this analysis are then passed through the criteria discussed in Section 5.5.3 to decide whether a significant rotation has been detected, at any of the angular configurations of the cluster.

In order to facilitate the visual verification of our results, we also construct for each cluster an aggregate plot with four panels, where we display:

(a) in the upper left panel the spatial distribution of the galaxies and their selected rotational centre, where residing and approaching galaxies are in red and blue colour, respectively, rejected galaxies due to velocity criteria are shown as black crosses, while rejected galaxies due to angular selection criteria as faint crosses,

(b) in the upper right panel the histogram of the line-of-sight galaxy velocities along with the fitted Gaussian,

(c) in the lower left panel the data rotation diagram (points with errorbars), the ideal rotation (red continuous curve) and random rotation curves (blue continuous curve with dashed curves corresponding to 1σ uncertainty), and

(d) in the bottom left panel the Kolmogorov-Smirnov probability diagram as a function of rotation angle θ.

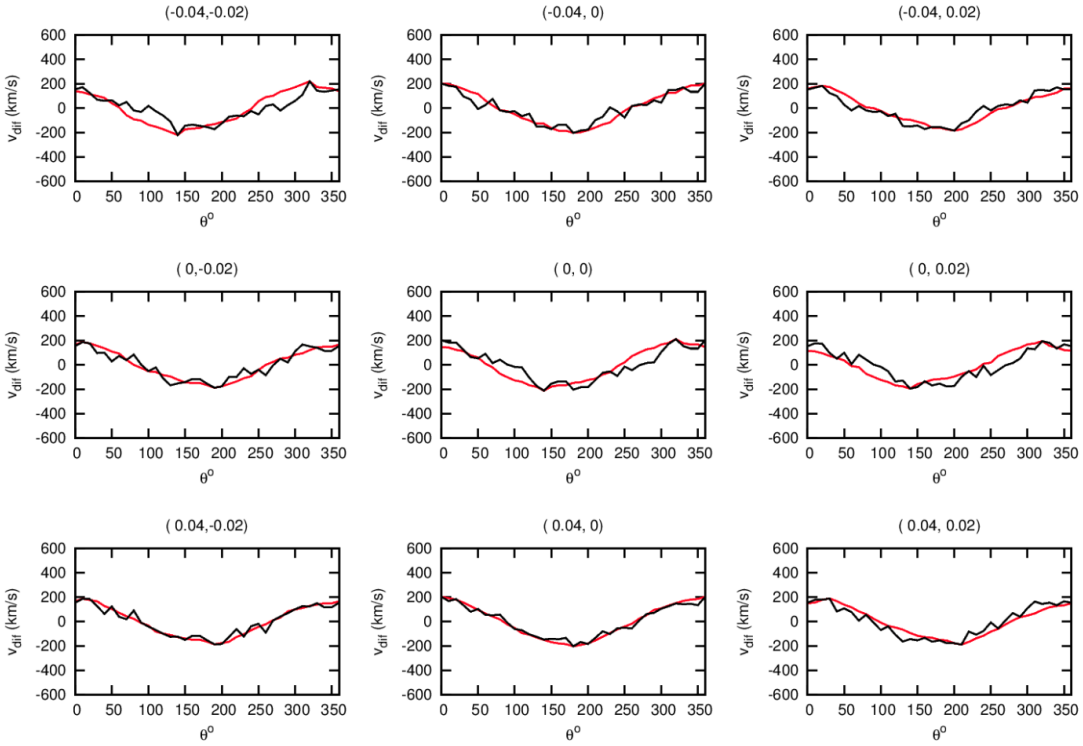

Figure 5.11 *The rotation diagrams for all the candidate rotational centres for Abell 85 ($r < 1.5h_{70}^{-1}$ Mpc). Black lines are the real rotation curves and red lines are the ideal rotation curves. Above each panel we indicate the coordinates (dy, dx) of the rotational centre. The final selected one is that with $(dy, dx) = (0.04, 0)$.*

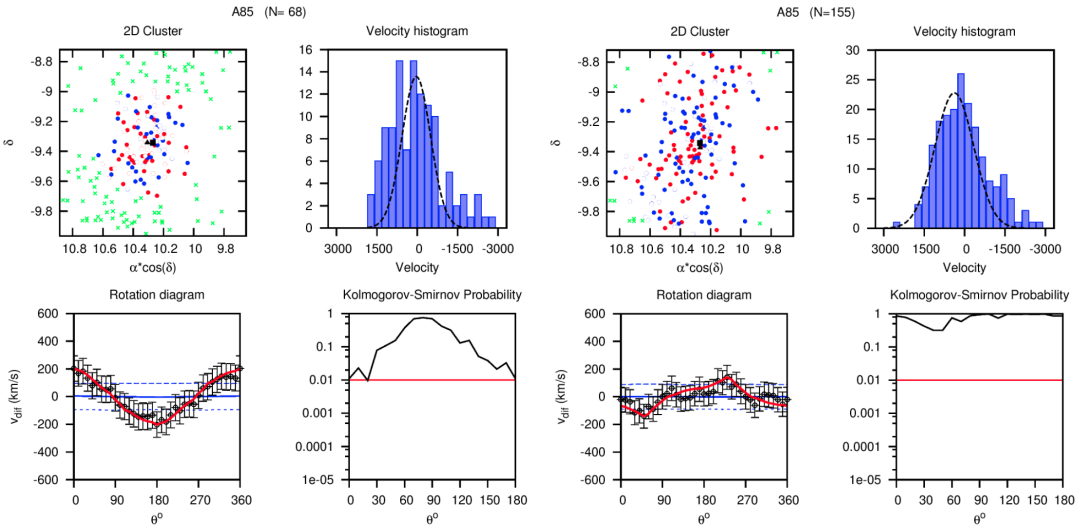

Figure 5.12 *The graphical outcome of the basic rotational diagram for Abell 85. Within a radius of 1.5 h_{70}^{-1} Mpc (left four panels) and after excluding the outliers of the velocity distribution (shown as empty points in the upper left panel), the smooth sinusoidal data rotational diagram is evident, although it falls within the loose criteria. Within the 2.5 h_{70}^{-1} Mpc (right four panels) the rotational diagram and the P_{KS} distribution are consistent with no rotation.*

We will not present such diagrams for all the clusters of our sample, except for a few examples here and some interesting cases in the Appendix. As one example, we present for A85 the corresponding plots for the two main angular configurations ($r < 1.5h_{70}^{-1}$ and $r < 2.5h_{70}^{-1}$ Mpc).

We remind the reader that A85 is a rather rich BM type 1 cluster at a redshift $\langle z \rangle = 0.055$, whose galaxy members with $m_r \lesssim 17.77$ (from SDSS DR10) vary between 68 and 155 at the two radii used. The relatively virialized nature of this cluster is confirmed by its smooth spherical X-ray profile (Jones and Forman, 1999), although there are strong indications, when one goes to much fainter galaxies, of substructures (Bravo-Alfaro et al., 2009, and references therein). However, if such substructures are manifested in the cluster velocity distribution they are already excluded by our "cleaning" procedure. Indeed there is such a case in A85, appearing in velocity space at $|\langle v \rangle| \gtrsim \pm 1400$ km/sec (see the left velocity histogram in Fig. 5.12).

In Fig. 5.12 we present the basic results of our analysis for the two cluster radii. Although for the $r = 1.5h_{70}^{-1}$ Mpc case there is a smooth sinusoidal rotation curve,

exactly what expected for the ideal rotation (red curve), this cluster misses complying with the strict criteria of rotation, due to $\chi_r^2 < 1$. However, it complies with the loose criteria and thus it is considered as possibly rotating (but with a relatively low rotational velocity amplitude). When considering the larger cluster radius (right four panels of Fig. 5.12) we see that the indications of rotation vanish, a fact which could be due to small substructures acting as noise or due to a possibly different velocity distribution of the outskirt galaxies with respect to the inner ones; if for example they are infalling roughly isotropically to the cluster centre from the large-scale surrounding structure.

To complete the presentation of some characteristic examples, we show in Fig. 5.13 the relevant results for A1367, a rich and relatively nearby cluster ($z = 0.022$). After excluding the outliers of the Gaussian fit to the galaxy velocity distribution (the galaxies at < 1300 km/sec - see Fig. 5.13), we obtain what appears to be a strongly rotating cluster showing a significant and unambiguous sinusoidal rotation diagram (in all four radial configurations). Although this cluster is known to show significant substructures in its central regions (Cortese et al., 2004), we find even stronger rotational signals when excluding the central 0.3 or $0.5h^{-1}$ Mpc region, an indication that although there are substructures, there is also rotation not necessarily attributed to coherent substructure velocity differences.

5.6.2 Abell clusters with rotation

Clusters for which we detect significant rotation, using either the strict or the loose criteria of rotation detection, and which have not been tagged as being dominated by substrutures (see Section 5.5.1) are presented in Table 5.4 (for the $r = 1.5h_{70}^{-1}$ Mpc case), and Table 5.5 (for the $r = 2.5h_{70}^{-1}$ Mpc case). In each table we also indicate clusters that show rotation only when excluding the inner cluster core (those with the star symbol), since projection effects are more severe along the central part of clusters, where typically a larger volume along the line of sight direction is sampled. The tables list the final number of galaxy cluster members selected, their

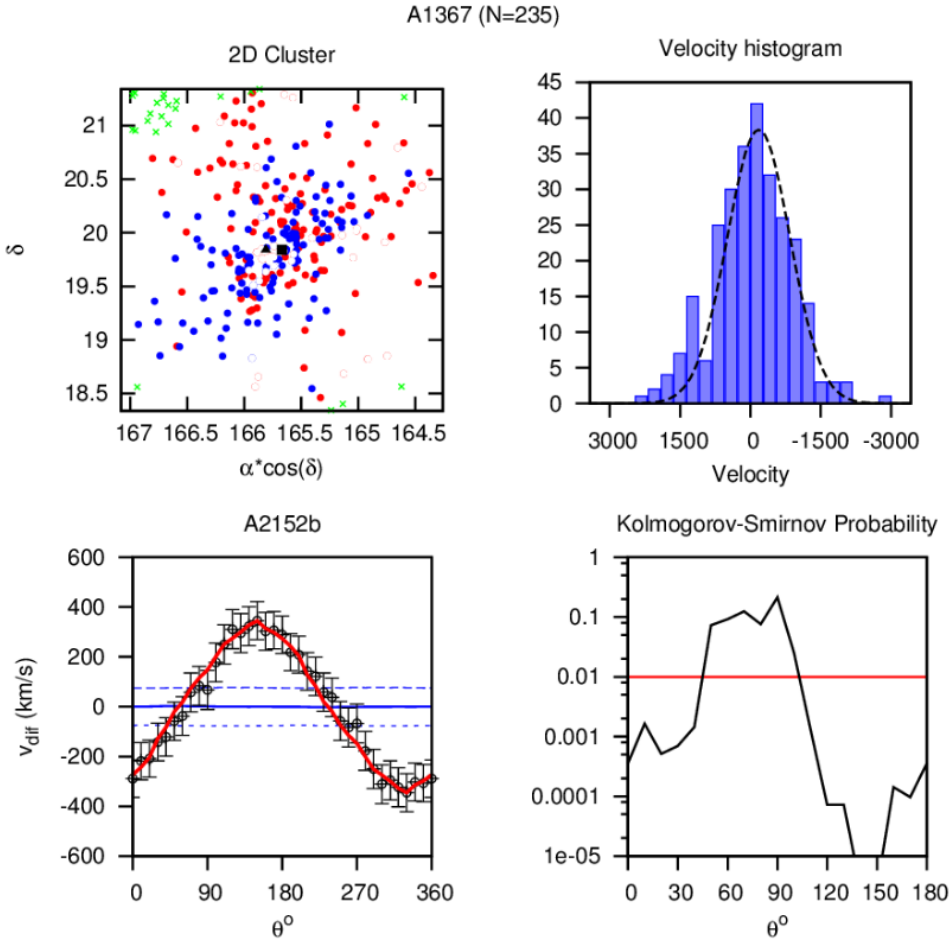

Figure 5.13 *The graphical outcome of the basic rotational diagram for Abell 1367 within a radius of 2.5 h_{70}^{-1} Mpc. The excluded (velocity) outliers (corresponding to known substructures) can be observed as empty circles in the upper left panel. Based on the remaining galaxies, a clear and significant sinusoidal rotational diagram is evident.*

mean redshift, the values of the four rotation indices discussed in Section 5.5.3, the angle θ_{rot} of the rotation axis, which is the angle of the maximum semicircle mean velocity difference, the rotation amplitude, v_{rot}, which the maximum velocity difference in the rotation diagram, the cluster velocity dispersion, σ_v, and the (crudely) corrected velocity dispersion after removing the cluster rotation (see Section 5.6.3).

5.6.2.1 Effect of excluding the cluster core region

Of the 14 clusters within $r = 1.5h_{70}^{-1}$ Mpc showing rotation under the strict criteria, two were detected only after excluding the inner $< 0.3h^{-1}$ Mpc core region (A2199, A2399), while only one cluster (A1913) is downgraded into the loose criteria rotation detection regime when excluding its inner core.

For the $r = 2.5h_{70}^{-1}$ Mpc case, out of the 19 clusters showing rotation under the strict criteria, 7 were detected only after excluding the inner $< 0.5h_{70}^{-1}$ Mpc core region. However, of these clusters four (A1913, A2089, A2147, and A2670) had originally been found rotating under the loose criteria. The only clusters found rotating under the strict criteria that lose completely their rotation when excluding the core region are: A426, A1228a and A1827. Other two clusters rotating under the strict criteria drop below the $n_{mem} = 50$ limit, when excluding their core region, but retain their significant rotation detection (A1035a, A1291a). Similarly, out of the remaining five clusters with rotation under the loose criteria (excluding the four that were upgraded to the strict regime when excluding the core region), one (A1238) was detected only when the core region was excluded. Finally, A1552 loses completely its rotation when excluding the core region.

5.6.3 Statistical results

In order to attempt to understand our results and possible causes of the cluster rotation, we will attempt to identify correlations between interesting cluster properties and rotation. To this end, we will use the Spearman correlation coefficient, R_s,

Table 5.4 *The clusters with significant rotation within $r = 1.5h_{70}^{-1}$ Mpc and with $n_{mem} \geq 50$, using either the strict or loose criteria of rotation detection. The first column is the Abell name of the cluster, the second is the mean redshift of the members, the third is the number of members used, the fourth is the orientation on the plane of the sky of the rotation axis, the fifth is the rotation amplitude with its uncertainty, the sixth and seventh are the coordinates of the chosen rotation centre, the eighth is the minimum value of the Kolmogorov-Smirnov probability, the next three columns are χ^2_{id}, χ^2_r, χ^2_{id}/χ^2_r, respectively, the twelfth is an indication for the direction of rotation (1 meaning clockwise and 2 anticlockwise). The last two columns correspond to the initial and corrected, for rotation, cluster velocity dispersion. Clusters that show significant rotation only when excluding the inner cluster core ($< 0.3h_{70}^{-1}$ Mpc) are indicated with an asterisk.*

Cluster	z	n_{mem}	$\theta_{rot}(^\circ)$	v_{rot}/km s^{-1}	α_{cent}	δ_{cent}	P_{KS}	χ^2_{id}/df	χ^2_r/df	χ^2_{id}/χ^2_r	$\mathcal{I}$	σ_v(km s^{-1})	$\sigma_{v,cor}$(km s^{-1})
Strict Criteria													
426	0.01729	136	10	498±128	37.178285	41.459958	0.000091	0.586	3.118	0.188	2	774	650
1035a	0.06803	54	90	420±168	120.755407	40.185375	0.002970	0.168	1.862	0.09	2	566	461
1169	0.05859	66	110	473±134	120.234036	43.96349	0.000668	0.087	1.542	0.056	2	528	410
1367	0.02124	177	130	271±90	165.754521	19.839167	0.005253	0.099	1.875	0.053	2	607	539
1913	0.05303	102	40	348±108	207.638535	16.695574	0.001095	0.308	2.441	0.126	2	565	478
2022	0.0581	51	90	362±107	198.830016	28.458548	0.003460	0.117	1.603	0.073	2	403	311
2061	0.07878	74	230	218±88	198.151902	30.641212	0.003008	0.129	1.21	0.107	1	379	325
2063	0.03457	102	140	441±149	228.196482	8.610653	0.005917	0.174	1.114	0.156	2	754	644
2107	0.04127	111	160	403±117	218.143467	21.797129	0.001450	0.294	2.044	0.144	2	621	520
2147	0.03573	223	130	303±102	231.317855	15.866537	0.000058	0.240	1.586	0.151	2	740	664
2151	0.03665	175	250	514±93	229.879249	17.721073	0.000001	0.138	5.528	0.025	1	613	484
2152	0.04442	85	140	286±76	231.466136	16.473324	0.000424	0.031	3.878	0.008	2	359	287
2199*	0.03042	172	100	363±113	190.591969	39.524444	0.007317	0.178	1.934	0.092	2	730	639
2399*	0.05743	68	280	333±108	326.378018	-7.776588	0.000330	0.287	1.74	0.165	1	443	360
Loose Criteria													
85	0.05518	68	0	214 ±97	10.306381	-9.3425	0.009683	0.062	0.807	0.077	2	415	362
1377	0.05194	62	110	429±166	99.476699	55.738889	0.000445	0.335	0.912	0.367	2	647	540
2670	0.07608	91	250	394±170	352.6738	-10.405	0.005093	0.157	0.872	0.18	1	792	693
1203*	0.07514	59	300	299±117	128.491013	40.294167	0.002565	0.048	0.91	0.053	1	442	368

Table 5.5 *As in Table 5.4 but for clusters with significant rotation within $r = 2.5h_{70}^{-1}$ Mpc. Clusters that show significant rotation only when excluding the inner cluster core ($< 0.5h_{70}^{-1}$) are indicated with an asterisk.*

Cluster	z	n_{mem}	$\theta_{rot}(^\circ)$	v_{rot}/km s^{-1}	α_{cent}	δ_{cent}	P_{KS}	χ^2_{id}/df	χ^2_r/df	χ^2_{id}/χ^2_r	$\mathcal{I}$	σ_v(km s^{-1})	$\sigma_{v,cor}$(km s^{-1})
Strict Criteria													
426	0.01722	155	20	405±122	37.315636	41.423283	0.007321	0.249	2.045	0.122	2	770	669
1035a	0.06803	56	120	406±166	120.766955	40.185843	0.009703	0.283	1.885	0.15	2	559	458
1228a	0.03521	65	70	157±53	140.673644	34.373472	0.006379	0.124	1.809	0.068	2	219	180
1228b	0.04253	60	10	335±94	141.249465	34.190492	0.000019	0.411	3.077	0.133	2	322	239
1291a	0.05087	50	30	382±103	96.411645	56.134474	0.000322	0.125	3.89	0.032	2	416	321
1367	0.02148	237	150	354±75	165.810952	19.839167	0.000002	0.217	4.802	0.045	2	582	493
1827	0.06516	50	300	190±93	194.65102	21.707222	0.001018	0.119	1.152	0.103	1	315	268
2065	0.07224	170	70	712±176	204.198262	27.74665	0.000019	0.125	2.518	0.049	2	1166	988
2151	0.03668	276	220	432±70	229.739375	17.748611	0	0.877	9.896	0.089	1	594	486
2199	0.03057	344	80	325±77	190.728415	39.634998	0.000245	0.094	3.237	0.029	2	712	631
2399	0.05754	103	250	201±85	326.401605	-7.764684	0.008962	0.177	1.134	0.156	1	428	378
2152	0.04408	122	170	320±62	231.474846	16.403915	0.000095	0.379	6.029	0.063	2	374	294
1185*	0.03362	140	330	292±89	147.127123	28.729761	0.001011	0.358	2.024	0.177	1	500	427
1775a*	0.07523	57	160	308±112	184.073873	26.433694	0.00341	0.264	1.733	0.152	2	439	362
1913*	0.05277	119	30	407±94	207.663393	16.708548	0.000142	0.745	4.214	0.177	2	536	435
2022*	0.05798	53	50	423±103	198.830016	28.452586	0.000243	0.073	2.084	0.035	2	379	273
2089*	0.07377	59	180	316±107	205.849001	28.039546	0.00044	0.064	1.136	0.056	1	431	352
2147*	0.03624	327	230	304±95	231.281004	15.847379	0.000106	0.155	1.844	0.084	1	837	761
2670*	0.07598	94	250	376±153	352.691984	-10.42811	0.008033	0.178	1.441	0.124	1	670	595
Loose Criteria													
1169	0.05887	83	120	248±147	120.30184	43.916405	0.009778	0.077	0.339	0.228	2	537	475
1203	0.07527	89	300	244±92	128.476726	40.270752	0.00059	0.093	0.914	0.102	1	441	380
1552	0.08611	104	200	261±125	183.577159	11.740556	0.002124	0.14	0.663	0.211	1	642	577
1809	0.07911	88	170	272±102	207.530865	5.131838	0.002476	0.127	0.696	0.182	2	471	403
1238*	0.07392	70	210	225±115	170.662776	1.068283	0.003468	0.173	0.82	0.212	1	487	431

between any two parameters and the probability, $\mathcal{P}$, that the correlations are consistent with the random expectation. Positive R_s means positive correlation, while negative R_s means anticorrelation; a value near zero means the two parameters are not correlated. A small value of $\mathcal{P}$ indicates a significant correlation or anticorrelation at that level. We will report only relatively strong and relatively significant correlations, and as such we define: $|R_s| > 0.3$ and $\mathcal{P} < 0.05$.

A first observation is that all the indices that we use to deduce rotation are correlated strongly among themselves, as can be seen in Fig. 5.14, where we plot only clusters that have not been excluded from the analysis due to strong substructuring (see Section 5.5.1). The value of the Kolmogorov-Smirnov probability, P_{KS}, and the value of the ratio of the χ^2 minimium values between the ideal and real rotation diagrams are strongly correlated with each other in all angular configurations. For example, for the $r = 1.5h^{-1}$ Mpc case we obtain $R_s = 0.75$ and $\mathcal{P} < 10^{-10}$. Also the amplitude of the rotation, v_{rot}, is strongly correlated with both rotation indices with R_s & 0.6 and $\mathcal{P} < 10^{-9}$. This also should be expected since when the rotational velocity is large, the rotation will be more clearly identified, and vice-versa.

5.6.3.1 Check for systematic biases of the rotation indices

Before we present our main results it is important to make sure that we understand the possible systematic effects of the resulting rotation indices for the clusters studied. We have already investigated and quantified the effect of shot-noise and undetected substructures (Section 5.5.3), however, we further check for correlation of the resulting rotation indices on the number of galaxy members, n_{mem}, and on z. As we already showed, n_{mem} needs to be relatively large in order to unambiguously detect a rotation if such exist. However, since the input galaxy catalogue (the SDSS DR10 spectroscopic catalogue) is limited to $m_r \sim 17.77$, when we look at larger distances we observe less and brighter galaxy cluster members. Therefore, there will be an unavoidable redshift dependence of the cluster galaxy membership and thus a redshift dependence of the rotation indices is possible. This does not necessarily

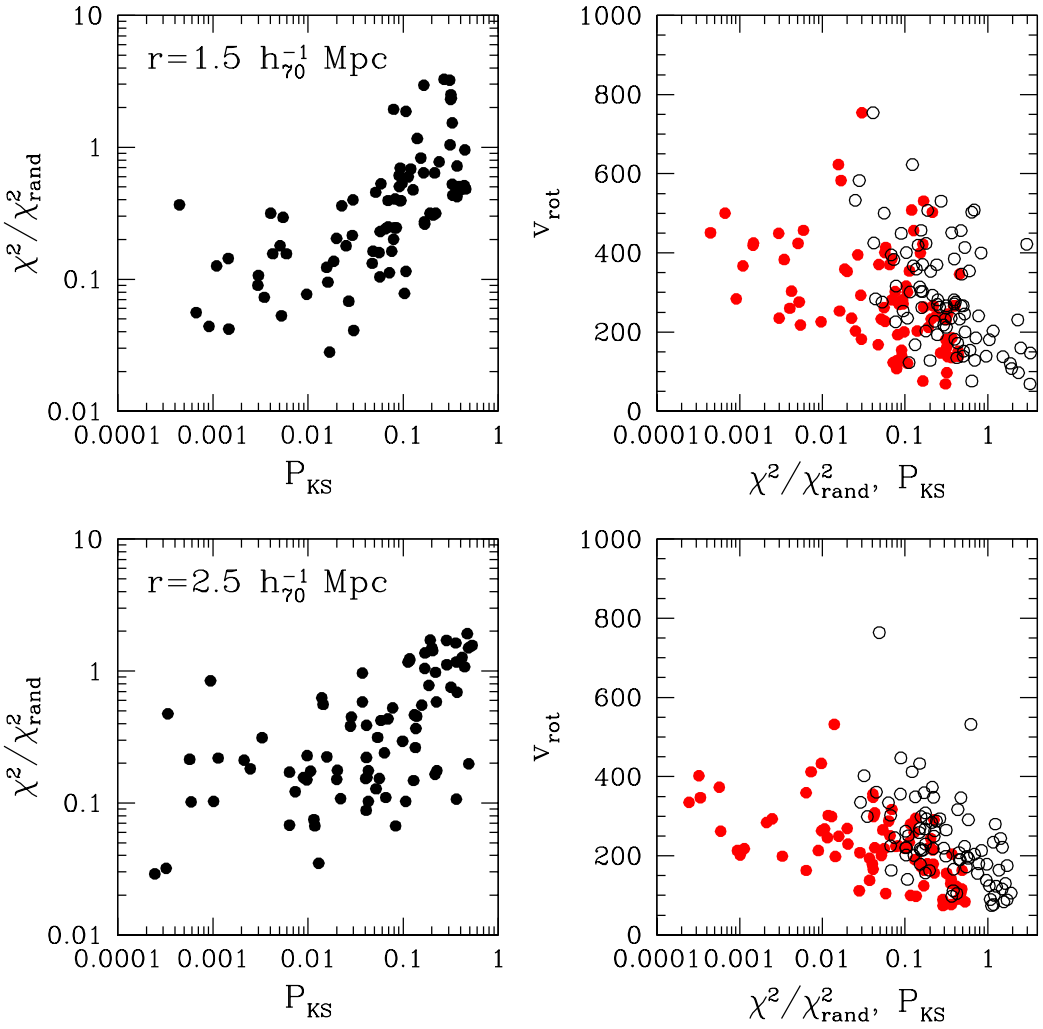

Figure 5.14 *Left-hand Panels: the scatter diagram between the two rotation indices (upper for the $r = 1.5h_{70}^{-1}$ Mpc case and lower for the $r = 2.5h_{70}^{-1}$ Mpc case). Right-hand Panels: The rotation amplitude, v_{rot}, as a function of the Kolmogorov-Smirnov probability (red filled symbols) and as a function of the χ^2_{min} ratio value (empty black symbols).*

imply an important problem but rather that the fraction of rotating clusters found should be considered a lower limit.

In any case, we have tested for such a dependence for the $n_{mem} \geq 50$ case and we find weak and marginally significant correlations, in any case below the limit we set in Section 5.6.2. Only in the case of the Kolmogorov-Smirnov test, which due to its nature a dependence of P_{KS} on n_{mem} is expected and, since the latter is anticorrelated with z (as discussed previously), we expect a correlation of P_{KS} with z. Indeed we find such a weak but relatively significant dependence ($R_s = 0.33$ and $\mathcal{P} \simeq 0.013$) for the $r = 1.5h_{70}^{-1}$ Mpc and $n_{mem} \geq 50$ case. For the $r = 2.5h_{70}^{-1}$ Mpc case the above correlation becomes weaker.

5.6.3.2 Fraction of rotating clusters

In this Section we present some basic statistics regarding the fraction of clusters that show indications of rotation, based on both strict and loose rotation criteria, as defined in the previous section. In Table 5.6 we present the number of clusters and the corresponding fraction of the total that show strict or loose indications of rotation for clusters with $n_{mem} \geq 50$, for which the rotation identification is quite secure. The fractions are slightly different when limiting the studied area within 1.5 or 2.5 h_{70}^{-1} Mpc of the cluster centre, with the latter being slightly smaller than the former. We also present the final overall number of unique clusters rotating using any of the four spatial configurations, as discussed below.

Overall, it is secure to say that Abell clusters with $n_{mem} \geq 50$ showing significant indications of rotation, within either of the two limiting radii, range between $\sim 25\%$ (for the strict criteria) and $\sim 32\%$ (for the loose criteria) of the total.

It should be noted however, that the specific clusters showing rotation at the different radii are not always the same. In particular, out of the 18 rotating clusters of Table 5.4, five are missed when using $r = 2.5h_{70}^{-1}$ Mpc. Also, quite a few more clusters appear to be rotating when we extend our analysis to $r = 2.5h_{70}^{-1}$ Mpc than within $r = 1.5h_{70}^{-1}$ Mpc. In particular, out of the 24 clusters listed in Table 5.5 only 13 are

Table 5.6 *Fraction of clusters showing rotation under the strict and loose criteria, for the analysed clusters with ≥ 50 members (which are less prone to random errors). The final, corrected for the expected number of false detections according to our simulations, fraction of rotating clusters is also listed.*

Radius/h_{70}^{-1}Mpc	N_{clus}	Strict	Loose
1.5	56	14 (25%)	18 (32%)
2.5	86	19 (22%)	24 (28%)
Overall	86	23 (27%)	29 (34%)
Corrected	86	23%	28%

found rotating within $r = 1.5h_{70}^{-1}$ Mpc, taking also into account one that drops below the $n_{mem} = 50$ limit.

We can reach an overall number, and the corresponding final fraction of rotating clusters with $n_{mem} \geq 50$ at any of the two radii and taking also into account results based on excluding the core region. Using the strict criteria we find 23 such clusters, corresponding to $\sim 27\%$ of the total (86), while using the loose criteria we find 29 such clusters, corresponding to $\sim 34\%$ of total.

5.6.3.3 Fraction of clockwise and anticlockwise rotating clusters

As we discussed in Section 5.3.1 our algorithm provides us with the direction of rotation for the rotating clusters. What is expected in an initially irrotational Universe on large-scales is the lack of a preferred direction of cluster rotation. In Tables 5.4 and 5.5 we present the direction of rotation for each of our rotating clusters, indicated by the symbol $\mathcal{I}$ which takes the value 1 for rotation or 2 for counter rotation. Using only the results based on the strict criteria, we obtain for the $r = 1.5h_{70}^{-1}$ Mpc case 11 anticlockwise and only 3 clockwise rotating clusters, while for the $r = 2.5h_{70}^{-1}$ Mpc case we have 12 and 7, respectively. There appears to be a slight preference for clockwise rotating clusters, but what is the significance of the number difference, $\Delta = 8$ for the former case and $\Delta = 5$ for the latter case? The Poisson uncertainty of Δ is $\sigma_{\Delta} \simeq 3.7$ and 4.4 for the two cases, respectively, a fact which implies that

the difference is significant only at a 2.1σ and 1.1σ level, respectively. We do not consider as overwhelming the former significance and we conclude that there is no significant evidence for a preferred direction of rotation among the rotating clusters.

5.6.3.4 Correcting the cluster velocity dispersion for rotation

In order to correct the cluster velocity dispersion, assumed to be due to roughly isotropic galaxy orbits, for the rotational modes, we assume that the two velocity components are independent and that the expected cluster velocity dispersion due to the rotational velocity v_{rot} can be approximated, assuming an ideal rotation, as:

$$\sigma_{rot}^2 \simeq 2 \times \left(\frac{v_{rot}}{2}\right)^2 \ . \tag{5.7}$$

Therefore, the corrected cluster velocity dispersion, $\sigma_{v,cor}$, is approximately provided by the following:

$$\sigma_{v,cor}^2 \simeq \sigma_{v,raw}^2 - \sigma_{rot}^2 = \sigma_{v,raw}^2 - \frac{v_{rot}^2}{2} \ . \tag{5.8}$$

For the majority of the rotating clusters, the corrected velocity dispersion is not dramatically altered, but the correction is not insignificant. Defining the fractional difference between corrected and uncorrected cluster velocity dispersion as

$$\delta\sigma_v = \frac{\sigma_{v,raw} - \sigma_{v,cor}}{\sigma_{v,raw}}$$

we obtain for the $r = 1.5h_{70}^{-1}$ Mpc case a median value of ∼10%, and a mean value of $\langle\delta\sigma_v\rangle \sim 12\%$. A similar analysis for cluster rotation out to $r = 2.5h_{70}^{-1}$ Mpc provides the following fractional differences: a median value of ∼12%, and a mean value of $\langle\delta\sigma_v\rangle \sim 15\%$. The corresponding corrected cluster mass is given by:

$$M_{cor} \simeq M_{raw}(1 - \delta\sigma_v)^2 \ ,$$

implying a corrected cluster mass reduced by 20% - 30% on average, with respect to that uncorrected for rotation.

5.6.3.5 Correlations between cluster rotation and cluster physical parameters

We attempt to investigate whether there are correlations between the rotation indices and the different physical properties of the clusters, dynamical or other. We correlate the two main rotation indices, ie., χ^2_{id}/χ^2_r and P_{KS} with the characteristics of the cluster dynamical state, ie., BM type and X_r (defined in Section 5.5.1), and with the cluster mass, characterized either by the number of bright galaxies, N_*, or by the cluster velocity dispersion, σ_v (defined in Section 5.5.1).

For both radii we find no significant correlations between cluster mass or cluster dynamical state and rotation indices. However, since the majority of clusters do not show signs of rotation they would act as noise weakening possible correlations between rotation and cluster parameters for those clusters that show significant indications of rotation. Indeed, selecting only the latter clusters we find relatively significant correlations but only between the strength and significance of rotation and the cluster dynamical state (not with cluster mass), in the direction of a correlation between rotation strength and dynamical youth (see Table 5.7).When we analyse clusters that show rotation for the $r = 2.5h_{70}^{-1}$ Mpc case, we find correlations only between BM or X_s and P_{KS}, ie., not with the prime indicator of rotation (χ^2_{id}/chi^2_{ran}), but only with the significance of the semicircle velocity difference.

We can conclude that there are indications that the cluster rotation is related to the earlier phases of cluster virialization but after the initial anisotropic accretion and merging has taken place (since we have excluded all clusters showing significant substructure in projected or velocity space).

Table 5.7 *Spearman's correlation coefficient and the probability that the detected correlation is consistent with the random expectation for the indicated pairs of parameters using rotating, under trict rotation criteria, clusters with* $n_{mem} \geq 30$.

	$r = 1.5h^{-1}$ Mpc			$r = 2.5h^{-1}$ Mpc	
	BM-P_{ks}	BM-χ^2_{id}/χ^2_r	$X_s - \chi^2_{id}/\chi^2_r$	BM-P_{ks}	$X_s - P_{ks}$
N	15	15	12	20	15
R_s	-0.49	-0.44	-0.62	-0.41	-0.52
$\mathcal{P}$	0.062	0.096	0.033	0.076	0.045

5.7 MUSIC clusters' rotation

5.7.1 Motivation

The rotation of the MUSIC[2] clusters (Sembolini et al., 2013) ICM was studied in Baldi et al. (2017) through the angular momentum, tangential and random velocity of the gas. The cluster sample, the MUSIC-2 clusters (see Section 5.7.2) were further selected to be relaxed in all the three flavours (NR, CSF, AGN) in order to avoid contamination in the rotation signal from merging clusters or clusters with large substructures, leaving the numbers of clusters in the sample to 146. Their spin parameter was calculated in order to classify them as rotating or not. A high threshold of spin value ensured a strong rotation signal in the rotating clusters. 4% of these clusters were found to be rotating in a model which is a modification of the circular velocity profile derived from the NFW dark matter density distribution, a non-solid body rotation model. For 40% of these clusters, the spin of the gas and dark matter are correlated in direction and modulus, showing a co-rotation of the two constituents.

This result is contradictory to the 23-25% of the 103 relaxed Abell clusters that were found to be rotating. This contradiction has raised questions about the nature and origin of the rotation in galaxy clusters and, therefore, whether galaxies co-rotate together with the ICM and dark matter. The discrepant percentages found could be an outcome of the different rotation identification method used in the two studies, the

[2] music.ft.uam.es

different selection and cluster identification in the two samples or it could be a hint of an internal difference that exists in the rotational motion of the clusters constituents.

This Section aims to answer the above questions and to discover more about the internal dynamics of galaxy clusters by studying the galaxies, gas and dark matter. The following work is a collaboration with the authors of Baldi et al. (2017), who provided the MUSIC cluster data. We will start with describing the MUSIC clusters selection, the comparison of the results of the two different methods, the Baldi et al. (B17 hereafter; 2017) and Manolopoulou and Plionis (MP17 hereafter; 2017), on an individual MUSIC cluster and we will finish with the study of the rotation of the galaxies of all MUSIC clusters using the Manolopoulou and Plionis (2017) method.

5.7.2 MUSIC clusters

The MUSIC dataset is a combination of two catalogues of galaxy clusters, MUSIC-1 and MUSIC-2, which are created from re-simulations of two large-volume N-body simulations (Sembolini et al., 2013). The MUSIC-2 sample contains 282 galaxy clusters which are selected from the $1h^{-1}$ Gpc^3 volume MultiDark simulation (Prada et al., 2012). Here, we study the 154 relaxed (from CSF only data) and most massive galaxy clusters extracted from the MUSIC-2 set, with virial masses of $M_{vir} > 5 \times 10^{14}h^{-1}$ M$_\odot$ at redshift $z = 0$, a mass complete sample of clusters at this redshift. Three of these clusters are shown in Fig. 5.15. The fact that these clusters are massive makes their rotation identification through the calculation of their angular momentum easier (Baldi et al., 2017). The clusters were zoomed in and re-simulated with implementation of smoothed particle hydrodynamics (SPH; Springel, 2005) with higher mass resolution and in spherical regions around the cluster centres with radii of $6h^{-1}$ Mpc. The simulations in B17 were made using three different models to describe the baryon physics; in this section, we used the clusters simulated with the CSF model, which includes cooling and star formation processes in the gas modelling. The gas particles have different masses, depending e.g. on whether they will produce stars or not, that are of the order of $1.9 \times 10^8 h^{-1}$ M$_\odot$, while dark matter particles

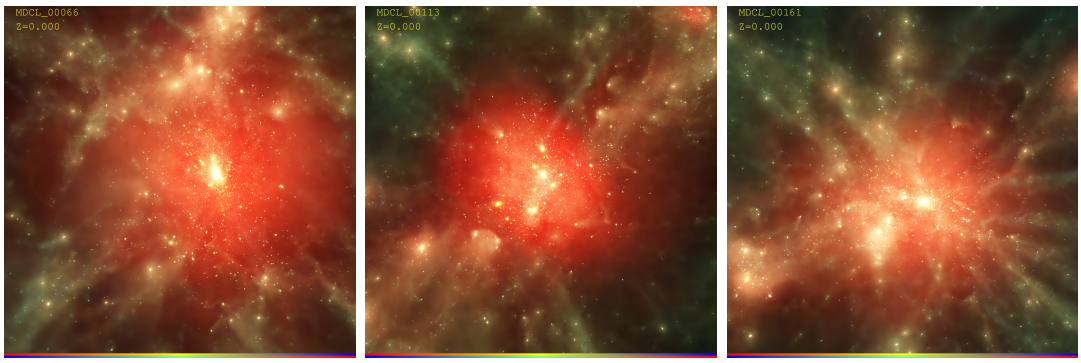

Figure 5.15 *From left to right, the resimulated MUSIC-2 clusters 66, 113 and 161 at $z = 0$ selected from MultiDark simulations. Images are taken from* music.ft.uam.es.

have all masses equal to $9.0 \times 10^8 h^{-1}$ $M_\odot$.

5.7.3 Method comparison

Before beginning to compare the two methods, we rewrote the MP17 code that was initially written in Fortran, in Python 2.7 language. In order for it to apply to 3-dimensional simulation data rather than the 2-dimensional observational data, some changes had to be made: the 3D coordinates and velocities of the simulated cluster galaxies were projected to specific planes and the "observed" rotation at each plane was studied. This method is chosen in order to directly compare the results of the MUSIC clusters to the results from observational data in MP17. In addition, this method is ideal for measuring the potentially observed rotational signal from the MUSIC clusters. The selection of the projection planes is described for every test individually.

In order to locate the origin of rotation in the cluster and the galaxy population that dictates it, we measure the rotational signal coming from various spatial cluster configurations and from galaxies with different masses. The spatial configurations are cuts in the galaxies used to measure the signal depending on their distance from the cluster centre. These cuts are made before the cluster is projected to the observed plane. The configurations used are:

V1: four consecutive shells of $0.25 \times R_{vir}$ width each (i.e. V1a is the sphere with radius 0.25 R_{vir}, V1b is the shell within radii 0.25-0.5 R_{vir}, V1c is the shell within radii 0.5-0.75 R_{vir} and V1d is the shell within radii 0.75-1 R_{vir}),

V2: the whole cluster, all galaxies within R_{vir},

V3: the shell within radii 0.1-1 R_{vir},

V4: the shell within radii 0.2-1 R_{vir} and

V5: the sphere with radius 0.5 R_{vir},

with R_{vir} being the virial radius of the cluster. Using the above configurations, we can locate the rotation signal in the cluster if it comes from a specific group of galaxies and measure its contribution to the rotation signal coming from the whole cluster (V2 configuration).

Moreover, four different groups of galaxies were studied in terms of their mass. This is to help identify whether the rotation originates from the more or less massive cluster galaxies, if there is such discrimination. The four groups are:

M1: all the galaxies in the cluster,

M2: all galaxies with $M_{star} > 10^{10}$ $M_{\odot}$,

M3: all galaxies with $M_{star} > 10^{11}$ $M_{\odot}$ and

M4: all the galaxies in the cluster, but with their velocity weighted respectively to their M_{star},

with M_{star} being the stellar mass of the galaxy.

5.7.3.1 The most rotating cluster

To ensure that both methods give the same results on the rotation of the cluster ICM, we begin by measuring the rotation of the gas of the most rotating cluster

of the sample according to B17, cluster 93 (see Table 5.10 and left panel of Fig. 5.20), using the MP17 method. In order to do so, we randomly extract as many gas particles belonging to the cluster as galaxies, i.e. 355, and treat those particles as fake galaxies. The cluster is rotated so the gas angular momentum axis coincides with axis Z. The planes the cluster is projected to measure its rotation are 5: the XY plane, the YZ plane, the ZX plane, the plane at a 45^o angle from the YZ plane (plane YZ45 hereafter) and the plane at a 45^o angle from the ZX plane (plane ZX45 hereafter). The latter two planes are perpendicular to XY. The same criteria as in MP17 are used to define rotation in the cluster and similar plots of the results are shown in Fig. 5.16.

After studying the gas rotation of the cluster in V2 and M1 configurations, strong rotation signal was found in planes YZ45, ZX and ZX45 and weak rotation in plane YZ. No rotation was found in plane XY, as expected from the analysis in B17, considering the rotation axis coincides with Z axis. In Fig. 5.16, the weak rotational signal from plane YZ is shown on the top panel and the strong rotational signal from plane ZX45 is shown on the bottom panel. Overall, the results agree with the ones found with B17 method.

5.7.4 Results

We can now study the rotation of the cluster constituents, galaxies, gas and dark matter for all the clusters in MUSIC-2 sample. The dark matter and ICM rotation is studied by treating the dark matter and gas particles as "galaxies" and applying the MP17 algorithm. The number of particles needed to accurately measure the rotation signal is studied using cluster 93, the most rotating cluster, and cluster 21, a non-rotating and non-relaxed cluster.

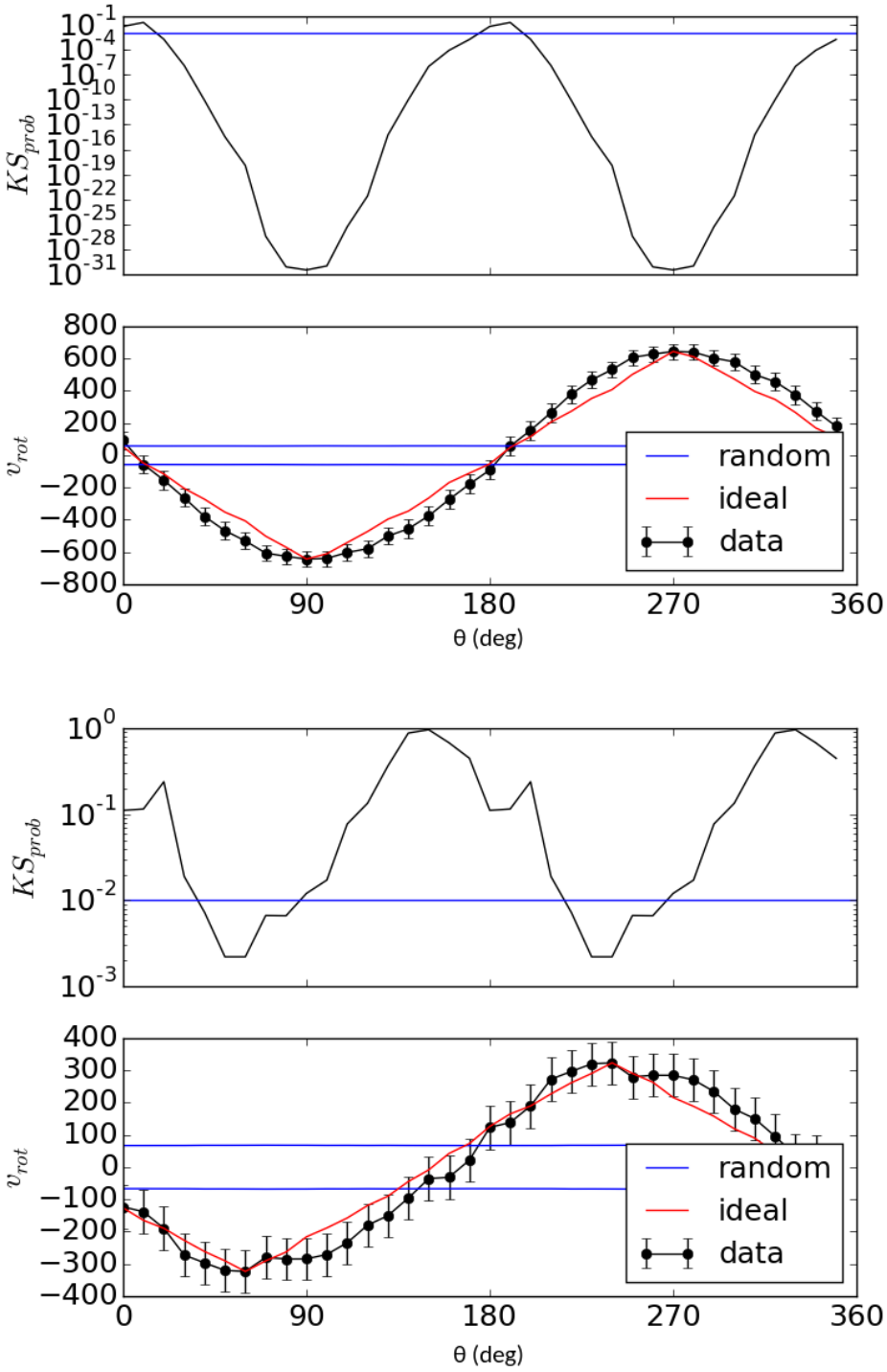

Figure 5.16 *The weak (top two panels) and strong (bottom two panels) rotation signal from the gas "galaxies" of cluster 93 when projected on planes YZ and ZX45 respectively. The cluster was studied in V2 and M1 configurations. Top panels show the Kolmogorov-Smirnov (KS hereafter) probability as a function of the rotation angle θ (blue line is the KS probability threshold to pass the rotation criteria) and the bottom panels show the rotation diagram (points with errorbars), the ideal rotation (red continuous curve) and random rotation curves (blue curves corresponding to 1σ uncertainty). The panels are similar to the lower panels of Fig. 5.12.*

5.7.4.1 Number of particles

We apply the MP17 algorithm to all the gas and dark matter particles available from the simulation and to subsamples of them to check if the rotation signal depends on the number of particles. If so, the number of particles for which the results of the rotation signal becomes stable should be used for the study of the ICM and dark matter rotation for the rest of the clusters.

We test the rotation signal recovery coming from the gas and dark matter of cluster 93 and 21 for different-sized subsamples including the whole amount of particles. The results are shown in the Fig. 5.17, where the x axis is the percentage of the whole number of particles used and y axis is the "mean rotation signal" recovered. The latter is the mean of the rotation signals found in the 4 planes perpendicular to XY, i.e. planes YZ, YZ45, ZX and ZX45. Signal 0 is given if no rotation signal is recovered, signal 1 is given if there is weak rotation signal (loose criteria) and signal 2 is given if there is strong rotation signal (strict criteria) in the given projection. As seen in Fig. 5.17, the mean rotation signal becomes stable when 0.1% of the particles or more are used for both cluster 93 and cluster 21. Therefore, for computational speed, we choose to use 0.1% of the dark matter and gas particles available in each cluster from the simulations, the least amount needed for a stable signal.

5.7.4.2 Cluster 93

Before studying the statistical results from the rotation of the constituents of all clusters of our sample, we focus on the test case, cluster 93. We use all the available gas and dark matter particles of the cluster, which are 919,827 and 1,231,324 respectively, and all the galaxies available (M1 configuration), 355 in number and within the whole virial radius (V2 spatial configuration).

While gas and dark matter seem to co-rotate with remarkable similarity, the galaxies only weakly follow this rotation. In more detail, both ICM and dark matter show weak indications of rotation with the same rotation axis, axis Z, same rotational velocity and

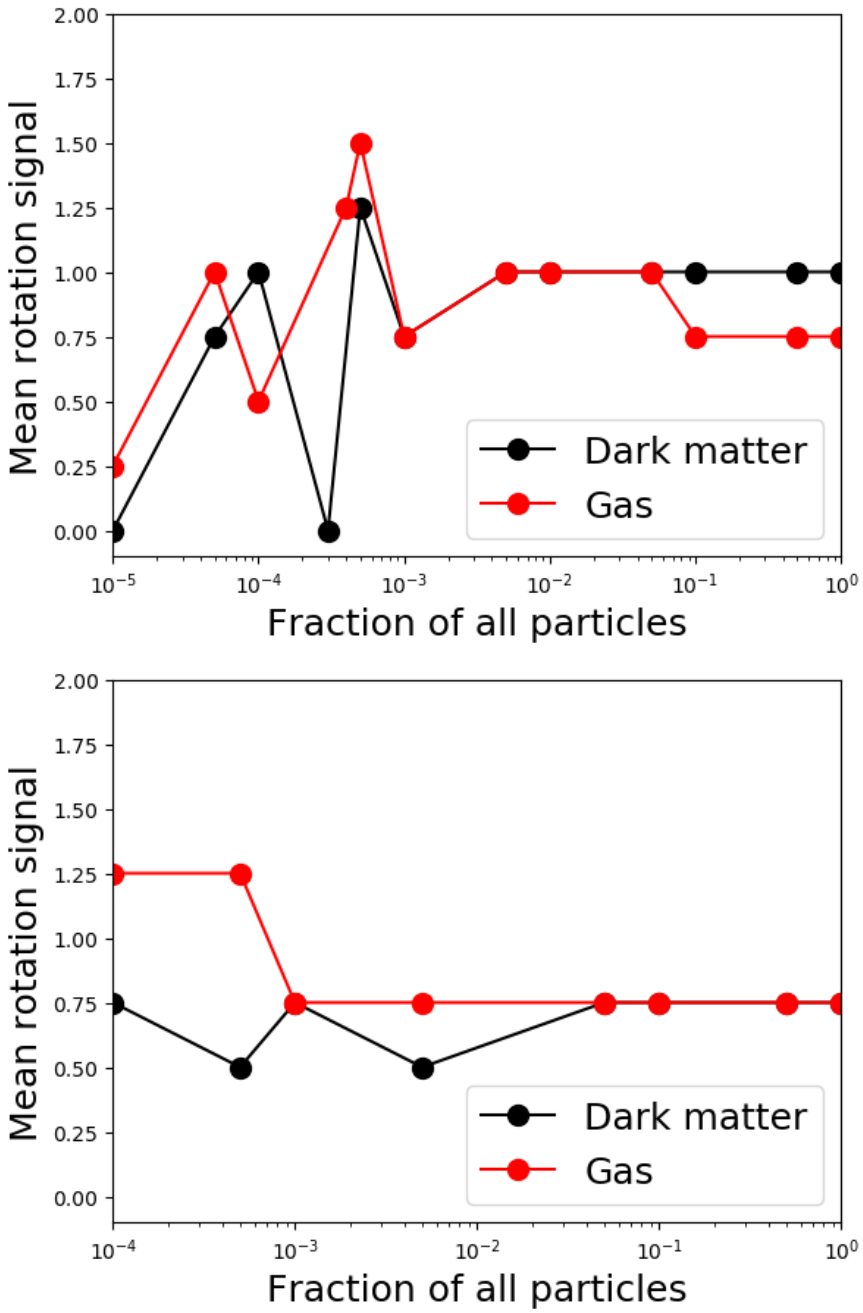

Figure 5.17 *The mean rotation signal (see definition in text) as a function of the number of particles used to study the rotation of ICM (red line/dots) and dark matter (black line/dots) of cluster 93 (top panel) and cluster 21 (bottom panel). The signal stabilises when using 0.1% of the particles of clusters 93 and 21 available.*

same direction of rotation in the projected planes YZ, YZ45 and ZX45. In plane ZX, dark matter shows weak indications of rotation, while ICM does not. No indications of rotation are found in plane XY. As for galaxies, no indications of rotation were found in these configurations. As described in Section 5.9.2, the rotation of the galaxies is mainly coming from the most massive galaxies in larger radii from the centre. In Fig. 5.18, the rotation diagrams from ICM and dark matter particles are shown for the projected planes YZ and YZ45.

The results from cluster 93 hint that rotation originates from the dark matter of the clusters, which due to its large mass affects the ICM dynamics that follows dark matter's rotation. The galaxies are less affected by this rotation or the signal is considerably weaker because of the small number of galaxies compared to the number of dark matter and ICM particles in the cluster.

5.7.4.3 Galaxies, gas and dark matter rotation

We move to the results of the rotation of the clusters galaxies using all the available galaxies in each cluster within the whole virial radius and comparing this rotation with the ICM and dark matter rotation using 0.1% of the available particles for each cluster and with the ICM and dark matter spin parameter calculated in B17.

We study the rotation of the galaxies, gas and dark matter in the projected planes YZ, YZ45, ZX and ZX45 and each time we find a weak or strong rotation signal in one of them, we append 1 point to the cluster. This way, each cluster ends up with a "rotation score" between 0 and 4, with 4 being the score of the most rotating clusters and 0 the score of the least rotating clusters. This score can be compared with the gas and dark matter spin parameter of each cluster, as found in B17. The values of the spin parameter vary between ~ 0.01 and 0.12 with a median of 0.085 for ICM and 0.078 for dark matter. In B17, the threshold of 0.07 was used to discriminate the rotating from non-rotating clusters.

We apply the Spearman correlation test between the cluster galaxies rotation score and the ICM and dark matter rotation score and spin parameter for all the 154 CSF

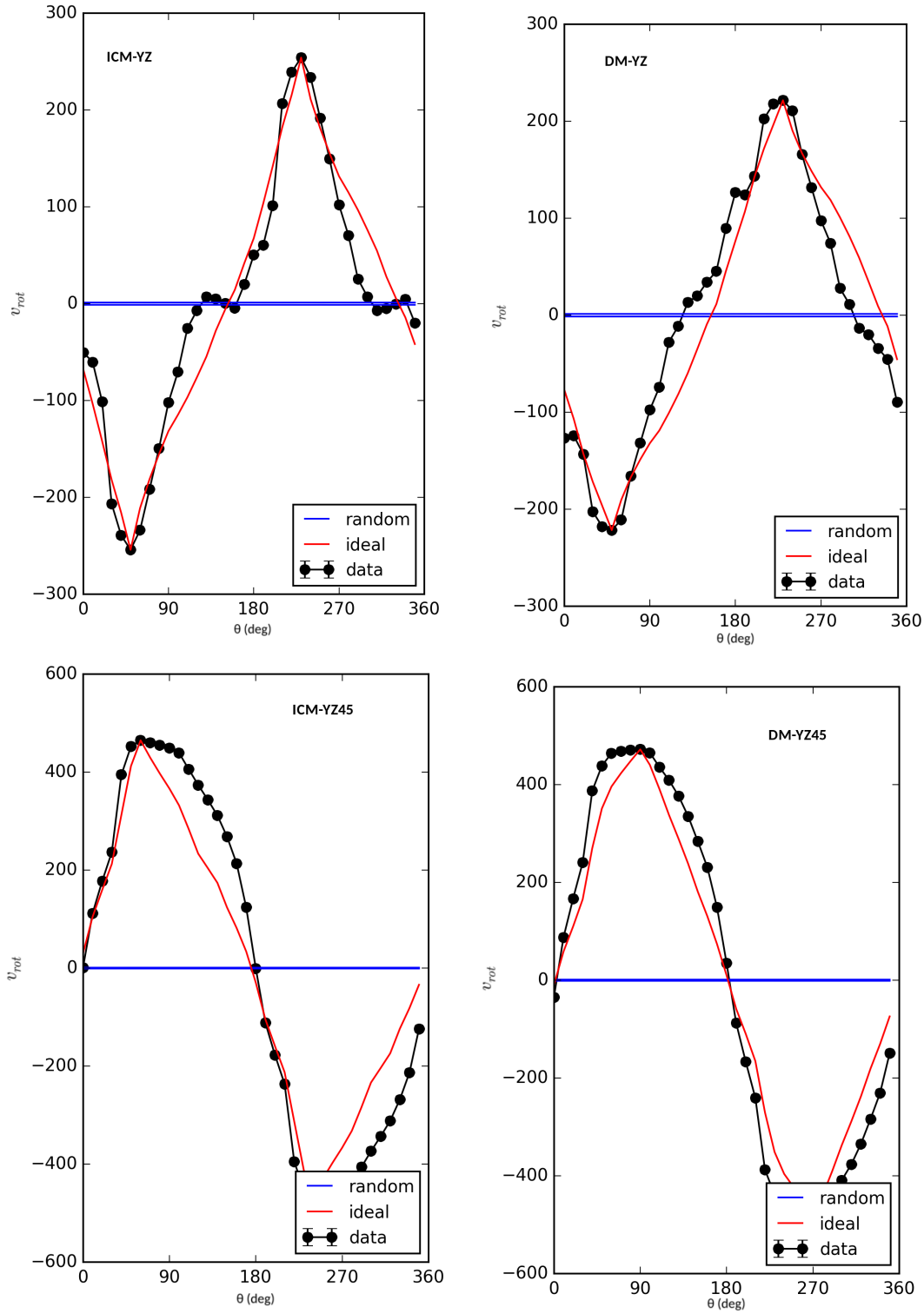

Figure 5.18 *The weak rotation signal of cluster 93 ICM (left panels) and dark matter (right panels) for the YZ (top panels) and YZ45 (bottom panels) projected planes. The ICM and dark matter are rotating around the same axis, with the same velocity and in the same direction a fact that shows the two constituents are co-rotating. The panels are similar to the lower panels of Fig. 5.12.*

Table 5.8 *The Spearman correlation test results between the cluster galaxies, ICM or dark matter rotation score, RS, and ICM or dark matter spin parameter, SP.*

	Corr. Coeff.	p-value
Galaxies RS–Gas RS	-0.05	0.501
Galaxies RS–Dark matter RS	0.03	0.712
Galaxies RS–Gas SP	0.15	0.072
Galaxies RS–Dark matter SP	0.26	0.001
Gas RS–Gas SP	0.03	0.741
Dark matter RS–Dark Matter SP	-0.07	0.419

relaxed massive MUSIC clusters. The results are shown in Table 5.8. There seem to be no correlation between the rotation score of galaxies and ICM or dark matter. When using the ICM and dark matter spin parameters instead of their rotation score, only weak correlations appear, with the correlation between galaxies rotation score and dark matter spin parameter being stronger. This suggests that the rotation of galaxies does not necessarily follow the rotation of ICM and/or dark matter in galaxy clusters. Moreover, having seen the effect of the number of particles on the identification of rotation, the results could also suggest that the significantly less amount of galaxies than ICM or dark matter particles do not allow the identification of rotation. Looking at the last two rows of the table which compare the spin parameter and rotation score using the ICM and dark matter, we see that the two methods do not correlate. This can be due to the projection effects that appear when projecting the cluster on a 2-dimensional plane and are absent in the spin parameter calculation which is done on the 3-dimensional cluster and the fact that only 4 projection planes are taken into the calculation of the rotation score.

When cluster rotation appears in 3 or 4 out of the 4 planes studied, we classify this cluster as rotating. Under this assumption, in 17 out of the 154 clusters their galaxies were found to be rotating, while in 113 and 112 clusters respectively their ICM and dark matter particles were found to be rotating. On the other hand, only for 9 of the total 154 clusters have ICM spin parameter larger than 0.07 and for 2 of the total 154 have dark matter spin parameter larger than 0.07. Some additional statistics of the rotation of the three constituents are shown in Table 5.9. Looking at the results

Table 5.9 *Number of clusters that show rotation using the rotation score (RS) or their spin parameter (SP) in one, two or all constituents rotate. The conditions of the three first columns must all hold in order to get the number shown in the last two columns. "Y" means the constituent is rotating, while "N" means it does not classify as rotating with either the B17 criteria (fourth column) or the criteria set in this work (fifth column). The percentage of the whole sample is shown in parentheses.*

Galaxies	ICM	Dark matter	No of clusters (RS)	No of clusters (SP)
Y	Y	Y	10 (6%)	1 (1%)
Y	N	Y or N	4 (3%)	15 (10%)
Y	Y or N	N	6 (4%)	16 (10%)
Y	N	N	3 (2%)	15 (10%)
N	Y	Y or N	100 (65%)	7 (5%)
N	Y or N	Y	101 (66%)	1 (1%)
N	Y	Y	79 (51%)	1 (1%)
Y or N	Y	N	24 (16%)	7 (5%)
Y or N	N	Y	23 (15%)	0 (0%)
Y or N	Y	Y	89 (58%)	2 (1%)

in this table that concern the rotation score, ICM and dark matter co-rotate for more than a third of the clusters in the sample. When evaluating the rotation using the spin parameter, in only few cases the gas or the dark matter is found to rotate and rotation seems to be more prominent in the galaxies of the clusters than in the ICM or dark matter. This is an effect of the high spin parameter threshold used to discriminate a rotating from a non-rotating cluster.

The statistical results on Table 5.9 show that the ICM and dark matter co-rotate in most of the clusters, in 79 out of 112 and 1 out of 2 clusters with rotating dark matter when using the rotation score and the spin parameter respectively. When looking at the rotation scores, galaxies rotation sometimes follows the ICM and dark matter co-rotation (89-79=10 out of 17 times galaxies were found to rotate), but this is not a regular event. When looking at the spin parameter scores, given that in only 2 clusters dark matter was found to rotate, it is difficult to conclude whether galaxies co-rotate with it, since it happens in 1 out of the 2 clusters with rotating dark matter. Cluster 93 seems to be a representative cluster from the sample, since its dark matter and ICM rotate with a hint that galaxies follow this rotation. Even though the two rotation identification methods do not correlate, they seem to produce similar

qualitative results, a fact that suggests that perhaps the inclusion of more projected planes in the rotation score would reflect better the variety of rotation profiles in the cluster sample.

Overall, there are clear results that ICM and dark matter in clusters co-rotate, confirming the results from Baldi et al. (2017). There is not a clear sign whether cluster galaxies follow this rotation or not, given that roughly in half of the clusters with ICM and dark matter co-rotation, galaxies do co-rotate with them, but do not co-rotate in the rest of them. This is likely to be because of the projection effects being added when projecting the cluster in a 2-dimensional plane, which affects the galaxies analysis in a greater amount given their smaller number compared to the ICM or dark matter particles. Also, we have shown that 0.1% of the dark matter and ICM particles available in each cluster are needed to extract the rotation signal (Fig. 5.17); maybe the galaxies are not appropriate proxy of rotation in clusters. Moreover, the high threshold of the spin parameter being higher than 0.07 in order to call a cluster rotating has given a low number of ICM and dark matter rotating clusters, which is not enough for statistical analysis; however, thosee few clusters should be the most representative cases of rotating clusters.

5.8 Conclusions

We searched for possible cluster rotation in a sample of Abell clusters using galaxy-member redshifts from the SDSS DR10 spectroscopic data base. We developed a new algorithm in order to be able to deduce rotation using the line-of-sight velocities of the galaxy members. We verified the performance of this algorithm by applying it on various Monte Carlo simulated clusters with known rotational characteristics. We also compared our method with that of the Hwang and Lee (2007) method.

Our algorithm provides the significance of the rotation identification (with a set of indices), the rotation amplitude, the position angle of the rotation axis, whether the rotation is clock or anticlockwise and the rotation centre. We find that the amplitude

of the rotation is correlated with the indications of rotation; the larger the rotation amplitude the more significant are the indications of rotation. This implies that small amplitude rotation may not be easy to identify, and thus it could pass undetected.

We then applied our algorithm to our sample of Abell clusters using two different sets of criteria for rotation identification, the so-called strict and loose criteria and two different outer cluster radii (1.5 and 2.5 h_{70}^{-1} Mpc). Out of 86 cluster with more than 50 member galaxies we have found in total 23 rotating clusters (in any of the 2 radii studied) using the strict criteria of rotation identification and 29 such clusters using the loose criteria of rotation identification. Taking into account the expected fraction ($\sim 10\% - 15\%$) of misidentified coherent substructure velocities for rotation, provided by our Monte Carlo simulation analysis, the corresponding final fraction of rotating clusters is $\sim 23\%$ and $\sim 28\%$, respectively, under the strict and loose criteria. These results appear to be in tension with recent numerical N-body simulations (Baldi et al., 2017) which find a significantly smaller fraction of rotating clusters; however with slightly different criteria of rotation.

Finally, when we use the inner radius case (1.5 h_{70}^{-1} Mpc) and clusters that show indications for rotation, we find relatively significant correlations between the cluster dynamical state (X-ray isophotal shape as well as the BM type) and the significance of cluster rotation, a fact which implies that the cluster rotation could be related to the dynamically younger phases of cluster formation but after the initial anisotropic accretion and merging have taken place. This hints towards the inner radius rotation being related to the initial anisotropically accreted matter having significant angular momentum, which gets amplified by collapse. The fact that we find fewer such correlations when we use clusters with rotation within the outer cluster radius (2.5 h_{70}^{-1} Mpc) possibly hints towards a different cause or a different phase of the relevant rotation, possibly being related to the imprint of coherent rotational motions of galaxies in the cluster outskirts prior to dynamically disturbing the cluster inner regions.

The study of the rotation of the MUSIC clusters using the MP17 method has so far given intriguing results. The methods of MP17 and B17 were found to agree in

the classification of the clusters' ICM rotation. The study of the example cluster 93 showed that dark matter and ICM co-rotate, but only very massive outer galaxies of the cluster follow this rotation. The study of the rotation of all cluster constituents in the whole cluster sample showed that the cluster galaxies rotation does not necessarily follow the ICM or dark matter co-rotation; the reason behind this can be the projection effects that are larger for the low number of cluster galaxies available in each cluster, the low number statistics available from galaxies (few thousands of dark matter and ICM particles where needed in order to extract the correct rotation signal in clusters 93 and 21) and the high spin parameter threshold that was used in B17 to discriminate a rotating from a non-rotating cluster, which resulted in a small sample of clusters with rotating ICM or dark matter.

We gained valuable insight on the internal dynamics of galaxy clusters by studying the rotation of the different cluster contents. Given that the sample of clusters studied contains only relaxed clusters and that there are hints that all three contents, galaxies, ICM and dark matter, co-rotate, that means that cluster rotation is an important process taking place in a fraction of relaxed clusters and it would be interesting to discover the reason behind this. Given that in 51% of the MUSIC clusters sample there is ICM–dark matter co-rotation, the correction of the dynamically calculated cluster masses is necessary. Further investigation on whether tha galaxies follow the ICM and dark matter rotation is needed, relating to the quantification of the effect of the projection effect to the galaxies rotation signal and to the higher number of ICM and dark matter rotating clusters according to the 3-dimensional, spin parameter criterion. If galaxies are found not to co-rotate, that could hint that galaxies are still being accreted in clusters and that are not yet virialised in order to follow the larger scale rotation.

5.9 Appendix: Results on individual clusters

5.9.1 Clusters successfully divided in substrustures

We list here those clusters in our sample that were found to consist in velocity space of two or more well-separated substructures. These clusters were separated into their different components, which were individually analysed for rotation when possible.

- **Abell 1035**

  This cluster presents a background subcluster in all four configurations studied. One of the two subclusters was found to have a significant rotational mode.

- **Abell 1228**

  Abell 1228 was found to consist of three well-separated components in velocity space aligned along the line-of-sight, in all four spatial configurations (see Fig. 5.13). Two components are rich enough to be analysed for rotation and indeed they show strong indications of rotation, in the 2.5 h_{70}^{-1} Mpc and 0.5-2.5 h_{70}^{-1}Mpc configurations, with rotational velocity amplitude of ~ 200 km/s (A1228a) and ~ 400 km/s (A1228b). The two subclusters rotate in the same direction ($\mathcal{I} = 2$) but have their (projected on the plane of the sky) rotation axes perpendicular to each other (Fig. 5.19).

- **Abell 1291**

  Another interesting case is Abell 1291. Studying its galaxy member velocity distribution we again identify 3 different peaks, clearly separated from each other. The third and most distant substructure could not be studied due to its small richness. From the other two only the nearest one (A1291a) show indications of rotation for the 2.5 h_{70}^{-1} Mpc and 0.5-2.5 h_{70}^{-1} Mpc configurations.

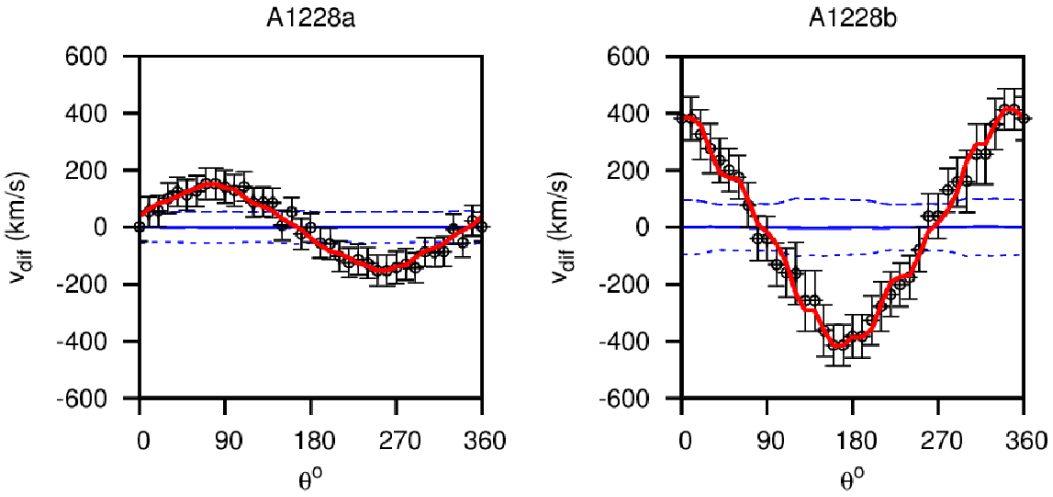

Figure 5.19 *The rotational diagram for Abell 1228a (left) and 1228b (right) within a radius of 2.5 h_{70}^{-1} Mpc. The two subclusters have perpendicular rotation axes.*

- **Abell 1775**

  We found a foreground group of galaxies in velocity space and in all the four spatial configurations. This substructure is placed south-east of the main cluster of galaxies and was not found to present any indications of rotation in any of the configurations, while the main cluster is found to rotate in the 0.5-2.5 h_{70}^{-1} Mpc configuration.

- **Abell 2152**

  Abell 2152 presents a main group of galaxies found to have strong indications of rotation in all configurations. In all configurations foreground galaxies (part of the Hercules supercluster) are found with a wide velocity distribution, which we succesfully exclude from our analysis. The main cluster is then found to have a significant rotational mode.

Table 5.10 *The 5 most and 5 least rotating clusters in the sample, their virial radius R_{vir}, number of galaxy members and spin parameter value.*

Most rotating				Least rotating			
Cluster	R_{vir} (kpc/h)	Galaxies	Spin	Cluster	R_{vir} (kpc/h)	Galaxies	Spin
93	2,268.00	355	0.079382	219	1,960.00	238	0.005222
46	1,934.33	194	0.079382	141	2,118.62	306	0.009965
98	2,154.70	336	0.073543	147	1,973.80	248	0.041161
205	1,967.11	218	0.077137	150	2,236.85	398	0.008347
256	2,008.99	226	0.077224	174	2,057.27	270	0.008677

5.9.2 The ten most and least rotating clusters

For further comparison of the two methods, the MP17 and B17, we study the rotation of the galaxies of some representative clusters from the MUSIC cluster sample, the 5 most and 5 least rotating clusters of the 154 in total in the sample; the clusters with the highest (larger than 0.07) and lowest (smaller than 0.01) spin value within the sample respectively. Their properties are given in Table 5.10 and the resimulated images of the most (cluster 93) and least (cluster 219) rotating cluster are shown in Fig. 5.20. All the clusters in this Section have been rotated in order for their gas angular momentum axis to coincide with axis Z, which makes comparison of results easier.

We can now study the cluster galaxy rotation of the most and least rotating clusters. we project the galaxy distribution and measure the rotation signal in three planes XY, YZ and ZX and study all mass and spatial configurations and in XY, YZ, YZ45, ZX and ZX45 planes and study V1 and M2 configurations. Considering that the angular momentum axis of the gas is the Z axis, if the rotation of the cluster galaxies follows the rotation of the gas, then the results would show strong or weak rotation signal (according to the criteria in MP17) at the projected planes ZX or YZ and not in XY plane.

- **Cluster 93**

  Weak rotation signal of cluster 93 galaxies is found in V1c and V2 configurations

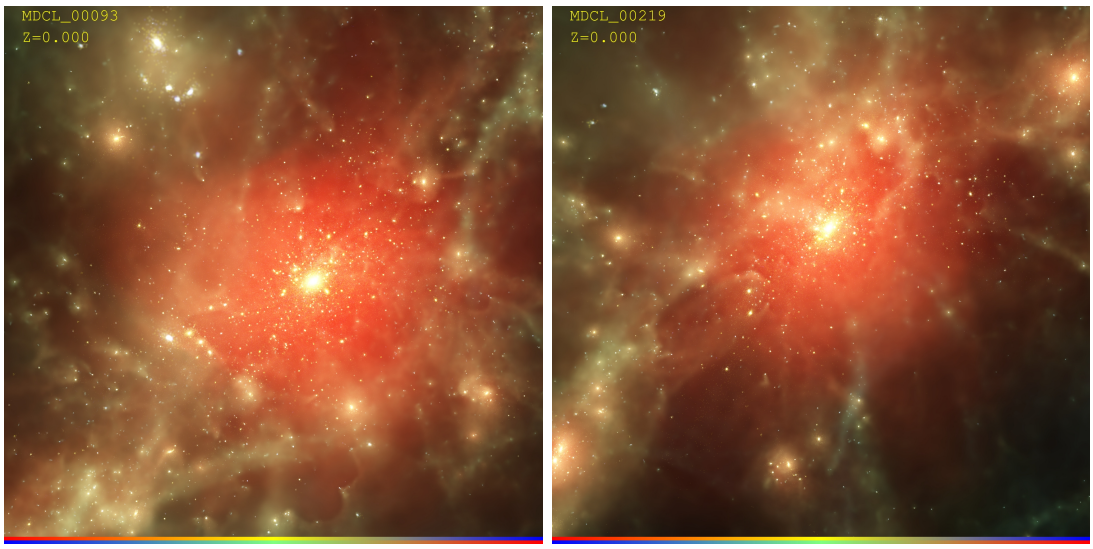

Figure 5.20 *The most rotating cluster in the MUSIC sample, cluster 93, on the left and the least rotating cluster, cluster 219, on the right, according to the analysis in B17. Images are taken from* music.ft.uam.es.

for M2 galaxies, in V2 for M4 galaxies and in V3 for M3 galaxies. This hints that the rotation of the galaxies does not come from galaxies in the centre of the cluster, but more likely from galaxies in distances of 0.75-1 R_{vir} and from the most massive galaxies.

A weak rotation signal is also found only in the M2 case, which means it comes from intermediate mass galaxies (10^{10} $M_{\odot}$ < M_{star} < 10^{11} $M_{\odot}$) on the YZ plane and in the inner regions of the cluster (found in V1a, V5 and V3 spatial configurations). This rotation does not appear in the gas dynamics in B17. However, the signal is not detected in the V2 configuration, i.e. when studying all galaxies within the virial radius, a fact that makes it less significant and likely to be an effect of more projected galaxies in the centre of the cluster than the outskirts.

Overall, the most massive galaxies mainly further away from the cluster centre show rotation signal on the XY plane, following the rotation of the gas.

- **Cluster 46**

  A strong rotation signal of the galaxies of cluster 46 is found on the YZ plane in V2, V3 and V1d areas from M2 galaxies, i.e. the galaxies with $M_{star} > 10^{10}$

$M_{\odot}$.

Strong rotation is found from and M2 galaxies in V1b shell in XY plane and weak rotation in V1 space by M2 galaxies in the same plane. However, this rotation does not appear in the galaxies of the whole cluster (V2 case), a fact that does not make it comparable with the rotation of the gas found within R_{vir} in B17.

Like cluster 93, the cluster rotation signal in cluster 46 originates from more massive clusters in larger distances from the cluster centre, and follows the gas angular momentum.

- **Cluster 98**

  Strong rotation signal of galaxies of cluster 98 is found on planes YZ45, ZX and ZX45, while weak signal comes from plane YZ. This rotation originates from the outer shells of the cluster and agrees with the rotation of the gas found in B17, as the previous two clusters.

  There is also weak rotation signal in plane XY from the inner shells of the cluster, which, amongst other configurations, also appears on V2 from M4 galaxies. This shows additional rotation of galaxies that does not necessarily follow the rotation of the gas in the cluster core. However, since the discrimination of gas rotation or not in B17 happens depending on the spin parameter within the virial radius, the comparison of this rotation with the ICM rotation is not possible.

- **Cluster 205**

  Cluster 205 shows strong rotation signal in V2 space in YZ and ZX planes and no rotation in XY plane. The rotation on ZX plane comes mainly from the 0.75-1 R_{vir} shell, while the rotation on plane YZ comes mainly from the 0.25-0.5 R_{vir} shell. The galaxy members rotation follows the gas rotation found in B17.

- **Cluster 256**

  Cluster 256 shows rotation on YZ and ZX planes. The rotation on YZ comes mainly from the galaxies 0.25-0.75 R_{vir} and shows in the whole cluster (V2 case) as well, and rotation on ZX comes from the whole distance range of galaxies. This signal agrees with the ICM rotation results from B17.

  Additionally, there is a strong signal of rotation on plane XY coming from the 0.5-0.75 R_{vir}, but does not show on the V2 case, where all cluster galaxies are taken into account and, therefore, cannot be compared to the ICM rotation in B17.

- **Cluster 219**

  Cluster 219 is the cluster with the lowest value of spin parameter in B17. Using the MP17 method, there is a weak rotation signal on the XY plane from the 0.25-0.5 R_{vir} shell, which also appears in the V2 case. This signal is likely to be a false detection because of projection effects on XY plane.

- **Cluster 141**

  Cluster 141 shows no rotation as a whole, but only in some shells when projected in YZ and ZX planes. These are either strong or weak signals, mainly coming from the 0.75-1 R_{vir} shell. The results of the gas and galaxy members rotation in this cluster agree, as none of them has signals of rotation when studying the cluster as a whole.

- **Cluster 147**

  No signal of rotation of the cluster 147 galaxies is found from the whole virial radius. This agrees with the gas rotation findings in B17. However, there are signs of weak and strong rotation on the ZX plane in some shells, the strong one showing within 0.5 R_{vir} of the cluster (V5 case).

- **Cluster 150**

  Cluster 150 shows weak and strong rotation of the galaxies within the whole virial radius in planes YZ and YZ45 respectively. This is contradictory to the non-rotating ICM found in B17.

- **Cluster 174**

  Cluster 174 shows strong rotation on planes XY and ZX, with only the former appearing when including all galaxies within the virial radius. This is also contradictory to the findings of B17 for the gas rotation within the cluster virial radius.

Overall, the galaxies and ICM rotation seem to agree well for most of the clusters studied here. If that is true for most of the clusters in the whole sample, that would show a co-rotation between them and the dark matter, since the ICM and dark matter co-rotation has already been discussed in B17.

Chapter 6

Conclusions and Future Work

In this work we have presented the construction of a new optically-selected X-ray cluster catalogue of the XMM Cluster Survey covering the SDSS DR13 area (Manolopoulou et al., 2018b). The extended and PSF-sized sources with X-ray soft band counts >200 were optically eyeballed using SDSS images and resulted in a sample of 1,255 clusters with 203 of the being new discoveries. 1,225 are assigned with optically confirmed spectroscopic (1,048) or photometric (177) redshfits using a variety of our own and literature estimates, 1,223 are assigned with richness estimates using the GMPhoRCC code and 1,143 have assigned X-ray luminosity and temperature, calculated using improved pipelines since XCS DR1.

We have created 3 subsamples from our catalogue, defined such as to aid with specific research studies using clusters: the clusters with spectroscopic redshifts, ideal for cosmological studies, cluster scaling relation studies and any other research that requires large sample with reliable observable measuremements, the clusters with high temperatures ($T_{\rm X}$ >5 keV), ideal to be detected through their SZ signature anf used for comparison/normalisation of X-ray properties, and the clusters in high redshifts ($z \geq 0.8$), ideal for studies of the evolution of galaxy member properties and the effect of their environment. The large range and high quality of redshifts ($z \leq$1.2 with median of 0.28), luminosities ((4.8 $\times 10^{-5}$ - 1.6 $\times 10^{2}$) $\times 10^{44}$ erg/s

with a median of $4.8{\times}10^{-1} \times 10^{44}$ erg/s) and temperatures ($0.2 - 13.8$ keV with a median of 2.6 keV), as well as the large number of X-ray selected clusters in the catalogue, the largest so far, makes this sample a very useful tool to study cosmology with galaxy clusters and galaxy evolution. The catalogue has already been used by members of the XCS collaboration to measure the cluster $L_{\rm X} - T_{\rm X}$ scaling relation and its evolution (Ebrahimpour et al., 2018).

We continued to use the XCS DR2–SDSS cluster catalogue along with other X-ray and optical cluster catalogues to study the effect of the density of the clusters environment to their properties (Manolopoulou et al., 2018a). We used both observational and simulation cluster catalogues and constructed our own void catalogues that correspond to each of the cluster ones. We compared the distribution of widely used cluster observables using the Kolmogorov-Smirnov two sample test in different density environments, determined by both geometrical criteria (within/outside voids) and by the density in the clusters' local neighbourhood. We discovered that there are more clusters in underdense environments in lower redshifts and that clusters in underdense regions present significantly lower X-ray and i-band luminosities, X-ray temperatures, richnesses and masses than clusters in overdense regions. The cluster mass functions and X-ray luminosity–temperature relations are sometimes affected by those differences.

We believe that those differences are possible evidence of the different merger histories of clusters of different environments or different cluster formation models and initial parameters. We concluded that a selection of a cluster sample based on one of the above properties introduces an environmental bias which should be taken into account in cosmological studies that use or attempt to calculate cluster masses from cluster scaling relations wit the aim to constrain cosmological parameters. We found that the possibility of detecting such signal of differences between cluster properties depends on the cluster sample size used. Given the smaller size of X-ray cluster selected catalogues nowadays, improvements and more insight can be given using larger observational X-ray cluster catalogues (Predehl et al., 2010). The next step on this study is to study the luminosity–temperature relations using a more sophisticated

algorithm (Ebrahimpour et al., 2018), that takes into account effects such as the sample selection functions and the evolution of the cluster properties.

Finally, we studied the dynamics of the galaxy clusters, more specifically, their rotation, with the aim to quantify the correction needed when calculating cluster masses using cluster dynamics. We developed a new algorithm to detect the clusters' rotation and applied it to Abell clusters without substructures using SDSS DR10 spectroscopic galaxy redshifts (Manolopoulou and Plionis, 2017). $\sim 23\%$ ($\sim 28\%$) of the sample was found to be rotating with the strict (loose) rotation criteria. The correlation between the cluster dynamical state infered from the X-ray isophotal shape showed that cluster rotation could be related to the dynamically younger phases of cluster formation. These results were in contradiction with the much smaller fraction of relaxed clusters from simulations that their ICM was found to be rotating (Baldi et al., 2017).

We applied our algorithm to the MUSIC clusters from Baldi et al. (2017) in order to understand the discrepancy. The study of an example cluster showed that ICM and dark matter co-rotate, but only the most massive outer galaxies follow this rotation. Comparing the galaxies rotation for the whole cluster sample and the ICM and dark matter rotation score and spin parameter from Baldi et al. (2017), we confirmed the co-rotation of the ICM and dark matter in clusters and found that sometimes galaxies follow this rotation too. More investigation on the latter using more ICM and dark matter rotating clusters would be valuable in order to have a clear conclusion on the cluster galaxies rotation. The fact that in some of the relaxed, massive MUSIC clusters all three contents, galaxies, ICM and dark matter, were found to co-rotate, shows that cluster rotation is a important process taking place in a fraction of relaxed clusters. Given that a large fraction of the clusters show rotation in their ICM and dark matter (51%), the correction of the dynamically calculated cluster masses is necessary.

To sum up, this thesis was dedicated into creating a both large and reliable X-ray selected sample of galaxy clusters that can be used by the community for a variety of scientific research, from galaxy evolution to cosmology. We explored the variety of

the different cluster observable properties introduced by the environment they live in and the implications these have on using those for cosmological research. We finally dived into the dynamics of galaxy clusters - more specifically, the rotation of their constituents from the cluster's rotation axis. Galaxies clusters are proven to be very interesting and useful in many areas of astronomical research. There is a wealth of information still waiting to be discovered about their formation, evolution, dynamics and observational properties. In this thesis, we attempted to solve some of them, by constructing our own tools, catalogues, algorithms and methods. The future work is going to give more insight on these remarkable objects and ease their use as invaluable cosmological probes.

Bibliography

Abazajian, K. N., J. K. Adelman-McCarthy, M. A. Agüeros, S. S. Allam, C. Allende Prieto, D. An, K. S. J. Anderson, S. F. Anderson, J. Annis, N. A. Bahcall, and et al. "The Seventh Data Release of the Sloan Digital Sky Survey." *ApJS* 182: 543-558.

Abbott, T. M. C., F. B. Abdalla, S. Allam, A. Amara, J. Annis, J. Asorey, S. Avila, O. Ballester, M. Banerji, W. Barkhouse, L. Baruah, M. Baumer, K. Bechtol, M. R. Becker, A. Benoit-Lévy, G. M. Bernstein, E. Bertin, J. Blazek, S. Bocquet, D. Brooks, D. Brout, E. Buckley-Geer, D. L. Burke, V. Busti, R. Campisano, L. Cardiel-Sas, A. C. arnero Rosell, M. Carrasco Kind, J. Carretero, F. J. Castander, R. Cawthon, C. Chang, C. Conselice, G. Costa, M. Crocce, C. E. Cunha, C. B. D'Andrea, L. N. da Costa, R. Das, G. Daues, T. M. Davis, C. Davis, J. De Vicente, D. L. DePoy, J. DeRose, S. Desai, H. T. Diehl, J. P. Dietrich, S. Dodelson, P. Doel, A. Drlica-Wagner, T. F. Eifler, A. E. Elliott, A. E. Evrard, A. Farahi, A. Fausti Neto, E. Fernandez, D. A. Finley, M. Fitzpatrick, B. Flaugher, R. J. Foley, P. Fosalba, D. N. Friedel, J. Frieman, J. García-Bellido, E. Gaz tanaga, D. W. Gerdes, T. Giannantonio, M. S. S. Gill, K. Glazebrook, D. A. Goldstein, M. Gower, D. Gruen, R. A. Gruendl, J. Gschwend, R. R. Gupta, G. Gutierrez, S. Hamilton, W. G. Hartley, S. R. Hinton, J. M. Hislop, D. Hollowood, K. Honscheid, B. Hoyle, D. Huterer, B. Jain, D. J. James, T. Jeltema, M. W. G. Johnson, M. D. Johnson, S. Juneau, T. Kacpr zak, S. Kent, G. Khullar, M. Klein, A. Kovacs, A. M. G. Koziol, E. Krause, A. Kremin, R. Kron, K. Kuehn, S. Kuhlmann, N. Kuropatkin, O. Lahav, J. Lasker, T. S. Li, R. T. Li, A. R. Liddle, M. Lima, H. Lin, P. López-Reyes, N. MacCrann, M. A. G. Maia, J. D. Maloney, M. Manera, M. March, J. Marriner, J. L. Marshall, P. Martini, T. McClintock, T. McKay, R. G. McMahon, P. Melchior, F. Menanteau, C. J. Miller, R. Miquel, J. J. Mohr, E. Morganson, J. Mould, E. Neilsen, R. C. Nichol, D. Nidever, R. Nikutta, F. Nogueira, B. Nord, P. Nugent, L. Nunes, R. L. C. Ogando, L. Old, K. Olsen, A. B. Pace, A. Palmese, F. Paz-Chinchón, H. V. Peiris, W. J. Percival, D. Petravick, A. A. Plazas, J. Poh, C. Pond, A. Por redon, A. Pujol, A. Refregier, K. Reil, P. M. Ricker, R. P. Rollins, A. K. Romer, A. Roodman, P. Rooney, A. J. Ross, E. S. Rykoff, M. Sako, E. Sanchez, M. L. Sanchez, B. Santiago, A. Saro, V. Scarpine, D. Scolnic, A. Scott, S. Serrano, I. Sevilla-Noarbe, E. Sheldon, N. Shipp, M. L. Silveira, R. C. Smith, J. A. Smith, M. Smith, M. Soares-Santos, F. Sobre ira, J. Song, A. Stebbins, E. Suchyta, M. Sullivan, M. E. C. Swanson, G. Tarle, J. Thaler, D. Thomas, R. C. Thomas, M. A. Troxel, D. L. Tucker, V. Vikram, A. K. Vivas, A. R. Wal ker, R. H. Wechsler,

J. Weller, W. Wester, R. C. Wolf, H. Wu, B. Yanny, A. Zenteno, Y. Zhang, and J. Zuntz. "The Dark Energy Survey Data Release 1." *ArXiv e-prints* .

Abell, G. O. "The Distribution of Rich Clusters of Galaxies." *ApJS* 3: (1958) 211.

Abell, G. O., H. G. Corwin, Jr., and R. P. Olowin. "A catalog of rich clusters of galaxies." *ApJS* 70: (1989) 1–138.

Ahn, C. P., R. Alexandroff, C. Allende Prieto, F. Anders, S. F. Anderson, T. Anderton, B. H. Andrews, É. Aubourg, S. Bailey, F. A. Bastien, and et al. "The Tenth Data Release of the Sloan Digital Sky Survey: First Spectroscopic Data from the SDSS-III Apache Point Observatory Galactic Evolution Experiment." *ApJS* 211: 17.

Aihara, H., R. Armstrong, S. Bickerton, J. Bosch, J. Coupon, H. Furusawa, Y. Hayashi, H. Ikeda, Y. Kamata, H. Karoji, S. Kawanomoto, M. Koike, Y. Komiyama, R. H. Lupton, S. Mineo, H. Miyatake, S. Miyazaki, T. Morokuma, Y. Obuchi, Y. Oishi, Y. Okura, P. A. Price, T. Takata, M. M. Tanaka, M. Tanaka, Y. Tanaka, T. Uchida, F. Uraguchi, Y. Utsumi, S.-Y. Wang, Y. Yamada, H. Yamanoi, N. Yasuda, N. Arimoto, M. Chiba, F. Finet, H. Fujimori, S. Fujimoto, J. Furusawa, T. Goto, A. Goulding, J. E. Gunn, Y. Harikane, T. Hattori, M. Hayashi, K. G. Helminiak, R. Higuchi, C. Hikage, P. T. P. Ho, B.-C. Hsieh, K. Huang, S. Huang, M. Imanishi, I. Iwata, A. T. Jaelani, H.-Y. Jian, N. Kashikawa, N. Katayama, T. Kojima, A. Konno, S. Koshida, A. Leauthaud, C.-H. Lee, L. Lin, Y.-T. Lin, R. Mandelbaum, Y. Matsuoka, E. Medezinski, S. Miyama, R. Momose, A. More, S. More, S. Mukae, R. Murata, H. Murayama, T. Nagao, F. Nakata, H. Niikura, A. J. Nishizawa, M. Oguri, N. Okabe, Y. Ono, M. Onodera, M. Onoue, M. Ouchi, T.-S. Pyo, T. Shibuya, K. Shimasaku, M. Simet, J. Speagle, D. N. Spergel, M. A. Strauss, Y. Sugahara, N. Sugiyama, Y. Suto, N. Suzuki, P. J. Tait, M. Takada, T. Terai, Y. Toba, E. L. Turner, H. Uchiyama, K. Umetsu, Y. Urata, T. Usuda, S. Yeh, and S. Yuma. "First Data Release of the Hyper Suprime-Cam Subaru Strategic Program." *ArXiv e-prints* .

Akritas, M. G., and M. A. Bershady. "Linear Regression for Astronomical Data with Measurement Errors and Intrinsic Scatter." *ApJ* 470: (1996) 706.

Allen, S. W., A. E. Evrard, and A. B. Mantz. "Cosmological Parameters from Observations of Galaxy Clusters." *ARA&A* 49: (2011) 409–470.

Allen, S. W., D. A. Rapetti, R. W. Schmidt, H. Ebeling, R. G. Morris, and A. C. Fabian. "Improved constraints on dark energy from Chandra X-ray observations of the largest relaxed galaxy clusters." *MNRAS* 383: (2008) 879–896.

AMI Consortium, T. W. Shimwell, C. Rodríguez-Gonzálvez, F. Feroz, T. M. O. Franzen, K. J. B. Grainge, M. P. Hobson, N. Hurley-Walker, A. N. Lasenby, E. J. Lloyd-Davies, M. Olamaie, Y. C. Perrott, G. G. Pooley, C. Rumsey, A. K. Romer, R. D. E. Saunders, A. M. M. Scaife, M. P. Schammel, P. F. Scott, D. J. Titterington, and E. M. Waldram. "Sunyaev-Zel'dovich observations with AMI of the hottest galaxy clusters detected in the XMM-Newton Cluster Survey." *MNRAS* 433: (2013) 2920–2937.

Andreon, S., G. Trinchieri, A. Moretti, and J. Wang. "Intrinsic scatter of caustic masses and hydrostatic bias: An observational study." *A&A* 606: A25.

Annis, J., M. Soares-Santos, M. A. Strauss, A. C. Becker, S. Dodelson, X. Fan, J. E. Gunn, J. Hao, Ž. Ivezić, S. Jester, L. Jiang, D. E. Johnston, J. M. Kubo, H. Lampeitl, H. Lin, R. H. Lupton, G. Miknaitis, H.-J. Seo, M. Simet, and B. Yanny. "The Sloan Digital Sky Survey Coadd: 275 deg^2 of Deep Sloan Digital Sky Survey Imaging on Stripe 82." *ApJ* 794: 120.

Arnaud, K. A. "XSPEC: The First Ten Years." *Astronomical Data Analysis Software and Systems V* 101: (1996) 17. http://adsabs.harvard.edu/abs/1996ASPC..101...17A.

Arnaud, M., E. Pointecouteau, and G. W. Pratt. "The structural and scaling properties of nearby galaxy clusters. II. The M-T relation." *Astronomy and Astrophysics* 441: (2005) 893–903. http://adsabs.harvard.edu/abs/2005A{&}A...435....1P.

Arnaud, M., E. Pointecouteau, and G. W. Pratt. "Calibration of the galaxy cluster M{500}-Y{X} relation with XMM-Newton." *A&A* 474: (2007) L37–L40.

Baldi, A. S., M. De Petris, F. Sembolini, G. Yepes, L. Lamagna, and E. Rasia. "On the coherent rotation of diffuse matter in numerical simulations of clusters of galaxies." *MNRAS* 465: (2017) 2584–2594.

Bartelmann, M., and M. Steinmetz. "A Comparison of X-ray and Strong Lensing Properties of Simulated X-ray Clusters." *MNRAS* 283: (1996) 431–446.

Basilakos, S., M. Plionis, and S. J. Maddox. "The apparent and intrinsic shape of the APM galaxy clusters." *MNRAS* 316: (2000) 779–785.

Bautz, L. P., and W. W. Morgan. "On the Classification of the Forms of Clusters of Galaxies." *ApJL* 162: (1970) L149.

Baxter, E. J., E. Rozo, B. Jain, E. Rykoff, and R. H. Wechsler. "Constraining the mass-richness relationship of redMaPPer clusters with angular clustering." *MNRAS* 463: (2016) 205–221.

Becker, M. R., and A. V. Kravtsov. "On the Accuracy of Weak-lensing Cluster Mass Reconstructions." *ApJ* 740: 25.

Beers, T. C., K. Flynn, and K. Gebhardt. "Measures of location and scale for velocities in clusters of galaxies - A robust approach." *AJ* 100: (1990) 32–46.

Benítez, N. "Bayesian Photometric Redshift Estimation." *ApJ* 536: (2000) 571–583.

Bermeo-Hernandez et al., A. .

Bertin, E. "Displaying Digital Deep Sky Images." In *Astronomical Data Analysis Software and Systems XXI*, edited by P. Ballester, D. Egret, and N. P. F. Lorente. 2012, volume 461 of *Astronomical Society of the Pacific Conference Series*, 263.

Bertin, E., Y. Mellier, M. Radovich, G. Missonnier, P. Didelon, and B. Morin. "The TERAPIX Pipeline." In *Astronomical Data Analysis Software and Systems XI*, edited by D. A. Bohlender, D. Durand, and T. H. Handley. 2002, volume 281 of *Astronomical Society of the Pacific Conference Series*, 228.

Bianconi, M., S. Ettori, and C. Nipoti. "Gas rotation in galaxy clusters: signatures and detectability in X-rays." *MNRAS* 434: (2013) 1565–1575.

Bleem, L. E., B. Stalder, T. de Haan, K. A. Aird, S. W. Allen, D. E. Applegate, M. L. N. Ashby, M. Bautz, M. Bayliss, B. A. Benson, S. Bocquet, M. Brodwin, J. E. Carlstrom, C. L. Chang, I. Chiu, H. M. Cho, A. Clocchiatti, T. M. Crawford, A. T. Crites, S. Desai, J. P. Dietrich, M. A. Dobbs, R. J. Foley, W. R. Forman, E. M. George, M. D. Gladders, A. H. Gonzalez, N. W. Halverson, C. Hennig, H. Hoekstra, G. P. Holder, W. L. Holzapfel, J. D. Hrubes, C. Jones, R. Keisler, L. Knox, A. T. Lee, E. M. Leitch, J. Liu, M. Lueker, D. Luong-Van, A. Mantz, D. P. Marrone, M. McDonald, J. J. McMahon, S. S. Meyer, L. Mocanu, J. J. Mohr, S. S. Murray, S. Padin, C. Pryke, C. L. Reichardt, A. Rest, J. Ruel, J. E. Ruhl, B. R. Saliwanchik, A. Saro, J. T. Sayre, K. K. Schaffer, T. Schrabback, E. Shirokoff, J. Song, H. G. Spieler, S. A. Stanford, Z. Staniszewski, A. A. Stark, K. T. Story, C. W. Stubbs, K. Vanderlinde, J. D. Vieira, A. Vikhlinin, R. Williamson, O. Zahn, and A. Zenteno. "Galaxy Clusters Discovered via the Sunyaev-Zel'dovich Effect in the 2500-Square-Degree SPT-SZ Survey." *ApJS* 216: 27.

Boch, T., and P. Fernique. "Aladin Lite: Embed your Sky in the Browser." In *Astronomical Data Analysis Software and Systems XXIII*, edited by N. Manset, and P. Forshay. 2014, volume 485 of *Astronomical Society of the Pacific Conference Series*, 277.

Böhringer, H., P. Schuecker, L. Guzzo, C. A. Collins, W. Voges, R. G. Cruddace, A. Ortiz-Gil, G. Chincarini, S. De Grandi, A. C. Edge, H. T. MacGillivray, D. M. Neumann, S. Schindler, and P. Shaver. "The ROSAT-ESO Flux Limited X-ray (REFLEX) Galaxy cluster survey. V. The cluster catalogue." *A&A* 425: (2004) 367–383.

Böhringer, H., P. Schuecker, L. Guzzo, C. A. Collins, W. Voges, S. Schindler, D. M. Neumann, R. G. Cruddace, S. De Grandi, G. Chincarini, A. C. Edge, H. T. MacGillivray, and P. Shaver. "The ROSAT-ESO flux limited X-ray (REFLEX) galaxy cluster survey. I. The construction of the cluster sample." *A&A* 369: (2001) 826–850.

Böhringer, H., W. Voges, J. P. Huchra, B. McLean, R. Giacconi, P. Rosati, R. Burg, J. Mader, P. Schuecker, D. Simiç, S. Komossa, T. H. Reiprich, J. Retzlaff, and J. Trümper. "The Northern ROSAT All-Sky (NORAS) Galaxy Cluster Survey. I. X-Ray Properties of Clusters Detected as Extended X-Ray Sources." *ApJS* 129: (2000) 435–474.

Bond, J. R., L. Kofman, and D. Pogosyan. "How filaments of galaxies are woven into the cosmic web." *Nature* 380: (1996) 603–606.

Bonnarel, F., P. Fernique, O. Bienaymé, D. Egret, F. Genova, M. Louys, F. Ochsenbein, M. Wenger, and J. G. Bartlett. "The ALADIN interactive sky atlas. A reference tool for identification of astronomical sources." *A&AS* 143: (2000) 33–40.

Bonometto, S. A., and S. Matarrese. "The contribution to baryon excess from gravitational interaction after the Planck time." *Physics Letters B* 110: (1982) 456–460.

Borgani, S. "Cosmology with Clusters of Galaxies." In *A Pan-Chromatic View of Clusters of Galaxies and the Large-Scale Structure*, edited by M. Plionis, O. López-Cruz, and D. Hughes. 2008, volume 740 of *Lecture Notes in Physics, Berlin Springer Verlag*, 24.

Bower, R. G., J. R. Lucey, and R. S. Ellis. "Precision photometry of early-type galaxies in the Coma and Virgo clusters: A test of the universality of the colour-magnitude relation. I - The data. II. Analysis." *MNRAS* 254: (1992) 589–613.

Brammer, G. B., P. G. van Dokkum, and P. Coppi. "EAZY: A Fast, Public Photometric Redshift Code." *ApJ* 686: 1503-1513.

Bravo-Alfaro, H., C. A. Caretta, C. Lobo, F. Durret, and T. Scott. "Galaxy evolution in Abell 85. I. Cluster substructure and environmental effects on the blue galaxy population." *A&A* 495: (2009) 379–387.

Burenin, R. A., A. Vikhlinin, A. Hornstrup, H. Ebeling, H. Quintana, and A. Mescheryakov. "The 400 Square Degree ROSAT PSPC Galaxy Cluster Survey: Catalog and Statistical Calibration." *ApJS* 172: (2007) 561–582.

Ceccarelli, L., D. Paz, M. Lares, N. Padilla, and D. G. Lambas. "Clues on void evolution - I. Large-scale galaxy distributions around voids." *MNRAS* 434: (2013) 1435–1442.

Chincarini, G., and H. J. Rood. "The structure of the galaxy cluster A 194." *ApJ* 214: (1977) 351–358.

Chluba, J., and K. Mannheim. "Kinetic Sunyaev-Zeldovich effect from galaxy cluster rotation." *A&A* 396: (2002) 419–427.

Clerc, N., A. Merloni, Y.-Y. Zhang, A. Finoguenov, T. Dwelly, K. Nandra, C. Collins, K. Dawson, J.-P. Kneib, E. Rozo, E. Rykoff, T. Sadibekova, J. Brownstein, Y.-T. Lin, J. Ridl, M. Salvato, A. Schwope, M. Steinmetz, H.-J. Seo, and J. Tinker. "SPIDERS: the spectroscopic follow-up of X-ray selected clusters of galaxies in SDSS-IV." *MNRAS* 463: (2016) 4490–4515.

Clerc, N., T. Sadibekova, M. Pierre, F. Pacaud, J.-P. Le Fèvre, C. Adami, B. Altieri, and I. Valtchanov. "The cosmological analysis of X-ray cluster surveys - II. Application of the CR-HR method to the XMM archive." *MNRAS* 423: (2012) 3561–3583.

Cooray, A., and X. Chen. "Kinetic Sunyaev-Zeldovich Effect from Halo Rotation." *ApJ* 573: (2002) 43–50.

Coronel-Brizio, H. F., and A. R. Hernández-Montoya. "The Anderson-Darling test of fit for the power-law distribution from left-censored samples." *Physica A Statistical Mechanics and its Applications* 389: (2010) 3508–3515.

Cortese, L., G. Gavazzi, A. Boselli, J. Iglesias-Paramo, and L. Carrasco. "Multiple merging in the Abell cluster 1367." *A&A* 425: (2004) 429–441.

Cross, N. J. G., R. S. Collins, R. G. Mann, M. A. Read, E. T. W. Sutorius, R. P. Blake, M. Holliman, N. C. Hambly, J. P. Emerson, A. Lawrence, and K. T. Noddle. "The VISTA Science Archive." *A&A* 548: A119.

Cruz, M., L. Cayón, E. Martínez-González, P. Vielva, and J. Jin. "The Non-Gaussian Cold Spot in the 3 Year Wilkinson Microwave Anisotropy Probe Data." *ApJ* 655: (2007) 11–20.

Csabai, I., T. Budavári, A. J. Connolly, A. S. Szalay, Z. Győry, N. Benítez, J. Annis, J. Brinkmann, D. Eisenstein, M. Fukugita, J. Gunn, S. Kent, R. Lupton, R. C. Nichol, and C. Stoughton. "The Application of Photometric Redshifts to the SDSS Early Data Release." *AJ* 125: (2003) 580–592.

Danese, L., G. de Zotti, and G. di Tullio. "On velocity dispersions of galaxies in rich clusters." *A&A* 82: (1980) 322–327.

Darvish, B., N. Z. Scoville, C. Martin, B. Mobasher, T. Diaz-Santos, and L. Shen. "Similar Scaling Relations for the Gas Content of Galaxies across Environments to z ˜ 3.5." *ArXiv e-prints* .

Davis, M., G. Efstathiou, C. S. Frenk, and S. D. M. White. "The evolution of large-scale structure in a universe dominated by cold dark matter." *ApJ* 292: (1985) 371–394.

de Haan, T., B. A. Benson, L. E. Bleem, S. W. Allen, D. E. Applegate, M. L. N. Ashby, M. Bautz, M. Bayliss, S. Bocquet, M. Brodwin, J. E. Carlstrom, C. L. Chang, I. Chiu, H.-M. Cho, A. Clocchiatti, T. M. Crawford, A. T. Crites, S. Desai, J. P. Dietrich, M. A. Dobbs, A. N. Doucouliagos, R. J. Foley, W. R. Forman, G. P. Garmire, E. M. George, M. D. Gladders, A. H. Gonzalez, N. Gupta, N. W. Halverson, J. Hlavacek-Larrondo, H. Hoekstra, G. P. Holder, W. L. Holzapfel, Z. Hou, J. D. Hrubes, N. Huang, C. Jones, R. Keisler, L. Knox, A. T. Lee, E. M. Leitch, A. von der Linden, D. Luong-Van, A. Mantz, D. P. Marrone, M. McDonald, J. J. McMahon, S. S. Meyer, L. M. Mocanu, J. J. Mohr, S. S. Murray, S. Padin, C. Pryke, D. Rapetti, C. L. Reichardt, A. Rest, J. Ruel, J. E. Ruhl, B. R. Saliwanchik, A. Saro, J. T. Sayre, K. K. Schaffer, T. Schrabback, E. Shirokoff, J. Song, H. G. Spieler, B. Stalder, S. A. Stanford, Z. Staniszewski, A. A. Stark, K. T. Story, C. W. Stubbs, K. Vanderlinde, J. D. Vieira, A. Vikhlinin, R. Williamson, and A. Zenteno. "Cosmological Constraints from Galaxy Clusters in the 2500 Square-degree SPT-SZ Survey." *ApJ* 832: 95.

Dolag, K., S. Borgani, G. Murante, and V. Springel. "Substructures in hydrodynamical cluster simulations." *MNRAS* 399: (2009) 497–514.

Dubinski, J. "The Origin of the Brightest Cluster Galaxies." *ApJ* 502: (1998) 141–149.

Dunkley, J., E. Komatsu, M. R. Nolta, D. N. Spergel, D. Larson, G. Hinshaw, L. Page, C. L. Bennett, B. Gold, N. Jarosik, J. L. Weiland, M. Halpern, R. S. Hill, A. Kogut, M. Limon, S. S. Meyer, G. S. Tucker, E. Wollack, and E. L. Wright. "Five-Year Wilkinson Microwave Anisotropy Probe Observations: Likelihoods and Parameters from the WMAP Data." *ApJS* 180: (2009) 306–329.

Ebeling, H., A. C. Edge, H. Bohringer, S. W. Allen, C. S. Crawford, A. C. Fabian, W. Voges, and J. P. Huchra. "The ROSAT Brightest Cluster Sample - I. The compilation of the sample and the cluster log N-log S distribution." *MNRAS* 301: (1998) 881–914.

Ebeling, H., A. C. Edge, and J. P. Henry. "MACS: A Quest for the Most Massive Galaxy Clusters in the Universe." *ApJ* 553: (2001) 668–676.

Ebeling, H., A. C. Edge, A. Mantz, E. Barrett, J. P. Henry, C. J. Ma, and L. van Speybroeck. "The X-ray brightest clusters of galaxies from the Massive Cluster Survey." *MNRAS* 407: (2010) 83–93.

Ebrahimpour, L., P. T. P. Viana, M. Manolopoulou, C. Vergara-Cervantes, A. K. Romer, S. Bhargava, P. Giles, A. Bermeo-Hernandez, C. A. Collins, M. Hilton, B. Hoyle, A. R. Liddle, R. G. Mann, J. A. Mayers, C. J. Miller, R. C. Nichol, P. J. Rooney, M. Sahlén, and J. P. Stott. "The XMM Cluster Survey: joint modelling of the $L\_\mathrm{X} - T$ scaling relation for clusters and groups of galaxies." *ArXiv e-prints* .

Eddington, A. S. "The Expansion of the Universe." *JRASC* 26: (1932) 26.

Edge, A. C., G. C. Stewart, A. C. Fabian, and K. A. Arnaud. "An X-Ray Flux-Limited Sample of Clusters of Galaxies - Evidence for Evolution of the Luminosity Function." *MNRAS* 245: (1990) 559.

Einasto, M., L. J. Liivamägi, E. Tempel, E. Saar, J. Vennik, P. Nurmi, M. Gramann, J. Einasto, E. Tago, P. Heinämäki, A. Ahvensalmi, and V. J. Martínez. "Multimodality of rich clusters from the SDSS DR8 within the supercluster-void network." *A&A* 542: A36.

Einstein, A. "Kosmologische Betrachtungen zur allgemeinen Relativitätstheorie." *Sitzungsberichte der Königlich Preußischen Akademie der Wissenschaften (Berlin), Seite 142-152.* .

Eisenstein, D. J., D. H. Weinberg, E. Agol, H. Aihara, C. Allende Prieto, S. F. Anderson, J. A. Arns, É. Aubourg, S. Bailey, E. Balbinot, and et al. "SDSS-III: Massive Spectroscopic Surveys of the Distant Universe, the Milky Way, and Extra-Solar Planetary Systems." *AJ* 142: 72.

Fang, T., P. Humphrey, and D. Buote. "Rotation and Turbulence of the Hot Intracluster Medium in Galaxy Clusters." *ApJ* 691: (2009) 1648–1659.

Friedmann, A. "Über die Krümmung des Raumes." *Zeitschrift fur Physik* 10: (1922) 377–386.

Gioia, I. M., J. P. Henry, T. Maccacaro, S. L. Morris, J. T. Stocke, and A. Wolter. "The Extended Medium Sensitivity Survey distant cluster sample - X-ray cosmological evolution." *ApJ* 356: (1990) L35–L38.

Gladders, M. D., O. López-Cruz, H. K. C. Yee, and T. Kodama. "The Slope of the Cluster Elliptical Red Sequence: A Probe of Cluster Evolution." *ApJ* 501: (1998) 571–577.

Gladders, M. D., and H. K. C. Yee. "The Red-Sequence Cluster Survey. I. The Survey and Cluster Catalogs for Patches RCS 0926+37 and RCS 1327+29." *ApJS* 157: (2005) 1–29.

Gunn, J. E., J. G. Hoessel, and J. B. Oke. "A systematic survey for distant galaxy clusters." *ApJ* 306: (1986) 30–37.

Gupta, N., A. Saro, J. J. Mohr, K. Dolag, and J. Liu. "SZE observables, pressure profiles and centre offsets in Magneticum simulation galaxy clusters." *MNRAS* 469: (2017) 3069–3087.

Guth, A. H. "Inflation and eternal inflation." *Phys. Rep.* 333: (2000) 555–574.

Halliday, C., B. Milvang-Jensen, S. Poirier, B. M. Poggianti, P. Jablonka, A. Aragón-Salamanca, R. P. Saglia, G. De Lucia, R. Pelló, L. Simard, D. I. Clowe, G. Rudnick, J. J. Dalcanton, S. D. M. White, and D. Zaritsky. "Spectroscopy of clusters in the ESO Distant Cluster Survey (EDisCS). Redshifts, velocity dispersions and substructure for 5 clusters." *A&AP* 427: (2004) 397–413.

Hallman, E. J., B. W. O'Shea, J. O. Burns, M. L. Norman, R. Harkness, and R. Wagner. "The Santa Fe Light Cone Simulation Project. I. Confusion and the Warm-Hot Intergalactic Medium in Upcoming Sunyaev-Zel'dovich Effect Surveys." *ApJ* 671: (2007) 27–39.

Hambly, N. C., R. S. Collins, N. J. G. Cross, R. G. Mann, M. A. Read, E. T. W. Sutorius, I. Bond, J. Bryant, J. P. Emerson, A. Lawrence, L. Rimoldini, J. M. Stewart, P. M. Williams, A. Adamson, P. Hirst, S. Dye, and S. J. Warren. "The WFCAM Science Archive." *MNRAS* 384: (2008) 637–662.

Hamden, E. T., C. M. Simpson, K. V. Johnston, and D. M. Lee. "Measuring Transverse Motions for Nearby Galaxy Clusters." *ApJ* 716: (2010) L205–L208.

Hansen, S. M., E. S. Sheldon, R. H. Wechsler, and B. P. Koester. "The Galaxy Content of SDSS Clusters and Groups." *ApJ* 699: (2009) 1333–1353.

Hao, J., B. P. Koester, T. A. Mckay, E. S. Rykoff, E. Rozo, A. Evrard, J. Annis, M. Becker, M. Busha, D. Gerdes, D. E. Johnston, E. Sheldon, and R. H. Wechsler. "Precision Measurements of the Cluster Red Sequence Using an Error-Corrected Gaussian Mixture Model." *ApJ* 702: (2009) 745–758.

Hao, J., T. A. McKay, B. P. Koester, E. S. Rykoff, E. Rozo, J. Annis, R. H. Wechsler, A. Evrard, S. R. Siegel, M. Becker, M. Busha, D. Gerdes, D. E. Johnston, and E. Sheldon. "A GMBCG Galaxy Cluster Catalog of 55,424 Rich Clusters from SDSS DR7." *ApJS* 191: (2010) 254–274.

Harrison, C. D., C. J. Miller, J. W. Richards, E. J. Lloyd-Davies, B. Hoyle, A. K. Romer, N. Mehrtens, M. Hilton, J. P. Stott, D. Capozzi, C. A. Collins, P.-J. Deadman, A. R. Liddle, M. Sahlén, S. A. Stanford, and P. T. P. Viana. "The XMM Cluster Survey: The Stellar Mass Assembly of Fossil Galaxies." *ApJ* 752: 12.

Hasselfield, M., M. Hilton, T. A. Marriage, G. E. Addison, L. F. Barrientos, N. Battaglia, E. S. Battistelli, J. R. Bond, D. Crichton, S. Das, M. J. Devlin, S. R. Dicker, J. Dunkley, R. Dünner, J. W. Fowler, M. B. Gralla, A. Hajian, M. Halpern, A. D. Hincks, R. Hlozek, J. P. Hughes, L. Infante, K. D. Irwin, A. Kosowsky, D. Marsden, F. Menanteau, K. Moodley, M. D. Niemack, M. R. Nolta, L. A. Page, B. Partridge, E. D. Reese, B. L. Schmitt, N. Sehgal, B. D. Sherwin, J. Sievers, C. Sifón, D. N. Spergel, S. T. Staggs, D. S. Swetz, E. R. Switzer, R. Thornton, H. Trac, and E. J. Wollack. "The Atacama Cosmology Telescope: Sunyaev-Zel'dovich selected galaxy clusters at 148 GHz from three seasons of data." *J. Cosmology Astropart. Phys.* 7: 008.

Heymans, C., L. Van Waerbeke, L. Miller, T. Erben, H. Hildebrandt, H. Hoekstra, T. D. Kitching, Y. Mellier, P. Simon, C. Bonnett, J. Coupon, L. Fu, J. Harnois Déraps, M. J. Hudson, M. Kilbinger, K. Kuijken, B. Rowe, T. Schrabback, E. Semboloni, E. van Uitert, S. Vafaei, and M. Velander. "CFHTLenS: the Canada-France-Hawaii Telescope Lensing Survey." *MNRAS* 427: (2012) 146–166.

Hilton, M., C. A. Collins, S. A. Stanford, C. Lidman, K. S. Dawson, M. Davidson, S. T. Kay, A. R. Liddle, R. G. Mann, C. J. Miller, R. C. Nichol, A. K. Romer, K. Sabirli, P. T. P. Viana, and M. J. West. "The XMM Cluster Survey: The Dynamical State of XMMXCS J2215.9-1738 at z = 1.457." *ApJ* 670: (2007) 1000–1009.

Hilton, M., M. Hasselfield, C. Sifón, N. Battaglia, S. Aiola, V. Bharadwaj, J. R. Bond, S. K. Choi, D. Crichton, R. Datta, M. J. Devlin, J. Dunkley, R. Dünner, P. A. Gallardo, M. Gralla, A. D. Hincks, S.-P. P. Ho, J. Hubmayr, K. M. Huffenberger, J. P. Hughes, B. J. Koopman, A. Kosowsky, T. Louis, M. S. Madhavacheril, T. A. Marriage, L. Maurin, J. McMahon, H. Miyatake, K. Moodley, S. Naess, F. Nati, L. Newburgh, M. D. Niemack, M. Oguri, L. A. Page, B. Partridge, B. L. Schmitt, J. Sievers, D. N. Spergel, S. T. Staggs, H. Trac, A. van Engelen, E. M. Vavagiakis, and E. J. Wollack. "The Atacama Cosmology Telescope: The Two-Season ACTPol Sunyaev-Zel'dovich Effect Selected Cluster Catalog." *ArXiv e-prints* .

Hilton, M., E. Lloyd-Davies, S. A. Stanford, J. P. Stott, C. A. Collins, A. K. Romer, M. Hosmer, B. Hoyle, S. T. Kay, A. R. Liddle, N. Mehrtens, C. J. Miller, M. Sahlén, and P. T. P. Viana. "The XMM Cluster Survey: Active Galactic Nuclei and Starburst Galaxies in XMMXCS J2215.9-1738 at z = 1.46." *ApJ* 718: (2010) 133–147.

Hilton, M., A. K. Romer, S. T. Kay, N. Mehrtens, E. J. Lloyd-Davies, P. A. Thomas, C. J. Short, J. A. Mayers, P. J. Rooney, J. P. Stott, C. A. Collins, C. D. Harrison, B. Hoyle, A. R. Liddle, R. G. Mann, C. J. Miller, M. Sahlén, P. T. P. Viana, M. Davidson, M. Hosmer, R. C. Nichol, K. Sabirli, S. A. Stanford, and M. J. West. "The XMM Cluster Survey: evidence for energy injection at high redshift from evolution of the X-ray luminosity-temperature relation." *MNRAS* 424: (2012) 2086–2096.

Hilton, M., S. A. Stanford, J. P. Stott, C. A. Collins, B. Hoyle, M. Davidson, M. Hosmer, S. T. Kay, A. R. Liddle, E. Lloyd-Davies, R. G. Mann, N. Mehrtens, C. J. Miller, R. C. Nichol, A. K. Romer, K. Sabirli, M. Sahlén, P. T. P. Viana, M. J. West, K. Barbary, K. S. Dawson, J. Meyers, S. Perlmutter, D. Rubin, and N. Suzuki. "The XMM Cluster Survey: Galaxy Morphologies and the Color-Magnitude Relation in XMMXCS J2215.9 - 1738 at z = 1.46." *ApJ* 697: (2009) 436–451.

Hogg, D. W., I. K. Baldry, M. R. Blanton, and D. J. Eisenstein. "The K correction." *ArXiv Astrophysics e-prints* .

Holz, D. E., and S. Perlmutter. "The Most Massive Objects in the Universe." *ApJ* 755: L36.

Hood, R. J., and R. G. Mann. "Characterizing the optical properties of galaxy clusters with GMPhoRCC." *MNRAS* 469: (2017) 3851–3871.

Hoyle, B., R. Jimenez, and L. Verde. "Implications of multiple high-redshift galaxy clusters." *Phys. Rev. D* 83, 10: 103502.

Hoyle, F., M. S. Vogeley, and D. Pan. "Photometric properties of void galaxies in the Sloan Digital Sky Survey Data Release 7." *MNRAS* 426: (2012) 3041–3050.

Hubble, E. "A Relation between Distance and Radial Velocity among Extra-Galactic Nebulae." *Proceedings of the National Academy of Science* 15: (1929) 168–173.

Hubble, E. P. "The classification of spiral nebulae." *The Observatory* 50: (1927) 276–281.

Hwang, H. S., and M. G. Lee. "Searching for Rotating Galaxy Clusters in SDSS and 2dFGRS." *ApJ* 662: (2007) 236–249.

Jee, M. J., P. Rosati, H. C. Ford, K. S. Dawson, C. Lidman, S. Perlmutter, R. Demarco, V. Strazzullo, C. Mullis, H. Böhringer, and R. Fassbender. "Hubble Space Telescope Weak-lensing Study of the Galaxy Cluster XMMU J2235.3 - 2557 at z ˜ 1.4: A Surprisingly Massive Galaxy Cluster When the Universe is One-third of its Current Age." *ApJ* 704: (2009) 672–686.

Jones, C., and W. Forman. "Einstein Observatory Images of Clusters of Galaxies." *ApJ* 511: (1999) 65–83.

Kalinkov, M., T. Valchanov, I. Valtchanov, I. Kuneva, and M. Dissanska. "Rotation of the cluster of galaxies A2107." *MNRAS* 359: (2005) 1491–1497.

Kapińska, A. D., I. Terentev, O. I. Wong, S. S. Shabala, H. Andernach, L. Rudnick, L. Storer, J. K. Banfield, K. W. Willett, F. de Gasperin, C. J. Lintott, Á. R. López-Sánchez, E. Middelberg, R. P. Norris, K. Schawinski, N. Seymour, and B. Simmons. "Radio Galaxy Zoo: A Search for Hybrid Morphology Radio Galaxies." *AJ* 154: 253.

King, I. "The structure of star clusters. I. an empirical density law." *AJ* 67: (1962) 471.

Koester, B. P., T. A. McKay, J. Annis, R. H. Wechsler, A. Evrard, L. Bleem, M. Becker, D. Johnston, E. Sheldon, R. Nichol, C. Miller, R. Scranton, N. Bahcall, J. Barentine, H. Brewington, J. Brinkmann, M. Harvanek, S. Kleinman, J. Krzesinski, D. Long, A. Nitta, D. P. Schneider, S. Sneddin, W. Voges, and D. York. "A MaxBCG Catalog of 13,823 Galaxy Clusters from the Sloan Digital Sky Survey." *ApJ* 660: (2007) 239–255.

Komatsu, E., K. M. Smith, J. Dunkley, C. L. Bennett, B. Gold, G. Hinshaw, N. Jarosik, D. Larson, M. R. Nolta, L. Page, D. N. Spergel, M. Halpern, R. S. Hill, A. Kogut, M. Limon, S. S. Meyer, N. Odegard, G. S. Tucker, J. L. Weiland, E. Wollack, and E. L. Wright. "Seven-year Wilkinson Microwave Anisotropy Probe (WMAP) Observations: Cosmological Interpretation." *ApJS* 192: 18.

Koopmans, A. L. H., D. B. Owen, and J. I. Rosenblatt. "Confidence Intervals for the Coefficient of Variation for the Normal and Log Normal Distributions." *Biometrika* 51, 1: (1964) 25–32.

Kowalski, M., D. Rubin, G. Aldering, R. J. Agostinho, A. Amadon, R. Amanullah, C. Balland, K. Barbary, G. Blanc, P. J. Challis, A. Conley, N. V. Connolly, R. Covarrubias, K. S. Dawson, S. E. Deustua, R. Ellis, S. Fabbro, V. Fadeyev, X. Fan, B. Farris, G. Folatelli, B. L. Frye, G. Garavini, E. L. Gates, L. Germany, G. Goldhaber, B. Goldman, A. Goobar, D. E. Groom, J. Haissinski, D. Hardin, I. Hook, S. Kent, A. G. Kim, R. A. Knop, C. Lidman, E. V. Linder, J. Mendez, J. Meyers, G. J. Miller, M. Moniez, A. M. Mourão, H. Newberg, S. Nobili, P. E. Nugent, R. Pain, O. Perdereau, S. Perlmutter, M. M. Phillips, V. Prasad, R. Quimby, N. Regnault, J. Rich, E. P. Rubenstein, P. Ruiz-Lapuente, F. D. Santos, B. E. Schaefer, R. A. Schommer, R. C. Smith, A. M. Soderberg, A. L. Spadafora, L.-G. Strolger, M. Strovink, N. B. Suntzeff, N. Suzuki, R. C. Thomas, N. A. Walton, L. Wang, W. M. Wood-Vasey, and J. L. Yun. "Improved Cosmological Constraints from New, Old, and Combined Supernova Data Sets." *ApJ* 686: 749-778.

Krause, E., C. M. Hirata, C. Martin, J. D. Neill, and T. K. Wyder. "Halo occupation distribution modelling of green valley galaxies." *MNRAS* 428: (2013) 2548–2564.

Kravtsov, A. V., and S. Borgani. "Formation of Galaxy Clusters." *Annual Review of Astronomy and Astrophysics* 50, 1: (2012) 353–409. http://arxiv.org/abs/1205.5556.

Land, K., A. Slosar, C. Lintott, D. Andreescu, S. Bamford, P. Murray, R. Nichol, M. J. Raddick, K. Schawinski, A. Szalay, D. Thomas, and J. Vandenberg. "Galaxy Zoo: the large-scale spin statistics of spiral galaxies in the Sloan Digital Sky Survey." *MNRAS* 388: (2008) 1686–1692.

Lemaître, G. "Expansion of the universe, A homogeneous universe of constant mass and increasing radius accounting for the radial velocity of extra-galactic nebulae." *MNRAS* 91: (1931) 483–490.

Liao, S., and L. Gao. "Impact of filaments on galaxy formation in their residing dark matter haloes." *ArXiv e-prints* .

Linde, A. "Inflationary cosmology." *Phys. Rep.* 333: (2000) 575–591.

Lintott, C. J., K. Schawinski, A. Slosar, K. Land, S. Bamford, D. Thomas, M. J. Raddick, R. C. Nichol, A. Szalay, D. Andreescu, P. Murray, and J. Vandenberg. "Galaxy Zoo: morphologies derived from visual inspection of galaxies from the Sloan Digital Sky Survey." *MNRAS* 389: (2008) 1179–1189.

Liu, T., P. Tozzi, E. Tundo, A. Moretti, P. Rosati, J.-X. Wang, G. Tagliaferri, S. Campana, and M. Giavalisco. "The Swift X-Ray Telescope Cluster Survey. III. Cluster Catalog from 2005-2012 Archival Data." *ApJS* 216: 28.

Lloyd-Davies, E. J., A. K. Romer, N. Mehrtens, M. Hosmer, M. Davidson, K. Sabirli, R. G. Mann, M. Hilton, A. R. Liddle, P. T. P. Viana, H. C. Campbell, C. A. Collins, E. N. Dubois, P. Freeman, C. D. Harrison, B. Hoyle, S. T. Kay, E. Kuwertz, C. J. Miller, R. C. Nichol, M. Sahlén, S. A. Stanford, and J. P. Stott. "The XMM Cluster Survey: X-ray analysis methodology." *MNRAS* 418: (2011) 14–53.

Łokas, E. L., F. Prada, R. Wojtak, M. Moles, and S. Gottlöber. "The complex velocity distribution of galaxies in Abell 1689: implications for mass modelling." *MNRAS* 366: (2006) L26–L30.

Manolopoulou, M., and M. Plionis. "Galaxy cluster's rotation." *MNRAS* 465: (2017) 2616–2633.

Manolopoulou et al., M. "The *XMM* Cluster Survey: Environmental dependence of X-ray and optical properties of galaxy clusters." *to be submitted to MNRAS* .

———. "The *XMM* Cluster Survey: The second XCS data release in the SDSS DR13 footprint." *to be submitted to MNRAS* .

Mantz, A., S. W. Allen, H. Ebeling, D. Rapetti, and A. Drlica-Wagner. "The observed growth of massive galaxy clusters - II. X-ray scaling relations." *MNRAS* 406: (2010a) 1773–1795.

Mantz, A., S. W. Allen, D. Rapetti, and H. Ebeling. "The observed growth of massive galaxy clusters - I. Statistical methods and cosmological constraints." *MNRAS* 406: (2010b) 1759–1772.

Mao, Q., A. A. Berlind, R. J. Scherrer, M. C. Neyrinck, R. Scoccimarro, J. L. Tinker, C. K. McBride, D. P. Schneider, K. Pan, D. Bizyaev, E. Malanushenko, and V. Malanushenko. "A Cosmic Void Catalog of SDSS DR12 BOSS Galaxies." *ApJ* 835: 161.

Marrone, D. P., G. P. Smith, N. Okabe, M. Bonamente, J. E. Carlstrom, T. L. Culverhouse, M. Gralla, C. H. Greer, N. Hasler, D. Hawkins, R. Hennessy, M. Joy, J. W. Lamb, E. M. Leitch, R. Martino, P. Mazzotta, A. Miller, T. Mroczkowski, S. Muchovej, T. Plagge, C. Pryke, A. J. R. Sanderson, M. Takada, D. Woody, and Y. Zhang. "LoCuSS: The Sunyaev-Zel'dovich Effect and Weak-lensing Mass Scaling Relation." *ApJ* 754: 119.

Martínez-González, E., M. Cruz, L. Cayón, and P. Vielva. "The non-Gaussian cold spot in WMAP." *New A Rev.* 50: (2006) 875–879.

Martizzi, D., and H. Agrusa. "Mass modeling of galaxy clusters: quantifying hydrostatic bias and contribution from non-thermal pressure." *ArXiv e-prints* .

Materne, J., and U. Hopp. "The cluster of galaxies SC0316-44 - Does it rotate?" *A&A* 124: (1983) L13–L15.

Matthews, D. J., J. A. Newman, A. L. Coil, M. C. Cooper, and S. D. J. Gwyn. "Extended Photometry for the DEEP2 Galaxy Redshift Survey: A Testbed for Photometric Redshift Experiments." *ApJS* 204: 21.

Maughan, B. J., P. A. Giles, K. J. Rines, A. Diaferio, M. J. Geller, N. Van Der Pyl, and M. Bonamente. "Hydrostatic and caustic mass profiles of galaxy clusters." *MNRAS* 461: (2016) 4182–4191.

Mayers, J. A., K. Romer, A. Fahari, J. P. Stott, P. Giles, P. J. Rooney, A. Bermeo-Hernandez, C. A. Collins, M. Hilton, B. Hoyle, A. R. Liddle, R. G. Mann, C. J. Miller, R. C. Nichol, M. Sahlén, C. Vergara-Cervantes, and P. T. P. Viana. "Correlations between X-ray properties and Black Hole Mass in AGN: towards a new method to estimate black hole mass from short exposure X-ray observations." *ArXiv e-prints* .

Mehrtens, N., A. K. Romer, M. Hilton, E. J. Lloyd-Davies, C. J. Miller, S. A. Stanford, M. Hosmer, B. Hoyle, C. A. Collins, A. R. Liddle, P. T. P. Viana, R. C. Nichol, J. P. Stott, E. N. Dubois, S. T. Kay, M. Sahlén, O. Young, C. J. Short, L. Christodoulou, W. A. Watson, M. Davidson, C. D. Harrison, L. Baruah, M. Smith, C. Burke, J. A. Mayers, P.-J. Deadman, P. J. Rooney, E. M. Edmondson, M. West, H. C. Campbell, A. C. Edge, R. G. Mann, K. Sabirli, D. Wake, C. Benoist, L. da Costa, M. A. G. Maia, and R. Ogando. "The XMM Cluster Survey: optical analysis methodology and the first data release." *MNRAS* 423: (2012) 1024–1052.

Mehrtens, N., A. K. Romer, R. C. Nichol, C. A. Collins, M. Sahlén, P. J. Rooney, J. A. Mayers, A. Bermeo-Hernandez, M. Bristow, D. Capozzi, L. Christodoulou, J. Comparat, M. Hilton, B. Hoyle, S. T. Kay, A. R. Liddle, R. G. Mann, K. Masters, C. J. Miller, J. K. Parejko, F. Prada, A. J. Ross, D. P. Schneider, J. P. Stott, A. Streblyanska, P. T. P. Viana, M. White, H. Wilcox, and I. Zehavi. "The XMM Cluster Survey: the halo occupation number of BOSS galaxies in X-ray clusters." *MNRAS* 463: (2016) 1929–1943.

Meneghetti, M., E. Rasia, J. Merten, F. Bellagamba, S. Ettori, P. Mazzotta, K. Dolag, and S. Marri. "Weighing simulated galaxy clusters using lensing and X-ray." *A&A* 514: A93.

Mewe, R., J. Lemen, and G. van den Oord. "Calculated X-radiation from optically thin plasmas. VI - Improved calculations for continuum emission and approximation formulae for nonrelativistic average Gaunt factors." *aaps* 65: (1986) 511–536.

Migkas, K., and T. H. Reiprich. "Anisotropy of the galaxy cluster X-ray luminosity-temperature relation." *ArXiv e-prints* .

Miller, C. J., A. K. Romer, S. A. Stanford, M. Hilton, M. Hosmer, N. Merhtens, and XCS Consortium. "The NOAO-XCS Survey Program." In *American Astronomical Society Meeting Abstracts*. 2006, volume 38 of *Bulletin of the American Astronomical Society*, 998.

Montero-Dorta, A. D., and F. Prada. "The SDSS DR6 luminosity functions of galaxies." *MNRAS* 399: (2009) 1106–1118.

Morrison, R., and D. McCammon. "Interstellar photoelectric absorption cross sections, 0.03-10 keV." *The Astrophysical Journal* 270: (1983) 119. http://adsabs.harvard.edu/doi/10.1086/161102.

Nadathur, S. "Testing cosmology with a catalogue of voids in the BOSS galaxy surveys." *MNRAS* 461: (2016) 358–370.

Nadathur, S., and S. Hotchkiss. "A robust public catalogue of voids and superclusters in the SDSS Data Release 7 galaxy surveys." *MNRAS* 440: (2014) 1248–1262.

———. "The nature of voids - II. Tracing underdensities with biased galaxies." *MNRAS* 454: (2015) 889–901.

Nagai, D., A. Vikhlinin, and A. V. Kravtsov. "Testing X-Ray Measurements of Galaxy Clusters with Cosmological Simulations." *ApJ* 655: (2007) 98–108.

Navarro, J. F., C. S. Frenk, and S. D. M. White. "A Universal Density Profile from Hierarchical Clustering." *ApJ* 490: (1997) 493–508.

Neyrinck, M. C. "ZOBOV: a parameter-free void-finding algorithm." *MNRAS* 386: (2008) 2101–2109.

Oegerle, W. R., and J. M. Hill. "Structure, rotation, and the peculiar velocity cD galaxy in Abell 2107." *AJ* 104: (1992) 2078–2085.

Oguri, M., Y.-T. Lin, S.-C. Lin, A. J. Nishizawa, A. More, S. More, B.-C. Hsieh, E. Medezinski, H. Miyatake, H.-Y. Jian, L. Lin, M. Takada, N. Okabe, J. S. Speagle, J. Coupon, A. Leauthaud, R. H. Lupton, S. Miyazaki, P. A. Price, M. Tanaka, I. Chiu, Y. Komiyama, Y. Okura, M. M. Tanaka, and T. Usuda. "An optically-selected cluster catalog at redshift 0.1¡z¡1.1 from the Hyper Suprime-Cam Subaru Strategic Program S16A data." *ArXiv e-prints* .

Oort, J. H. "The force exerted by the stellar system in the direction perpendicular to the galactic plane and some related problems." *Bull. Astron. Inst. Netherlands* 6: (1932) 249.

Pacaud, F., N. Clerc, P. A. Giles, C. Adami, T. Sadibekova, M. Pierre, B. J. Maughan, M. Lieu, J. P. Le Fèvre, S. Alis, B. Altieri, F. Ardila, I. Baldry, C. Benoist, M. Birkinshaw, L. Chiappetti, J. Démoclès, D. Eckert, A. E. Evrard, L. Faccioli, F. Gastaldello, L. Guennou, C. Horellou, A. Iovino, E. Koulouridis, V. Le Brun, C. Lidman, J. Liske, S. Maurogordato, F. Menanteau, M. Owers, B. Poggianti, D. Pomarède, E. Pompei, T. J. Ponman, D. Rapetti, T. H. Reiprich, G. P. Smith, R. Tuffs, P. Valageas, I. Valtchanov, J. P. Willis, and F. Ziparo. "The XXL Survey. II. The bright cluster sample: catalogue and luminosity function." *A&A* 592: A2.

Pacaud, F., M. Pierre, C. Adami, B. Altieri, S. Andreon, L. Chiappetti, A. Detal, P.-A. Duc, G. Galaz, A. Gueguen, J.-P. Le Fèvre, G. Hertling, C. Libbrecht, J.-B. Melin, T. J. Ponman, H. Quintana, A. Refregier, P.-G. Sprimont, J. Surdej, I. Valtchanov, J. P. Willis, D. Alloin, M. Birkinshaw, M. N. Bremer, O. Garcet, C. Jean, L. R. Jones, O. Le Fèvre, D. Maccagni, A. Mazure, D. Proust, H. J. A. Röttgering, and G. Trinchieri. "The XMM-LSS survey: the Class 1 cluster sample over the initial 5 deg^2 and its cosmological modelling." *MNRAS* 382: (2007) 1289–1308.

Paz, D., M. Lares, L. Ceccarelli, N. Padilla, and D. G. Lambas. "Clues on void evolution-II. Measuring density and velocity profiles on SDSS galaxy redshift space distortions." *MNRAS* 436: (2013) 3480–3491.

Peacock, J. A. *Cosmological Physics*. 1999.

Penzias, A. A., and R. W. Wilson. "A Measurement of Excess Antenna Temperature at 4080 Mc/s." *ApJ* 142: (1965) 419–421.

Percival, W. J., B. A. Reid, D. J. Eisenstein, N. A. Bahcall, T. Budavari, J. A. Frieman, M. Fukugita, J. E. Gunn, Ž. Ivezić, G. R. Knapp, R. G. Kron, J. Loveday, R. H. Lupton, T. A. McKay, A. Meiksin, R. C. Nichol, A. C. Pope, D. J. Schlegel, D. P. Schneider, D. N. Spergel, C. Stoughton, M. A. Strauss, A. S. Szalay, M. Tegmark, M. S. Vogeley, D. H. Weinberg, D. G. York, and I. Zehavi. "Baryon acoustic oscillations in the Sloan Digital Sky Survey Data Release 7 galaxy sample." *MNRAS* 401: (2010) 2148–2168.

Piffaretti, R., M. Arnaud, G. W. Pratt, E. Pointecouteau, and J.-B. Melin. "The MCXC: a meta-catalogue of x-ray detected clusters of galaxies." *A&A* 534: A109.

Planck Collaboration, P. A. R. Ade, N. Aghanim, C. Armitage-Caplan, M. Arnaud, M. Ashdown, F. Atrio-Barandela, J. Aumont, H. Aussel, C. Baccigalupi, and et al. "Planck 2013 results. XXIX. The Planck catalogue of Sunyaev-Zeldovich sources." *A&A* 571: A29.

Planck Collaboration, P. A. R. Ade, N. Aghanim, C. Armitage-Caplan, M. Arnaud, M. Ashdown, F. Atrio-Barandela, J. Aumont, C. Baccigalupi, A. J. Banday, and et al. "Planck 2013 results. XX. Cosmology from Sunyaev-Zeldovich cluster counts." *A&A* 571: A20.

Planck Collaboration, P. A. R. Ade, N. Aghanim, M. Arnaud, M. Ashdown, J. Aumont, C. Baccigalupi, A. J. Banday, R. B. Barreiro, R. Barrena, and et al. "Planck 2015 results. XXVII. The second Planck catalogue of Sunyaev-Zeldovich sources." *A&A* 594: A27.

Planck Collaboration, P. A. R. Ade, N. Aghanim, M. Arnaud, M. Ashdown, J. Aumont, C. Baccigalupi, A. J. Banday, R. B. Barreiro, J. G. Bartlett, and et al. "Planck 2015 results. XIII. Cosmological parameters." *A&A* 594: A13.

Plionis, M., J. D. Barrow, and C. S. Frenk. "Projected and intrinsic shapes of galaxy clusters." *MNRAS* 249: (1991) 662–677.

Poggianti, B. M. "K and evolutionary corrections from UV to IR." *A&AS* 122: (1997) 399–407.

Poole, G. B., A. Babul, I. G. McCarthy, M. A. Fardal, C. J. Bildfell, T. Quinn, and A. Mahdavi. "The impact of mergers on relaxed X-ray clusters - II. Effects on global X-ray and Sunyaev-Zel'dovich properties and their scaling relations." *MNRAS* 380: (2007) 437–454.

Poudel, A., P. Heinämäki, P. Nurmi, P. Teerikorpi, E. Tempel, H. Lietzen, and M. Einasto. "Multifrequency studies of galaxies and groups. I. Environmental effect on galaxy stellar mass and morphology." *A&A* 590: A29.

Prada, F., A. A. Klypin, A. J. Cuesta, J. E. Betancort-Rijo, and J. Primack. "Halo concentrations in the standard Λ cold dark matter cosmology." *MNRAS* 423: (2012) 3018–3030.

Predehl, P., H. Böhringer, H. Brunner, M. Brusa, V. Burwitz, N. Cappelluti, E. Churazov, K. Dennerl, M. Freyberg, P. Friedrich, G. Hasinger, E. Kendziorra, I. Kreykenbohm, C. Schmid, J. Wilms, G. Lamer, N. Meidinger, M. Mühlegger, M. Pavlinsky, J. Robrade, A. Santangelo, J. Schmitt, A. Schwope, M. Steinmetz, L. Strüder, R. Sunyaev, and C. Tenzer. "eROSITA on SRG." *X-ray Astronomy 2009; Present Status, Multi-Wavelength Approach and Future Perspectives* 1248: (2010) 543–548.

Randall, S. W., C. L. Sarazin, and P. M. Ricker. "The Effect of Merger Boosts on the Luminosity, Temperature, and Inferred Mass Functions of Clusters of Galaxies." *ApJ* 577: (2002) 579–594.

Reiprich, T. H., and H. Böhringer. "The Mass Function of an X-Ray Flux-limited Sample of Galaxy Clusters." *ApJ* 567: (2002) 716–740.

Ricciardelli, E., A. Cava, J. Varela, and A. Tamone. "Morphological Segregation in the Surroundings of Cosmic Voids." *ApJ* 846: L4.

Ritchie, B. W., and P. A. Thomas. "Hydrodynamic simulations of merging clusters of galaxies." *MNRAS* 329: (2002) 675–688.

Robertson, H. P. "Kinematics and World-Structure." *ApJ* 82: (1935) 284.

Robitaille, T., and E. Bressert. "APLpy: Astronomical Plotting Library in Python." Astrophysics Source Code Library, 2012.

Romer, A. K., P. T. P. Viana, A. R. Liddle, and R. G. Mann. "A Serendipitous Galaxy Cluster Survey with XMM: Expected Catalog Properties and Scientific Applications." *ApJ* 547: (2001) 594–608.

Rosati, P., R. Della Ceca, C. Norman, and R. Giacconi. "The ROSAT Deep Cluster Survey: The X-Ray Luminosity Function out to z = 0.8." *ApJ* 492: (1998) L21–L24.

Rozo, E., E. Rykoff, B. Koester, B. Nord, H.-Y. Wu, A. Evrard, and R. Wechsler. "Extrinsic Sources of Scatter in the Richness-mass Relation of Galaxy Clusters." *ApJ* 740: 53.

Rozo, E., and E. S. Rykoff. "redMaPPer II: X-Ray and SZ Performance Benchmarks for the SDSS Catalog." *ApJ* 783: 80.

Rozo, E., R. H. Wechsler, E. S. Rykoff, J. T. Annis, M. R. Becker, A. E. Evrard, J. A. Frieman, S. M. Hansen, J. Hao, D. E. Johnston, B. P. Koester, T. A. McKay, E. S. Sheldon, and D. H. Weinberg. "Cosmological Constraints from the Sloan Digital Sky Survey maxBCG Cluster Catalog." *ApJ* 708: (2010) 645–660.

Rudnick, L., S. Brown, and L. R. Williams. "Extragalactic Radio Sources and the WMAP Cold Spot." *ApJ* 671: (2007) 40–44.

Rykoff, E. S., E. Rozo, M. T. Busha, C. E. Cunha, A. Finoguenov, A. Evrard, J. Hao, B. P. Koester, A. Leauthaud, B. Nord, M. Pierre, R. Reddick, T. Sadibekova, E. S. Sheldon, and R. H. Wechsler. "redMaPPer. I. Algorithm and SDSS DR8 Catalog." *ApJ* 785: 104.

Rykoff, E. S., E. Rozo, D. Hollowood, A. Bermeo-Hernandez, T. Jeltema, J. Mayers, A. K. Romer, P. Rooney, A. Saro, C. Vergara Cervantes, R. H. Wechsler, H. Wilcox, T. M. C. Abbott, F. B. Abdalla, S. Allam, J. Annis, A. Benoit-Lévy, G. M. Bernstein, E. Bertin, D. Brooks, D. L. Burke, D. Capozzi, A. Carnero Rosell, M. Carrasco Kind, F. J. Castander, M. Childress, C. A. Collins, C. E. Cunha, C. B. D'Andrea, L. N. da Costa, T. M. Davis, S. Desai, H. T. Diehl, J. P. Dietrich, P. Doel, A. E. Evrard, D. A. Finley, B. Flaugher, P. Fosalba, J. Frieman, K. Glazebrook, D. A. Goldstein, D. Gruen, R. A. Gruendl, G. Gutierrez, M. Hilton,

K. Honscheid, B. Hoyle, D. J. James, S. T. Kay, K. Kuehn, N. Kuropatkin, O. Lahav, G. F. Lewis, C. Lidman, M. Lima, M. A. G. Maia, R. G. Mann, J. L. Marshall, P. Martini, P. Melchior, C. J. Miller, R. Miquel, J. J. Mohr, R. C. Nichol, B. Nord, R. Ogando, A. A. Plazas, K. Reil, M. Sahlén, E. Sanchez, B. Santiago, V. Scarpine, M. Schubnell, I. Sevilla-Noarbe, R. C. Smith, M. Soares-Santos, F. Sobreira, J. P. Stott, E. Suchyta, M. E. C. Swanson, G. Tarle, D. Thomas, D. Tucker, S. Uddin, P. T. P. Viana, V. Vikram, A. R. Walker, Y. Zhang, and DES Collaboration. "The RedMaPPer Galaxy Cluster Catalog From DES Science Verification Data." *ApJS* 224: 1.

Sachs, R. K., and A. M. Wolfe. "Perturbations of a Cosmological Model and Angular Variations of the Microwave Background." *ApJ* 147: (1967) 73.

Sahlén, M., P. T. P. Viana, A. R. Liddle, A. K. Romer, M. Davidson, M. Hosmer, E. Lloyd-Davies, K. Sabirli, C. A. Collins, P. E. Freeman, M. Hilton, B. Hoyle, S. T. Kay, R. G. Mann, N. Mehrtens, C. J. Miller, R. C. Nichol, S. A. Stanford, and M. J. West. "The XMM Cluster Survey: forecasting cosmological and cluster scaling-relation parameter constraints." *MNRAS* 397: (2009) 577–607.

Scharf, C. A., H. Ebeling, E. Perlman, M. Malkan, and G. Wegner. "The Wide-Angle ROSAT Pointed X-Ray Survey of Galaxies, Groups, and Clusters. I. Method and First Results." *ApJ* 477: (1997) 79–92.

Schechter, P. "An analytic expression for the luminosity function for galaxies." *ApJ* 203: (1976) 297–306.

Scodeggio, M., L. Guzzo, B. Garilli, B. R. Granett, M. Bolzonella, S. de la Torre, U. Abbas, C. Adami, S. Arnouts, D. Bottini, A. Cappi, J. Coupon, O. Cucciati, I. Davidzon, P. Franzetti, A. Fritz, A. Iovino, J. Krywult, V. Le Brun, O. Le Févre, D. Maccagni, K. Malek, A. Marchetti, F. Marulli, M. Polletta, A. Pollo, L. A. M. Tasca, R. Tojeiro, D. Vergani, A. Zanichelli, J. Bel, E. Branchini, G. De Lucia, O. Ilbert, H. J. McCracken, T. Moutard, J. A. Peacock, G. Zamorani, A. Burden, M. Fumana, E. Jullo, C. Marinoni, Y. Mellier, L. Moscardini, and W. J. Percival. "The VIMOS Public Extragalactic Redshift Survey (VIPERS). Full spectroscopic data and auxiliary information release (PDR-2)." *ArXiv e-prints* .

SDSS Collaboration, F. D. Albareti, C. Allende Prieto, A. Almeida, F. Anders, S. Anderson, B. H. Andrews, A. Aragon-Salamanca, M. Argudo-Fernandez, E. Armengaud, and et al. "The Thirteenth Data Release of the Sloan Digital Sky Survey: First Spectroscopic Data from the SDSS-IV Survey MApping Nearby Galaxies at Apache Point Observatory." *ArXiv e-prints* .

Sembolini, F., G. Yepes, M. De Petris, S. Gottlöber, L. Lamagna, and B. Comis. "The MUSIC of galaxy clusters - I. Baryon properties and scaling relations of the thermal Sunyaev-Zel'dovich effect." *MNRAS* 429: (2013) 323–343.

Shanks, T., N. Metcalfe, B. Chehade, J. R. Findlay, M. J. Irwin, E. Gonzalez-Solares, J. R. Lewis, A. K. Yoldas, R. G. Mann, M. A. Read, E. T. W. Sutorius, and S. Voutsinas. "The VLT Survey Telescope ATLAS." *MNRAS* 451: (2015) 4238–4252.

Shaw, L. D., G. P. Holder, and P. Bode. "The Impact of Halo Properties, Energy Feedback, and Projection Effects on the Mass-SZ Flux Relation." *ApJ* 686: 206-218.

Sheth, R. K., and R. van de Weygaert. "A hierarchy of voids: much ado about nothing." *MNRAS* 350: (2004) 517–538.

Smethurst, R. J., C. J. Lintott, S. P. Bamford, R. E. Hart, S. J. Kruk, K. L. Masters, R. C. Nichol, and B. D. Simmons. "Galaxy Zoo: the interplay of quenching mechanisms in the group environment." *MNRAS* 469: (2017) 3670–3687.

Smirnov, N. "Table for Estimating the Goodness of Fit of Empirical Distributions." *Ann. Math. Statist.* 19, 2: (1948) 279–281. http://dx.doi.org/10.1214/aoms/1177730256.

Springel, V. "The cosmological simulation code GADGET-2." *MNRAS* 364: (2005) 1105–1134.

Springel, V., C. S. Frenk, and S. D. M. White. "The large-scale structure of the Universe." *Nature* 440: (2006) 1137–1144.

Springel, V., S. D. M. White, A. Jenkins, C. S. Frenk, N. Yoshida, L. Gao, J. Navarro, R. Thacker, D. Croton, J. Helly, J. A. Peacock, S. Cole, P. Thomas, H. Couchman, A. Evrard, J. Colberg, and F. Pearce. "Simulations of the formation, evolution and clustering of galaxies and quasars." *Nature* 435: (2005) 629–636.

Springel, V., S. D. M. White, G. Tormen, and G. Kauffmann. "Populating a cluster of galaxies - I. Results at [formmu2]z=0." *MNRAS* 328: (2001) 726–750.

Stanford, S. A., A. K. Romer, K. Sabirli, M. Davidson, M. Hilton, P. T. P. Viana, C. A. Collins, S. T. Kay, A. R. Liddle, R. G. Mann, C. J. Miller, R. C. Nichol, M. J. West, C. J. Conselice, H. Spinrad, D. Stern, and K. Bundy. "The XMM Cluster Survey: A Massive Galaxy Cluster at z = 1.45." *ApJ* 646: (2006) L13–L16.

Steinhardt, P. J. "Quintessence and the Missing Energy Problem." *Physica Scripta Volume T* 85: (2000) 177–182.

Stott, J. P., C. A. Collins, M. Sahlén, M. Hilton, E. Lloyd-Davies, D. Capozzi, M. Hosmer, A. R. Liddle, N. Mehrtens, C. J. Miller, A. K. Romer, S. A. Stanford, P. T. P. Viana, M. Davidson, B. Hoyle, S. T. Kay, and R. C. Nichol. "The XMM Cluster Survey: The Build-up of Stellar Mass in Brightest Cluster Galaxies at High Redshift." *ApJ* 718: (2010) 23–30.

Stott, J. P., R. C. Hickox, A. C. Edge, C. A. Collins, M. Hilton, C. D. Harrison, A. K. Romer, P. J. Rooney, S. T. Kay, C. J. Miller, M. Sahlén, E. J. Lloyd-Davies, N. Mehrtens, B. Hoyle, A. R. Liddle, P. T. P. Viana, I. G. McCarthy, J. Schaye, and C. M. Booth. "The XMM Cluster Survey: the interplay between the brightest cluster galaxy and the intracluster medium via AGN feedback." *MNRAS* 422: (2012) 2213–2229.

Sunyaev, R. A., and Y. B. Zeldovich. "Small-Scale Fluctuations of Relic Radiation." *Ap&SS* 7: (1970) 3–19.

Sutter, P. M., G. Lavaux, B. D. Wandelt, D. H. Weinberg, M. S. Warren, and A. Pisani. "Voids in the SDSS DR9: observations, simulations, and the impact of the survey mask." *MNRAS* 442: (2014) 3127–3137.

Takey, A., A. Schwope, and G. Lamer. "The 2XMMi/SDSS Galaxy Cluster Survey. II. The optically confirmed cluster sample and the L_X - T relation." *A&A* 558: A75.

The Astropy Collaboration, A. M. Price-Whelan, B. M. Sipőcz, H. M. Günther, P. L. Lim, S. M. Crawford, S. Conseil, D. L. Shupe, M. W. Craig, N. Dencheva, A. Ginsburg, J. T. VanderPlas, L. D. Bradley, D. Pérez-Suárez, M. de Val-Borro, T. L. Aldcroft, K. L. Cruz, T. P. Robitaille, E. J. Tollerud, C. Ardelean, T. Babej, M. Bachetti, A. V. Bakanov, S. P. Bamford, G. Barentsen, P. Barmby, A. Baumbach, K. L. Berry, F. Biscani, M. Boquien, K. A. Bostroem, L. G. Bouma, G. B. Brammer, E. M. Bray, H. Breytenbach, H. Buddelmeijer, D. J. Burke, G. Calderone, J. L. Cano Rodríguez, M. Cara, J. V. M. Cardoso, S. Cheedella, Y. Copin, D. Crichton, D. DÁvella, C. Deil, É. Depagne, J. P. Dietrich, A. Donath, M. Droettboom, N. Earl, T. Erben, S. Fabbro, L. A. Ferreira, T. Finethy, R. T. Fox, L. H. Garrison, S. L. J. Gibbons, D. A. Goldstein, R. Gommers, J. P. Greco, P. Greenfield, A. M. Groener, F. Grollier, A. Hagen, P. Hirst, D. Homeier, A. J. Horton, G. Hosseinzadeh, L. Hu, J. S. Hunkeler, Ž. Ivezić, A. Jain, T. Jenness, G. Kanarek, S. Kendrew, N. S. Kern, W. E. Kerzendorf, A. Khvalko, J. King, D. Kirkby, A. M. Kulkarni, A. Kumar, A. Lee, D. Lenz, S. P. Littlefair, Z. Ma, D. M. Macleod, M. Mastropietro, C. McCully, S. Montagnac, B. M. Morris, M. Mueller, S. J. Mumford, D. Muna, N. A. Murphy, S. Nelson, G. H. Nguyen, J. P. Ninan, M. Nöthe, S. Ogaz, S. Oh, J. K. Parejko, N. Parley, S. Pascual, R. Patil, A. A. Patil, A. L. Plunkett, J. X. Prochaska, T. Rastogi, V. Reddy Janga, J. Sabater, P. Sakurikar, M. Seifert, L. E. Sherbert, H. Sherwood-Taylor, A. Y. Shih, J. Sick, M. T. Silbiger, S. Singanamalla, L. P. Singer, P. H. Sladen, K. A. Sooley, S. Sornarajah, O. Streicher, P. Teuben, S. W. Thomas, G. R. Tremblay, J. E. H. Turner, V. Terrón, M. H. van Kerkwijk, A. de la Vega, L. L. Watkins, B. A. Weaver, J. B. Whitmore, J. Woillez, and V. Zabalza. "The Astropy Project: Building an inclusive, open-science project and status of the v2.0 core package." *ArXiv e-prints* .

Tovmassian, H. M. "Do clusters of galaxies rotate?" *ArXiv Astrophysics e-prints* .

———. "The Rotation of Galaxy Clusters." *Astrophysics* 58: (2015) 328–337.

Tremaine, S. D., and D. O. Richstone. "A test of a statistical model for the luminosities of bright cluster galaxies." *ApJ* 212: (1977) 311–316.

van Haarlem, M. P., C. S. Frenk, and S. D. M. White. "Projection effects in cluster catalogues." *MNRAS* 287: (1997) 817–832.

Varela, J., J. Betancort-Rijo, I. Trujillo, and E. Ricciardelli. "The Orientation of Disk Galaxies around Large Cosmic Voids." *ApJ* 744: 82.

Vergara-Cervantes et al., C. .

Viana, P. T. P., A. da Silva, E. P. R. G. Ramos, A. R. Liddle, E. J. Lloyd-Davies, A. K. Romer, S. T. Kay, C. A. Collins, M. Hilton, M. Hosmer, B. Hoyle, J. A. Mayers, N. Mehrtens, C. J. Miller, M. Sahlén, S. A. Stanford, and J. P. Stott. "The XMM Cluster Survey: predicted overlap with the Planck Cluster Catalogue." *MNRAS* 422: (2012) 1007–1013.

Viana, P. T. P., N. Mehrtens, C. D. Harrison, A. K. Romer, C. A. Collins, M. Hilton, B. Hoyle, S. T. Kay, A. R. Liddle, J. A. Mayers, C. J. Miller, P. J. Rooney, M. Sahlén, and J. P. Stott. "The XMM Cluster Survey: Present status and latest results." *Astronomische Nachrichten* 334: (2013) 462.

Vikhlinin, A., R. A. Burenin, H. Ebeling, W. R. Forman, A. Hornstrup, C. Jones, A. V. Kravtsov, S. S. Murray, D. Nagai, H. Quintana, and A. Voevodkin. "Chandra Cluster Cosmology Project. II. Samples and X-Ray Data Reduction." *ApJ* 692: (2009a) 1033–1059.

Vikhlinin, A., A. V. Kravtsov, R. A. Burenin, H. Ebeling, W. R. Forman, A. Hornstrup, C. Jones, S. S. Murray, D. Nagai, H. Quintana, and A. Voevodkin. "Chandra Cluster Cosmology Project III: Cosmological Parameter Constraints." *ApJ* 692: (2009b) 1060–1074.

Vikhlinin, A., S. Murray, R. Gilli, P. Tozzi, M. Paolillo, N. Brandt, G. Tagliaferri, M. Bautz, S. Allen, M. Donahue, A. Evrad, K. Flanagan, P. Rosati, S. Borgani, R. Giacconi, M. Weisskopf, A. Ptak, D. Alexander, G. Pareschi, W. Forman, and C. Jones. "X-ray Cluster Cosmology." In *astro2010: The Astronomy and Astrophysics Decadal Survey*. 2009c, volume 2010 of *Astronomy*.

Walker, A. G. "On the formal comparison of Milne's kinematical system with the systems of general relativity." *MNRAS* 95: (1935) 263–269.

Wang, L., P. Norberg, S. Brough, M. J. I. Brown, E. da Cunha, L. J. Davies, S. P. Driver, B. W. Holwerda, A. M. Hopkins, M. A. Lara-Lopez, J. Liske, J. Loveday, M. W. Grootes, C. C. Popescu, and A. H. Wright. "Galaxy And Mass Assembly (GAMA): The environmental dependence of the galaxy main sequence." *ArXiv e-prints* .

Weigel, A. K., K. Schawinski, N. Caplar, A. Carpineti, R. E. Hart, S. Kaviraj, W. C. Keel, S. J. Kruk, C. J. Lintott, R. C. Nichol, B. D. Simmons, and R. J. Smethurst. "Galaxy Zoo: Major Galaxy Mergers Are Not a Significant Quenching Pathway." *ApJ* 845: 145.

Wen, Z. L., and J. L. Han. "Calibration of the Optical Mass Proxy for Clusters of Galaxies and an Update of the WHL12 Cluster Catalog." *ApJ* 807: 178.

Wen, Z. L., J. L. Han, and F. S. Liu. "A Catalog of 132,684 Clusters of Galaxies Identified from Sloan Digital Sky Survey III." *ApJS* 199: 34.

Wilcox, H., D. Bacon, R. C. Nichol, P. J. Rooney, A. Terukina, A. K. Romer, K. Koyama, G.-B. Zhao, R. Hood, R. G. Mann, M. Hilton, M. Manolopoulou, M. Sahlén, C. A. Collins, A. R. Liddle, J. A. Mayers, N. Mehrtens, C. J. Miller, J. P. Stott, and P. T. P. Viana. "The XMM Cluster Survey: testing chameleon gravity using the profiles of clusters." *MNRAS* 452: (2015) 1171–1183.

Wilson, S., M. Hilton, P. J. Rooney, C. Caldwell, S. T. Kay, C. A. Collins, I. G. McCarthy, A. K. Romer, A. Bermeo, R. Bernstein, L. da Costa, D. Gifford, D. Hollowood, B. Hoyle, T. Jeltema, A. R. Liddle, M. A. G. Maia, R. G. Mann, J. A. Mayers, N. Mehrtens, C. J. Miller, R. C. Nichol, R. Ogando, M. Sahlén, B. Stahl, J. P. Stott, P. A. Thomas, P. T. P. Viana, and H. Wilcox. "The XMM Cluster Survey: evolution of the velocity dispersion-temperature relation over half a Hubble time." *MNRAS* 463: (2016) 413–428.

Zhang, Y., C. Miller, T. McKay, P. Rooney, A. E. Evrard, A. K. Romer, R. Perfecto, J. Song, S. Desai, J. Mohr, H. Wilcox, A. Bermeo-Hernandez, T. Jeltema, D. Hollowood, D. Bacon, D. Capozzi, C. Collins, R. Das, D. Gerdes, C. Hennig, M. Hilton, B. Hoyle, S. Kay, A. Liddle, R. G. Mann, N. Mehrtens, R. C. Nichol, C. Papovich, M. Sahlén, M. Soares-Santos, J. Stott, P. T. Viana, T. Abbott, F. B. Abdalla, M. Banerji, A. H. Bauer, A. Benoit-Lévy, E. Bertin, D. Brooks, E. Buckley-Geer, D. L. Burke, A. Carnero Rosell, F. J. Castander, H. T. Diehl, P. Doel, C. E. Cunha, T. F. Eifler, A. Fausti Neto, E. Fernandez, B. Flaugher, P. Fosalba, J. Frieman, E. Gaztanaga, D. Gruen, R. A. Gruendl, K. Honscheid, D. James, K. Kuehn, N. Kuropatkin, O. Lahav, M. A. G. Maia, M. Makler, J. L. Marshall, P. Martini, R. Miquel, R. Ogando, A. A. Plazas, A. Roodman, E. S. Rykoff, M. Sako, E. Sanchez, V. Scarpine, M. Schubnell, I. Sevilla, R. C. Smith, F. Sobreira, E. Suchyta, M. E. C. Swanson, G. Tarle, J. Thaler, D. Tucker, V. Vikram, and L. N. da Costa. "Galaxies in X-Ray Selected Clusters and Groups in Dark Energy Survey Data. I. Stellar Mass Growth of Bright Central Galaxies since z˜1.2." *ApJ* 816: 98.

Zhang, Y., C. J. Miller, P. Rooney, A. Bermeo, A. K. Romer, C. Vergara cervantes, E. S. Rykoff, C. Hennig, R. Das, T. Mckay, J. Song, H. Wilcox, D. Bacon, S. L. Bridle, C. Collins, C. Conselice, M. Hilton, B. Hoyle, S. Kay, A. R. Liddle, R. G. Mann, N. Mehrtens, J. Mayers, R. C. Nichol, M. Sahlen, J. Stott, P. T. P. Viana, R. H. Wechsler, T. Abbott, F. B. Abdalla, S. Allam, A. Benoit-levy, D. Brooks, E. Buckley-geer, D. L. Burke, A. Carnero rosell, M. Carrasco kind, J. Carretero, F. J. Castander, M. Crocce, C. E. Cunha, C. B. Dandrea, L. N. Da costa, H. T. Diehl, J. P. Dietrich, T. F. Eifler, B. Flaugher, P. Fosalba, J. Garcia-bellido, E. Gaztanaga, D. W. Gerdes, D. Gruen, R. A. Gruendl, J. Gschwend, G. Gutierrez, K. Honscheid, D. J. James, T. Jeltema, K. Kuehn, N. Kuropatkin, M. Lima, H. Lin, M. A. G. Maia, M. March, J. L. Marshall, P. Melchior, F. Menanteau, R. Miquel, R. L. C. Ogando, A. A. Plazas, E. Sanchez, M. Schubnell, I. Sevilla-noarbe, M. Smith, M. Soares-santos, F. Sobreira, E. Suchyta, M. E. C. Swanson, G. Tarle, and A. R. Walker. "Galaxies in X-ray Selected Clusters and Groups in Dark Energy Survey Data II: Hierarchical Bayesian Modeling of Red-Sequence Galaxy Luminosity Function." *ArXiv e-prints* .

Zhang, Y.-Y., N. Okabe, A. Finoguenov, G. P. Smith, R. Piffaretti, R. Valdarnini, A. Babul, A. E. Evrard, P. Mazzotta, A. J. R. Sanderson, and D. P. Marrone. "LoCuSS: A Comparison of Cluster Mass Measurements from XMM-Newton and Subaru—Testing Deviation from Hydrostatic Equilibrium and Non-thermal Pressure Support." *ApJ* 711: (2010) 1033–1043.

Zhang et al., Y. .

Zwicky, F. "Die Rotverschiebung von extragalaktischen Nebeln." *Helvetica Physica Acta* 6: (1933) 110–127.

Zwicky, F., E. Herzog, P. Wild, M. Karpowicz, and C. T. Kowal. *Catalogue of galaxies and of clusters of galaxies, Vol. I*. 1961.